



**USE OF DIMPLES TO SUPPRESS
BOUNDARY LAYER SEPARATION ON A
LOW PRESSURE TURBINE BLADE**

THESIS

Kurt P. Rouser, Captain, USAF

AFIT/GAE/ENY/02-13

**DEPARTMENT OF THE AIR FORCE
AIR UNIVERSITY**

AIR FORCE INSTITUTE OF TECHNOLOGY

Wright-Patterson Air Force Base, Ohio

APPROVED FOR PUBLIC RELEASE; DISTRIBUTION UNLIMITED.

The views expressed in this thesis are those of the author and do not reflect the official policy or position of the United States Air Force, Department of Defense, or the United States Government.

AFIT/GAE/ENY/02-13

USE OF DIMPLES TO SUPPRESS BOUNDARY LAYER SEPARATION ON A
LOW PRESSURE TURBINE BLADE

THESIS

Presented to the Faculty
Department of Aeronautics and Astronautics
Graduate School of Engineering and Management
Air Force Institute of Technology
Air University
Air Education and Training Command
In Partial Fulfillment of the Requirements for the
Degree of Master of Science in Aeronautical Engineering

Kurt P. Rouser, BS, MS

Captain, USAF

December 2002

APPROVED FOR PUBLIC RELEASE; DISTRIBUTION UNLIMITED.

USE OF DIMPLES TO SUPPRESS BOUNDARY LAYER SEPARATION ON A
LOW PRESSURE TURBINE BLADE

Kurt P. Rouser, BS, MS
Captain, USAF

Approved:

/signed/

Dr. Paul I. King (Chairman)

date

/signed/

LtCol Raymond C. Maple (Member)

date

/signed/

Maj Richard J. McMullan (Member)

date

ACKNOWLEDGMENTS

I would like to express my sincere appreciation to my faculty advisor, Dr. Paul King, for his guidance and support throughout the course of this thesis. I would, also, like to thank my sponsor, Dr. Rolf Sondergaard, from the Air Force Research Laboratory. I am grateful for his timely support and latitude. His knowledge and expertise during experimental data collection and analysis were invaluable.

This work was also supported in part by a grant of computer time from the DOD High Performance Computing Modernization Program at ASC MSRC. I am especially indebted to Dr. Hugh Thornburg who invested much of his time and skill in helping to produce and refine computational models and teach me CFD fundamentals. Special thanks are also in order for the MSRC personnel who were so helpful in collecting computational results.

I also want to thank the members of my thesis committee who provided first rate advice through out my research. I am especially thankful for LtCol Maple's support in the computer lab.

Additionally, I am grateful for the regular assistance from the 88th Weather Squadron, especially from Mr. Ron Caldwell and TSgt Donald Shane.

Lastly, and most important, I want to thank my wife and parents for their unwavering support and inspiration. I could not have done this without you.

Kurt P. Rouser

TABLE OF CONTENTS

	Page
Acknowledgments.....	iv
List of Figures.....	ix
List of symbols.....	xviii
Abstract	xxiii
Chapter 1. Introduction.....	1
1.1 Low Pressure Turbine Operation at Low Reynolds Numbers	3
1.2 Previous Experiments in Flow Separation on LPT Blades.....	4
1.3 Current Research Objectives.....	6
1.4 Chapter Summary	8
Chapter 2. BACKGROUND AND THEORY	9
2.1 Low Pressure Turbine Performance Evaluation	10
2.2 Low Pressure Turbine Boundary Layer Aerodynamics.....	16
2.2.1 Experimental Laminar-to-Turbulent Boundary Layer Transition	16
2.2.2 Numerical Models for Low Pressure Turbine Performance	17
2.3 Separation Control on Low Pressure Turbines	19
2.3.1 Active and Passive Controls	19
2.3.2 Previous Research in Dimples for Boundary Layer Control	23
Chapter 3. COMPUTATIONAL RESULTS AND ANALYSIS	26
3.1 Computational Software	27

	Page	
3.2	Grid Model Characteristics	28
3.2.1	Baseline Pak-B Grid Topology	29
3.2.2	Grid Topology for Pak-B with Spherical Dimples	30
3.2.3	Grid Topology for the Pak-B with Asymmetric Dimples.....	32
3.3	Flow Solver Characteristics	34
3.4	Computational Results	35
3.4.4	Velocity Profile Contours	36
3.4.5	Total Pressure Profile Contours	38
3.4.6	Static Pressure Profile Contours	40
3.4.7	Surface Pressure Coefficient Profiles	43
3.4.8	Location of Separation, Reattachment and Vortex Cores.....	46
3.4.9	Flow Structure Visualization	49
3.5	Summary and Conclusions of Computational Research.....	54
Chapter 4.	EXPERIMENTAL RESULTS AND ANALYSIS	55
4.1	Wind Tunnel and Cascade Characteristics	55
4.1.1	Wind Tunnel Geometry and Features	56
4.1.2	Cascade Features.....	57
4.1.3	Data Collection Locations.....	59
4.1.4	Test Section Characteristics	62
4.2	Instrumentation	69
4.2.1	Pressure Instrumentation.....	71

	Page	
4.2.2	Velocity Instrumentation	73
4.2.3	Temperature Instrumentation.....	77
4.3	Data Collection Methodology.....	77
4.3.1	Surface Pressure Scans	77
4.3.2	Boundary Layer Traverses.....	78
4.3.3	Inlet and Exit Traverses	79
4.4	Surface Pressure Coefficient Profiles	81
4.5	Boundary Layer Velocity and Turbulence Profiles	85
4.5.1	Boundary Layer Profiles for Baseline Pak-B at Tu 1%.....	86
4.5.2	Boundary Layer Profiles for Pak-B with Asymmetric Dimples at 55% and 65% axial chord at Tu 1%.....	88
4.6	Wake Velocity Pressure Profiles	92
4.6.1	Wake Velocity Profiles for Baseline Pak-B.....	92
4.6.2	Wake Velocity Profiles for Pak-B with Asymmetric and Spherical Dimples at 55% and 65% Axial Chord at Tu 1%	93
4.7	Pressure Loss Coefficient	96
4.7.1	Total Pressure Loss Coefficient Profiles for Baseline Pak-B	98
4.7.2	Total Pressure Loss Coefficient Profiles for a Pak-B with Asymmetric and Spherical Dimples at 55% and 65% Axial Chord at Tu 1%	101
4.7.3	Comparison of Average Total Pressure Loss Coefficients	103
4.8	Summary and Conclusions of Experimental Research.....	107
Chapter 5.	SUMMARY AND RECOMMENDATIONS.....	108
References	111

	Page
Appendix A. Experimental Data Collection Procedures	115
A.1 Pressure Transducer Calibration	115
A.2 Hot Wire and Hot Film Calibration	116
Appendix B. Boundary Layer Profiles	125
Appendix C. Wake Velocity Profiles	149
Appendix D. Local Total Pressure Loss Coefficient Profiles	163
Vita	177

LIST OF FIGURES

	Page
Figure 1. TeledyneRQ-4 Global Hawk UAV (illustration by Virginia Reyes).....	1
Figure 2. Unsteady wake passing over Pak-B airfoil	4
Figure 3. Lake's Pak-B blade with dimples at 50%, 55% and 65% axial chord (1).....	7
Figure 4. Brayton cycle for an ideal gas turbine engine.....	11
Figure 5. T-S diagram for a non-ideal turbine stage	13
Figure 6. T-S diagram illustrating possible improvement with higher turbine exit total pressure (1)	14
Figure 7. Linear relationship between reduction in loss coefficient and improvement in stage efficiency (1)	15
Figure 8. Three protruding surface vortex generator devices. Profile and surface views are shown with air flow depicted as an arrow (1).....	20
Figure 9. Various other vortex generator devices. Profile and surface views are shown with air flow depicted as an arrow (1).....	21
Figure 10. Porous surface separation control devices. Profile and surface views are shown with air flow depicted as an arrow (1).....	22
Figure 11. Various vortex generator devices with difficult application. Profile and surface views are shown with air flow depicted as an arrow (1).....	22
Figure 12. Baseline Pak-B surface topology	30
Figure 13. Baseline Pak-B mid-passage grid topology	31
Figure 14. Grid Topology for the Pak-B blade with spherical dimples	32
Figure 15. Grid Topology for the Pak-B blade with asymmetric dimples	33
Figure 16. CFD velocity magnitude profile contours for a baseline Pak-B blade at Re 25k with the legend shown in m/s	37

	Page
Figure 17. CFD velocity magnitude profile contours for a Pak-B blade with spherical dimples at 60% axial chord at Re 25k with the legend shown in m/s.....	37
Figure 18. CFD velocity magnitude profile contours for a Pak-B blade with asymmetric dimples at 60% axial chord at Re 25k with the legend shown in m/s.....	38
Figure 19. CFD total pressure contours for a baseline Pak-B blade at Re 25k with the legend shown in Pa	39
Figure 20. CFD total pressure profile contours for a Pak-B blade with spherical dimples at 60% axial chord at Re 25k with the legend shown in Pa	39
Figure 21. CFD total pressure contours for a Pak-B blade with asymmetric dimples at 60% axial chord at Re 25k with the legend shown in Pa	40
Figure 22. Static pressure contours on a baseline Pak-B blade from CFD results at Re 25k with the legend in Pa	41
Figure 23. Static pressure contours on a Pak-B blade with a spherical dimple at 60% axial chord from CFD results at Re 25k with the legend in Pa.....	42
Figure 24. Static pressure contours on a Pak-B blade with an asymmetric dimple at 60% axial chord from CFD results at Re 25k with the legend in Pa	43
Figure 25. CFD surface pressure coefficient comparison between Pak-B baseline, Pak-B with spherical dimples and Pak-B with asymmetric dimples at Re 25k. Profiles are aligned with the Pak-B profile	45
Figure 26. Computational results for baseline Pak-B blade at Re 25k. Red indicates separation, and blue indicates reattachment. The suction surface is shown oriented with flow from left to right.....	47
Figure 27. Computational results for Pak-B blade with spherical dimples at 60% axial chord at Re 25k. Red indicates separation, blue indicates reattachment and yellow indicates the location of vortex cores. The suction surface is shown oriented with flow from left to right.....	48

	Page
Figure 28. Computational results for Pak-B blade with asymmetric dimples at 60% axial chord at Re 25k. Red indicates separation, blue indicates reattachment and yellow indicates the location of vortex cores. The suction surface is shown oriented with flow from left to right	49
Figure 29. CFD profile streamlines for a baseline Pak-B blade at Re 25k	50
Figure 30. CFD profile streamlines for a Pak-B blade with spherical dimples at 60% axial chord at Re 25k	51
Figure 31. CFD profile streamlines for a Pak-B blade with asymmetric dimples at 60% axial chord at Re 25k	51
Figure 32. CFD suction surface streamlines for a Pak-B blade with spherical dimples at 60% axial chord at Re 25k. The axial view shows flow from left to right.....	52
Figure 33. Enlarged view of CFD suction surface streamlines for a Pak-B blade with spherical dimples at 60% axial chord. The axial view shows flow from left to right.....	52
Figure 34. CFD suction surface streamlines for a Pak-B with asymmetric dimples at 60% axial chord at Re 25k. The axial view is shown with flow from top to bottom	53
Figure 35. Enlarged view of CFD suction surface streamlines for a Pak-B blade with asymmetric dimples at 60% axial chord at Re 25k. The axial view is shown with flow from left to right	53
Figure 36. Aerolab Corporation modified draw-down wind tunnel (illustration courtesy of AFRL)	55
Figure 37. Cross-sectional area of wind tunnel (1)	56
Figure 38. Turbulence grid. Passively generates Tu 4% (illustration courtesy of AFRL)	57
Figure 39. Removable cassette of eight Pak-B blades and endblade (illustration courtesy of AFRL)	58
Figure 40. Wind tunnel instrumentation locations (courtesy of AFRL)	60

	Page
Figure 41. Plan view of test section (illustration courtesy of AFRL)	63
Figure 42. Test section geometry	65
Figure 43. Test section inlet total pressure variation at Tu 1%.....	66
Figure 44. Test section inlet total pressure variation at Tu 4%.....	67
Figure 45. Test section inlet dynamic pressure variation at Tu 1%	68
Figure 46. Test section inlet dynamic pressure variation at Tu 4%	68
Figure 47. Instrumentation Schematic.....	69
Figure 48. Dead-weight tester schematic	71
Figure 49. Pressure instrumentation schematic	74
Figure 50. Process chart for correlating measured X-film angles and velocities.....	76
Figure 51. Comparison of current and previous experimental Cp curves for a baseline Pak-B blade at various Reynold's numbers and inlet freestream turbulence of 1%	82
Figure 52. Comparison of current and previous experimental Cp curves for a baseline Pak-B blade at various Reynold's numbers and inlet freestream turbulence of 4%	83
Figure 53. Comparison of CFD and experimental surface pressure coefficient profiles at Re 25k	84
Figure 54. Reynolds effect on boundary layer profiles of baseline Pak-B at Tu 1%....	87
Figure 55. Boundary layer profiles for Pak-B configurations at Re 45k and Tu 1%....	89
Figure 56. Boundary layer profiles for Pak-B configurations at Re 25k and Tu 1%....	91
Figure 57. Reynolds number effect on exit velocity angles	93
Figure 58. Reynolds effect on wake velocity profile of a baseline Pak-B blade at Tu 1%.....	94

	Page
Figure 59. Wake velocity profile comparison of a Pak -B blade with asymmetric and spherical dimples at 55% and 65% axial chord at Re 45k and Tu 1%..	95
Figure 60. Wake velocity profile comparison of a Pak-B blade with asymmetric and spherical dimples at 55% and 65% axial chord at Re 25k and Tu 1%..	96
Figure 61. Reynolds effect on total pressure loss coefficient of baseline Pak-B at Tu 1%.....	99
Figure 62. Comparison between experimental and computational local total pressure loss coefficient profiles for a baseline Pak-B at Re 25k.....	100
Figure 63. Comparison of dimpled Pak-B CFD and experimental local total pressure loss coefficient profiles at Re 25k	101
Figure 64. Local total pressure loss coefficient profile comparison of Pak-B blade with asymmetric and spherical dimples at 55% and 65% axial chord at Re 45k and Tu 1%.....	102
Figure 65. Local total pressure loss coefficient profile comparison of Pak-B blade with asymmetric and spherical dimples at 55% and 65% axial chord at Re 25k and Tu 1%.....	103
Figure 66. Comparison of previous and current average total pressure loss coefficients for baseline Pak-B related blades	104
Figure 67. Comparison of current and previous experimental results for loss reduction on a Pak-B blade using spherical dimples	105
Figure 68. Comparison of asymmetric and spherical dimple loss reduction on a Pak-B blade.....	106
Figure 69. Boundary layer profiles for baseline Pak-B at Re 100k and Tu 1%.....	125
Figure 70. Boundary layer profiles for baseline Pak-B at Re 45k and Tu 1%.....	126
Figure 71. Boundary layer profiles for baseline Pak-B at Re 25k and Tu 1%.....	127
Figure 72. Boundary layer profiles for baseline Pak-B at Re 100k and Tu 4%.....	128
Figure 73. Boundary layer profiles for baseline Pak-B at Re 45k and Tu 4%.....	129

	Page
Figure 74. Boundary layer profiles for baseline Pak-B at Re 25k and Tu 4%.....	130
Figure 75. Boundary layer profiles for Pak-B with asymmetric dimples at 50% axial chord at Re 100k and Tu 1%.....	131
Figure 76. Boundary layer profiles for Pak-B with asymmetric dimples at 50% axial chord at Re 45k and Tu 1%.....	132
Figure 77. Boundary layer profiles for Pak-B with asymmetric dimples at 50% axial chord at Re 25k and Tu 1%.....	133
Figure 78. Boundary layer profiles for Pak-B with asymmetric dimples at 50% axial chord at Re 100k and Tu 4%.....	134
Figure 79. Boundary layer profiles for Pak-B with asymmetric dimples at 50% axial chord at Re 45k and Tu 4%.....	135
Figure 80. Boundary layer profiles for Pak-B with asymmetric dimples at 50% axial chord at Re 25k and Tu 4%.....	136
Figure 81. Boundary layer profiles for Pak-B with asymmetric dimples at 55% axial chord at Re 100k and Tu 1%.....	137
Figure 82. Boundary layer profiles for Pak-B with asymmetric dimples at 55% axial chord at Re 45k and Tu 1%.....	138
Figure 83. Boundary layer profiles for Pak-B with asymmetric dimples at 55% axial chord at Re 25k and Tu 1%.....	139
Figure 84. Boundary layer profiles for Pak-B with asymmetric dimples at 55% axial chord at Re 100k and Tu 4%.....	140
Figure 85. Boundary layer profiles for Pak-B with asymmetric dimples at 55% axial chord at Re 45k and Tu 4%.....	141
Figure 86. Boundary layer profiles for Pak-B with asymmetric dimples at 55% axial chord at Re 25k and Tu 4%.....	142
Figure 87. Boundary layer profiles for Pak-B with asymmetric dimples at 65% axial chord at Re 100k and Tu 1%.....	143

	Page
Figure 88. Boundary layer profiles for Pak-B with asymmetric dimples at 65% axial chord at Re 45k and Tu 1%.....	144
Figure 89. Boundary layer profiles for Pak-B with asymmetric dimples at 65% axial chord at Re 25k and Tu 1%.....	145
Figure 90. Boundary layer profiles for Pak-B with asymmetric dimples at 65% axial chord at Re 100k and Tu 4%.....	146
Figure 91. Boundary layer profiles for Pak-B with asymmetric dimples at 65% axial chord at Re 45k and Tu 4%.....	147
Figure 92. Boundary layer profiles for Pak-B with asymmetric dimples at 65% axial chord at Re 25k and Tu 4%.....	148
Figure 93. Wake velocity profiles for baseline Pak-B at Tu 1%.....	149
Figure 94. Wake velocity profiles for baseline Pak-B at Tu 4%.....	150
Figure 95. Wake velocity profiles for Pak-B with asymmetric dimples at 50% at Tu 1%.....	151
Figure 96. Wake velocity profiles for Pak-B with asymmetric dimples at 50% at Tu 4%.....	152
Figure 97. Wake velocity profiles for Pak-B with asymmetric dimples at 55% at Tu 1%.....	153
Figure 98. Wake velocity profiles for Pak-B with asymmetric dimples at 55% at Tu 4%.....	154
Figure 99. Wake velocity profiles for Pak-B with asymmetric dimples at 65% at Tu 1%.....	155
Figure 100. Wake velocity profiles for Pak-B with asymmetric dimples at 65% at Tu 4%.....	156
Figure 101. Wake velocity profiles for Pak-B with spherical dimples at 50% at Tu 1%.....	157
Figure 102. Wake velocity profiles for Pak-B with spherical dimples at 50% at Tu 4%.....	158

	Page
Figure 103. Wake velocity profiles for Pak-B with spherical dimples at 55% at Tu 1%.....	159
Figure 104. Wake velocity profiles for Pak-B with spherical dimples at 55% at Tu 4%.....	160
Figure 105. Wake velocity profiles for Pak-B with spherical dimples at 65% at Tu 1%.....	161
Figure 106. Wake velocity profiles for Pak-B with spherical dimples at 65% at Tu 4%.....	162
Figure 107. Total pressure loss coefficient profiles for a baseline Pak-B at Tu 1%.....	163
Figure 108. Total pressure loss coefficient profiles for a baseline Pak-B at Tu 4%.....	164
Figure 109. Total pressure loss coefficient profiles for a Pak-B with asymmetric dimples at 50% axial chord at Tu 1%	165
Figure 110. Total pressure loss coefficient profiles for a Pak-B with asymmetric dimples at 50% axial chord at Tu 4%	166
Figure 111. Total pressure loss coefficient profiles for a Pak-B with asymmetric dimples at 55% axial chord at Tu 1%	167
Figure 112. Total pressure loss coefficient profiles for a Pak-B with asymmetric dimples at 55% axial chord at Tu 4%	168
Figure 113. Total pressure loss coefficient profiles for a Pak-B with asymmetric dimples at 65% axial chord at Tu 1%	169
Figure 114. Total pressure loss coefficient profiles for a Pak-B with asymmetric dimples at 65% axial chord at Tu 4%	170
Figure 115. Total pressure loss coefficient profiles for a Pak-B with spherical dimples at 50% axial chord at Tu 1%	171
Figure 116. Total pressure loss coefficient profiles for a Pak-B with spherical dimples at 50% axial chord at Tu 4%	172
Figure 117. Total pressure loss coefficient profiles for a Pak-B with spherical dimples at 55% axial chord at Tu 1%	173

	Page
Figure 118. Total pressure loss coefficient profiles for a Pak-B with spherical dimples at 55% axial chord at Tu 4%	174
Figure 119. Total pressure loss coefficient profiles for a Pak-B with spherical dimples at 65% axial chord at Tu 1%	175
Figure 120. Total pressure loss coefficient profiles for a Pak-B with spherical dimples at 65% axial chord at Tu 4%	176

LIST OF SYMBOLS

English

<u>Symbol</u>	<u>Definition</u>
A	Area (m^2)
C	Curve fit constant, curve intercept
C_D	Aircraft drag coefficient
C_L	Aircraft lift coefficient
C_p	Pressure coefficient
c	Axial chord length (m)
c	Specific fuel consumption ($\text{kg}/\text{N s}$)
c_P	Specific heat at constant pressure ($\text{J}/\text{kg K}$)
D	Curve fit constant, curve slope
D	Diameter (m)
dP	Differential/small change in pressure (Pa)
ds	Differential/small change in entropy ($\text{J}/\text{kg K}$)
dT	Differential/small change in temperature (K)
E	Energy (J)
\exp	Exponential
g	Acceleration due to gravity (m/s^2)
k	Depth (m)
k	Thousand
\ln	Natural log
m	Mass (kg)
\dot{m}	Mass flow rate (kg/s)

Nu	Nusselt number
P	Pressure (Pa)
q	Dynamic pressure (Pa)
Q	Heat transfer (J)
Q_R	Heat of Reaction (J)
R	Back pressure (Pa)
R	Gas constant (J/kg K)
R	Range (m)
Re	Reynolds number
s	Entropy (J/kg K)
T	Temperature (K)
Tu	Freestream turbulence level (%)
U	Velocity (m/s)
W	Work (J)
\dot{W}	Power (W)

Greek

<u>Symbol</u>	<u>Definition</u>
Δ	Change
∂	Partial derivative
γ	Ratio of specific heats
γ	Total pressure loss coefficient normalized by exit dynamic pressure
η	Efficiency
μ	Viscosity (kg/m s)

π	Pressure ratio
ρ	Density (kg/m ³)
τ	Temperature ratio
ω	Total pressure loss coefficient normalized by inlet dynamic pressure
ϖ	Uncertainty

Subscripts

<u>Symbol</u>	<u>Definition</u>
0-9	Engine station numbering
0	Total, stagnation, overall
c	Compressor
D	Drag
L	Lift
R	Relative
s	Static
t	Total

Superscripts

<u>Symbol</u>	<u>Definition</u>
$\bar{}$	Average, mean value
²	Squared
^o	Degree

Units

<u>Symbol</u>	<u>Definition</u>
cm	Centimeter
in H ₂ O	Inches of Water
J	Joule
K	Kelvin
kg	Kilogram
ks	Kilosamples
m	Meter
mm	Millimeter
N	Newton
Pa	Pascal
s	Second
W	Watt

Abbreviations

<u>Symbol</u>	<u>Definition</u>
2-D	Two dimensional
3-D	Three dimensional
AFB	Air Force Base
AIAA	American Institute of Aeronautics and Astronautics
ASC	Aeronautical Systems Center
ASD	Asymmetric dimple
ASME	American Society of Mechanical Engineers
CFD	Computational fluid dynamics

LPT	Low pressure turbine
MEMS	Micro-electromechanical systems
MSRC	Major Shared Resource Center
NACA	National Advisory Committee for Aeronautics
NASA	National Aerospace Administration
OSU	Oklahoma State University
PC	Personal computer
RANS	Reynolds averaged Navier Stokes
SD	Spherical dimple
UAV	Unmanned aerial vehicles
USAF	United States Air Force
USAFA	United States Air Force Academy
VBI	Vane blade interaction
VDG	Vortex generator device
VGJ	Vortex generator jet

ABSTRACT

Flow separation on a low pressure turbine blade is explored at Reynolds numbers of 25k, 45k and 100k. Experimental data is collected in a low-speed, draw-down wind tunnel using a cascade of eight Pak-B blades. Flow is examined from measurements of blade surface pressures, boundary layer parameters, exit velocities, and total pressure losses across the blade. Two recessed dimple shapes are assessed for suppressing flow separation and associated losses. One dimple is spherical, and the second is asymmetric, formed from a full dimple spanwise half-filled. A single row of each dimple shape is tested at 50%, 55% and 65% axial chord. Symmetric dimples reduce separation losses by as much as 28%, while asymmetric dimples reduce losses by as much as 23%. A complementary three-dimensional computational study is conducted to visualize local flow structure. Computational analysis uses Gridgen v13.3 as a mesh generator, Fluent[®] v6.0 as a flow solver and FIELDVIEW[®] v8.0 for graphic display and analysis. Computational results for Pak-B blades at a Reynolds number of 25k indicate that both dimple shapes cause a span-wise vortex to rollup within the dimple and provide a localized pressure drop.

USE OF DIMPLES TO SUPPRESS BOUNDARY LAYER SEPARATION ON A LOW PRESSURE TURBINE BLADE

CHAPTER 1. INTRODUCTION

Recent United States Air Force (USAF) use of Unmanned Aerial Vehicles (UAVs) such as Global Hawk (Figure 1) for high altitude reconnaissance has been constrained by low pressure turbine (LPT) efficiencies. LPT blades operating at low Reynolds numbers, such as occur in flight at high altitudes and low velocities, suffer losses in efficiency and loading. At these flight conditions, the LPT may operate at a Reynolds number below 25,000 which produces laminar boundary layers on the turbine airfoils. The combination of laminar flow and large turning angles that are typically associated with an LPT blade gives rise to flow separation over a broad portion of the trailing suction surface. The resulting drop in turbine efficiency and loading restricts the



Figure 1. TeledyneRQ-4 Global Hawk UAV (illustration by Virginia Reyes)

aircraft range, altitude and electrical power extracted from the engine. Changing blade geometries is not a practical solution because of the negative impact at higher Reynolds numbers. Therefore, boundary layer separation control techniques are investigated as a more feasible alternative.

The Pratt and Whitney Pak-B profile was introduced as a means to study and improve LPT efficiency at low Reynolds number conditions. The Pak-B two-dimensional (2-D) shape is derived from the commercially used Pratt and Whitney Pak airfoil. When this shape is extruded spanwise into a blade, it can be used for local three-dimensional (3-D) analysis. It is not a truly 3-D representation of an LPT because it does not have taper or twist.

James Lake investigated various passive control techniques on a Pak-B blade and found that recessed spherical dimples prevent separation if positioned just forward of the natural chordwise separation location (1). He reported as much as 51.7% reduction of losses while operating at a Reynolds number of 45,000 and a freestream turbulence level of 4%. He speculated that dimples are effective vortex generators, energizing the flow and forcing the laminar boundary layer to transition to turbulent before separation can occur.

A passive control technique such as recessed dimples provides great potential for reducing losses at low Reynolds number conditions while having a negligible adverse impact at higher speeds. Furthermore, these passive controls do not require additional power from the engine or additional weight and can be easily retrofitted into existing engine hardware. A better awareness of the flow mechanisms produced by these passive controls is very important to further parametric studies in engine design optimization.

This current research investigates further into the use of dimples for suppression of boundary layer separation on a low pressure turbine blade. The Pak-B profile is studied in a computational simulation and in a wind tunnel. The baseline blade (without dimples) is tested along with spherical and asymmetric dimple shapes at Re 100k through 25k. The computational study is intended to visualize flow structure, and the experimental study evaluates performance improvements.

1.1 Low Pressure Turbine Operation at Low Reynolds Numbers

Low pressure turbines have historically not been a limiting agent in turbomachinery design. Much of the emphasis is given to compressors for maximum pressure ratio and to high pressure turbines for maximum temperature capability. Any focus on the LPT is given to optimize aerodynamic characteristics and maximize loading and efficiency. This is especially true for the low Reynolds operating conditions associated with LPTs found in high altitude reconnaissance UAVs.

The operating environment around the LPT is an inherently unsteady one, in which the blades periodically shed wakes. As these wakes travel downstream and over the surface of subsequent blades, they generate high local freestream turbulence intensity as great as 20% (2; 3). Boundary layer separation is suppressed during these momentary high turbulence levels. During periods of low turbulence intensity between wakes, the flow is laminar and vulnerable to flow separation at low Reynolds number operation (Figure 2).

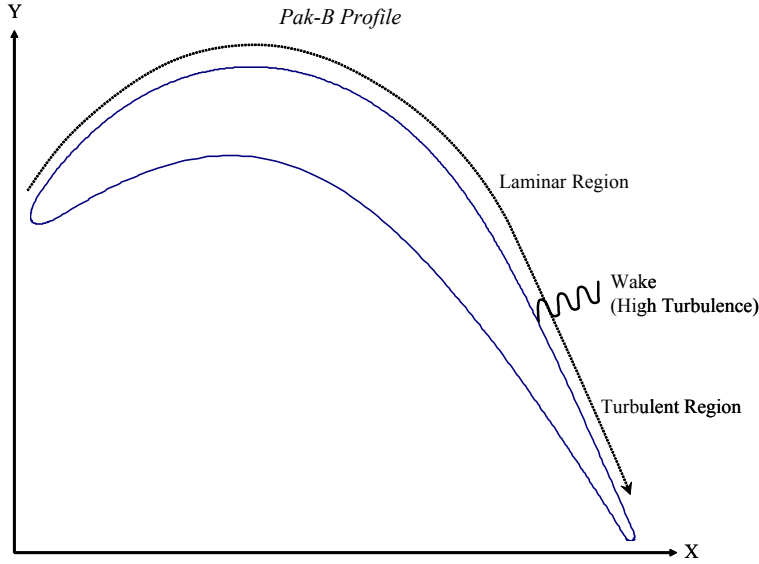


Figure 2. Unsteady wake passing over Pak-B airfoil

1.2 Previous Experiments in Flow Separation on LPT Blades

Previous experiments have helped increase the understanding of boundary layer behavior around LPT blades at low Reynolds numbers less than 200k. Sharma et al, revealed that Reynolds numbers less than 95k nearly tripled the loss coefficient compared to the loss coefficients for higher Reynolds numbers (4). Murawski et al. and Qiu and Simon linked the deteriorated LPT performance to losses from flow separation for a Pak-B blade at low Reynolds numbers (5; 6). Simon and Volino have also documented separation losses for the Pak-B blade at Reynolds operating conditions associated with high altitude UAVs (7). Furthermore, Hourmouziadis found severe profile losses and reduced efficiency at similar low Reynolds numbers (8). This general understanding of flow separation at low Reynolds numbers and the associated losses was quantified more precisely for the Pak-B profile by Lake (1). He determined a natural chordwise

separation location of about 70% on a Pak-B blade at a Reynolds number of 45,000 and confirmed a related increase in the total pressure loss coefficient and wake momentum deficit (1). LPT performance at low Reynolds operating conditions is now well understood.

Linear cascade tunnels are often used to simulate and study turbine aerodynamics within an engine operating environment. Linear cascades can be used to study two-dimensional effects, as the blades are not rotating, and the flow is nearly uniform in the spanwise direction as it enters the test section. A cascade consists of several blades lined-up pitchwise in a row from inboard to outboard, with the inlet at an angle to the exit flow. Chapter 4 discusses the current linear cascade tunnel in greater detail.

Past experiments using a linear cascade have documented several aspects of flow separation on turbine blades at low Reynolds numbers. Rivir examined turbulent length scale effects on transition location on a Langston airfoil (9). Murawski et al. and Qui and Simon showed Pak-B LPT flow separation at low Reynolds numbers, documenting velocities, surface pressures, separation location and boundary layer thickness (5; 6). Murawski et al. recorded separation from 75% to 90% axial chord at inlet axial chord Reynolds numbers as low as 53k (5). Qui and Simon demonstrated turbulent reattachment aft of the 90% axial chord location (6). These previous experiments have set the stage for the current research to investigate the use of dimples as a technique for suppressing boundary layer separation.

Boundary layer separation can be categorized into four major classifications, as reported by Werle: leading edge bubbles, transonic shock induced separation, pressure side bubbles, and trailing edge wake separation (10). Murawski et al. and Qui and Simon

found an additional classification at low Reynolds numbers in which laminar flow separates in the presence of a strong streamwise pressure gradient (5; 6). Transition may occur subsequent to suction surface laminar flow separation. Mayle and Halstead delineate three modes of boundary layer transition: natural, bypass and separated-flow (11; 12). Lake focused his research on the control of separated-flow transition and laminar separation on a Pak-B blade (1). He investigated the use of trip wires, spanwise V-grooves and submerged spherical dimples. Lake documented successful integration of surface modifications which reduced the losses associated with separated flow (1). Of the techniques he explored, dimples proved to be most promising (1).

1.3 Current Research Objectives

The objective of the current research is to investigate the flow mechanisms associated with the use of dimples in controlling laminar boundary layer separation. To this end, two dimple shapes are considered, a spherical dimple and an asymmetric dimple. The asymmetric dimple is fashioned as a semi-circle with a streamwise straight edge, being spanwise half-filled. Tests are extended to Reynolds numbers as low as 25k.

The effectiveness of dimple shape is assessed by mounting a single modified Pak-B blade in a linear cascade of eight total blades. The total pressure loss coefficient is measured for the modified blade at Reynolds numbers of 25, 45 and 100 thousand by taking wake traverses. Other performance indicators that were measured include wake velocity magnitude and total pressure loss profiles. Boundary layer measurements are also taken to see the effect of dimples on velocity and turbulence profiles inside the boundary layer. Lake's previously modified blade (Figure 3) is used in this research for comparison.

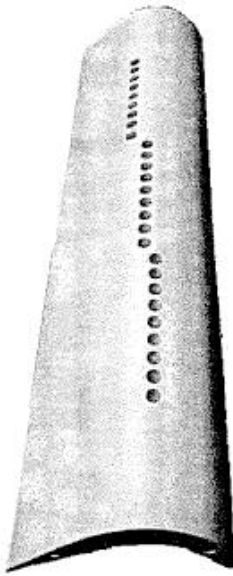


Figure 3. Lake's Pak-B blade with dimples at 50%, 55% and 65% axial chord (1)

comparison in loss reduction and validate the experimental set-up (1). Dimples are located at 50%, 55% and 65% axial chord. Asymmetric dimples are produced by filling a spanwise half of the current spherical dimples.

Flow structure inside and aft of the dimple is analyzed using a computational simulation. The computational study is meant to be a companion to the experimental work to aid in performance predictions and data analysis. The model is based on the Pak-B blade profile and given infinite span to analyze local three-dimensional phenomena. The model also makes use of periodic boundaries to simulate an infinite number of blades in a linear cascade arrangement. A baseline Pak-B blade is investigated along with Pak-B blades with both types of dimples. Dimples are set at 60% axial chord. Inlet axial chord Reynolds number is set to 25k. Dr. Hugh Thornburg ran the solution with laminar, as well as Spalart-Allamaras, K- ω and K- ε turbulence settings in Fluent[®]. These

turbulence models use a nominal 1% inlet turbulence. Surface pressure coefficients are produced along with profile contours for velocity, total pressure and static pressure. Surface flow is visualized with lines of separation and reattachment, as well as with lines for vortex cores. Streamlines are placed at two axial chord locations and visualized from profile and suction surface viewpoints.

1.4 Chapter Summary

Chapter 2 includes a discussion of low pressure turbine performance evaluation and boundary layer aerodynamics, including previous experimental and numerical research. This chapter also covers different separation control techniques. Chapter 3 covers the computational investigation, discussing the methods results. The experimental investigation is reported in Chapter 4, including the test facility, instrumentation, methods, and results.

CHAPTER 2. BACKGROUND AND THEORY

Before embarking on this experimental and computational research it is important to determine what data to collect, what fluid behavior is expected and what measure to use for comparison. This study has impact on aircraft flying high and slow. In this case, range, altitude, endurance and extracted power are of greatest interest. Therefore, parameters studied here relate to improvements in these qualities. Velocity and pressure are of particular interest, as they can be used to determine impact on engine and turbine efficiency. Temperature is also of interest; however, for the linear cascade test used in this study, it is not investigated directly. Rather, a correlation can be shown with pressure, indirectly indicating thermal performance.

Airfoil boundary layers are expected to separate at the Reynolds numbers being investigated. To capture this effect in the wind tunnel, boundary layer velocity and turbulence are measured. For a bulk assessment of flow separation, wake velocity and total pressure deficit is of interest. A non-dimensional analysis of these parameters is particularly useful in relating improvements to an operating engine environment.

The computational study investigates flow around the surface of the blade and in the passages between blades. Again, velocities and pressures are of interest, shedding light on flow structure and relating to impacts on engine efficiency. The computational study has an especially beneficial attribute in that it can also yield separation and reattachment lines, another measure of improvement.

2.1 Low Pressure Turbine Performance Evaluation

The Breguet range formula is used to estimate aircraft range and is related to engine efficiency:

$$R = \eta_{engine} \frac{C_L}{C_D} \ln\left(\frac{m_{initial}}{m_{final}}\right) \frac{Q_R}{g} \quad (1)$$

where η_{engine} is overall engine efficiency, Q_R is the heat of reaction of the fuel, g is the acceleration due to gravity, C_L is aircraft lift coefficient, C_D is aircraft drag coefficient, $m_{initial}$ is aircraft initial mass, and m_{final} is final aircraft mass (13:152). By solving for the term inside the natural log and taking the exponential of both sides of the equation, an expression is produced for fuel consumption (assuming no fuel reserves upon landing and munitions/payload delivered during the mission):

$$\Delta m_{final} = m_{final} \left[\exp\left(\frac{C_D R g}{C_L \eta_{engine} Q_R}\right) - 1 \right] \quad (2)$$

where $\Delta m_{final} = m_{initial} - m_{final}$. Therefore, it is apparent that increasing engine efficiency translates to decreasing fuel consumption and/or increasing aircraft range.

The impact of turbine efficiency/performance on overall engine efficiency is well illustrated with a T-S diagram, where T is temperature and S is entropy. The ideal jet engine is represented with the Brayton cycle as seen in Figure 4. In this cycle, temperature rises isentropically across the compressor from station 2 to 3. Accordingly, static pressure also rises, as stated in Charles' law. This is also consistent with Boyle's Law, which relates increasing pressure to decreasing volume. Because the Brayton cycle represents an ideal engine, no losses are present, and entropy is not produced. Between station 3 and 4, fuel (energy) is added and temperature increases in the combustor. This

is assumed to occur at a constant pressure. Across the turbine and nozzle (stations 4 to 9), the hot air is expanded isentropically. Temperature and pressure both decrease. Heat is then extracted from station 9 to 0 at a constant pressure.

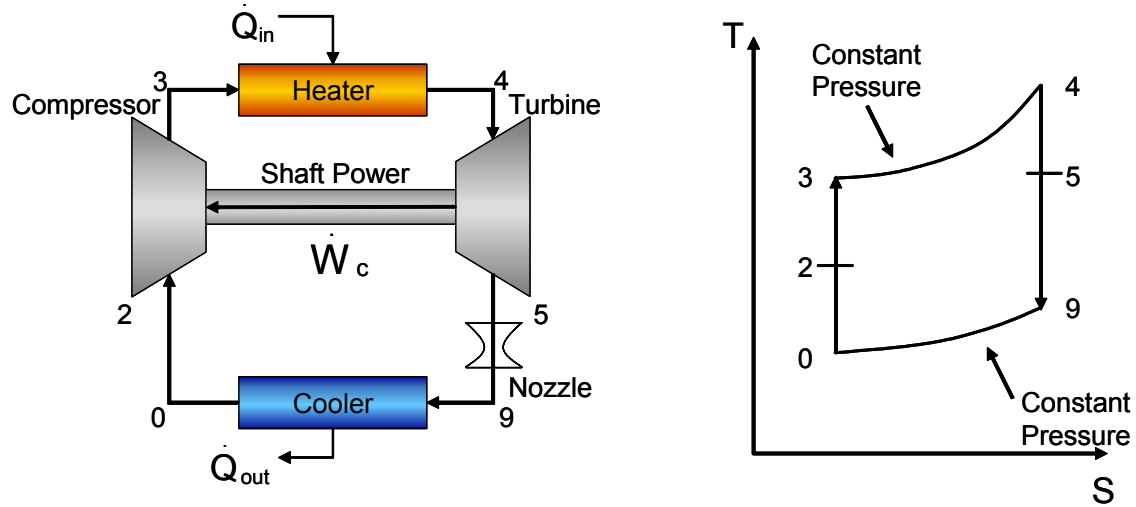


Figure 4. Brayton cycle for an ideal gas turbine engine

The first law of thermodynamics for a system can be stated in terms of heat transfer, work and internal energy as follows:

$$Q = \Delta E_0 + W \quad (3)$$

where Q is heat transfer, ΔE_0 is change in internal energy and W is work (14:27).

Assuming energy is conserved throughout the Brayton cycle, Q can be expressed in terms of temperature, and an expression can be written for power across the compressor and turbine such that:

$$W_c = m \ c_p (T_{t3} - T_{t2}) \quad (4)$$

$$W_t = m \ c_p (T_{t4} - T_{t5}) \quad (5)$$

where \dot{m} is mass flow rate, c_p is the ratio of specific heats at constant pressure and T_t is total temperature. The work of the compressor is balanced by the turbine such that

$\dot{W}_c = \dot{W}_t$ in an ideal engine. In reality, the work from the turbine is less than the ideal.

Flow separation is one mechanism associated with losses across the turbine.

Figure 5 shows a T-S diagram for a non-ideal turbine stage. Total temperature does not change over the stator, but entropy is generated and total pressure decreases. Entropy also increases over the rotor, while total pressure and temperature decrease. The drop in total pressure translates to a drop in efficiency. The Gibbs equation relates increased entropy to decreased total pressure as follows:

$$ds = c_p \frac{dT_t}{T_t} - R \frac{dP_t}{P_t} \quad (6)$$

where ds is the change in entropy, R is the gas constant, T_t is temperature, dT_t is the change in temperature, P_t is total pressure and dP_t is the change in total pressure (13).

For constant total temperature as shown in Figure 5, the expression is reduced to:

$$ds = -R \frac{dP_t}{P_t} \quad (7)$$

Mattingly relates pressure drop and efficiency for a turbine stage through the following expression:

$$\eta_t = \frac{1 - \tau}{1 - \pi_t^{(\gamma-1)/\gamma}} \quad (8)$$

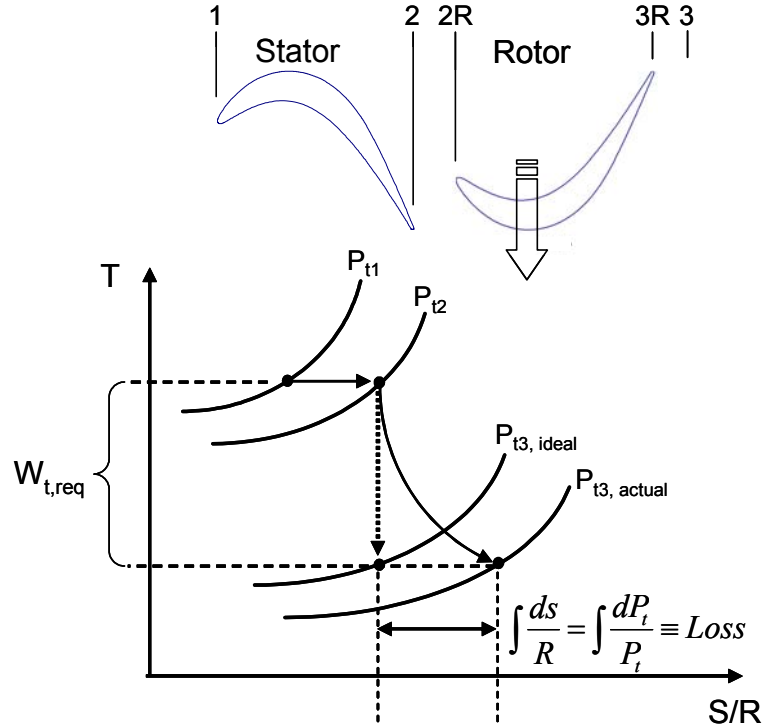


Figure 5. T-S diagram for a non-ideal turbine stage

where γ is the ratio of specific heats, $\tau = T_{t3}/T_{t1}$ and $\pi_t = P_{t3}/P_{t1}$ (14). This equation shows that for a fixed total temperature ratio, decreases in exit total pressure result in efficiency reduction. Therefore, turbine performance is directly linked exit total pressure. Total pressure loss coefficient is a means to evaluate the exit total pressure. The equations below show the total pressure loss coefficient as normalized by either the inlet or exit dynamic pressure:

$$\gamma = \frac{P_{t,inlet} - P_{t,exit}}{q_{exit}} \quad (9)$$

$$\omega = \frac{P_{t,inlet} - P_{t,exit}}{q_{inlet}} \quad (10)$$

where γ is defined as the loss coefficient normalized by exit dynamic pressure (q_{exit}), and ω is defined as the loss coefficient normalized by inlet dynamic pressure (q_{inlet}). From this expression, it is easy to see that as exit total pressure decreases γ or ω increase. Losses due to separated flow can be mitigated, resulting in higher exit total pressure and a smaller total pressure deficit across the stage. This study considers the use of dimples to decrease the ΔP , across the turbine stage and thereby increase stage efficiency. Figure 6 shows a relationship that Lake used to illustrate the impact of an improved exit total pressure (1). A turbine with separation controls (baseline) is depicted with a large amount of entropy generation. With even a small improvement in exit total pressure, the illustration shows significantly reduced entropy generation.

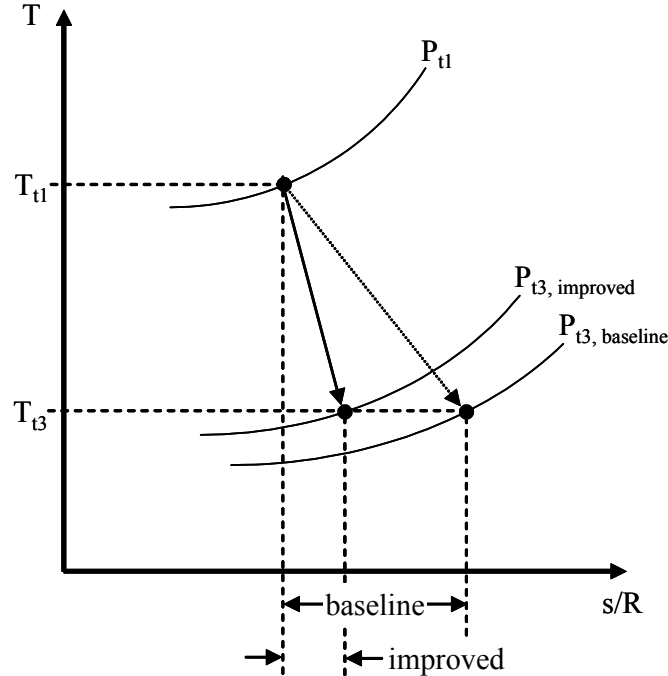


Figure 6. T-S diagram illustrating possible improvement with higher turbine exit total pressure (1)

In Figure 7, Lake shows a correlation in a percent increase in efficiency to a percent reduction in loss coefficient through the following equation (1:14):

$$\frac{\Delta\eta}{\eta} \approx 0.057 \left(\frac{\Delta\gamma}{\gamma} \right) \quad (11)$$

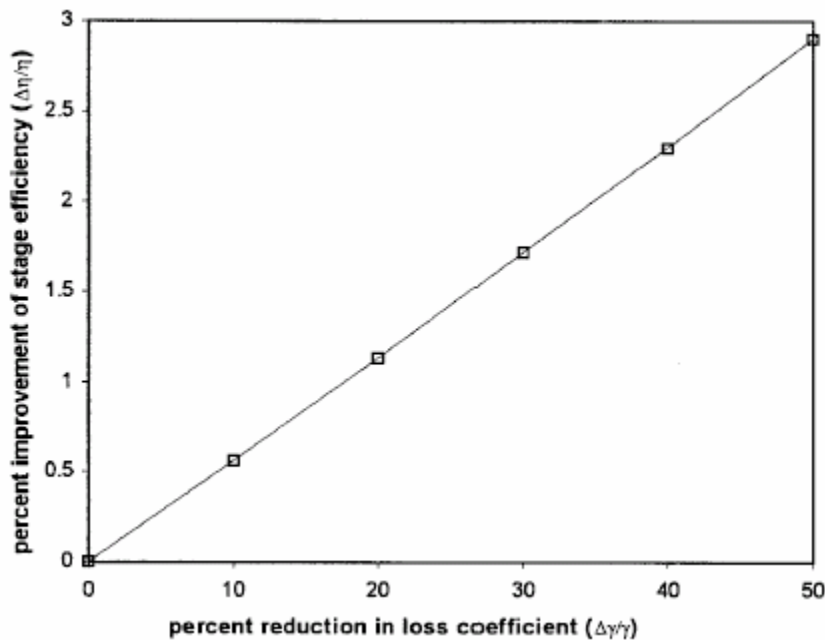


Figure 7. Linear relationship between reduction in loss coefficient and improvement in stage efficiency (1)

In his investigation, Lake realized a reduction in loss coefficient using dimples on the surface of a Pak-B blade. This translates to a significant potential improvement in turbine efficiency within a gas turbine engine. The current research shows the way in which dimples change the aerodynamics of the turbine suction surface, reducing loss coefficient. This information should prove helpful to future work in optimizing the use of dimples as a passive control technique.

2.2 Low Pressure Turbine Boundary Layer Aerodynamics

Low pressure turbine flowfields are difficult to examine. Halstead et al. documented the presence of freestream turbulence levels between 1% and 20% along with passing wakes, centrifugal effects and vortices, all of which make flowfield studies very challenging (2; 3). Werle, Mayle, and Addison and Hodson have shown through experimental studies that boundary layers on LPT blades operating at low axial chord Reynolds numbers undergo a gradual transition process from laminar to turbulent over the suction surface of the blade (10; 11; 15). The process is nearly steady, interrupted by time-dependent wake passing due to motion of the downstream rotor in relation to stator. This periodic environment is characterized by flow that trips quickly through transition to turbulent and back to a transitional state (3). This current study does not simulate the periodic wake passing; however, the process from laminar to turbulent boundary layer formation is found to become more unsteady when dimples are applied to the surface.

2.2.1 Experimental Laminar-to-Turbulent Boundary Layer Transition

Mayle and Walker showed through experimentation that flow enters transition through three basic means: natural transition, bypass transition, and separation bubble transition (11; 16). These transition modes depend on Reynolds number, freestream turbulence, and pressure gradients. The mode experienced with the Pak-B blade in this research is separation bubble transition.

Natural transition occurs with low freestream turbulence and no adverse pressure gradients. It begins with the formation of 2-D Tollmien-Schlichting waves that become unstable and create 3-D loop vortices and large fluctuations (11). The 3-D disturbances coalesce into turbulent spots, which grow as they move further downstream. Walker

identified the conclusion of natural transition as the creation of a fully turbulent boundary layer, resulting from the merging turbulent spots (16).

Bypass transition occurs in conditions with higher freestream turbulence levels on the order of 20%. In this turbulent environment, the entering laminar flow immediately forms turbulent spots without the presence of 2-D Tollmien-Schlichting waves. Despite some limitations, Walker found that linear stability theory can still be used to predict disturbances in this transition mode, helping predict the length of transitional flow (16).

A separation bubble may be formed by flow separating under adverse pressure gradients. The shear layer between the bubble and freestream can then transition to turbulent. While the flow is separated from the blade, it undergoes this transitional process. Qiu and Simon along with Mayle, demonstrated that once the separated flow is fully turbulent, the increased fluid energy encourages re-attachment to the blade surface (6; 11). This is the transition mode experienced by the Pak-B blade at low Reynolds numbers. The goal of this research is to identify mechanisms by which upstream dimples suppress this separation bubble.

2.2.2 Numerical Models for Low Pressure Turbine Performance

Past attempts to numerically model the complex flowfield around a low pressure turbine have shown limited success due in large part to the lack of experimental validation data for low Reynolds numbers (10). Halstead et al. tested four numerical models: STANX, KEP, a Navier-Stokes solver, and the Fan-Lakshminarayana code. Each produced unsatisfactory accuracy in the solutions(3; 17). Lake used the 2-D Allison Vane-Blade Interaction (VBI) code which typically renders good results, but has problems in low Reynolds number environments (1). The code was incapable of

simulating the separated flow region correctly. In addition, Lake was only able to run this code for the baseline blade due to the 3-D nature of the dimples (1).

Lake demonstrated limited success with the VBI code, using a combination of O-grids around the airfoil surface and H-grids in the passage (1). He was able to predict a separation bubble at a Reynolds number of 50k, but not for 100k or 200k. The current research uses a similar grid approach, extruding a structured 3-D grid around the blade surface in the fashion of an O-grid, generating hexahedral cells. The blade passages are filled unstructured tetrahedral-cells and merged with the structured, extruded surface cells. A viscous model without turbulence modeling demonstrates moderate success in predicting the onset of separation and the re-attachment location, as is discussed in greater detail in Chapter 3. Aft of turbulent re-attachment, the solution becomes less accurate. A better approach would likely include a turbulence model aft of the separation location. The use of Reynolds average Navier Stokes (RANS) turbulence models across the entire surface was also investigated in this study; however, they did not predict any separation, even with a 1% inlet turbulence. Better transition modeling is needed to understand the nature of the flow. In addition, these models will require experimental data to determine accuracy.

Freestream turbulence level, Reynolds number, and pressure gradients all influence numerical predictions. Reed et al. compared these influences by examining methods of predicting the linear stability of fluid flows (18). Methods examined by Reed et al. require prior knowledge of flow characteristics such a initial disturbance amplitude, as is the case with the e^N method (18). Sharma et al. found that the nonisotropic nature of turbulence within laminar and transitional boundary layers makes flow behavior difficult

to predict with numerical models (19). The difficulty in modeling flow behavior is rooted in the ability to predict the evolution and location of separation bubbles.

2.3 Separation Control on Low Pressure Turbines

2.3.1 Active and Passive Controls

Flow control techniques are categorized as either active or passive. Active controls have the advantage that they can be turned off at higher LPT Reynolds operating conditions in which flow separation does not occur, decreasing any negative impact on performance. Additionally, many active techniques can offer variable control to adjust control intensity depending on a changing separation location. Johnston and Nishi and Compton and Johnston demonstrated the effectiveness of vortex generator jets (VGJs) for separation control on flat plates under adverse pressure gradients (20; 21). Bons et al., subsequently applied VGJs to a Pak-B blade, showed that pulsating VGJs have the same effectiveness as steady flow jets with an order of magnitude less mass flow (22). To incorporate VGJs into a turbine engine, high pressure air would be required from the compressor; however, other active controls do not use additional air flow. Lin et al. explored several other separation control strategies including Helmholtz resonators (23), and Boregeson recently attempted use of micro-electromechanical systems (MEMS) to trip the flow and delay separation over a cylinder (24). The disadvantages of all these active control techniques are in their application and practicality in a turbine engine environment. MEMS are difficult to manufacture and apply to an LPT and currently cannot withstand the associated temperature loads. Vortex generating jets are not as difficult to manufacture; however, they require additional hardware that adds weight to the engine, and they are susceptible to clogging from combustor exhaust particulates.

Furthermore, both of these techniques are complex and require additional power from the engine.

Passive controls do not require power, are generally more robust, and are usually easy to install. Many possible passive techniques have been considered. One passive technique is the modification of blade shape to effect aerodynamic characteristics of the suction surface; however, the cost to overall engine performance is too great. Though a modified blade shape could be beneficial at controlling flow separation in the low Reynolds number operating environments, it may not perform as well in higher Reynolds number operating conditions of other mission legs. Another approach is to retain the blade shape, only making modifications to the suction surface. The following discussion covers a few examples of passive techniques that have been previously considered. Lin et al. examined submerged vortex-generators, large-eddy breakup devices, and elongated boundary-layer arches (23). Figure 8 shows protruding type passive controls. Chang, Austin and Gumerdinger and Shreeve explored the use of a triangular plow vortex generator device, VGD (25; 26; 27). Semi-circular and simple vane VGDs were studied by Rao and Kariya (28). They also considered parallel

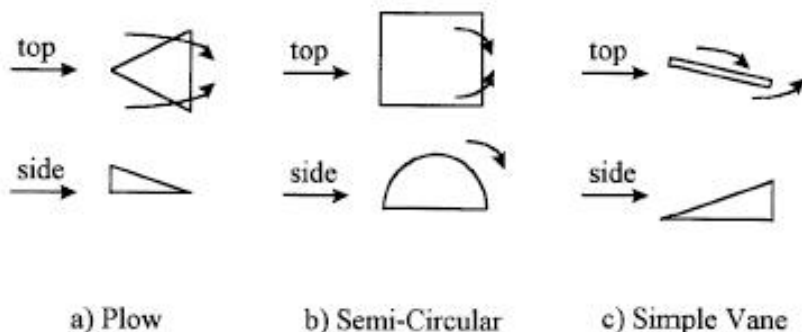


Figure 8. Three protruding surface vortex generator devices. Profile and surface views are shown with air flow depicted as an arrow (1).

concave slats constructed from Venetian blinds and attached to the surface of a flat plate (Figure 9). The disadvantage to protruding surfaces is the increased drag produced at

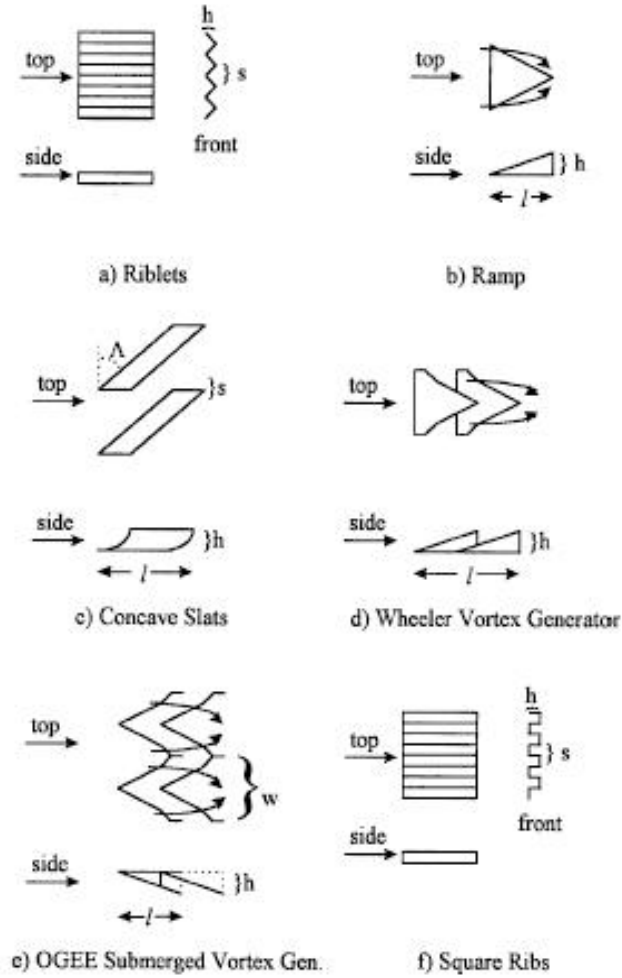


Figure 9. Various other vortex generator devices. Profile and surface views are shown with air flow depicted as an arrow (1)

higher Reynolds number operating conditions. One method to avoiding this drawback was considered by McCormick who used of a passive cavity method and a passive injection method (Figure 10), trying to taking advantage of the adverse pressure gradient behind the separation location (29). Figure 11 shows other alternatives to protruding surfaces which were proposed by Lin et al. who investigated the use of a ± 45 deg small-

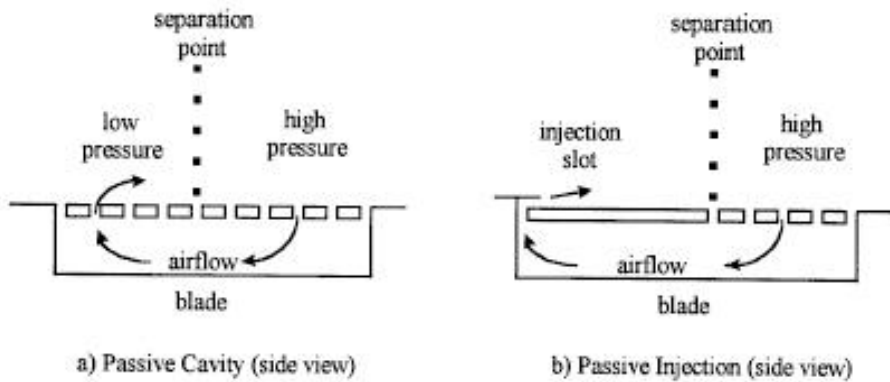


Figure 10. Porous surface separation control devices. Profile and surface views are shown with air flow depicted as an arrow (1)

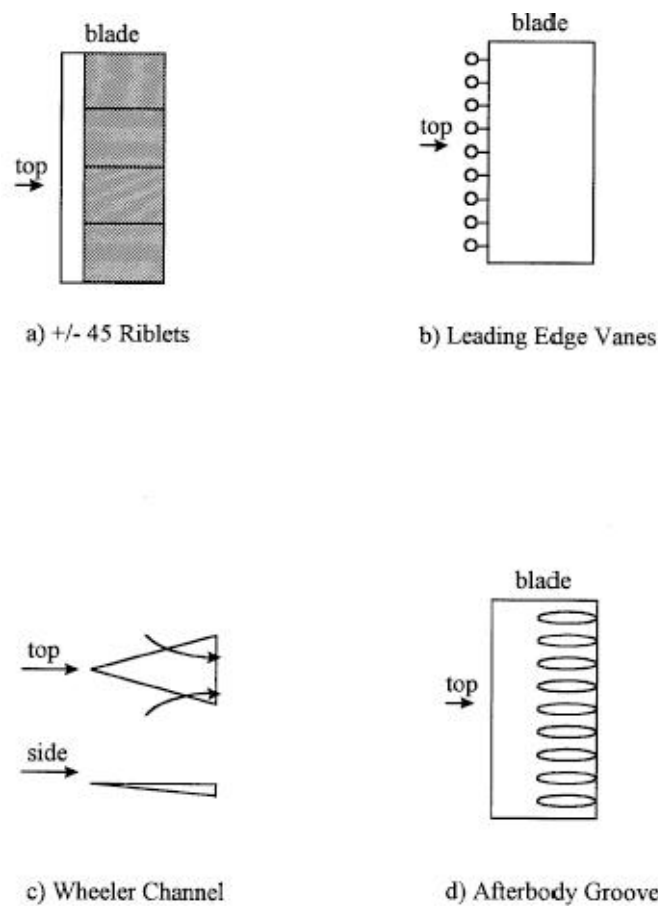


Figure 11. Various vortex generator devices with difficult application. Profile and surface views are shown with air flow depicted as an arrow (1)

scale riblet pattern, Wheeler doublets and transverse grooves (30). Wheeler doublets are similar to Ogee submerged vortex generators, having a reverse S-shape curve (Figure 9). Both were designed by Wheeler (31). Figure 11 shows another concept design by Wheeler in which a V-shaped groove is cut into a surface (31). Some previously techniques were not as easily integrated. Chang looked into leading edge vane VGDs (Figure 11), Walsh and Bacher and Smith investigated the use of small-scale V-groove riblets (Figure 9), and Maciejewski and Rivir tested small-scale square ribs and Taylor tested a large-scale vortex generator in the shape of a NACA 64-812 airfoil (25, 32-33, 35-38). A much simpler approach was proposed by Bloch and Mueller who experimented with the application of roughness strips (39). Lake tested the use of a V-groove channel, a boundary layer trip wire and spherical dimples (1). Lake concluded that of all these passive controls, each is sensitive to location and that dimples worked best (1).

2.3.2 Previous Research in Dimples for Boundary Layer Control

In general surface modifications can be categorized as protruding or recessed, as shown in the previous section. Protruding structures energize the boundary layer flow by drawing down faster moving freestream air (38). Furthermore, they produce trailing edge vortices that mix the freestream and boundary layer flows as they travel downstream. Lin et al. demonstrated that recessed vortex generators with a depth less than the boundary layer thickness have less drag than protruding structures of similar height; however, the effective distance of recessed generators is less than that for the protruding structures, requiring them to be placed closer to the natural separation location (30). Submerged structures are also more practical for engine application, being more robust and easier to

clean and manufacture. Lake capitalized on this notion, demonstrating great potential for the use of recessed spherical dimples as an effective passive control technique (1). This control technique is particularly desirable for the relative ease and low cost of installation and is the focus of the current research.

Lake based his dimple structure on previous experimentation by Bearman and Harvey (40; 41). Bearman and Harvey tested spherical and hexagonal dimples on a sphere, concluding that both were effective in generating downstream vortices (40; 41). Furthermore, they found that the hexagonal dimples were more efficient generators because of their sharp edges. Bearman and Harvey also tested dimples on a cylinder, finding a significant reduction in drag (40; 41). Their dimple depth was scaled to a non-dimensional roughness ratio of $k/D = 9 \times 10^{-3}$ where k is the maximum dimple depth and D is the diameter of the sphere/cylinder. Lake tested the baseline Pak-B blade, without modification, measuring the boundary layer thickness. He then applied the non-dimensional roughness ratio when milling dimples into the surface of a Pak-B blade. Dimples were milled into the blade to a depth of 1.588mm, using a 5.08 cm diameter ball end mill. The resulting impressions were elliptical due to blade curvature and had a streamwise length of 15.13 mm and spanwise length of 17.53 mm with a dimple spacing of 2.22 cm from center-to-center.

Lake studied spherical dimples at three axial chord locations using a cascade of eight Pak-B blades at Reynolds numbers of 50, 100 and 200 thousand (1). He positioned dimples upstream of the natural expected separation location, placing them at 50%, 55%, and 65% axial chord and testing the sensitivity of dimple location on reducing separation

losses. Lake demonstrated significant loss reduction, but did not optimize dimple shape, size, spacing or pattern.

The current research investigated the use of dimples as passive controls to suppress boundary layer separation. Lake's experimental blade was used to make comparison and to extend the ranged of tested Reynolds numbers down to 25k. The blade is tested in a baseline configuration with a thin transparent tape over the dimples. It is also tested with Lake's spherical dimples and then retrofitted to simulate the asymmetric dimple, filling a spanwise half of the full dimple with putty. Flow is examined from measurements for boundary layer profiles, surface static pressures, and wake properties. Furthermore, a complementary computational study is used for flow visualization.

CHAPTER 3. COMPUTATIONAL RESULTS AND ANALYSIS

Computational models were constructed for three configurations: the baseline unmodified Pak-B blade, the Pak-B blade with spherical dimples and the Pak-B blade with asymmetric dimples. Grid models were constructed from given Pak-B profile coordinates. The 2-D shape was extruded spanwise to generate surface grids. The baseline case was built with structured grids around the blade surface to include the boundary layer thickness and separated region, and unstructured grids filled the blade passage. The dimpled configurations were manufactured with a combination of structured and unstructured grids around the blade surface. Unstructured grids were used inside and around the dimple, and structured grids were created for leading edge, trailing edge, and pressure surfaces. As with the baseline case, unstructured grids filled the blade passage. Grid topology is discussed in greater detail in section 3.2.

A steady-state integration technique was initially applied to all three cases. The baseline configuration converged to a realistic solution; however, the dimpled cases appeared to be more unsteady, having unnatural results. A time-accurate technique was subsequently applied to the dimpled cases, using the steady-state results as initial conditions. All configurations were simulated with a Reynolds number of 25,000.

Laminar and turbulent viscous models were investigated. A Reynolds averaged Navier-Stokes (RANS) code incorporated three different turbulence models: K-w, K-e and Spalart-Allamaras. The turbulence models failed to predict any separation. The computations without turbulence showed the expected separation, but did not accurately predict flow aft of the separation location.

The primary purpose of the computational results is to help predict and interpret wind tunnel results. The results also give a sense of what might occur in an operating engine environment; however, by its very nature, the Pak-B is a 2-D profile and not truly representative of a fully 3-D, rotating blade assembly. The Pak-B profile is characteristic for a mid-span section of an operational turbine blade. The computational blade model is extruded spanwise to allow for 3-D flow over this localized blade shape. To enhance the 2-D effects, the blade is given infinite span, and the cascade is modeled with infinite blades. The primary utility of the model is to qualify trends in the flow behavior, document relative improvements from surface modifications and visualize flow structure.

3.1 Computational Software

Three software packages were used in this study: Gridgen v13.3, Fluent[®] v6.0, and FIELDVIEW[®] v8.0 (42-44). Gridgen was used to create a grid mesh over and around the surface of the blade. Good grid architecture is essential to flow analysis. Each grid point (or node) represents one point in space that will have with it values for various properties such as temperature, pressure, density and velocity at any given point in time. If the grid points are too far apart, then the model will not have enough resolution to accurately resolve the flow structure. Too many grid points can require excessive run time and memory requirements. Distribution of grid points is also critical. The grid was clustered tightly around regions in which flow gradients required resolution: stagnation points and locations of separated flow. Along with clustering points in appropriate locations, cells also need to be at good angles to each other, preferably close to orthogonal for hexahedra and equilateral for tetrahedra. Section 3.2 discusses grid topology in greater detail.

Fluent[®] is used to simulate flow around the blade. It uses a finite volume scheme to discretize the governing equations. Fluent[®] was run in a steady state mode, in which the time dependent evolution of the flow structure was not preserved. It was also run unsteady, or time-accurate. This mode ensured that at any one point in time, all grid points were assessed at an appropriate time step. Fluent[®] boundary conditions inputs included temperature, pressure, density and velocity. Periodic boundaries were used to allow the computer to simulate infinite span/dimples and infinite blades. Section 3.3 discusses flow solver attributes in greater detail.

FIELDVIEW[®] was used to graphically display grid structure and flow solver results. It was also be used to evaluate flow properties. Fluent[®] data files were exported to FIELDVIEW[®] with chosen flow variables: velocities, pressures, and wall shear stress. Cross sections of the flow field were taken, displaying contours of various variables, integrating values, and taking area weighted averages. It was also used to produce 2-D plots of data across a given cross section. Particle traces and surface flows were also accomplished in FIELDVIEW[®], displaying streamlines, separation locations, flow re-attachment, and vortex cores. These are useful to visualize flow structure and behavior.

3.2 Grid Model Characteristics

Dr. Hugh Thornburg imported 2-D Pak-B profile coordinates are into Gridgen, accurately describing the pressure and suction surfaces. The 2-D profile was then extruded in the Z-direction to render a 3-D span of 2.22 cm. The axial chord length is 17.78 cm. The stagger angle is 25° and the inlet angle is 35°. Combinations of structured and unstructured grids were created so that when structured grids were extruded, they

produced hexahedral cells, and when unstructured grids were extruded, they produced either tetrahedra (within dimples) or prisms (from blade surface). Where the structured and unstructured grids merge, there are mixed cells that include tetrahedral, pyramid and wedge cells.

3.2.1 Baseline Pak-B Grid Topology

For the baseline blade, a square structured grid is projected onto the blade surface with 41 nodes across the span. Surface grid points are clustered around the leading and trailing edges, as well as near the expected separation location (Figure 12). The total number of streamwise nodes around both the suction and pressure surfaces is 421. This surface grid is then extruded 42 steps with an initial step size of 0.0001m so as to cover the boundary layer thickness and expected separation region. The remaining duct regions were created by extruding the surface of the structured grid to mid-passage with a default unstructured grid produced by Gridgen such that there are 15 pitchwise nodes at the inlet and outlet faces and 231 nodes along either streamwise mid-passage face (Figure 13). The pitchwise length (or duct width) is consistent with cascade geometry, rendering an axial chord to spacing ratio (solidity) of 1.129. The Baseline model has a total of 830, 625 nodes and 1,319,992 cells (688,800 hexahedral and 631,192 mixed pyramid and tetrahedral).

The boundary conditions were set in Gridgen such that the inlet face was a “velocity inlet” for all three configurations. Dr. Thornburg set the spanwise boundaries to “periodic” to simulate infinite span. In the dimpled cases, this also simulates an infinite row of dimples. He also set the pitchwise boundaries to periodic, simulating an infinite number of blades in linear cascade form. The periodic boundary conditions allow

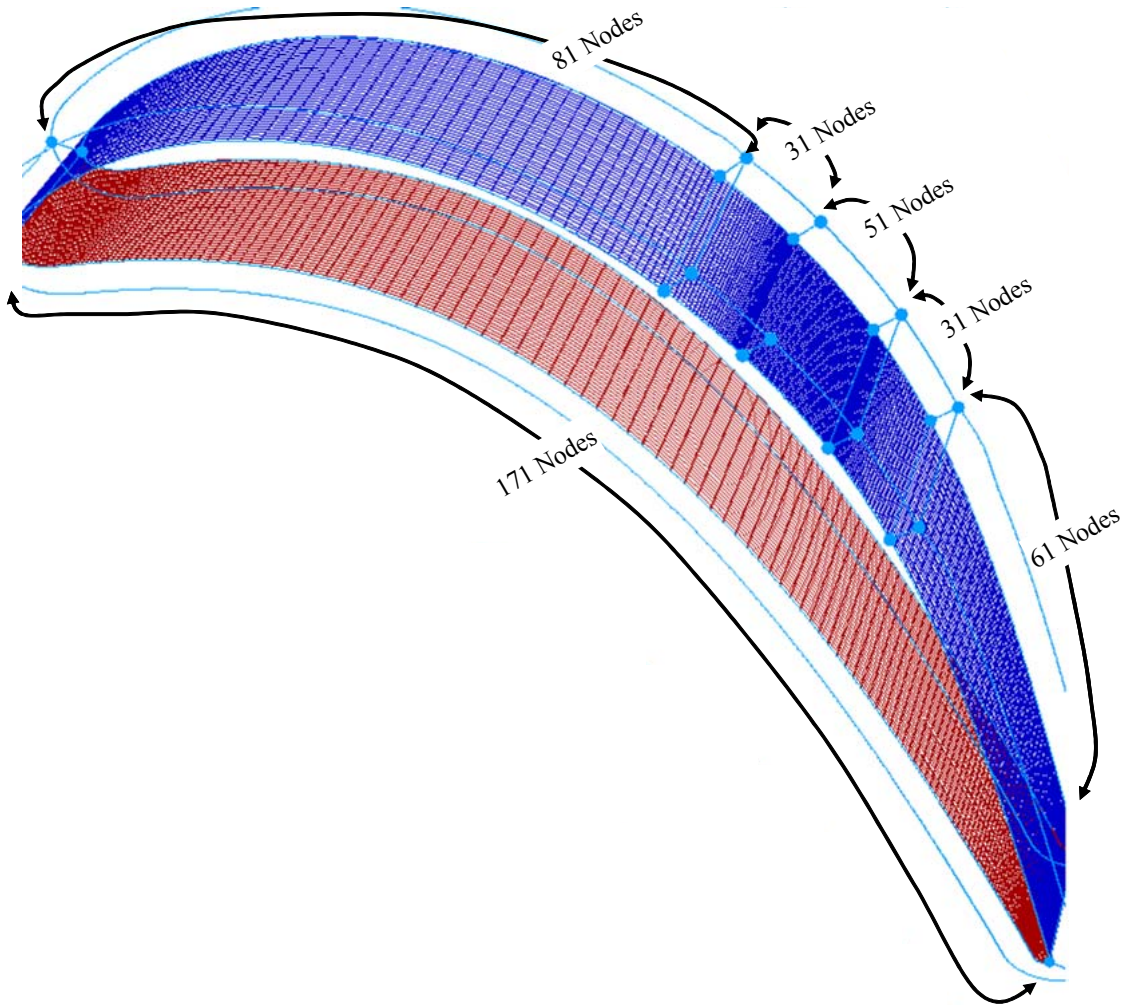


Figure 12. Baseline Pak-B surface topology

fluid flow in and out of the boundaries. The exit face was set to an “outflow” boundary condition that ensures continuity at the outlet.

3.2.2 Grid Topology for Pak-B with Spherical Dimples

Dimples are created in Gridgen by generating a spherical database structure with a 5.08 cm diameter. This sphere is then moved into the surface of the blade at 60% axial chord to a depth of 1.588 mm along an orthogonal axis. The surface of the sphere is intersected with surface of the blade to cut a circle onto the surface of the blade. This circle is then

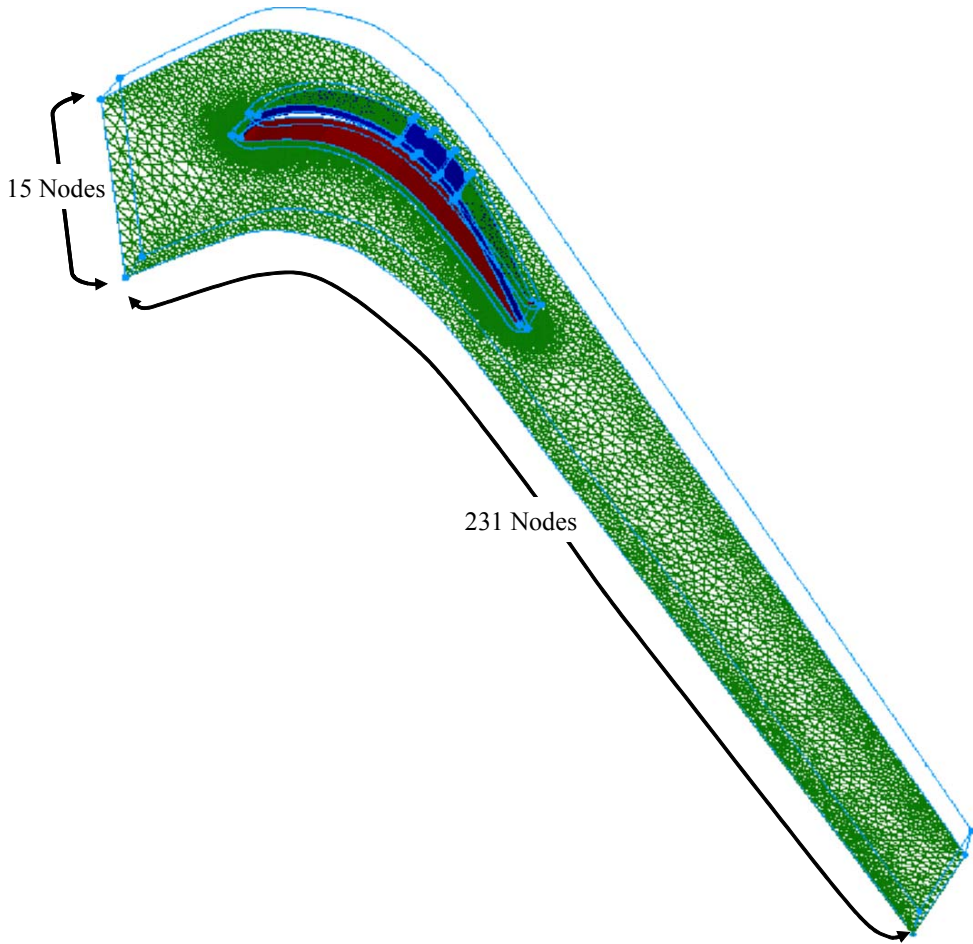


Figure 13. Baseline Pak-B mid-passage grid topology

given a domain that is subsequently projected onto the surface of the sphere to simulate the dimple. The spanwise surface nodes of the structured grid are increased to 81 for better resolution (Figure 14). The region around the dimple is created with an unstructured grid containing 21,408 nodes such that there are 61 streamwise nodes located at spanwise ends where there are 31 nodes on the baseline model and 101 nodes where there are 51 nodes on the baseline model. Spanwise between the dimple edge and spanwise edge, there are 21 nodes on either side. Additionally, there are 121 nodes used in the streamwise length of the aft structured grid surface. There are 444 nodes

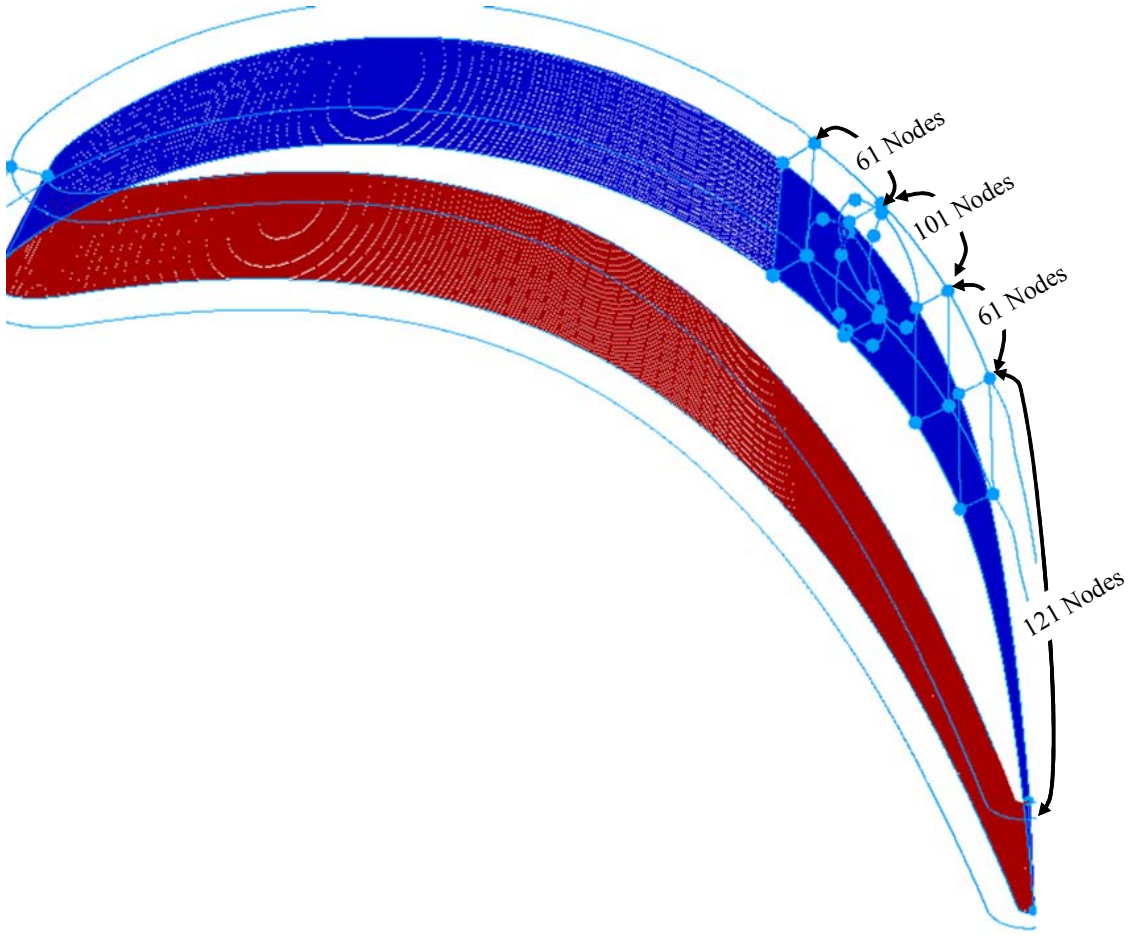


Figure 14. Grid Topology for the Pak-B blade with spherical dimples

around the dimple edge so that there are 25,411 nodes inside the dimple. The remaining grid structures are the same as that created for the baseline model. There are a total of 3,361,902 nodes with 1,213,000 hexahedral cells; 3,748,712 wedge cells; and 1,190,194 mixed cells.

3.2.3 Grid Topology for the Pak-B with Asymmetric Dimples

In the case of the asymmetric dimple, the circular intersection that defines the dimple edge is split in half down a streamwise axis. Half of the resulting semicircle is then given

a domain that is projected onto the blade surface. In addition, a vertical semicircular domain is created into the dimple to simulate a pitchwise wall oriented in a streamwise direction. In effect, the dimple is half-filled in the spanwise direction. Nodes are very tightly packed around and inside the dimples so that there are 3,064 nodes within the dimple, 2998 nodes on the semi-circular blade surface and 1078 nodes on the vertical semi-circular wall that defines the straight edge (Figure 15). The streamwise number of nodes along the spanwise edges is the same as that for the baseline case;

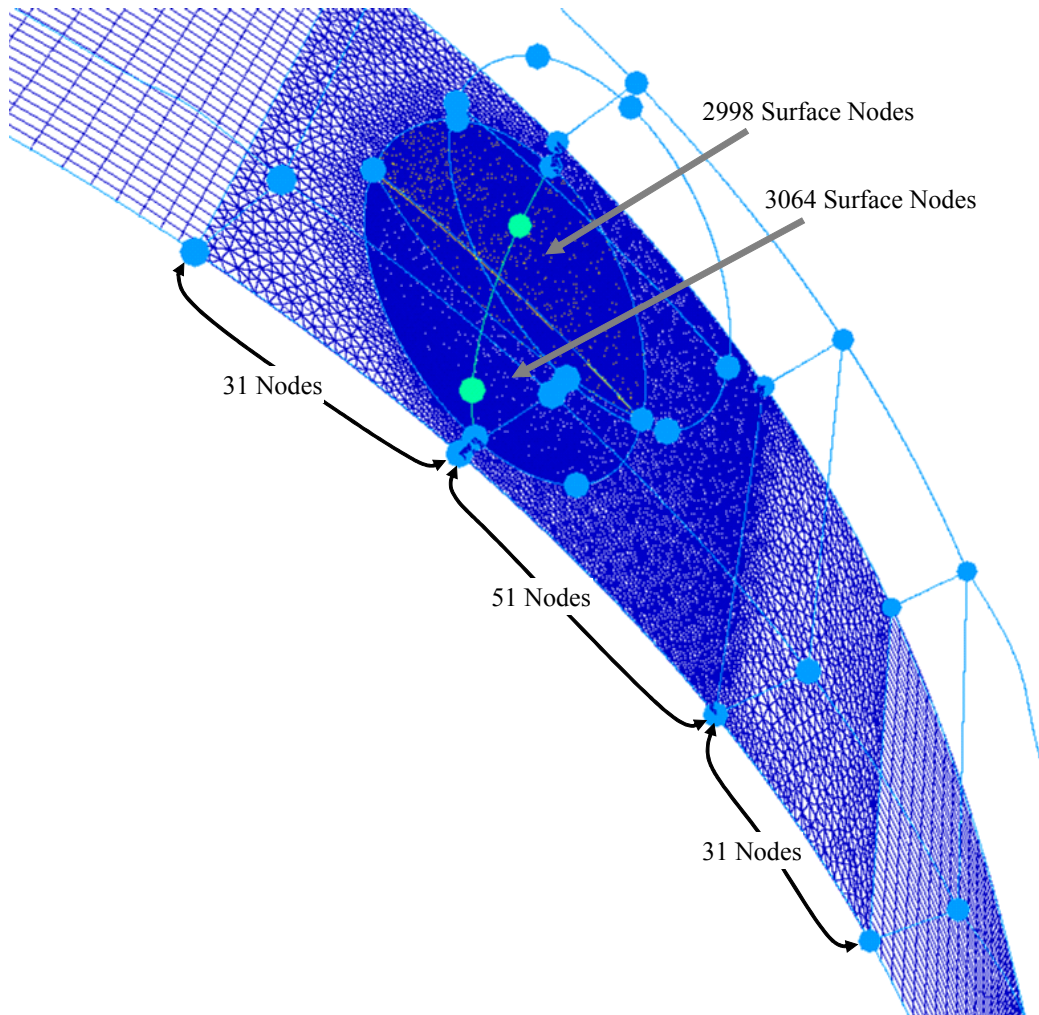


Figure 15. Grid Topology for the Pak-B blade with asymmetric dimples

however, the grid around the dimple is unstructured with 231 nodes around the circular circumference of the original full dimple circumference and 11 spanwise nodes between the spanwise and dimple edges. The downstream spanwise node distribution includes 81 nodes. Further downstream, there are 41 spanwise nodes that merge the unstructured and structured grids. As with the previous two cases mentioned, there are 42 layers extruded from the surface. The grid has a total of 1,132,305 nodes and 2,193,406 cells (508,400 hexahedral; 89,881 tetrahedral; 909,544 wedge cells; and 685,581 mixed cells).

3.3 Flow Solver Characteristics

Fluent[®] was run in 3-D, double precision and parallel mode for this study. The respective case file is read into the solver, and boundary conditions are set. The inlet face was set to a uniform 2.22 m/s, consistent with an inlet Reynolds number of 25,000 based on axial chord. The X-component of flow was 0.8192 and the Y-component was 0.5736, consistent with the 35° inlet angle for the Pak-B blade. The inlet pressure was set to 101,325 Pa. The blade surface was set as a no-slip wall. Therefore, the velocity at the surface of the wall is zero. The corresponding viscous setting was laminar. Other settings investigated included Spalart-Allamaras, K- ω and K- ε turbulence models and were incorporated by DR. Thornburg. The baseline Pak-B was run in steady state, as there was little unsteadiness associated with this flow. Convergence was arbitrarily determined when residuals stopped declining. The other two cases were run both initially run in steady-state mode. A time accurate mode was started from the stalled steady-state solution, using a 0.0001 s time step with a maximum of 20 iterations per time step. Run time was based on convergence of the local pressure iteration. Dr. Thornburg ran several cycles and qualitatively determined convergence based on observing random snapshots in

time. Run times were run long enough to ensure that transients were flushed out of the solution with confidence. After partitioning the files across available processors, files were then initialized, generating an associated data file. The case and data files were then run across several processors (as many as 24 at a time).

3.4 Computational Results

Computational results for the laminar settings follow expected trends with separation occurring between 66% and 73% axial chord at a Re 25k. For the current research, the laminar setting best represented the true flow and was chosen for post-processing flow structure and behavior.

Results are shown in terms of velocity, static pressure and total pressure profile contours, as well as surface pressure coefficient plots. The velocity and static pressure contours are useful in predicting blade performance as they relate to momentum deficit and blade loading, respectively. Total pressure contours are helpful in demonstrating locations and magnitudes of energy losses. The surface pressure coefficient plots are particularly important because they can be directly related to experimental results because they are normalized by inlet dynamic pressure. They are also instrumental in visualizing flow behavior, pointing separation locations.

Surface flows and streamlines are also shown to help visualize the airflow over the suction surface. Surface flows include separation and reattachment locations. Streamlines depict the particle flow paths and are the best method for viewing flow structure. For steady-state solutions, the particle path does not change with time. For the time-accurate results, a snapshot in time is viewed with the particle path integrated through the solution by virtue of velocity gradients.

3.4.4 Velocity Profile Contours

Figures 12 - 14 show velocity magnitude contours for the three Pak-B configurations at a Reynolds number of 25,000. The profile slices are taken at the same span-wise position; a location that is at the spherical dimple mid-span and close to the straight edge of the asymmetric dimple. The profiles were generated in FIELDVIEW[©] by first creating a coordinate surface orthogonal to the Z-axis (spanwise axis). The spanwise location was entered as previously noted, and then velocity magnitude was selected as the scalar function to be viewed. The coordinate surface was configured as smooth contours, and the legend was set to color spectrum. NASA-1 was selected as the legend type color map. The maximum value was set to 4.5 m/s (yellow), and the minimum value was set to zero (green). The view was taken from the Z+ direction. All color maps were set to the same scale to compare velocities.

As the velocity accelerates over the suction surface, static pressure is expected to decrease. When the flow separates, velocity magnitude decreases and static pressure rises, corresponding to a decrease in blade effectiveness related to momentum deficit. Figure 16 shows the velocity contours for the baseline Pak-B blade. Low velocity contours are present on the suction surface, downstream of 66% axial chord, indicating separation and loss in efficiency. Additionally, two pockets of high velocity appear near the trailing edge, hinting at vortical structures. Figure 17 shows the dramatic change in velocity contours with the addition of spherical dimples. At this particular time step, there is only one small pocket of low velocity near the trailing edge, denoting a small separation bubble. The asymmetric dimple offers an improvement over the baseline at this time step as seen in Figure 18; however, it is visibly less than the improvement

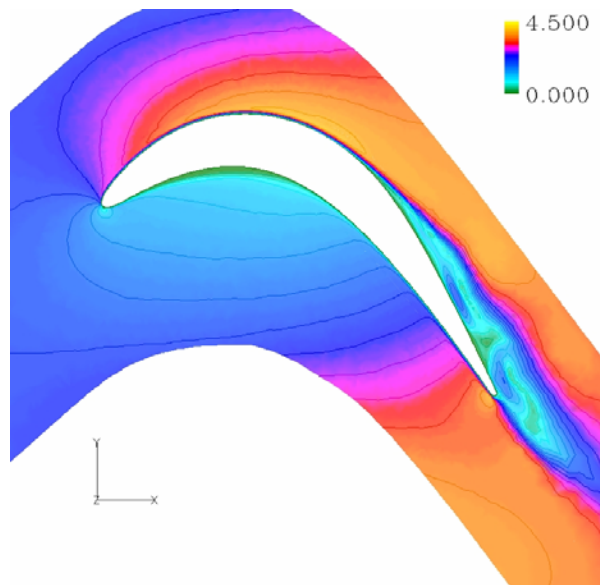


Figure 16. CFD velocity magnitude profile contours for a baseline Pak-B blade at Re 25k with the legend shown in m/s

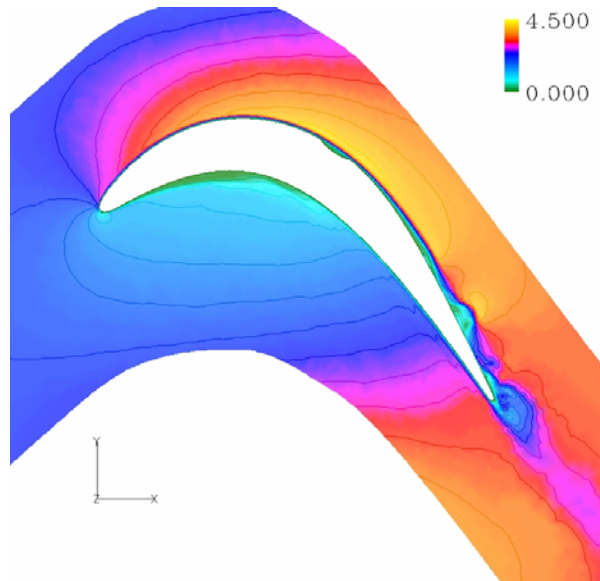


Figure 17. CFD velocity magnitude profile contours for a Pak-B blade with spherical dimples at 60% axial chord at Re 25k with the legend shown in m/s

shown by the spherical dimple. The pocket of low velocity contours is noticeably smaller than the baseline, beginning at 69% axial chord. There is one long separation bubble that

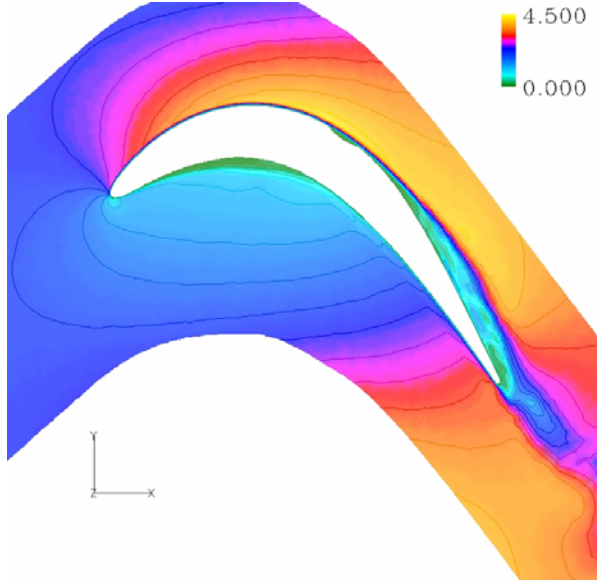


Figure 18. CFD velocity magnitude profile contours for a Pak-B blade with asymmetric dimples at 60% axial chord at Re 25k with the legend shown in m/s

extends past the trailing edge, but the boundary layer is significantly smaller than the baseline Pak-B blade.

3.4.5 Total Pressure Profile Contours

Figures 19 - 21 show total pressure contours of the three Pak-B configurations at Re 25k. The same profile slices were taken as used to view velocity magnitude contours, but the scalar function was set to view total pressure. The legend was set to a maximum value of 5.5 Pa and a minimum of -10.5 Pa. In each case, total pressure at the inlet is uniform. At the separation location, a low total pressure region grows, indicating a loss in total pressure and corresponding increase in entropy and reduction in blade efficiency. Direct comparison of these figures delineates the best configuration. Figure 19 shows the baseline blade with the largest region of losses, having the thickest region of total pressure loss that starts at 66% axial chord. Figure 20 shows the Pak-B with the spherical dimple at 60% axial chord. This configuration is the best of the three cases considered,

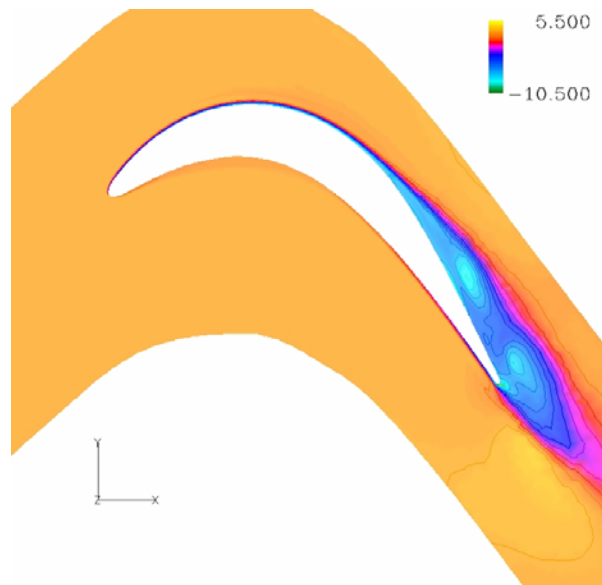


Figure 19. CFD total pressure contours for a baseline Pak-B blade at Re 25k with the legend shown in Pa

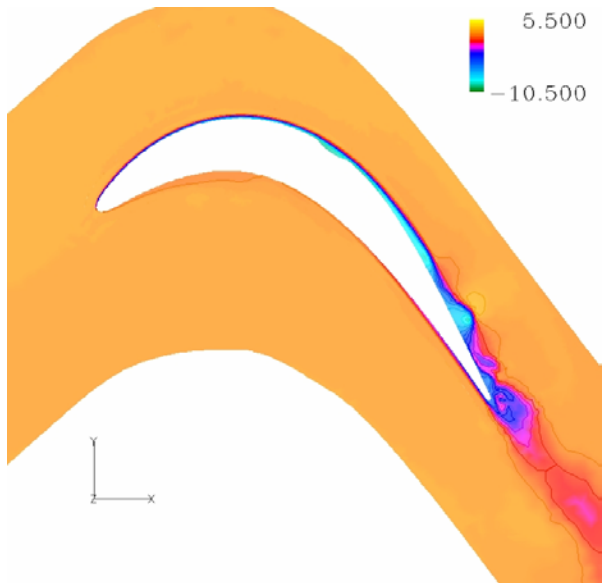


Figure 20. CFD total pressure profile contours for a Pak-B blade with spherical dimples at 60% axial chord at Re 25k with the legend shown in Pa

with only a small region of loss. The asymmetric dimple has improved performance over the baseline blade, but not as good as the spherical dimple (Figure 21). It delays the onset of total pressure deficit to 69% axial chord.

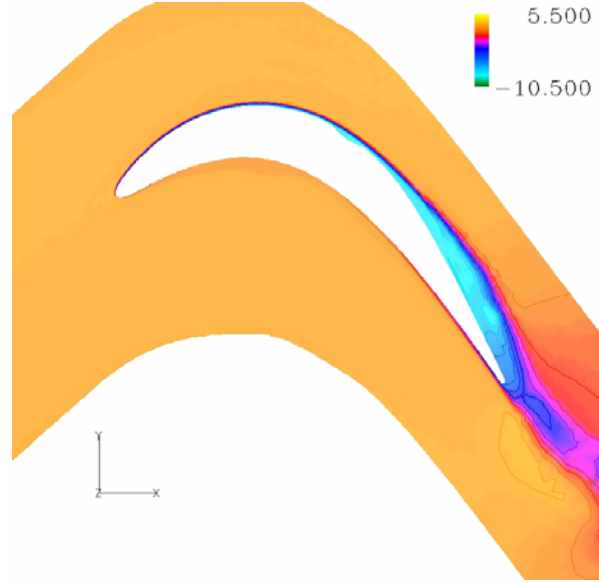


Figure 21. CFD total pressure contours for a Pak-B blade with asymmetric dimples at 60% axial chord at $Re = 25k$ with the legend shown in Pa

3.4.6 Static Pressure Profile Contours

The purpose of a low pressure turbine is to expand flow. To this end, static pressure profile contours show how effectively this is accomplished. Flow is expected to accelerate over the suction surface, and static pressure should drop. Figures 22 - 24 show regions of static pressure over the three Pak-B configurations at $Re = 25k$. The profiles were created using the same coordinate surface indicated in the previous two sections with the scalar function set to static pressure. The legend is set to a maximum value of 3.5 Pa and a minimum of -10.5 Pa.

The baseline Pak-B is depicted in Figure 18. There is a region of concentrated low pressure at about 56% axial chord. Just aft of this location at about 82% axial chord, there is a small pocket of slightly lower pressure centered just off the blade surface. This indicates the possible presence of a weak spanwise vortex. Further downstream at 92% axial chord, there is another pocket of low pressure. This low pressure region is the strongest of the three and is clearly detached from the surface of the blade. This indicates the presence of a stronger spanwise vortex. It is immediately followed by a region of much higher static pressure consistent with detached flow. These contours are consistent with expected trends. As the flow separates, the velocity is expected to decrease, and static pressure rises. This trade-off also is expected to occur within a vortex core where the relative velocity is near zero.

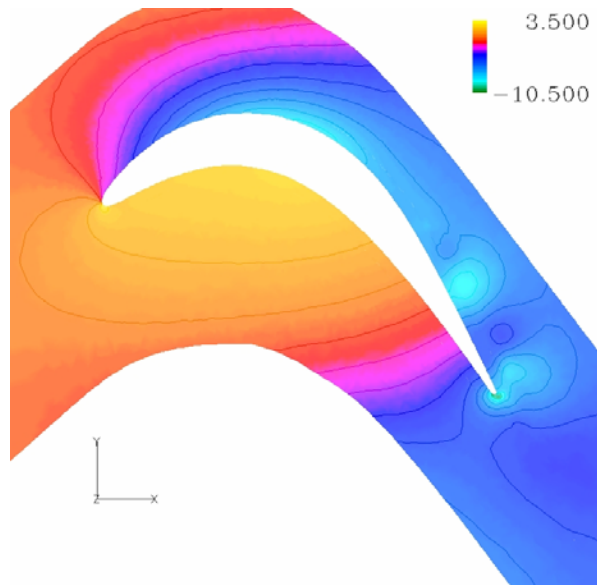


Figure 22. Static pressure contours on a baseline Pak-B blade from CFD results at Re 25k with the legend in Pa

Figure 19 shows the static pressure contours around the Pak-B blade with spherical dimples centered at 60% axial chord. In general, there is more suction occurring in this configuration than with the baseline blade. At 84% axial chord, there is a pocket of slightly lower pressure just off the blade surface, constituting the trailing edge of a large low pressure zone that extends upstream of the dimple. Further downstream at 94% axial chord, there is a small concentrated pocket of low pressure, indicative of a strong vortex possibly associated with tripped flow. The lowest surface static pressures reach -10.4 Pa, the lowest of the three blade configurations. The lowest pressures occur around the leading and trailing edges of the dimple. This indicates the presence of relatively high velocity air, consistent with the outer edge of a vortex.

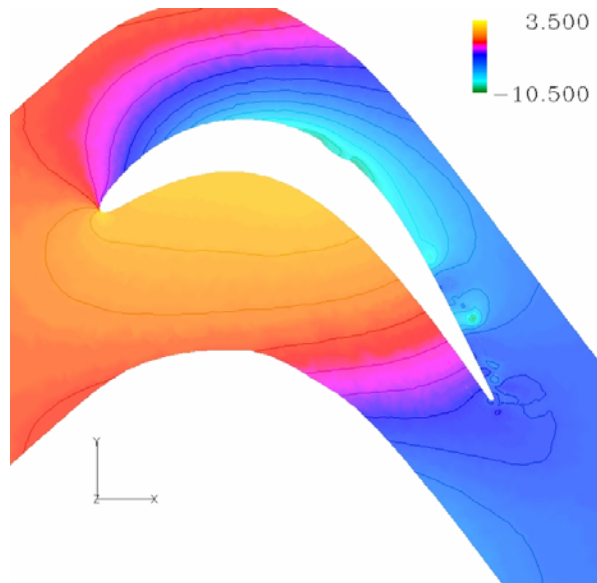


Figure 23. Static pressure contours on a Pak-B blade with a spherical dimple at 60% axial chord from CFD results at $Re = 25k$ with the legend in Pa

Figure 20 shows the static pressure contours for the Pak-B modified with an asymmetric dimple at 60% axial chord. There is a very large region of suction extending

nearly the entire length of the trailing suction surface. Within this region, there are two small pockets of very low pressure air at 93% and 97% axial chord. Unlike the case with the spherical dimple, there is little to no evidence of a downstream spanwise vortex aft of the dimple location. The lowest pressures reach -8.8 Pa as opposed to the -10.4 Pa achieved by the blade with the spherical dimple, indicating that the spherical dimple performs better.

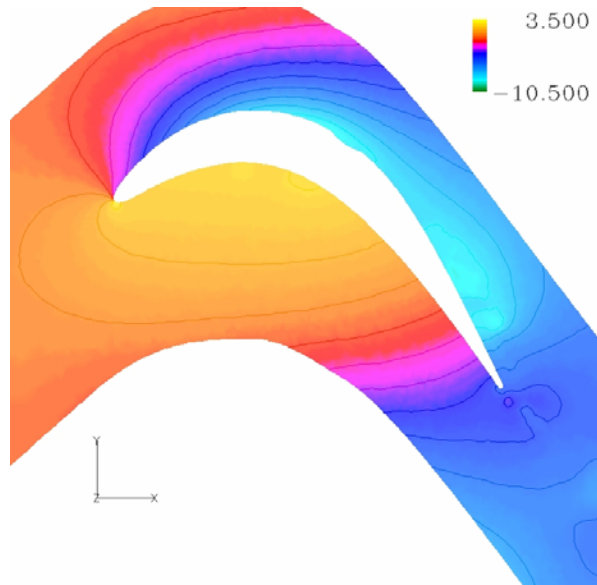


Figure 24. Static pressure contours on a Pak-B blade with an asymmetric dimple at 60% axial chord from CFD results at $Re = 25k$ with the legend in Pa

3.4.7 Surface Pressure Coefficient Profiles

Surface pressure coefficient plots were created using the 2-D plot function in FIELDVIEW®. The first step was to create a scalar function manually. In order to create the function, values for area-weighted average inlet total pressure and inlet dynamic pressure are captured. A coordinate surface is created one half axial chord length upstream of the leading edge. The coordinate surface is oriented in the axial plane (X+)

direction). Integration tools are used in FIELDVIEW[©] to compute an area-weighted average for a total pressure and for dynamic pressure. The area-weighted average is computed by summing the total number of scalar values within the area of the given plane and dividing by the number of samples. These values are then used to create a new function for surface pressure coefficient as follows:

$$Cp = \frac{\overline{P_{t_{inlet}}} - \text{"Pressure"} }{\overline{q_{inlet}}} \quad (12)$$

where $\overline{P_{t_{inlet}}}$, area-weighted average inlet total pressure, and $\overline{q_{inlet}}$, area-weighted average inlet dynamic pressure, are fixed numbers entered from the integration output, and “Pressure” is a FIELDVIEW[©] name for static pressure as imported from Fluent[©] at a grid location along the surface of interest. Within the 2-D plot tool, the blade surface is selected for an “XYZ Curve Plot” and a Z-cut is taken and plotted in the X-direction. The resulting plot shows Cp on the Y-axis and axial chord distance on the X-axis.

Surface pressure coefficient is proportional to static pressure as seen in Equation 12. Therefore, as static pressure decreases, pressure coefficient increases. Surface pressure plots indicate higher blade loading with higher pressure coefficients, a desirable characteristic for turbine blades. The higher blade load means more work from the turbine. Surface pressure coefficient plots are also useful to determine separation location. Separation is identified as the beginning of the horizontal data following the suction surface peak value. CFD is not expected to model reattached flow with much accuracy because re-attached flow is expected to be turbulent. The laminar integration technique is not able to resolve this condition.

Figures 25 is a 2-D plot of surface C_p along axial chord length. It shows a comparison of CFD surface pressure coefficient profiles for the three Pak-B blade configurations. Both the pressure and suction side surfaces are shown with the suction surface ranging from 0 (stagnation point of the leading edge) to nearly 4.5. The baseline blade has the least amount of loading with the suction surface reaching a maximum value of about 4.0. A plateau is apparent in the data around 65% axial chord, indication flow separation. Aft of 95% axial chord, the results become unrealistically high, showing a limitation in the laminar code. The asymmetric dimple appears to delay separation a little further aft to nearly 70% axial chord, where the data flattens. The asymmetric dimple

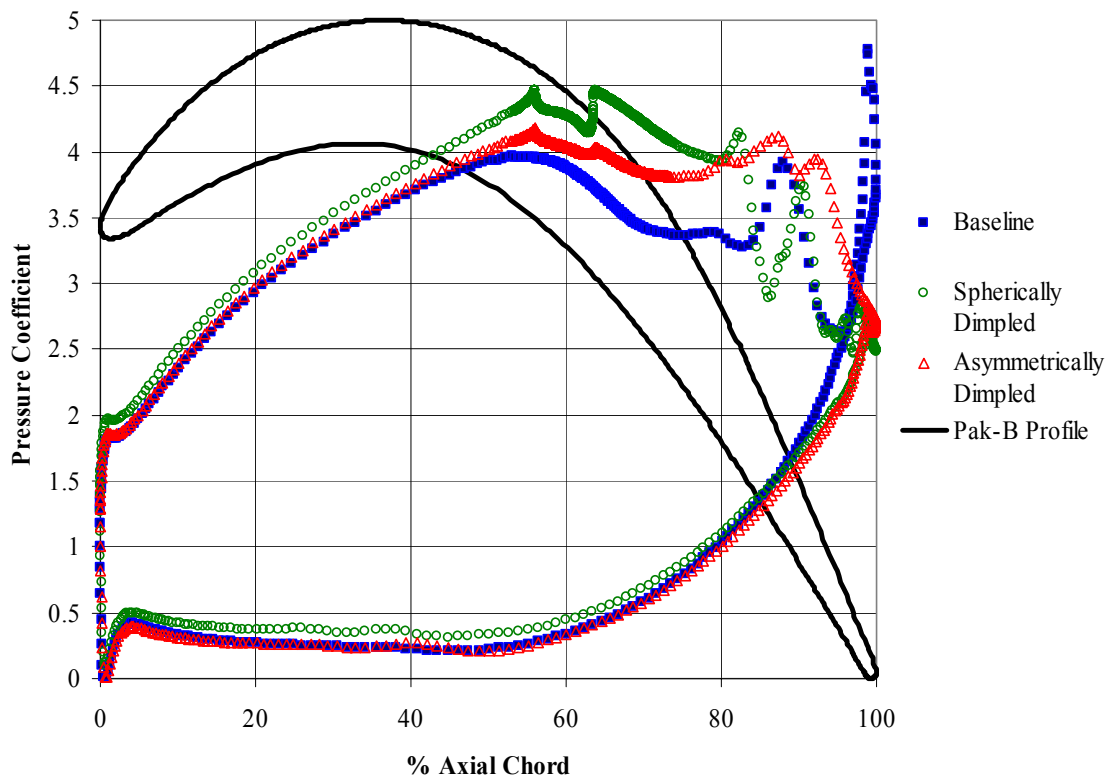


Figure 25. CFD surface pressure coefficient comparison between Pak-B baseline, Pak-B with spherical dimples and Pak-B with asymmetric dimples at $Re = 25k$. Profiles are aligned with the Pak-B profile

offers improved blade loading with a maximum C_p value greater than 4.2. There are two peaks in the data on either side of 60% axial chord. These indicate the edges of the dimple which are characterized by low static pressure consistent with relatively higher velocity air associated with a vortex. The slight dip in the data just aft of 60% axial chord denotes a possible vortex core. The spherical dimple performs better than the other two cases with a peak value reaching nearly 4.5. It is also characterized by two peaks on either side of 60%, denoting the possible presence of a vortex within the dimple. It appears to delay separation to almost 75 % axial chord. A feature unique to the C_p plot for the symmetric dimple is a higher profile across the leading edge surface from the stagnation point to about 50% axial chord. This indicates that the separation associated with the other two cases partially blocks the flow, transmitting higher static pressures upstream. Similarly, the data long the pressure surface leading edge is also lower for the spherically dimpled blade. This shows that the spherical dimple has a positive impact on both surfaces.

3.4.8 Location of Separation, Reattachment and Vortex Cores

FIELDVIEW[®] was used to view lines of separation and re-attachment, as well as vortex cores. These parameters are useful understanding flow structure and behavior. Under the FIELDVIEW[®] menu for “surface flows”, three surface flows are created “separation lines,” “reattachment lines,” and “vortex cores, eigenvalue analysis.” The X+ direction is selected for viewing, and three different geometric colors are used: red for separation, blue for reattachment, and yellow for vortex cores.

Figures 26 - 28 show the axial views of the computational results for separation and reattachment locations at Re 25k on three Pak-B configurations. The baseline Pak-B

is shown in Figure 26 with initial separation occurring at 66% axial chord, consistent with research conducted by Bons et al. at a Reynolds number of 25,000 (23). After the initial separation, there are two regions of fairly coherent reattachment and subsequent separation. This possibly indicates the presence of vortical structures.

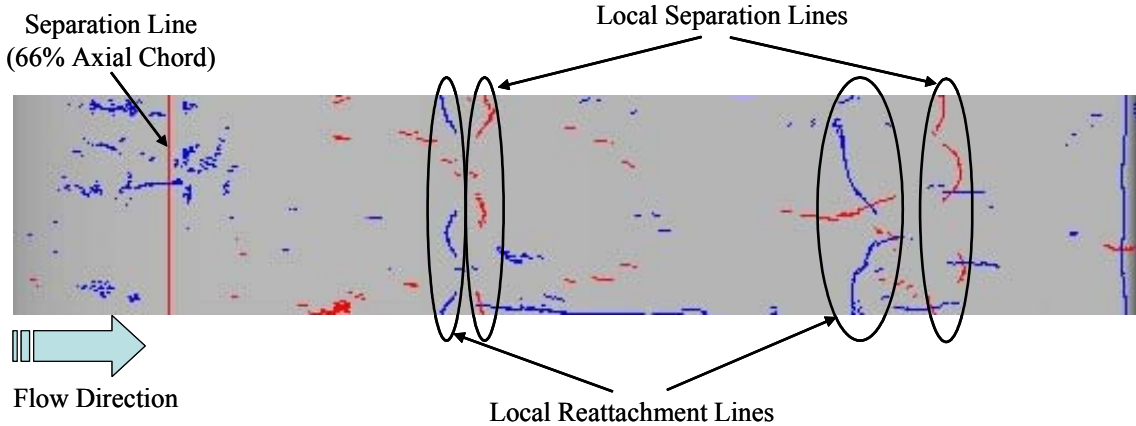


Figure 26. Computational results for baseline Pak-B blade at Re 25k. Red indicates separation, and blue indicates reattachment. The suction surface is shown oriented with flow from left to right

Figure 27 shows the laminar CFD solution for surface flow characteristics on a Pak-B with spherical dimples at 60% axial chord at Re 25k. The flow separates from the leading edge of the dimple and reattaches just before the trailing edge. There is a coherent vortex core within the dimple (vortex image shown later). The core is concaved slightly upstream. The separation line occurs at 73% axial chord. This is a 10% improvement over the baseline, indicating a related improvement in blade efficiency. Aft of the separation, there is a region of mixed flow structures, indicating energized flow.

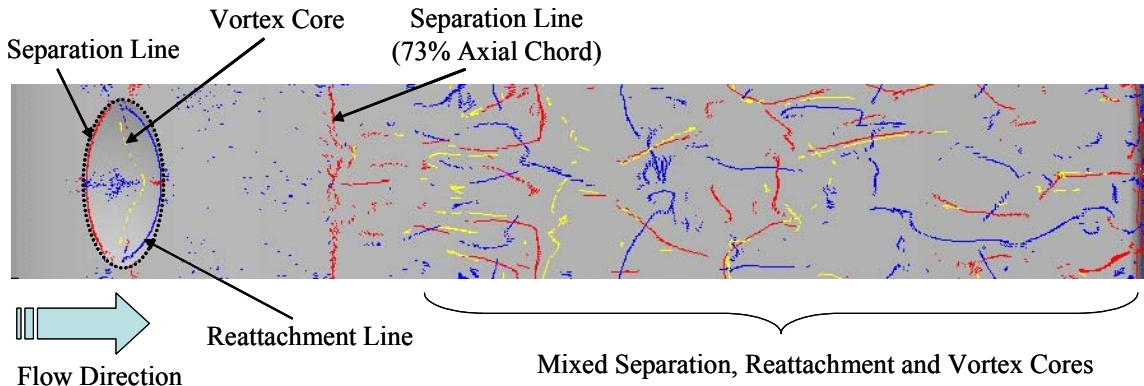


Figure 27. Computational results for Pak-B blade with spherical dimples at 60% axial chord at $Re = 25k$. Red indicates separation, blue indicates reattachment and yellow indicates the location of vortex cores. The suction surface is shown oriented with flow from left to right

Figure 28 shows laminar CFD results for the surface flow characteristics on a Pak-B with asymmetric dimples at 60% axial chord at $Re = 25k$. The flow around the dimple separates at the leading edge of the dimple and reattaches just before the trailing edge. Furthermore, a spanwise vortex core is present within the dimple. The vortex core appears to turn downstream near the straight edge of the dimple without ever leaving the dimple. There is a clear line of separation at 69% axial chord, indicating an improvement over the baseline but not as high as the Pak-B with spherical dimples. Downstream of this location, the flow is very erratic with some reattachment and separation. Spanwise vortex cores are found between and downstream of reattachment and separation lines, as well as vortex cores. On the whole, the spherical dimple does a better job of energizing the flow downstream of the separation location.

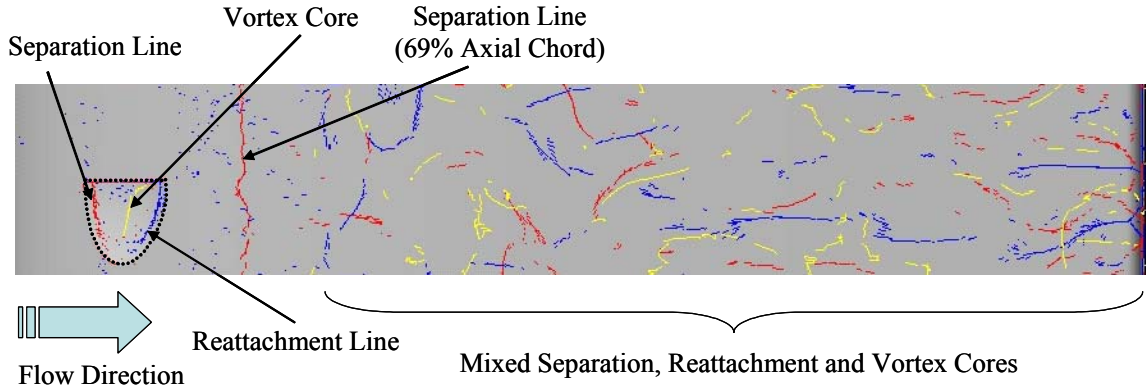


Figure 28. Computational results for Pak-B blade with asymmetric dimples at 60% axial chord at $Re = 25k$. Red indicates separation, blue indicates reattachment and yellow indicates the location of vortex cores. The suction surface is shown oriented with flow from left to right

3.4.9 Flow Structure Visualization

Flow structure over the suction surface of the blade is visualized using streamlines seeded about one node above the surface at two axial chord locations: just forward of the dimple leading edge and near the chordwise centerline of the dimple. In FIELDVIEW[®] this was accomplished by creating two different rakes and selecting 16 point ribbons to view flow direction and twist. To create a rake, two spanwise end points were chosen and then FIELDVIEW[®] automatically generated points that were evenly distributed between the two. Once the rakes were created, streamlines were calculated by the program, generating particle paths along integrated velocity gradients. Looking down on the suction surface of the baseline blade showed that the flow structure of the baseline Pak-B remains reasonably straight and parallel. Figure 29 shows a profile view of the flow structure, indicating the presence of a brief re-attachment near the trailing edge. This is consistent with the static pressure contours shown in Figure 22. The flow is

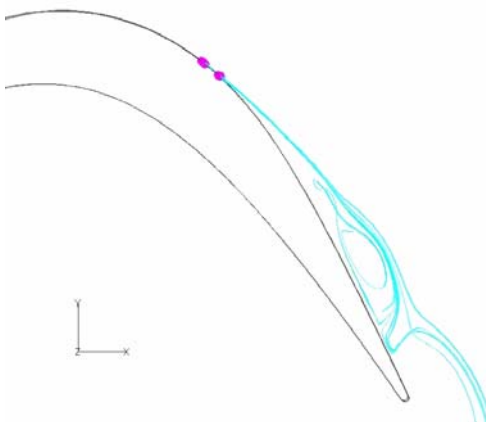


Figure 29. CFD profile streamlines for a baseline Pak-B blade at Re 25k

clearly separated with a large separation bubble centered around 92% axial chord.

Further downstream the flow is noticeably detached.

Figure 30 shows a profile view of the Pak-B blade with spherical dimples at 60% axial chord. Streamlines indicate that the separation bubble is much smaller, increasing the overall blade effectiveness. Furthermore, the flow leaving the trailing edge is less detached. This indicates less momentum deficit and reduction in the pressure loss coefficient.

Figure 31 shows a profile view of streamlines on a Pak-B blade with asymmetric dimples at 60% axial chord at Re 25k. The separation bubble is near the same location as the bubble on the baseline blade; however, it appears to be smaller. The detached region near the trailing edge is also improved. This figure indicates some possible improvement to blade efficiency, but the spherical dimple is clearly better.

Figure 32 shows the blade with spherical dimples from an axial view, looking down on the suction surface. Streamlines show that there is a significant spanwise vortex

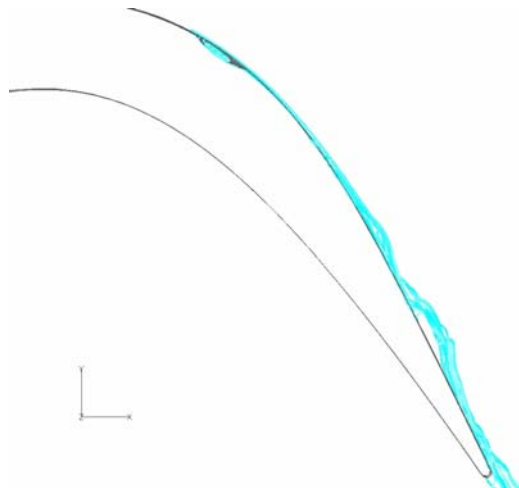


Figure 30. CFD profile streamlines for a Pak-B blade with spherical dimples at 60% axial chord at $Re\ 25k$

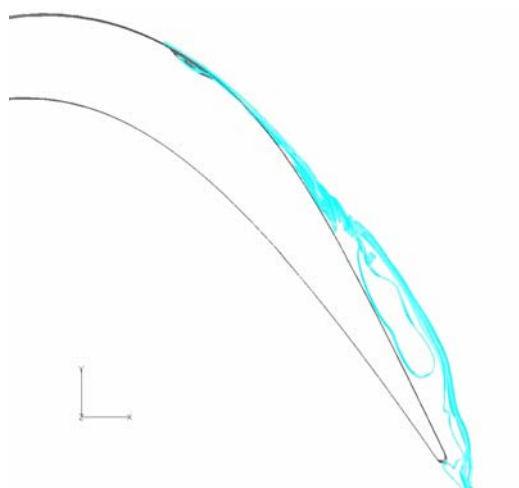


Figure 31. CFD profile streamlines for a Pak-B blade with asymmetric dimples at 60% axial chord at $Re\ 25k$

trapped within the dimple. The flow appears to be drawn toward the center of the dimple, exiting the dimple axially near centerline. This indicates the presence of low static pressure near the centerline of the dimple. The spanwise vortex appears to be of equal magnitude and opposite sense from either side of the dimple. This figure indicates that

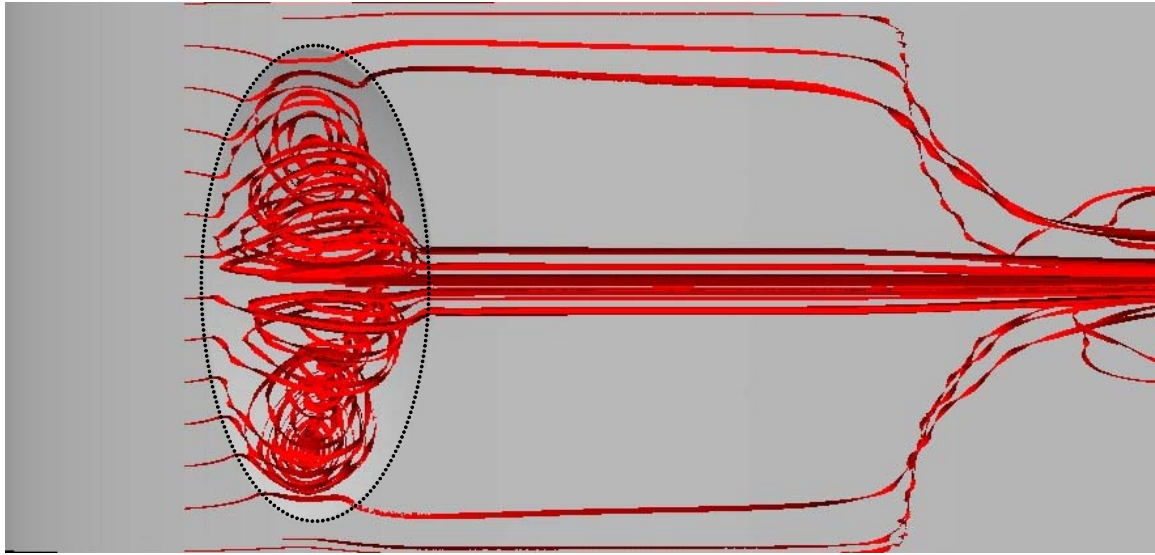


Figure 32. CFD suction surface streamlines for a Pak-B blade with spherical dimples at 60% axial chord at $Re = 25k$. The axial view shows flow from left to right

there is very little influence from neighboring dimples. At the separation location, flow that initially traveled around the edges of the dimple is entrained toward the centerline where the fluid is moving faster, having lower static pressure. Expanding the view, Figure 33 reinforces the notion that there is very little influence between dimples, except near the trailing edge.

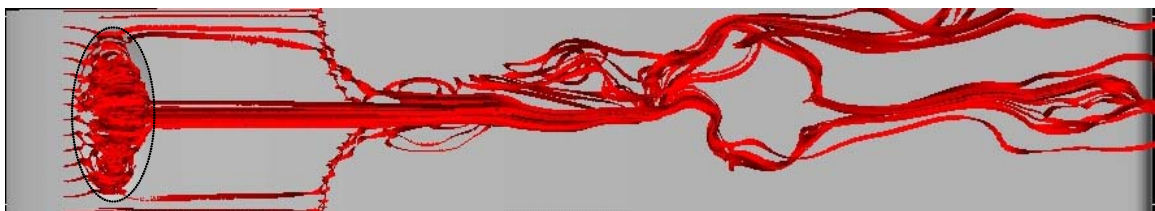


Figure 33. Enlarged view of CFD suction surface streamlines for a Pak-B blade with spherical dimples at 60% axial chord. The axial view shows flow from left to right

Figure 34 shows an axial view of the blade with the asymmetric dimple, looking down on the suction surface. Streamlines show that there is a spanwise vortex trapped

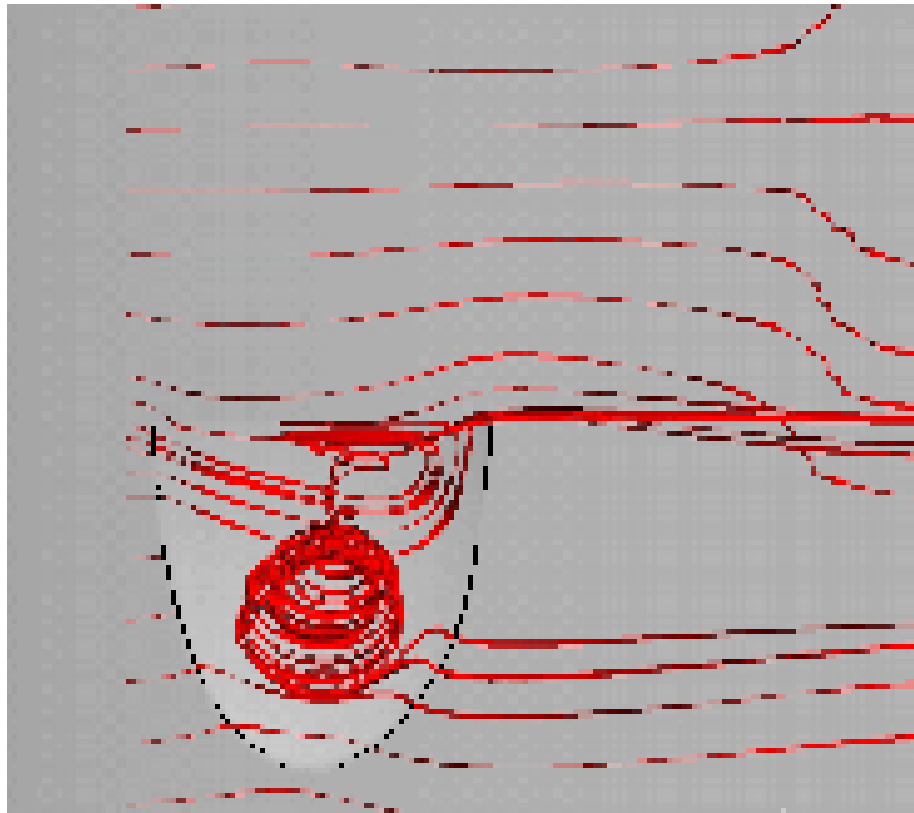


Figure 34. CFD suction surface streamlines for a Pak-B with asymmetric dimples at 60% axial chord at $Re = 25k$. The axial view is shown with flow from top to bottom

within the dimple. Flow appears to be drawn toward the dimple to leak out mostly from both outboard edges. This denotes a low pressure region within the dimple. From this figure, there appears to be little influence from adjacent dimples. Figure 35 is an enlarged view, showing the presence of some influence between dimples. It



Figure 35. Enlarged view of CFD suction surface streamlines for a Pak-B blade with asymmetric dimples at 60% axial chord at $Re = 25k$. The axial view is shown with flow from left to right

appears that the aft of the separation point flow is either entrained toward the flow behind the dimple or toward flow aft of the adjacent dimple. This occurs because the fast moving air exiting the dimple has a lower static pressure. Spanwise asymmetry in the flow is apparent; however, near the trailing edge, flow becomes more uniform.

3.5 Summary and Conclusions of Computational Research

CFD solutions suggest that the spherical dimple is more effective than the asymmetric dimple in controlling boundary layer separation and reducing the associated losses. Velocity and total pressure contours show that the dimples are effective in reduced momentum deficit and energy loss. Static pressure contours and Cp profiles show that dimples increase blade loading. Furthermore, the Cp plot indicates that flow separation partially blocks the flow, effecting upstream flow. There appears to be two contributing mechanisms. The first and perhaps most significant mechanism is the trapped vortex within the dimple. The asymmetric dimple is less effective in this regard because it is only half the size of a full dimple. The second most effective mechanism appears to be the ability of the trapped vortex to entrain the flow. As mid-passage airflow negotiates the dimple, it is entrained and mixes energy into the flow. Though the vortex with the asymmetric dimple may not be as effective, it appears to offer some improvement by entraining flow aft of the separation location. These results are only meant as a qualitative measure of what may possibly be happening in the airflow. Experimental testing is essential to evaluating one dimple configuration over another.

CHAPTER 4. EXPERIMENTAL RESULTS AND ANALYSIS

4.1 Wind Tunnel and Cascade Characteristics

Wind tunnel tests are conducted in a modified open loop Aerolab Corporation draw-down tunnel (Figure 36). The tunnel is modified to allow for variable turning angles within the test section. Within the test section are 8 Pak-B blades, comprising a removable cassette. Tests are conducted at Re 100k, 45k and 25k with turbulence levels of 1% and 4%. The tunnel and test section are the same as used by Lake with few modifications to the instrumentation set-up (1). National Instruments LabVIEWTM software is used as an interface to control instrumentation and collect, reduce and display data.

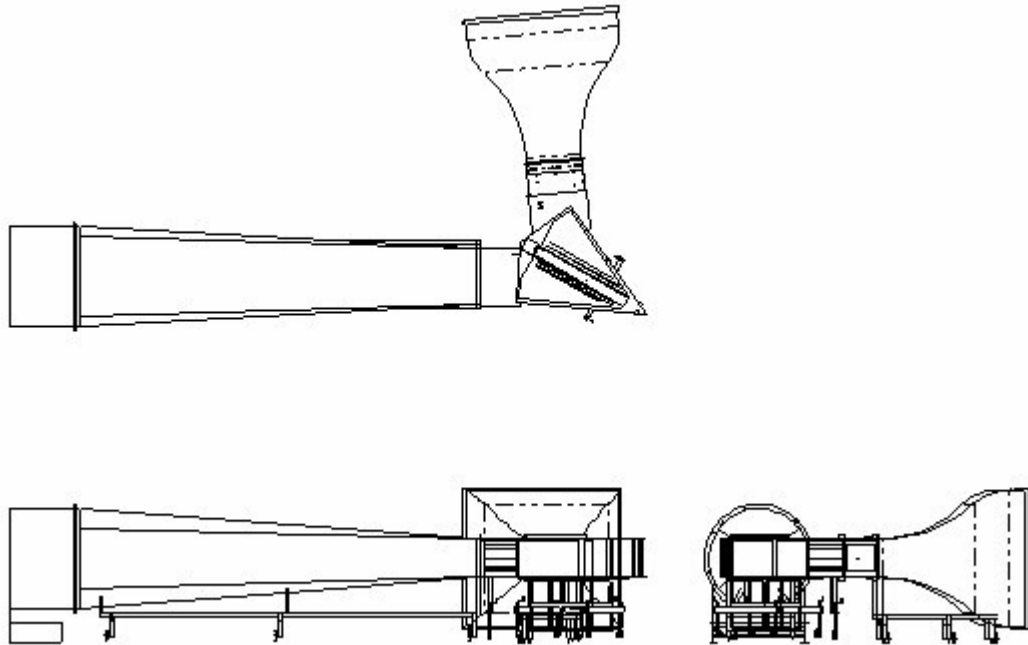


Figure 36. Aerolab Corporation modified draw-down wind tunnel (illustration courtesy of AFRL)

4.1.1 Wind Tunnel Geometry and Features

Air is drawn through the wind tunnel by a Joy Technologies Axivane axial flow fan with an outer radius of 114.3 cm. The fan is powered by a 93.2 kilowatt motor enclosed in a 124.5 cm long casing which contains the electric motor, axial fan, exit vanes and a wire mesh filter screen. The motor is controlled by a Harmon/Commonwealth Corporation variable frequency motor controller.

The inlet bell-mouth is 305 cm wide and 267 cm high with a honeycomb flow straightener and converging nozzle. The convergent section is 229 cm long and has an exit section that is 122 cm wide and 85.1 cm high. Corner vortices are minimized with the use of Styrofoam inserts that each extends into the test section 10.2 cm in the vertical plane and 12.7 cm in the horizontal plane (Figure 37). The inserts allow for freestream turbulence level as low as 1% when configured as a clean tunnel.

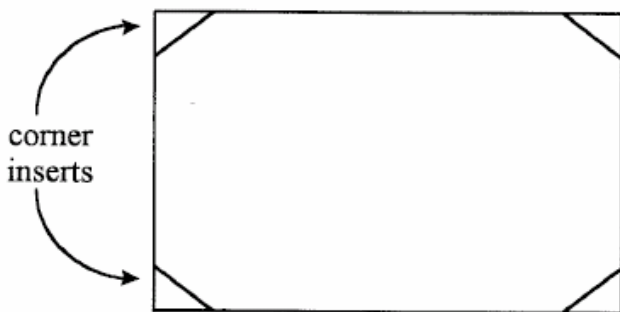


Figure 37. Cross-sectional area of wind tunnel (1)

The tunnel is equipped with a turbulence generator housing at 190.7 cm upstream of blade #1. The housing is 76.2 cm long and can be run empty, yielding a clean tunnel configuration with freestream turbulence of 1%. When the turbulence grid is installed,

4% turbulence is passively generated between 127 and 254 cm downstream. The grid is comprised of 2.54 cm diameter round stainless steel tubes arranged as a square mesh and capable of being run in an active or passive mode (Figure 38). The tubes are spaced 7.6 cm apart from center to center and are designed in accordance with Roach's isotropic turbulence grid guidelines (45). Lake ensured proper isotropy and turbulence length scales in accordance with Mayle et al. (1; 46) Several repeated measurements were taken to determine length scales using a single hot-wire probe and Air Force Research Laboratory software to integrate and average data.

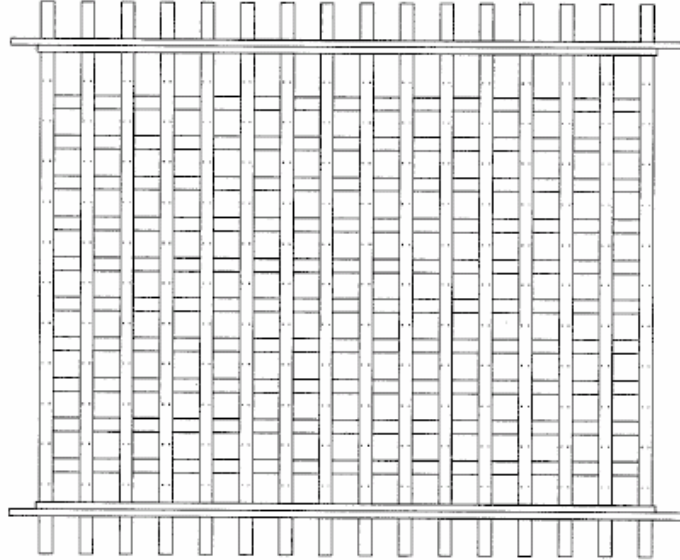


Figure 38. Turbulence grid. Passively generates Tu 4% (illustration courtesy of AFRL)

4.1.2 Cascade Features

The cascade consists of 8 Pak-B blades with 17.78 cm axial chord lengths and an axial chord-to-spacing ratio, or solidity, of 1.129 (Figure 39). True chord length is 25.995 cm. The Pak-B profile has a camber angle of 36° and a stagger angle of 25°. Lake recorded an incidence angle of -1° at Re 45k, yielding an inlet angle of 35° (1). He

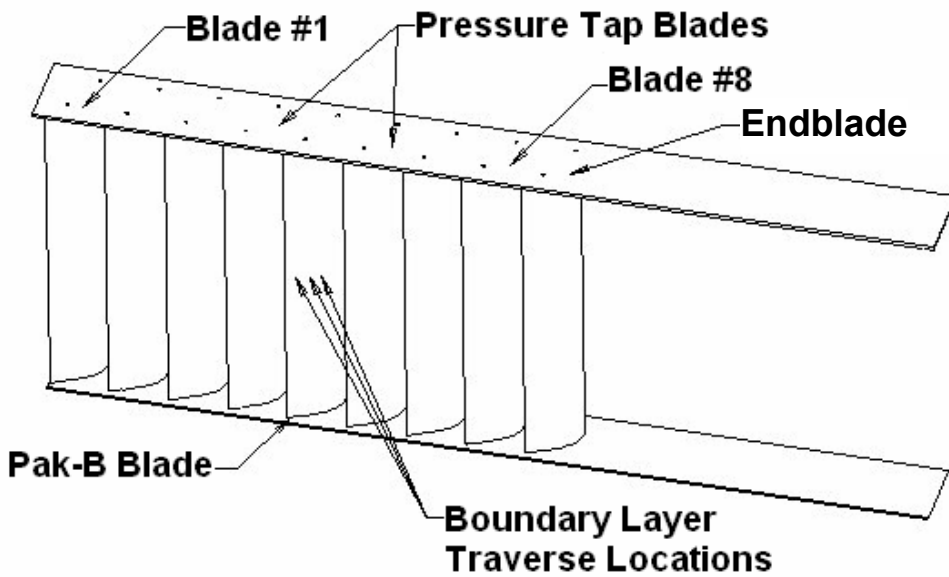


Figure 39. Removable cassette of eight Pak-B blades and endblade (illustration courtesy of AFRL)

also measured average exit angles, finding agreement with the designed 60°. The Pak-B blade is molded from Ultralloy 108 white resin with a 78.63 cm span to yield an aspect ratio of 4.92 to 1. This aspect ratio allows for a good 2-D flowfield about the mid-span, with negligible effects from endwalls. Blade #1 is furthermost inboard, 198 cm downstream of the turbulence grid. Blade #8 is furthermost outboard, 300 cm downstream of the turbulence grid. Lake modified blade #5 with three rows of nine spherical dimples: one row at 50%, one at 55%, and one at 65% axial chord (1). For the current research this same blade is used. To test the baseline Pak-B, this same blade was used with tape over the dimpled rows. The tape is 19mm wide, and is cut to a spanwise length so that there is only 2mm past the edge of the last dimple in a given row. The tape is about 0.1 mm thick. To create the asymmetric dimples, Playdough® is packed into the dimple and then smoothed with a razor to take the same contour of the blade surface.

The Playdough® in a spanwise half of each dimple is then removed so that the straight edge is parallel to the axial flow. A small strip of tape is laid over the remaining Playdough® to hold it in place. The Playdough® cures overnight.

4.1.3 Data Collection Locations

The wind tunnel has four thermocouples which are suspended from the top of the tunnel (Figure 40). These are used for measuring static temperature and calculating density. Because the flow was incompressible for this experiment, density was calculated from ambient room static pressure and tunnel temperature. Using the perfect gas law:

$$\rho = \frac{P}{R T} \quad (13)$$

where ρ is density, P is room static pressure, T is tunnel temperature and R is the gas constant for air.

Thermocouple #1 is located at the inlet upstream of the flow straightener screen. It is suspended 100 cm from the bottom of the bell-mouth and 61cm from the inboard wall. Thermocouple #2 is suspended 45.7 cm downstream of the turbulence grid and 145 cm upstream of blade #1. Thermocouple #3 is suspended at the 40% axial chord line of blade #1. Thermocouple #4 is suspended 76.2 cm downstream of blade #1. Thermocouples #2, 3 and 4 are spanwise aligned with inlet and exit flow for blade #1.

A fixed inlet hot film protrudes through the test section floor one axial chord length upstream of blade #5. This hot film is used to measure velocity and calculate Reynolds number. Tunnel flow speed is set to achieve a desired Reynolds number using

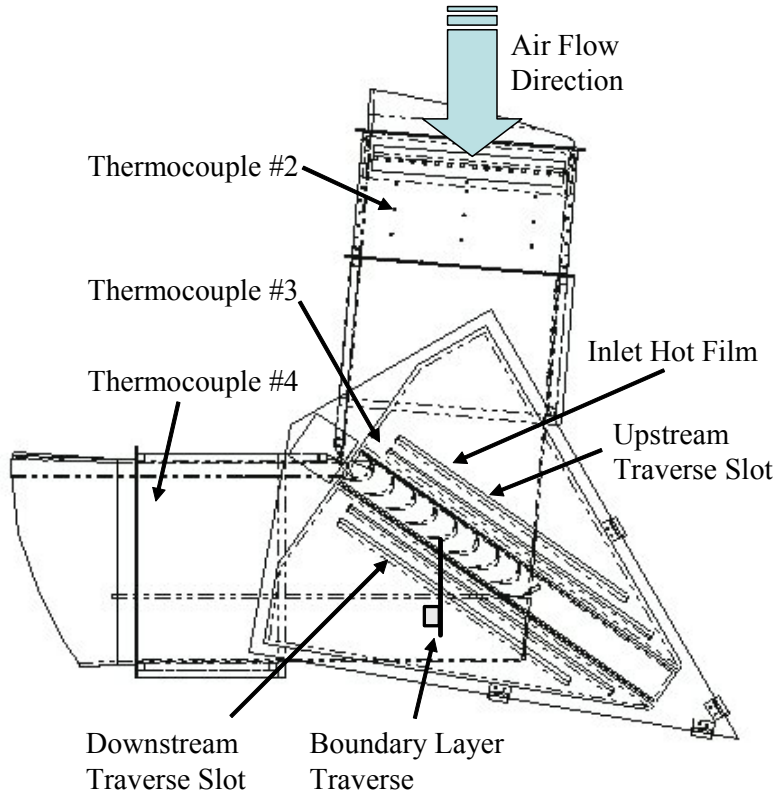


Figure 40. Wind tunnel instrumentation locations (courtesy of AFRL)

the inlet hot film, ambient pressure, tunnel temperature and the following equation:

$$Re_c = \frac{\rho U c}{\mu} = \frac{\left(\frac{P}{RT} \right) U c}{\mu} \quad (14)$$

Where c is axial chord, U is inlet velocity and μ is the viscosity of air.

Inlet dynamic pressure is based on the direct differential between upstream total and static pressure. This measurement is made from a pitot-static probe that extends 1.5 axial chord lengths upstream of the cascade. It is suspended through the ceiling from a Velmex traverse at a variable height so as not to influence downstream measurements with a wake. The traverse is capable moving the inlet pressure probe 182.88 cm from

inboard to outboard; however, the test section sweep is only 60 cm from inboard of blade #4 to outboard of blade #6, centerline-to-centerline of the respective blade passages. The traverse is controlled by a Velmex VP9000 controller, and the location is viewed on a Sony LH61 position display.

The movable pitot-static probe is also used for measuring differential total pressure between the upstream and downstream pressure probes. Total local pressure loss coefficient is the differential between inlet and exit total pressure divided by the differential between inlet total and static pressure:

$$\omega = \frac{\overline{(P_{t,inlet} - P_{t,exit})}}{\overline{(P_{t,inlet} - P_{s,inlet})}} \quad (15)$$

where $\overline{(P_{t,inlet} - P_{t,exit})}$ is a time average of direct differential samples of inlet and exit total pressures, and $\overline{(P_{t,inlet} - P_{s,inlet})}$ is a time average of direct differential samples of inlet total and static pressures.

Similarly, surface pressure coefficients are also based on dynamic pressure measured using the inlet pitot-static probe. Surface pressure coefficient is the differential between the inlet total pressure from the upstream pitot-static probe and surface static pressure divided by the differential between inlet total and static pressure:

$$Cp = \frac{\overline{(P_{t,inlet} - P_{s,local})}}{\overline{(P_{t,inlet} - P_{s,inlet})}} \quad (16)$$

where $\overline{(P_{t,inlet} - P_{s,local})}$ is a time average of direct differential samples of inlet total and local surface static pressures. Blades #4 and #6 are equipped with surface pressure taps to measure static pressure. There are 40 taps on each blade, though only 37 are usable on

blade #4 due to clogged passages from the manufacturing processes. Taps are staggered along a 30° line from each other, extending from leading to trailing edge and covering a 22.86 cm span across the center of the respective blade. The stagger limits cross-talk between holes so that one hole does not influence the adjacent downstream hole.

Wake velocity profiles are generated from velocity measured by an exit X-Film suspended one axial chord length downstream of the cascade at various heights corresponding to particular dimple rows. For the dimples at 50% and 65%, the probe is located 12 cm from blade mid-span. For the dimples at 55%, the probe is located at mid-span. It is connected to the same traverse as the upstream pressure probe, traveling across the cascade exit plane as well as in the spanwise direction. Also connected to the traverse and located along side the X-film (approximately 2 cm apart) is a Kiel probe that reads total pressure. The Kiel probe is not as sensitive to orientation angle as the inlet pitot-static probe, making it useful in exit flow that generates large angle variations.

A boundary layer probe containing a single element hot film is inserted through the outer tailboard through slots at three spanwise locations. These locations correspond to the dimple locations. The boundary layer probe is always oriented orthogonal to the blade surface (oriented by line of sight) and is moved to five different axial chord locations along the suction surface of blade #5. The five locations include 67.2%, 73.0%, 79.3% 84.8% and 89.8% axial chord (the same locations used by Lake).

4.1.4 Test Section Characteristics

The adjustable test section is capable of a flow turning angle up to 130° . It is hinged at a central pivot joint that allows the inlet and outlet angles to be independently adjusted. For the current research, the tunnel was set to design specifications for the Pak-

B blade; having a 35° inlet angle relative to the axial direction (normal to the cascade inlet plane) and a 60° exit angle (Figure 41). The innermost and outermost walls of the cascade are shaped to approximate the Pak-B suction and pressure surfaces, respectively.

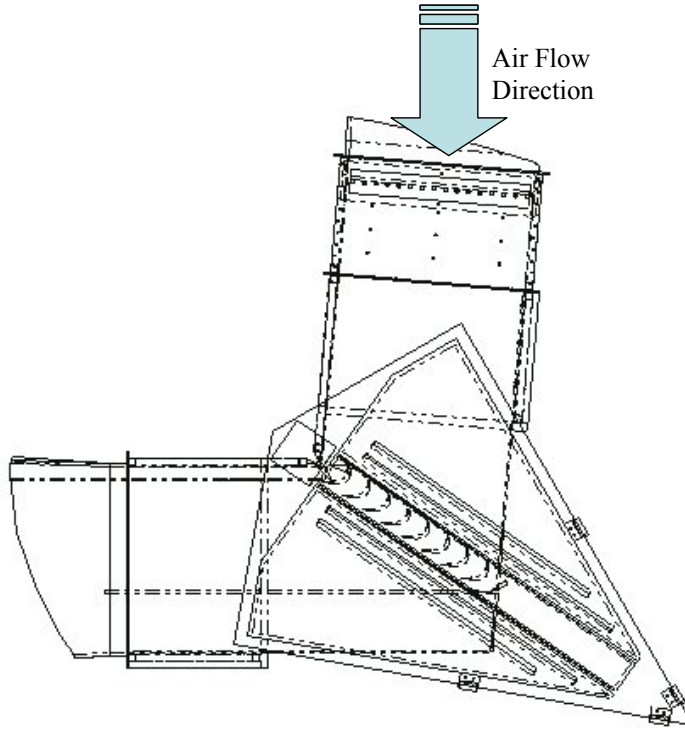


Figure 41. Plan view of test section (illustration courtesy of AFRL)

The blade cassette is fashioned with clear plexiglass top and bottom plates to which the blades are bolted. Each blade is held in place by two bolts positioned near the trailing and leading edges. The top and bottom plates are supported by two steel runners so that top and bottom plates are flush with tunnel inner surfaces.

The top and bottom of the test section are constructed from plexiglass sheets 2.54 cm thick. They are supported in a 6.4 mm deep groove so that they are flush with inner and outer surfaces. Traverse slots are cut into the plexiglass sheets so that they are

parallel to the leading and trailing edges of the cascade. The outboard walls are also made of plexiglass, allowing for good all-around visibility. In addition, there are inner and outer tailboards fashioned from plexiglass that adjust exit flow angles. The outer tailboard is in two sections such that the upstream section is 109 cm long, and the downstream portion is 91.4 cm long (Figure 42). The test section was tested with and without the downstream tailboard section to see the effect on loss coefficient and exit velocity profiles. There was no measurable effect for the Reynolds numbers being investigated.

For the same conditions used in this research, Lake measured air velocity magnitude and turbulence intensity across the blade row inlet and exit with a TSI 1210-T1.5 hot wire probe to ensure periodicity and uniformity (1). He found good periodicity with nearly 15.75 cm between each velocity peak. He also found good uniformity with each velocity minimum being nearly the same magnitude. Lake also used the hot wire data to measure inlet turbulence length scales (1). For the configuration with the turbulence grid removed (Tu 1%), length scales were 77.3 cm, 123.1 cm and 153.3 cm for Re 50k, 100k and 200k, respectively. For the configuration with passive turbulence in which the grid is installed (Tu 4%), length scales were 2.87 cm, 4.5 cm and 6.93 cm for Re 50k, 100k and 200k, respectively. Pitchwise inlet dynamic and total pressure variation is reported in the current study using the upstream pitot-static probe mounted to a traverse. The probe makes a single pass measuring the differential between inlet static and total pressure to estimate inlet dynamic pressure. It makes another pass to measure the differential between total inlet pressure and ambient air with one side of the transducer vented to room ambient pressure.

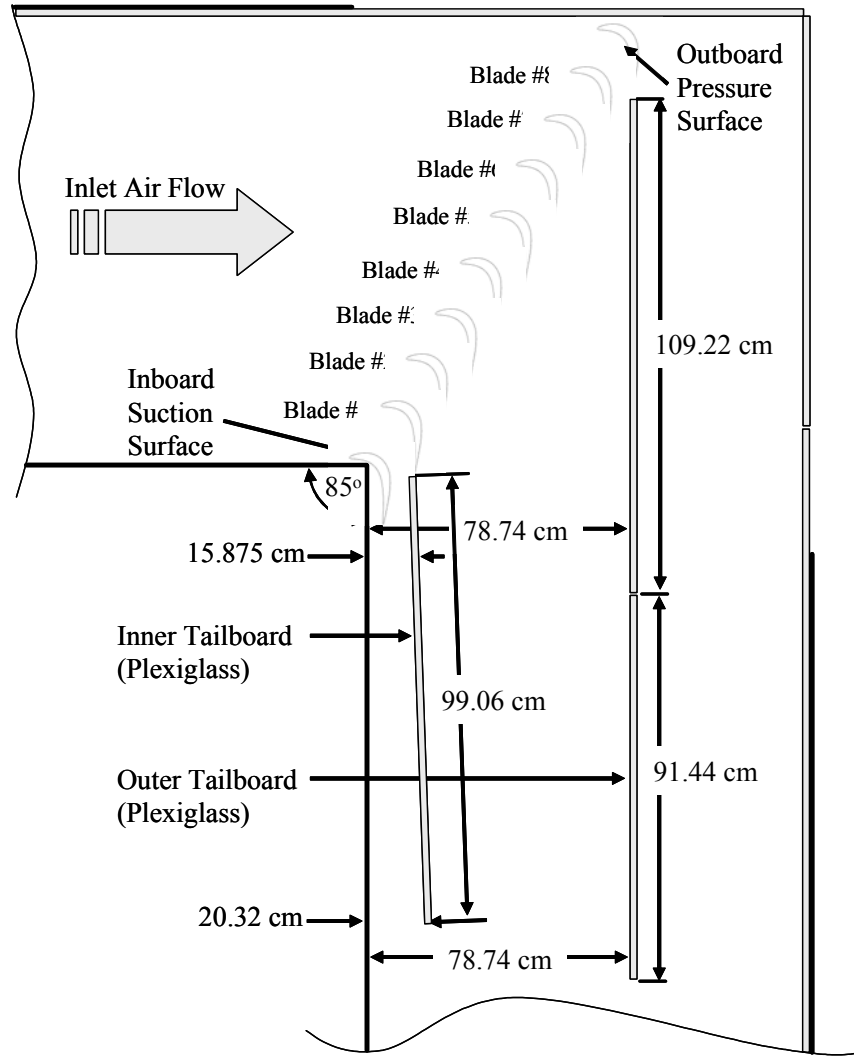


Figure 42. Test section geometry

Figure 43 shows no significant variation in total pressure at Tu 1%. The difference from the average (Δ Avg) is within 0.4 Pa. Figure 44 shows a slight variation at Re 45k and Tu 4%, but is always less than 0.4 Pa from the average value. Figure 45 shows very little variation in dynamic pressure across the inlet at Tu 1%. Figure 46 shows some variation in dynamic pressure at Re 25k and Tu 4%, but not a significant amount.

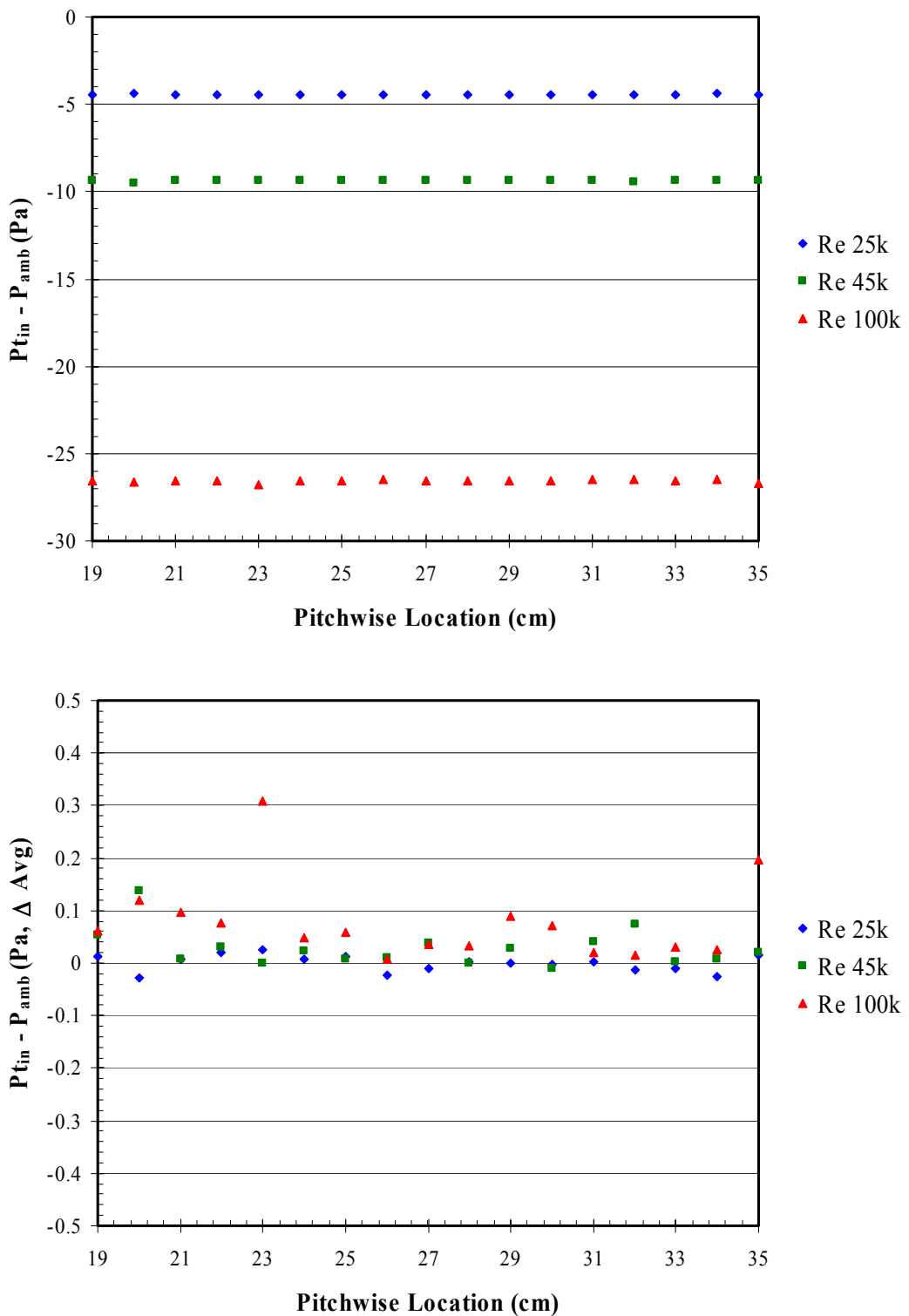


Figure 43. Test section inlet total pressure variation at Tu 1%

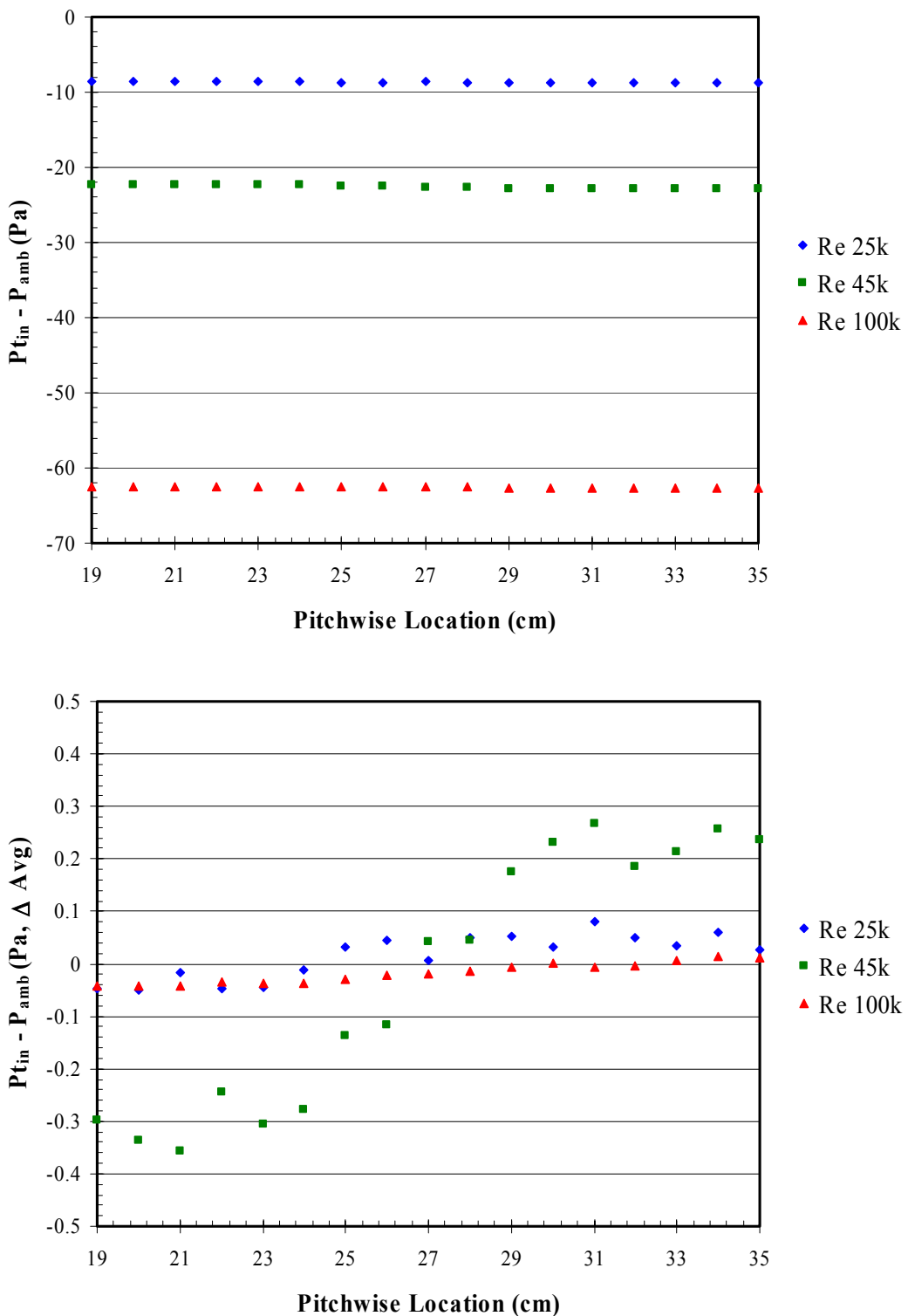


Figure 44. Test section inlet total pressure variation at Tu 4%

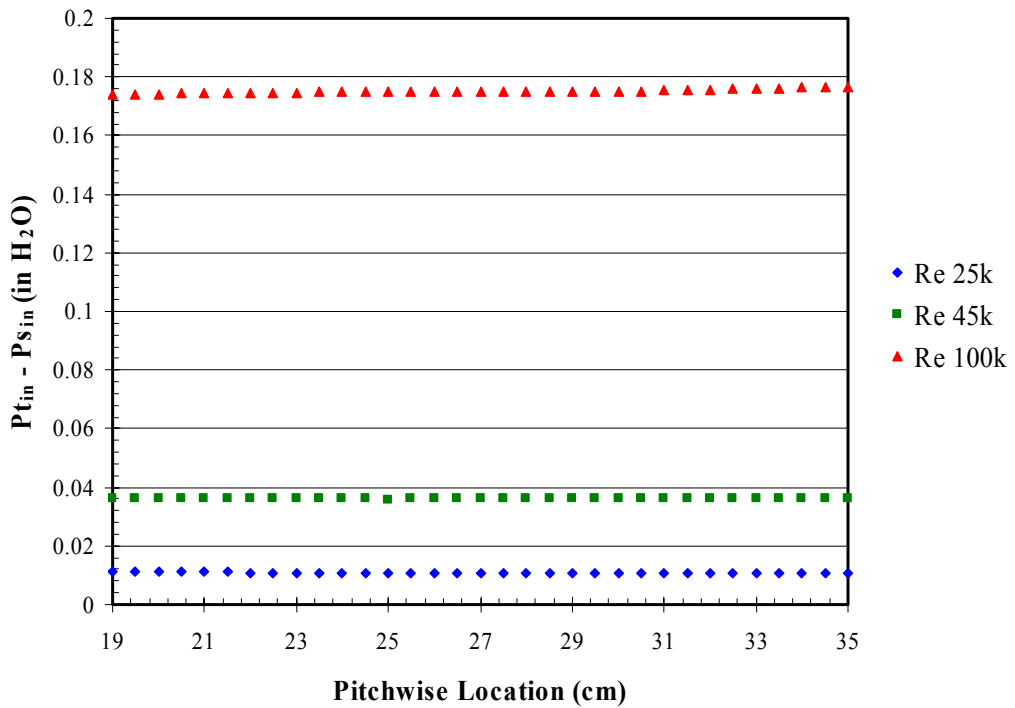


Figure 45. Test section inlet dynamic pressure variation at $Tu = 1\%$

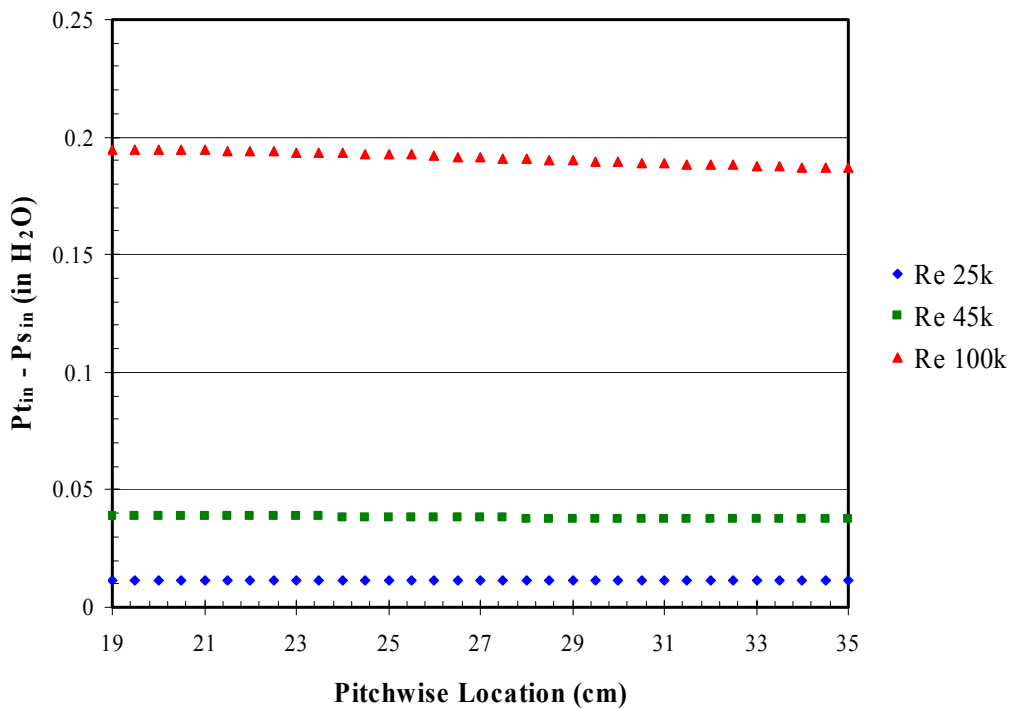


Figure 46. Test section inlet dynamic pressure variation at $Tu = 4\%$

4.2 Instrumentation

Figure 47 shows a schematic of the instrumentation used in the current research. The entire operation is controlled from a Dell Pentium 4 personal computer (PC). Within the Dell, there is an MXI-3 fiber-optic interface board that is connected to a National Instruments PXI 1010 chassis. The PC also contains three other PCI cards used to drive the traverses and collect hot/X-film voltage measurements.

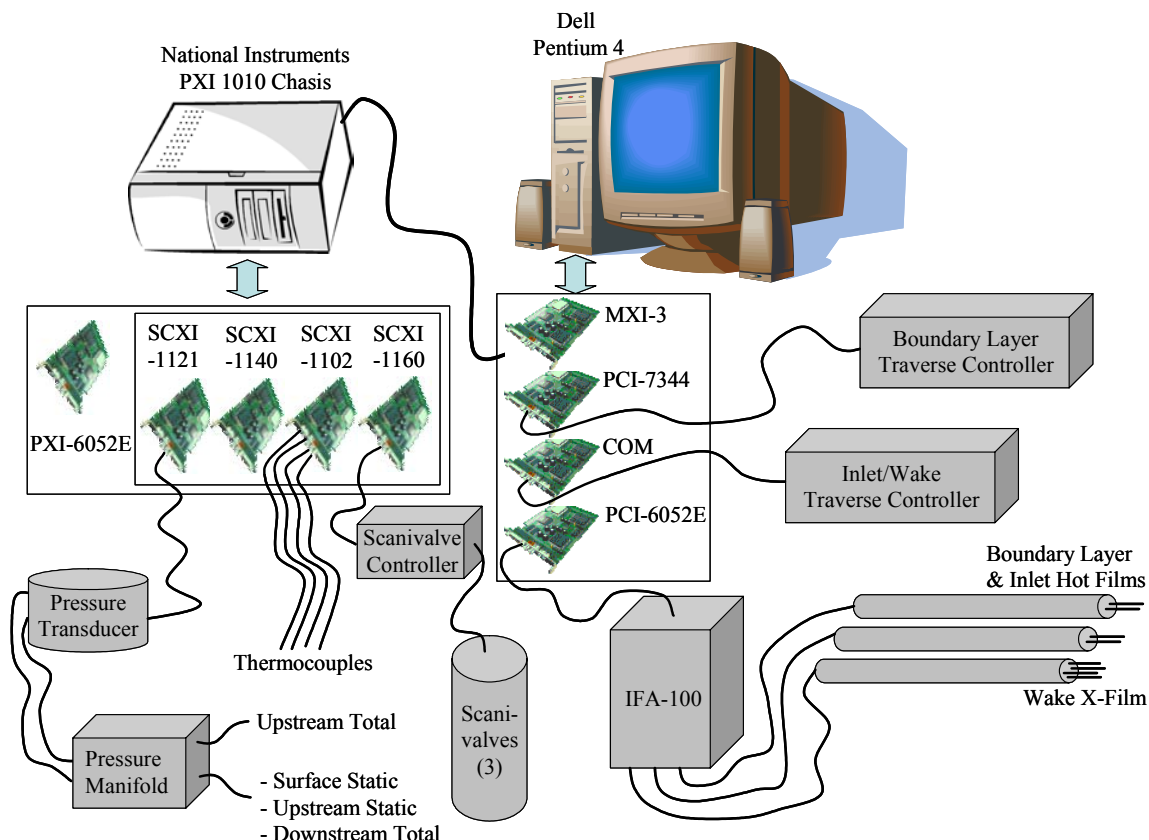


Figure 47. Instrumentation Schematic

The boundary layer traverse, a National Aperture, Inc. motorized 5.08 cm MM-3M micro traverse, is controlled through the PCI-7344 card inside the PC. It has a movement resolution of 20157.4 steps per cm. The traverse position encoder provides a

linear spatial resolution of $\pm 5.08 \times 10^{-5}$ cm. Traverse position is controlled and powered by a National Aperture, Inc. MC-3SA servo amplifier, which is in-turn connected to the PCI-7344 card.

Similarly, the main traverse which moves the upstream pitot-static probe and downstream Kiel probe and X-film is controlled through the PC by way of a standard RS 232 Com card. The main traverse is powered and controlled through a Velmex V-9000 controller with position displayed on a Sony LH61 digital read-out with ± 0.005 cm accuracy. A TSI, Inc. IFA-100 Flow Analyzer feeds hot film and X-film voltages directly to the PC through a National Instruments PCI-6052E A/D card which has a 16 bit resolution and a 333 ks/s sampling rate.

The PXI 1010 chassis contains a PXI-6052E A/D board which has a 16 bit resolution over ± 10 Volts. For this research, the pressure transducer had a calibration slope of 0.1998, yielding a least bit resolution of ± 0.06 Pa. The A/D board is connected to an SCXI cluster. This cluster includes an SCXI-1160 relay controller which commands the three Scanivalve controllers. There is an SCXI-1102 thermocouple board that is connected to the four reference thermocouples. A Druck LPM 5481 pressure transducer is connected to an SCXI-1121 signal conditioning card. It has a range of -0.2 to 0.8 in H₂O, requires a 10-30 voltage supply and outputs 0-5 volts. The pressure transducer is differential with one side always fed with the inlet total pressure from the upstream pitot-static probe through a manifold. The other side of the manifold is connected to a Scanivalve which selects either inlet static pressure from the upstream pitot-static probe, exit total pressure from the downstream Kiel probe, or surface static pressures from one of the two tapped blades.

4.2.1 Pressure Instrumentation

The primary interface for all measurements taken during this research is the Druck LPM 5481 pressure transducer. Before any other instrument calibration or data collection takes place, the pressure transducer is calibrated using a dead-weight tester. Figure 48 shows a schematic of the Pressure V1600/3D dead-weight tester.

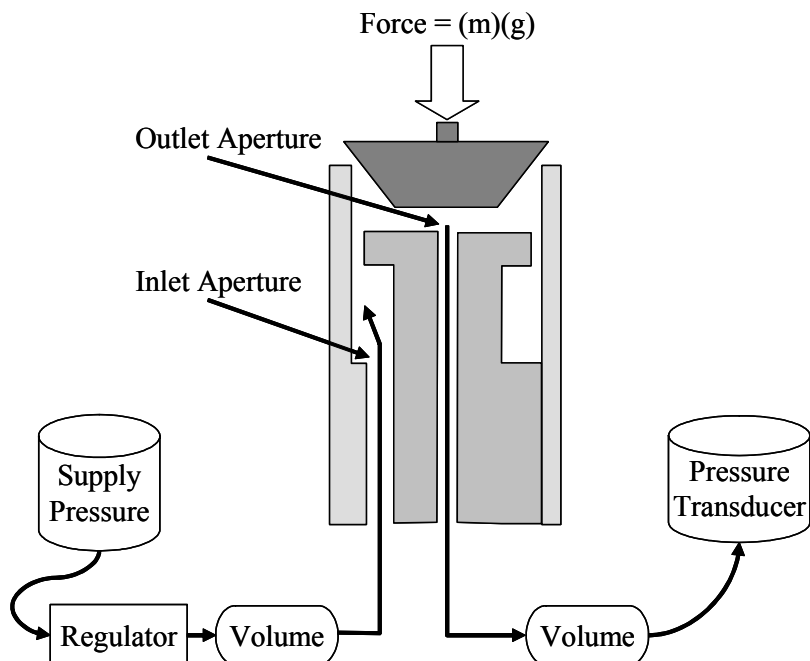


Figure 48. Dead-weight tester schematic

The operation of the tester is based on dynamic interaction of airflow with a non-cylindrical piston. A disk of known weight acts as a piston that is coaxially located in a cylinder, transforming force (known mass times local gravitational acceleration) into pneumatic pressure. The high accuracy is achieved by two cascade regulators, which also isolate the output pressure from any supply fluctuations. Air passes between the piston and cylinder such that a back-pressure is generated. A reference pressure to the

transducer is calculated as follows:

$$P = \frac{m g \left(1 - \frac{\rho a}{\rho w} \right) + R}{A_{cylinder}} \quad (17)$$

where P is the reference pressure, m is the known mass of the piston, g is the local acceleration due to gravity, R is back-pressure, $A_{cylinder}$ is the inner area of the cylinder, and the coefficient due to air buoyancy effect is:

$$\left(1 - \frac{\rho a}{\rho w} \right) \quad (18)$$

A correlation is then drawn between the known pressure and the voltage output from the pressure transducer. The calibration is accurate to within ± 0.01 Pa. Detailed calibration procedures are included in Appendix A. Before a pressure measurement is taken, the transducer intercept is reset by opening both manifold vents and reading a voltage across the transducer for zero differential.

Pressure measurements are used for calculating surface pressure coefficients, total pressure loss coefficients and dynamic pressure. Each calculation has the same uncertainty analysis because each calculation is merely one differential pressure reading divided by another. Using surface pressure coefficient as an example, the Kline and McClintock method for determining uncertainty first requires the calculation of partial derivatives as follows:

$$\frac{\partial Cp}{\partial \Delta P_{surface}} = \frac{1}{\Delta P_{dynamic}} \quad (19)$$

$$\frac{\partial Cp}{\partial \Delta P_{dynamic}} = \frac{-2 \Delta P_{surface}}{\Delta P_{dynamic}^2} \quad (20)$$

where Cp is surface pressure coefficient and equals $\Delta P_{surface}/\Delta P_{dynamic}$ (47). Next, the square of each partial is divided by the square of Cp (the parameter being calculated) as follows:

$$\frac{\left(\frac{\partial Cp}{\partial \Delta P_{surface}}\right)^2}{Cp} = \frac{1}{\Delta P_{surface}^2} \quad (21)$$

$$\frac{\left(\frac{\partial Cp}{\partial \Delta P_{dynamic}}\right)^2}{Cp} = \frac{1}{\Delta P_{dynamic}^2} \quad (22)$$

Therefore, the uncertainty in Cp is determined to be:

$$\varpi_{Cp} = Cp \sqrt{\left(\frac{\varpi_{\Delta P_{surface}}}{\Delta P_{surface}}\right)^2 + \left(\frac{\varpi_{\Delta P_{dynamic}}}{\Delta P_{dynamic}}\right)^2} \quad (23)$$

where ϖ is the uncertainty of the respective calculation or measurement.

Figure 49 shows a schematic of the pressure instrumentation. Note that a scanivalve selector sends the differential pressure transducer one of three possible pressure sources. The selected pressure is then fed to the pressure manifold along with upstream total pressure. The manifold then feeds the pressures to the transducer. The manifold is also capable of capping or venting either side of the transducer.

4.2.2 Velocity Instrumentation

Velocity measurements are made with hot films. Boundary layer and inlet velocities are measured using a single element hot film (TSI 1210-20), and exit velocity is measured with an X-film (TSI 1240-20). The boundary layer velocities are used to

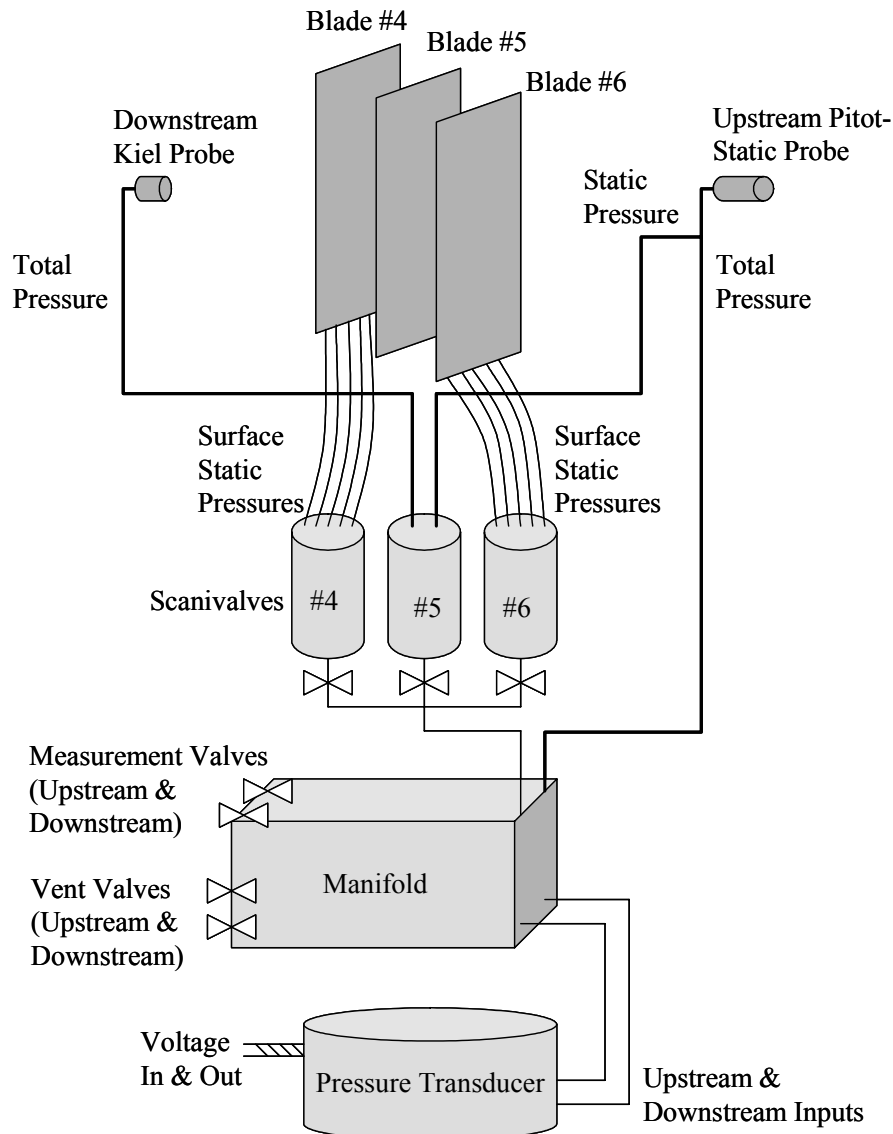


Figure 49. Pressure instrumentation schematic

create boundary layer velocity profiles. The inlet velocity is used to set the tunnel speed.

The exit velocities are recorded to generate wake velocity profiles.

Hot film calibrations are conducted after the IFA-100 is properly balanced according to procedures described in Appendix A. The single element hot films are calibrated using a non-dimensional curve fit between Nusselt and Reynolds number as

described by Bruun (48). The Nusselt number is based upon heat transfer across the film element. This heat transfer is determined by balancing a Wheatstone bridge within the IFA-100. Heat transfer is a function of velocity such that the non-dimensional relationship is as follows:

$$\text{Nu} = C + D (\text{Re}^{0.45}) \quad (24)$$

Where Nu is Nusselt number, C is the curve intercept on the Y-axis and D is the slope. The exponential value of 0.45 is chosen to provide an acceptable curve fit for measuring low speed flow. Calibration is accomplished using a TSI Model 1127 calibration stand and the Druck LPM 5481 pressure transducer. For the single element hot films, the element is placed over the calibrator air jet with a known velocity (based on the pressure transducer and regulated manually). The pressure is incremented and a correlation is then drawn between voltage and velocity according to Equation 22. For the X-film, elements are placed over the calibrator air jet at known angles with known velocities. Correlations are then drawn between voltages, velocities and angles. Detailed procedures for both single and dual element hot films are included in Appendix A.

Figure 50 shows the X-film measurement procedure which begins by comparing a measured angle to a known angle at the measured velocity. The corrected angle is used to correlate measured and to known velocities. The corrected velocity is then applied, and a new correlation is made between corrected and known angles, repeating the cycle until a specific tolerance is achieved. The result is an accurate reading for both velocity and angle.

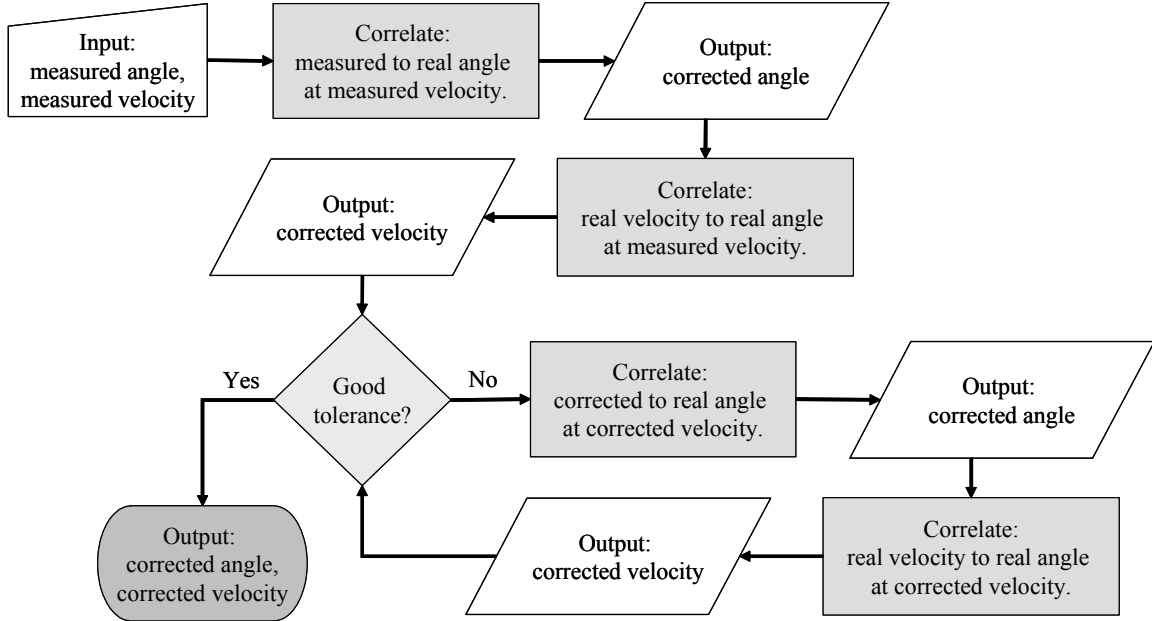


Figure 50. Process chart for correlating measured X-film angles and velocities

Hot films are calibrated using a differential pressure measurement between total and static (ambient) pressure, as well as room from pressure and temperature measurements. The relationship for velocity is as follows:

$$U = \sqrt{\frac{2 \Delta P_{dynamic} R T_{amb}}{P_{amb}}} \quad (25)$$

where U is velocity, $\Delta P_{dynamic}$ is dynamic pressure as a measured differential between total and static pressure, T_{amb} is based on thermocouple readings for ambient temperature and P_{amb} is measured by a Wallace and Tierman FA-129 pressure gauge which is accurate to ± 3.5 Pa. Using the same procedure used to calculate uncertainty for the surface pressure coefficient, the uncertainty for the velocity is:

$$\sigma_U = U \sqrt{\left(\frac{\sigma_{\Delta P_{dynamic}}}{2 \Delta P_{dynamic}} \right)^2 + \left(\frac{\sigma_{T_{amb}}}{2 T_{amb}} \right)^2 + \left(\frac{\sigma_{P_{amb}}}{2 P_{amb}} \right)^2} \quad (26)$$

4.2.3 Temperature Instrumentation

Temperature measurements within the tunnel are made with J-type thermocouples. Measurements are used in calculations for Reynolds number which is subsequently used to set the tunnel speed. Thermocouples are connected to the PXI 1010 chassis through the SCXI-1102 which is used as a signal conditioner. The SCXI-1102 is connected to an SCXI-1303 thermocouple block which uses a thermistor for a cold junction temperature reference. The SCXI-1102 makes a differential reading between thermocouples and the thermistor inside the SCXI-1303. Voltages are relayed through the PXI 1010 chassis to the A/D board in the PC. The computer then converts the voltages to temperatures.

4.3 Data Collection Methodology

All data collection begins with a zero differential reading from the pressure transducer to set the intercept. This is accomplished using a LabVIEWTM continuous A/D software program with user input for dew point temperature to account for hygroscopic effects. A LabVIEWTM current conditions software program is used to set the wind tunnel speed with inputs from the user for dew point temperature, ambient pressure and hotfilm calibration constants, as well as voltage inputs from the inlet hot film. All other collection methods require user input into the respective LabVIEWTM software programs for ambient pressure, dew point temperature, pressure transducer calibration constants and hotfilm calibration constants.

4.3.1 Surface Pressure Scans

Surface pressure measurements are taken on blades #4 and #6. Each blade is molded with 0.76 mm diameter taps leading to tubes within the blades. The tubes were

cast into the blades during the molding process. Blade #4 has 37 working taps, and blade #6 has 40. The three unusable taps on blade #4 were clogged during the manufacturing process and not are included in the current results. Locations of the taps are discussed in the previous section on data collection locations. Figure 47 shows the instrumentation layout for the surface pressure measurements. The pressure taps are connected to two Scanivalve Corporation 48-channel 48J9-1 multiplexers. Selected tap readings are relayed through the pressure manifold and ultimately to the pressure transducer. The multiplexer is powered by a CTRL 10P/S2-S6 Solenoid Controller as seen in Figure 45 and controlled by the SCXI-1160 within the PXI 1010 chassis. The PXI 1010 is subsequently controlled by the PC. The pressure transducer uses the upstream total pressure for a differential pressure reading with the selected surface static pressure. The differential is used to calculate a local surface pressure coefficient.

The procedure begins with setting the tunnel to a desired Reynolds number. Surface pressure scans are conducted for the baseline Pak-B at Reynolds numbers of 100k, 45k, and 25k. The tunnel was configured with the turbulence grid installed and removed, producing a total of six surface pressure coefficient profiles. Note that after pressure tap data is acquired, a zero pressure differential reading is made to ensure minimal thermal drift in the pressure transducer. This is accomplished when the Scanivalve selector switches to a port open to ambient pressure.

4.3.2 Boundary Layer Traverses

A TSI 1210-20 hot film is used to measure boundary layer velocity and turbulence. The hot film is inserted in a probe that is mounted to a National Aperture,

Inc. motorized 5.08 cm MM-3M micro-traverse as discussed in the previous section on data collection locations.

The procedure begins with setting the tunnel to a Reynolds number of 100k, where the flow is mostly attached. Setting the tunnel speed is discussed in section 4.1.3. The traverse starts away from the blade surface by about 40 mm. It is slowly maneuvered through user inputs, approaching the blade in small increments. The computer screen provides real-time feedback to the operator, displaying up-to-date velocity and turbulence profiles. When the displayed velocity is less than half of the freestream velocity (about 7 or 8 m/s), the traverse is stopped, and the nominal wall location is recorded. The traverse is then backed away to the starting location. The tunnel is then reduced to a Reynolds number of 45k. The procedure is repeated, traversing the probe down to the recorded wall location. This is duplicated for a Reynolds number of 25k. The tunnel is then shutdown, and the turbulence grid is installed or removed (as appropriate). The procedure is repeated again for all three Reynolds numbers, using the recorded wall location. After six total sweeps, the tunnel is shutdown, and the traverse is moved to the next axial chord location. For the baseline blade, 30 unique profiles were documented (6 sweeps at 5 axial chord locations). For the blade with asymmetric dimples, 90 unique profiles were documented (6 sweeps, 5 axial chord locations and 3 spanwise locations corresponding to 3 dimple axial chord locations). Lake measure profiles behind dimples and behind spaces between dimples, noting no significant spanwise variation (1).

4.3.3 Inlet and Exit Traverses

Inlet and exit traverses are used to measure wake velocity profiles and calculate

pressure loss coefficients. An X-film mounted on the downstream traverse is used for the exit velocity measurements, a Kiel probe is also mounted downstream to collect exit total pressure and a pitot-static tube is mounted upstream of the cascade to collect inlet total and static pressure. Upstream and downstream differential total pressure measurements are used along with upstream total and static differential pressure readings to calculate total pressure loss coefficients ($\Delta P_{total}/\Delta P_{dynamic}$). Traverses are taken across blades #4, #5 and #6 centerline-to-centerline, in a 50 cm pitchwise sweep. Measurements are recorded for all three blade configurations: baseline, Pak-B with spherical dimples and Pak-B with asymmetric dimples. For the dimpled configurations, sweeps were made at three spanwise locations corresponding to the three dimple axial chord locations. Spanwise variation in total pressure differential is assessed for baseline and dimpled blades with no significant variation noted. Lake made traverses across the exit plane, collecting upstream total pressure from a fixed location (1). This configuration was tested in the current research, showing no significant difference in measurements made with traversing upstream total pressure instrumentation. Note that both methods average the total pressure differentials when calculating total pressure loss coefficients. As was discussed in the previous section on test section characteristics, there is little variation dynamic and total pressure across the inlet plane.

The procedure for collecting data on a pitchwise traverse is simple. The traverse first moves from inboard to outboard in 0.5 cm increments, measuring exit velocity with X-film and total pressure differential between the upstream and downstream pressure probes. At the furthermost outboard position, the Scanivalve selector switches to the upstream static pressure input. The traverse returns to the inboard position in 10 equal

increments, measuring the upstream total to static differential pressure (dynamic pressure). At the beginning and end of a traverse, the Scanivalve selector switches to an ambient pressure port to record zero pressure differential, ensuring minimal thermal drift in the pressure transducer.

4.4 Surface Pressure Coefficient Profiles

Figures 51 and 52 show comparisons of surface pressure coefficient profiles for the baseline Pak-B blade at Reynolds numbers ranging from 25k to 100k and at freestream turbulence levels of 1% and 4%, respectively. Lake's data is included along with the current research (1). Lake measured C_p using inlet velocity from a hot wire, ambient room temperature from a thermocouple, and ambient pressure through a scanivalve port open to room air. The current research takes a direct differential reading to measure dynamic pressure. In both cases, measurements are made with time averaged measurements. The curves are produced using the following definitions:

$$C_p = \frac{P_{t_{inlet}} - P_{s_{local}}}{P_{dynamic}} = \left(\frac{\left(\frac{P_{t_{inlet}} - P_{s_{local}}}{P_{t_{inlet}} - P_{s_{local}}} \right)}{\frac{1}{2} \frac{P_{amb}}{RT_{amb}} (\bar{U})^2} \right)_{Lake} = \left(\frac{\left(\frac{P_{t_{inlet}} - P_{s_{local}}}{P_{t_{inlet}} - P_{s_{inlet}}} \right)}{\left(\frac{P_{t_{inlet}} - P_{s_{local}}}{P_{t_{inlet}} - P_{s_{inlet}}} \right)_{Rouser}} \right)_{Rouser} \quad (27)$$

where $P_{t_{inlet}}$ is the total pressure measured upstream of the cascade using a fixed pitot-static probe located 1.5 axial chord lengths ahead of blade #4 at mid-span, and \bar{U} is the time averaged mean velocity measured upstream of the cascade using a fixed single element hot film located one axial chord length ahead of blade #4 at mid-span. Lake squared the average which yields a slightly different result than when averaging the square of the velocity. The local static pressure of each tap is denoted by $P_{s_{local}}$. Density

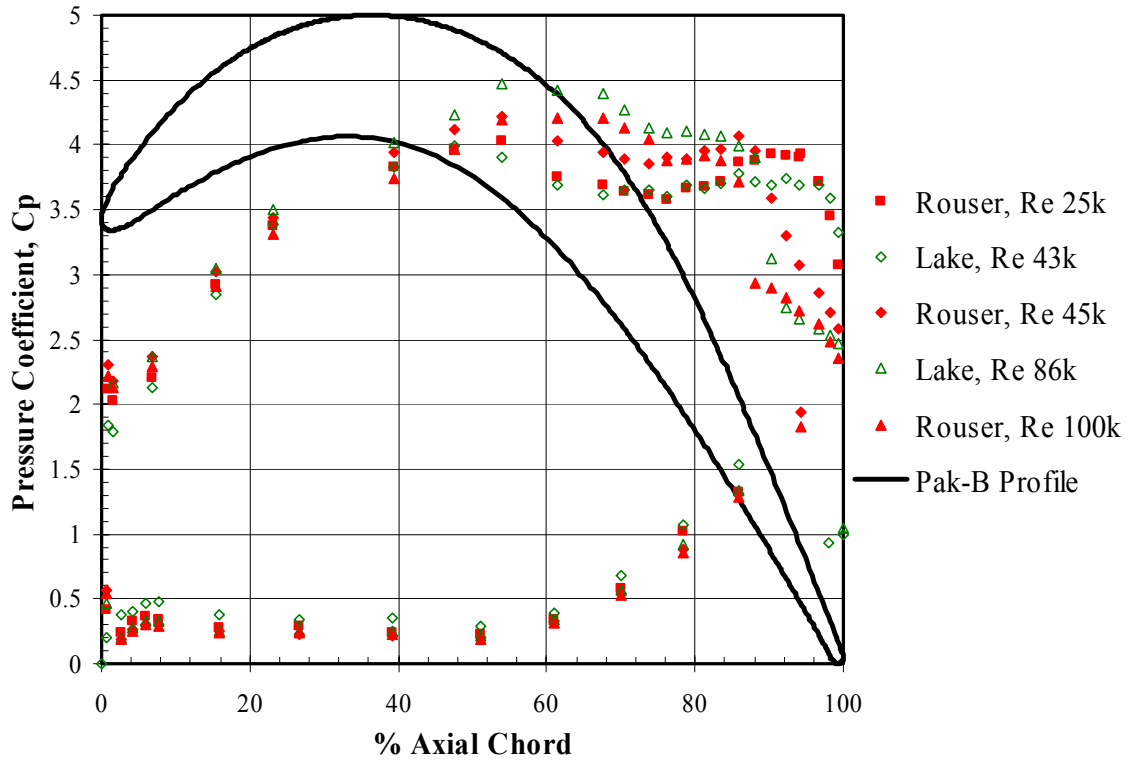


Figure 51. Comparison of current and previous experimental C_p curves for a baseline Pak-B blade at various Reynold's numbers and inlet freestream turbulence of 1%

is measured using ambient room pressure (P_{amb}) and tunnel temperature (T_{amb}). $P_{s_{inlet}}$ is the static pressure at the inlet and is collected with the aforementioned upstream pitot-static probe. Compressibility corrections were not used because the operating Mach numbers were very low (on the order of 0.006 to 0.026). Equation 25 produces positive numbers such that as surface static pressure decreases, C_p increases.

C_p curves are useful in determining the onset of boundary layer separation. It is important to note that Lake's uncertainties in C_p are ± 0.59 and ± 0.18 for Reynolds numbers of 43k and 86k, respectively (1). The uncertainty for the current research is ± 0.015 , ± 0.004 and ± 0.001 for Reynolds numbers of 25k, 45k and 100k, respectively.

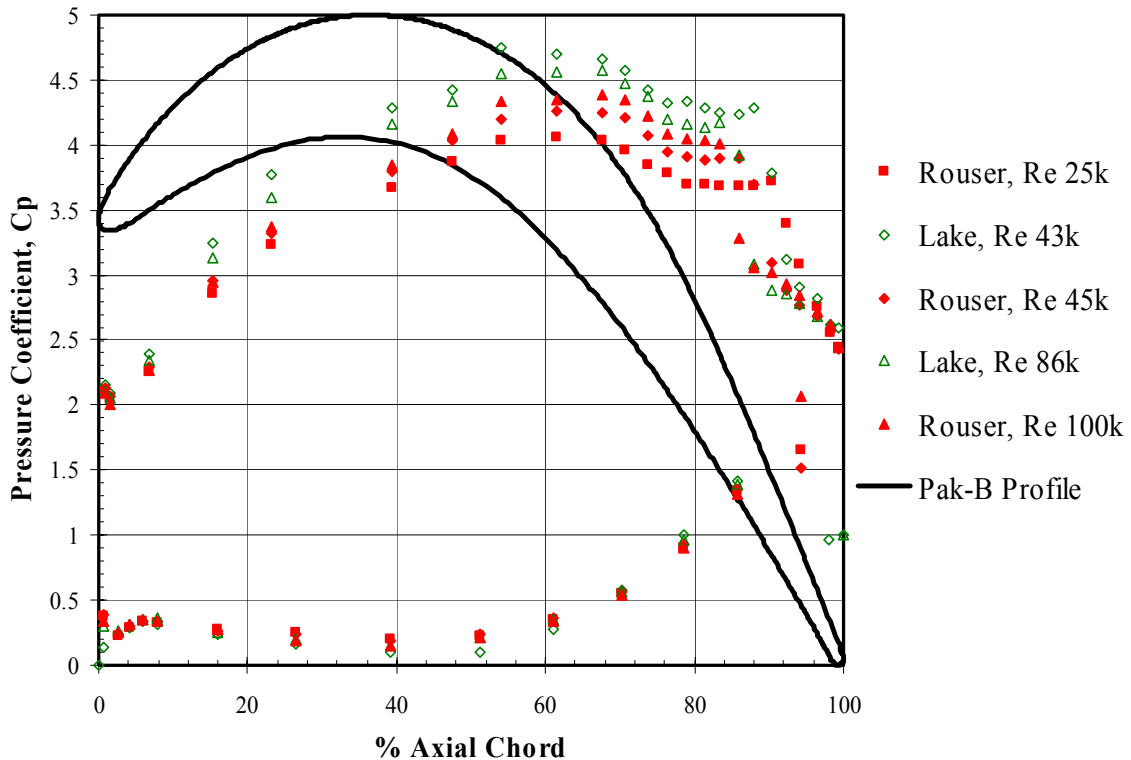


Figure 52. Comparison of current and previous experimental C_p curves for a baseline Pak-B blade at various Reynold's numbers and inlet freestream turbulence of 4%

The current data falls within the uncertainty and demonstrates the same trends. As the flow speeds up, the separation bubble decreases in size, moving further aft. This trend is also observed as inlet freestream turbulence intensity increases. Increasing inlet velocity and turbulence intensity increases the energy of the airflow, encouraging attached flow

The onset of boundary layer separation is identified on the C_p profile as the first point at which the data becomes flat, creating a plateau. Reattachment is identified to be around the last point of the plateau. Lake shows that at $Re = 43k$, boundary layer separation begins to occur between the 62% and 67% axial chord data points, at $Tu = 1\%$ (1). The current data agrees with this determination at $Re = 45k$. At $Re = 25k$, it appears that

separation occurs earlier than it does at Re 45k, but still within the 62% and 67% data points. Note that as Reynolds number decreases, the peak magnitude of C_p decreases, making the curve more level and the separation point more difficult to determine. Recall, the current CFD results indicate flow separation at 66% axial chord, which is consistent with the experimental data at a Reynolds number of 25,000 (Figure 53). At the higher

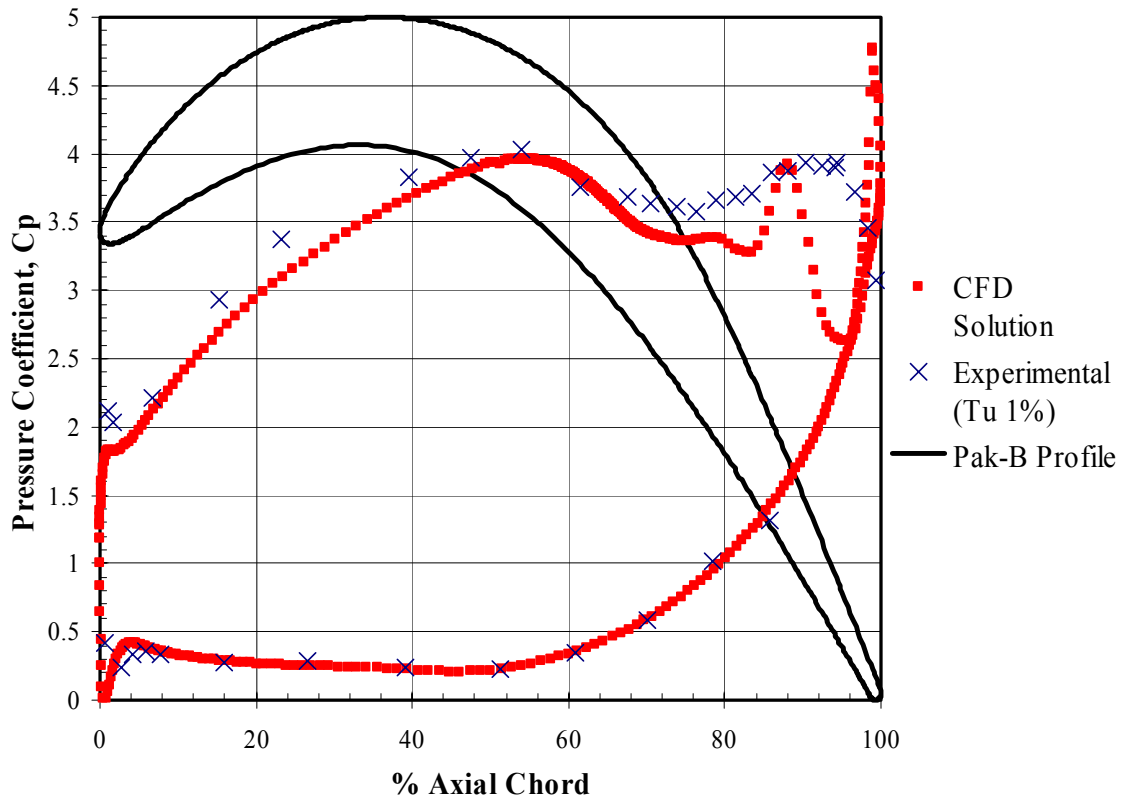


Figure 53. Comparison of CFD and experimental surface pressure coefficient profiles at Re 25k

Reynolds numbers of 86k and 100k, flow separation begins to occur between 67% and 71% axial chord. At the higher turbulence level of 4%, all of the C_p curves show separation beginning further downstream between 71% and 75% axial chord. The only

exception to this is at $Re = 25k$ which begins to separate between 67% and 71% axial chord.

It appears that reattachment is more significantly affected by the change in Reynolds number than does separation. This is important in that reattachment is central in determining the size of the separation bubble and hence the amount of reduction in efficiency. At the low turbulence case of 1%, flow reattaches between 86% and 88% axial chord for $Re = 100k$. Lake's data for $Re = 86k$ shows reattachment beginning between 88% and 90% axial chord (1). At $Re = 45k$ and below, reattachment does not take place. For the higher turbulence case of 4%, flow at $Re = 100k$ begins to reattach between 83% and 86% axial chord. Lake's data for $Re = 86k$ shows reattachment begins between 86% and 88% axial chord (1). At $Re = 45k$ and $43k$, reattachment appears to begin between 88% and 90% axial chord. Lastly, at $Re = 25k$ flow begins to reattach between 90% and 92% axial chord. By general inspection of the curves, it is very apparent that at $Re = 25k$, there is a significantly larger separation bubble, indicating higher losses in efficiency as expected.

4.5 Boundary Layer Velocity and Turbulence Profiles

Boundary layer profiles are another way to determine the onset of flow separation and are useful for visualizing flow structure. For instance, for the same Reynolds number, a laminar boundary layer velocity profile is characteristically thinner than a turbulent boundary layer profile and has lower unsteadiness. Separated flow has a velocity profile that is nearly vertical near the wall with zero velocity, while an attached flow has a profile with more curvature. The onset of separation is identified when the profile has a double inflection. Turbulence profiles are also helpful in visualizing flow

structure. When the laminar flow is attached, the turbulence profile is nearly vertical with a small magnitude. As flow separates, unsteadiness increases dramatically at the surface, giving more shape to the profile. As the separation bubble forms, turbulence is generated in the shear layer between the bubble upper surface and freestream air flow. This development is seen in the turbulence profile as increased turbulence at the wall followed by a bump in the profile that moves toward freestream. Lake recorded boundary layer profiles for the baseline Pak-B blade and the Pak-B with spherical dimples for Reynolds numbers as low as 43k (1). The current research, presents profiles for the baseline blade and the Pak-B with asymmetric dimples for Reynolds numbers as low as 25k. A complete set of velocity and turbulence profiles from the current research is included in Appendix B. An attempt was also made to compare experimental results with the Blasius solution for laminar flow over a flat plate with no angle of attack or pressure gradient; however, the results were inconclusive.

4.5.1 Boundary Layer Profiles for Baseline Pak-B at Tu 1%

Figure 54 shows the effect of Reynolds number on boundary layer profiles for the baseline Pak-B blade at 1% Tu. The flow at 67.2% axial chord looks very similar for all three Reynolds number shown. By 73% axial chord, the flow at Re 25k clearly changes shape, indicating flow separation. By 79.3% axial chord, a separation bubble is very apparent at Re 25k, and the profile is changing for the Re 45k flow, indicating separated flow. At 89.8% axial chord, the Re 25k boundary layer is more than 12 mm thick, a clear separation bubble is visible at Re 45k, and flow at Re 100k is visibly separated. Turbulence profiles also help illustrate the progression toward separation. At 79.3 % axial chord, the Re 25k flow is the first to clearly separate. At 84.8% axial chord, the Re 45k

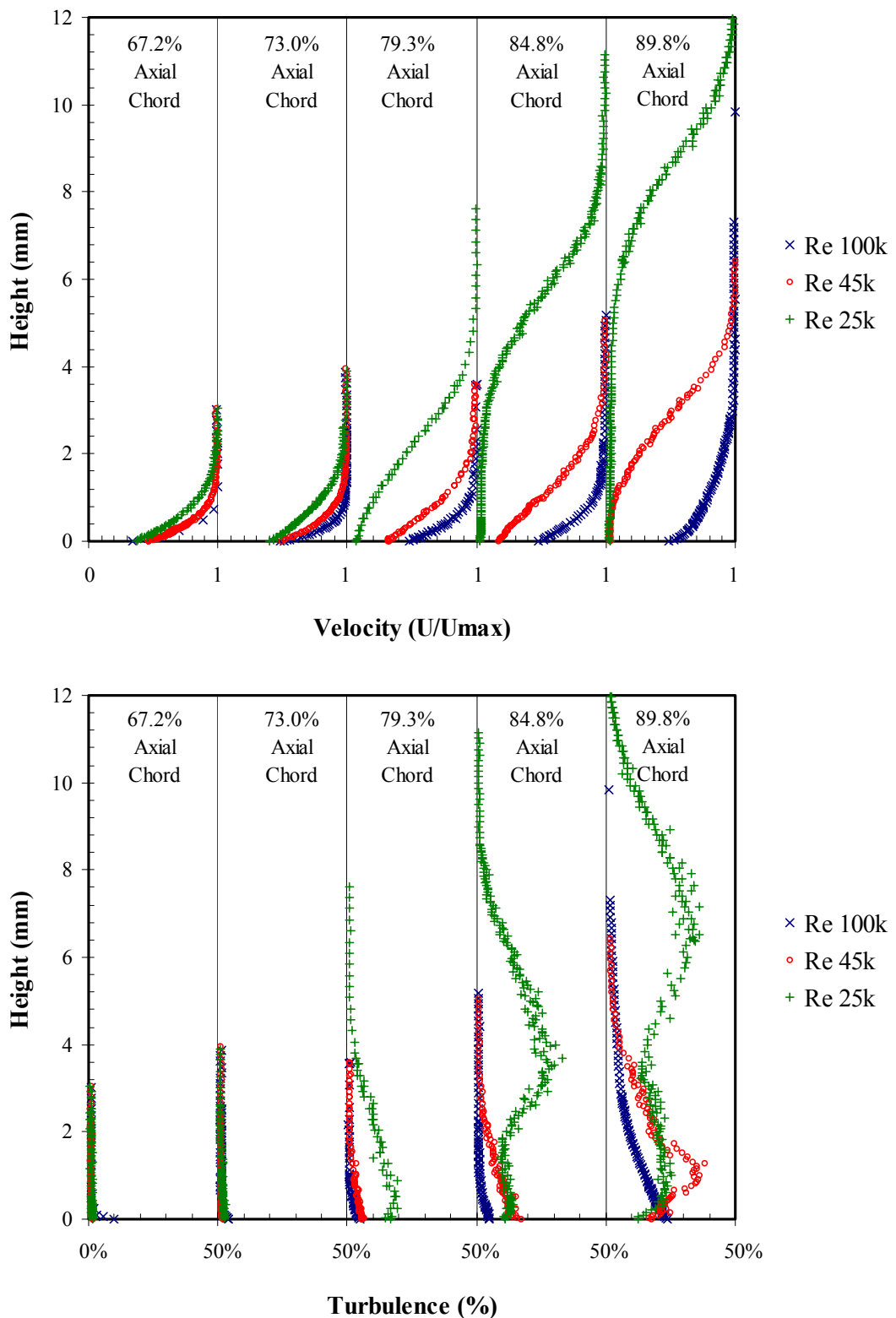


Figure 54. Reynolds effect on boundary layer profiles of baseline Pak-B at $Tu 1\%$

flow is next to follow. At 89.8% axial chord, the Re 100k increases to a turbulent intensity of 25%.

4.5.2 Boundary Layer Profiles for Pak-B with Asymmetric Dimples at 55% and 65% axial chord at Tu 1%

Figures 55 and 56 show a comparison between the baseline Pak-B and the Pak-B with asymmetric dimples at 55% and 65% axial chord at Re 25k and Re 45k with Tu 1%. These two operating conditions were most notable, highlighting the benefits of dimples in reducing losses. At the higher turbulence level and Reynolds number, improvements from the baseline are not as dramatic because the flow is more stable with less separation. Dimples at 50% are not effective, as Lake reported, and are not shown here, though Appendix B contains a complete set (1).

Figure 55 shows a comparison of boundary layer profiles of the baseline Pak-B blade and the blade with asymmetric dimples at Re 45k and Tu 1%. The baseline blade profiles are significantly different from the modified blade profiles. Asymmetric dimples are contrasted at 55% and 65% axial chord. Between the two locations, there is a lot of similarity at the 89.8% axial chord location. At first, the blade with dimples at 65% axial chord has a thicker boundary layer (at 67.2% axial chord). At 73% axial chord, the dimples at 55% axial chord apparently cause separation. Meanwhile the baseline blade appears to remain laminar. At 79.3% axial chord, the difference between the two profiles grows with the dimples at 55% axial chord continuing to generate the thicker boundary layer. The trend continues at 84.8%, but by the time the flow reaches 89.8% axial chord, the profiles are nearly directly on top of each other. It is also very important to note the differences in the turbulence profiles. At 73% axial chord, the dimples located at 55%

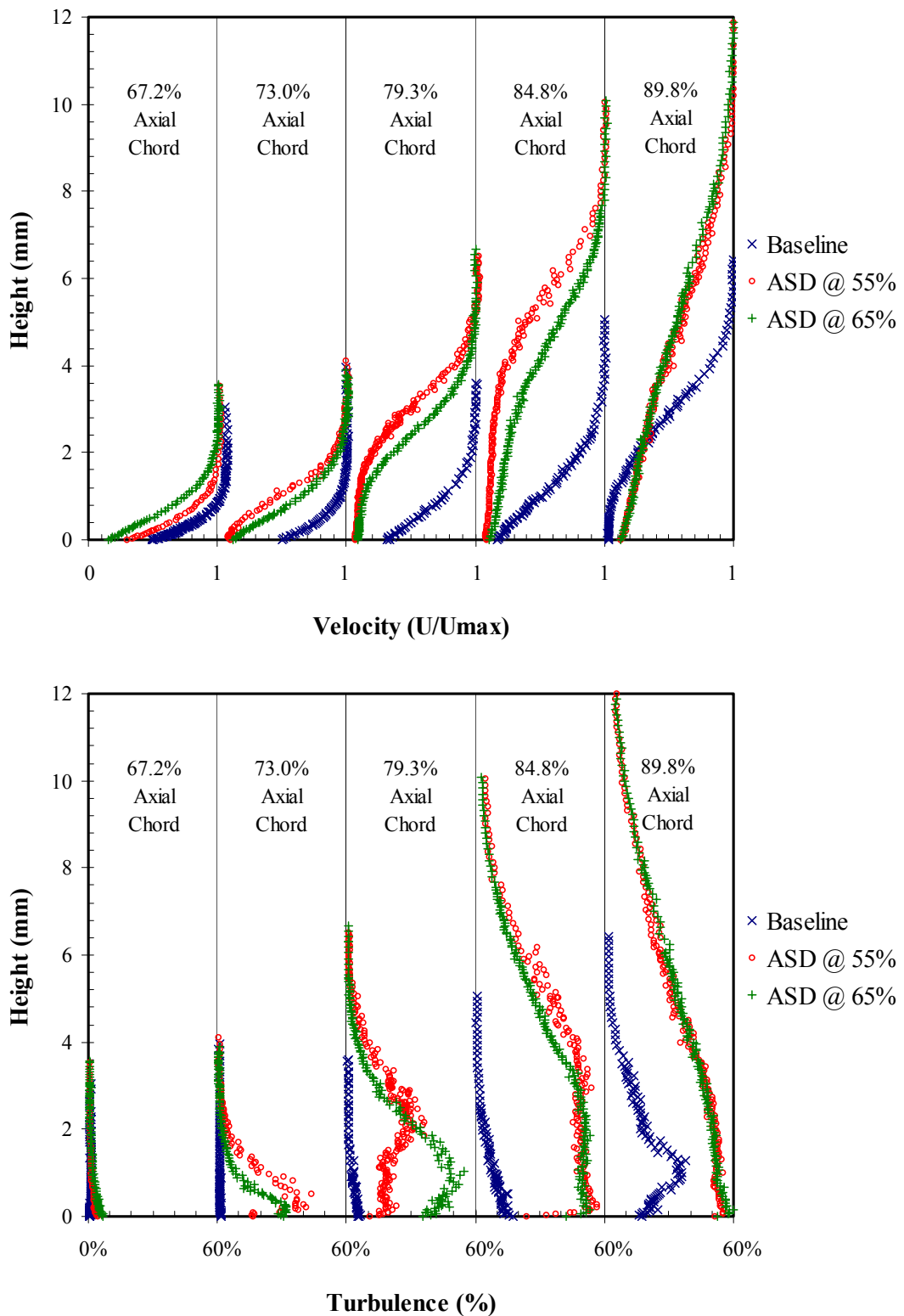


Figure 55. Boundary layer profiles for Pak-B configurations at $Re = 45k$ and $Tu = 1\%$

produce a higher turbulence level. At 79.3% axial chord, it appears that the dimples at 55% axial chord produce a turbulence profile that attempts to reattach. At this same location, the dimples at 65% axial chord produce a higher level of turbulence near the surface of the blade. At the two downstream locations, the turbulence profiles are nearly identical. From this figure, it would appear the dimples at 55% axial chord are more effective in tripping the flow and transitioning it to a re-attached turbulent boundary layer.

Figure 56 shows the same comparison of boundary layer profiles at $Re = 25k$. At this operating condition, all three profiles appear to be very different. At every axial chord location, the baseline velocity profile is substantially thinner. At 67.2% axial chord, the profiles for the modified blade are indistinguishable; however, by 73% axial chord there is a dramatic difference. The boundary layer behind the dimples at 55% axial chord is much thicker, having a distinct inflection point near the surface. At this same location, the dimples at 65% produce a profile similar to the baseline with a barely noticeable inflection very near the surface. The trends continue at the 79.3% axial chord location with boundary layers continuing to grow thicker. At the 84.8% axial chord location, the velocity profiles behind both dimple locations take on a new shape near the blade surface, indicating turbulent re-attachment. Both profiles begin to concave back toward an attached profile. This is even more apparent at 89.8% axial chord, where the flow behind the dimples at 65% axial chord is most developed. These trends are very informative when compared to the respective turbulence profiles. At the 73% axial chord, the dimpled blades produce a bubble in the turbulence profile, denoting the shear layer between the separation bubble and freestream. At 79.3% axial chord, the turbulent

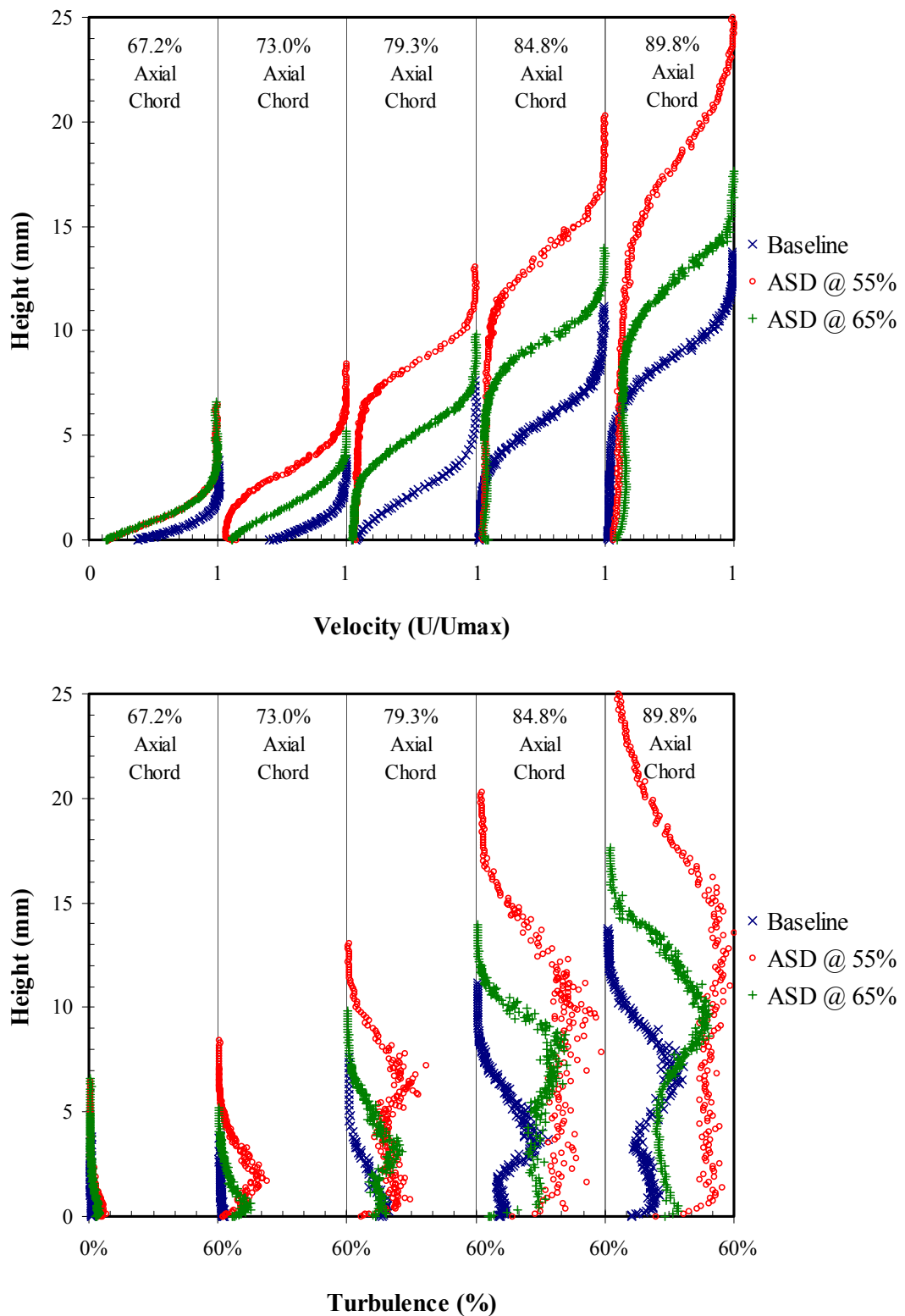


Figure 56. Boundary layer profiles for Pak-B configurations at $Re = 25k$ and $Tu = 1\%$

bubble moves away from the blade surface. At 84.8% axial chord, the turbulence profile behind the 65% dimples begins to take a shape that concaves downstream, indicating flow reattachment. At 89.8% axial chord, both profiles show this same shape, with the dimples at 65% axial chord generating the more developed and smooth curvature. From this figure, it would appear the dimples at 65% axial chord are more effective in tripping the flow to turbulent and transitioning it to a re-attached turbulent boundary layer.

4.6 Wake Velocity Pressure Profiles

Wake velocity profiles are a means to evaluate blade effectiveness. As airflow passes through the cascade, it exits with a velocity profile, having a peak around the centerline of a passage and a valley behind a blade. At the lower Reynolds numbers, the velocity dip is expected to shift outboard such that there is less turning across the cascade (Figure 57). When the inlet flow reaches a critically low Reynolds number, the flow separates across the blades, and there is even less turning, effectively changing the shape of the airfoil. In an operating engine, the more the flow is turned, the higher the load on the turbine blades, and the more work can be extracted. Flow is expected to separate at the Re 45k and 25k, widening the wake velocity profiles and shifting them outboard. All profiles generated in this study are non-dimensional for comparison sake. Velocity is normalized by the peak velocity recorded across the cascade. A complete set of profiles is included in Appendix C.

4.6.1 Wake Velocity Profiles for Baseline Pak-B

Figure 58 shows the effect of Reynolds number on wake velocity profiles. The profile is shown from pitchwise centerline to centerline of the passage on either side of blade #5 (19cm to 35 cm), representing one full wake (15.75 cm). At Re 25k, the

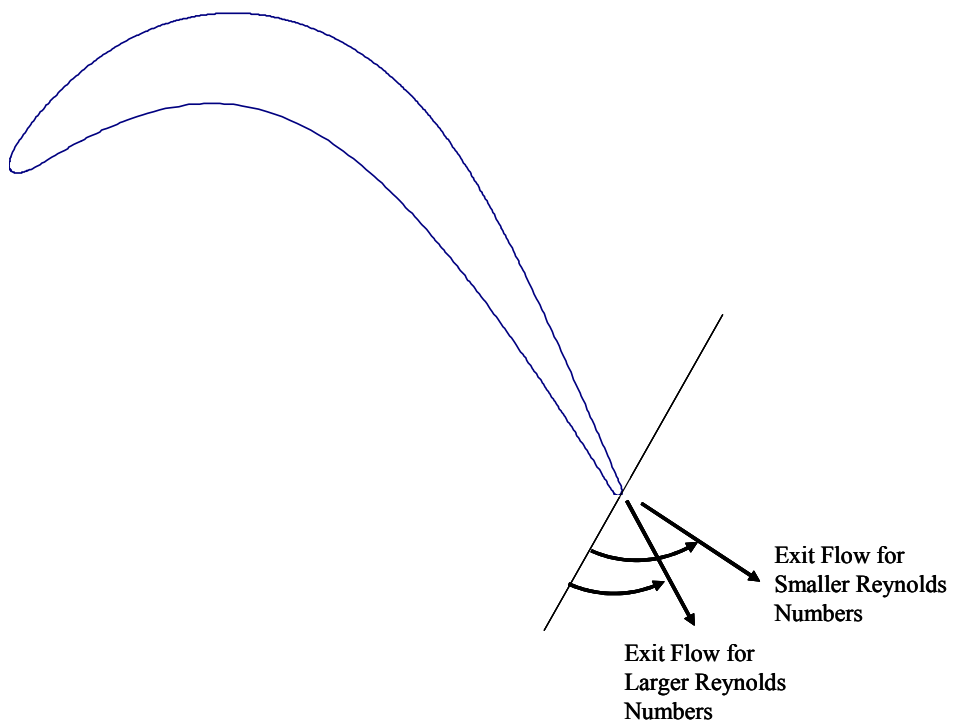


Figure 57. Reynolds number effect on exit velocity angles

velocity dip reaches 80% of the maximum and is centered around 27.5 cm. The velocity dip at Re 100k reaches 90% of the maximum, a difference of 10% from Re 25k. Furthermore, it is shifted further inboard by 6 cm to a dip centered on 21.5 cm, indicating a higher blade loading. At Re 45k, the dip is centered around 23.5 cm at about 85% of the maximum exit velocity. As expected, when the Reynolds number decreases, the velocity profiles widen with a growth in suction side wake. The blade is significantly less effective in turning the flow at Re 25k.

4.6.2 Wake Velocity Profiles for Pak-B with Asymmetric and Spherical Dimples at 55% and 65% Axial Chord at Tu 1%

Figures 59 and 60 compare the wake velocity profiles of the baseline Pak-B blade and the blades modified with asymmetric and symmetric dimples at two different axial chord

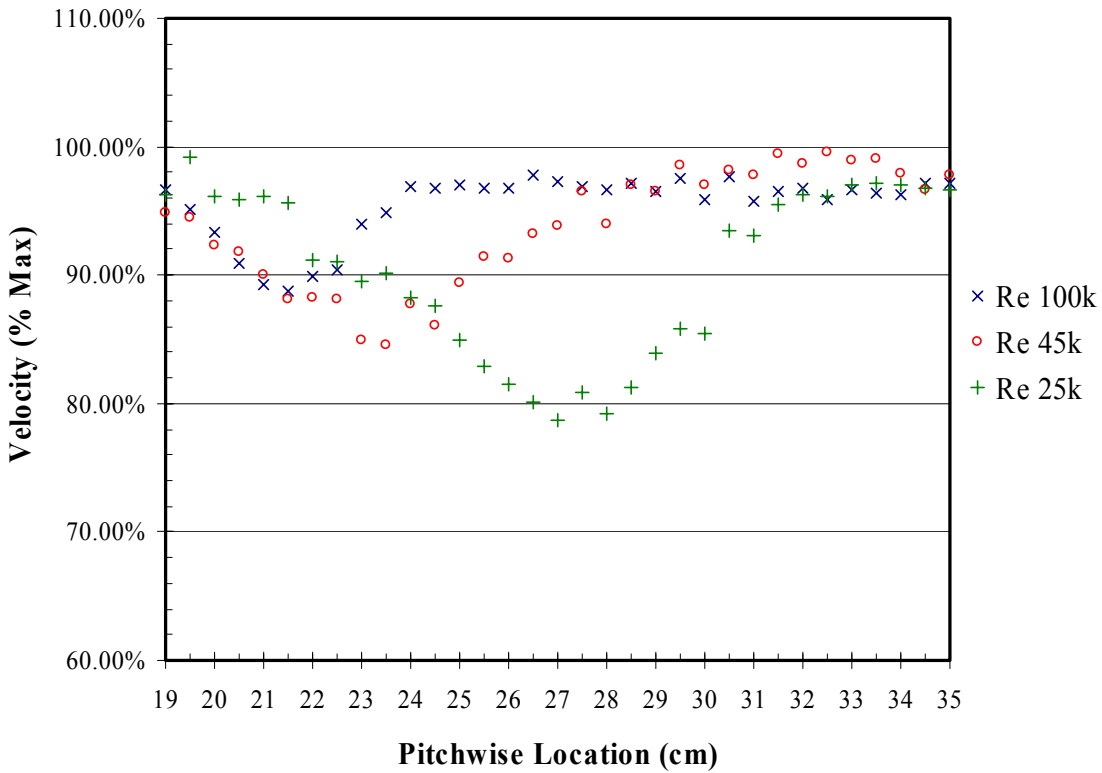


Figure 58. Reynolds effect on wake velocity profile of a baseline Pak-B blade at $Tu = 1\%$

locations of 55% and 65%. Figure 59 compares profiles at $Re = 45k$. The dimples do not offer a notable improvement at this operating condition. With the exception of the asymmetric dimples at 55% axial chord, the other configurations seem to shift the profile up 2% of the maximum velocity and shift the center of the dip inboard by 1 cm. The asymmetric dimples at 55% axial chord shift the profile up 2% of the maximum velocity but do not shift the dip inboard. From this figure, it is apparent that the effective range of the spherical dimple is larger than for the asymmetric dimple. It is most noteworthy that dimples do not have a significant effect on wake velocity profile at $Re = 45k$.

Figure 60 compares wake velocity profiles at $Re = 25k$. It is very apparent that the both dimples offer an improvement when placed at 65% axial chord, shifting the wake

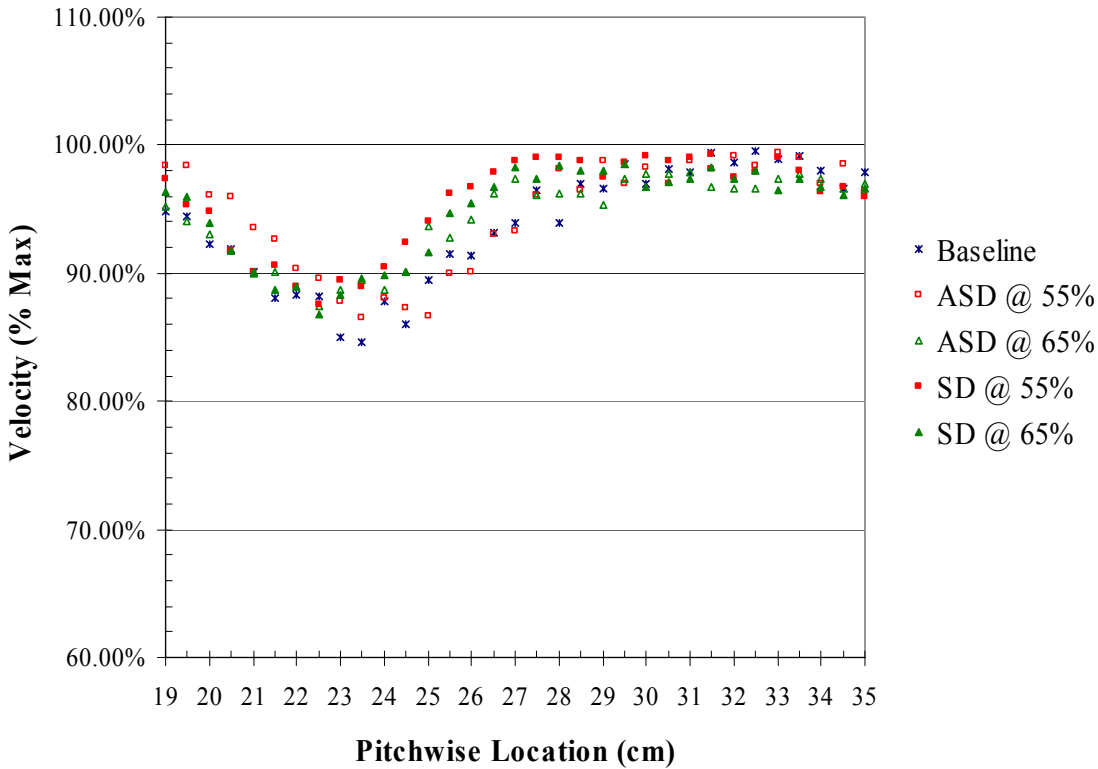


Figure 59. Wake velocity profile comparison of a Pak -B blade with asymmetric and spherical dimples at 55% and 65% axial chord at $Re = 45k$ and $Tu = 1\%$

profile inboard. At this location, there is very little difference between the velocity profiles of the asymmetric and spherical dimples. The dimples located at 55% axial chord match wake velocity profiles with the baseline blade having a dip centered around 27.5 cm at 80% maximum velocity. In contrast, the dimples located at 65% axial shift the wake profile inboard so that the dip is centered around 24 cm at 86% maximum velocity. From this figure, it would seem that the best location for a dimple at $Re = 25k$ is 65% axial chord.

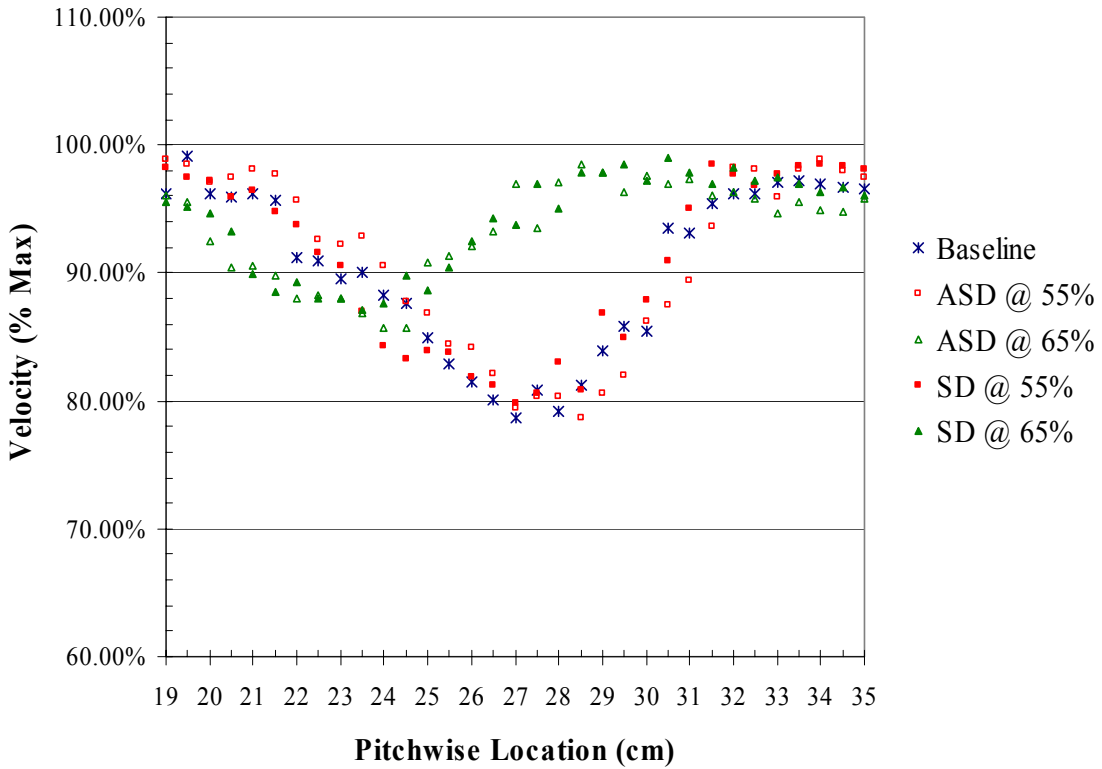


Figure 60. Wake velocity profile comparison of a Pak-B blade with asymmetric and spherical dimples at 55% and 65% axial chord at $Re = 25k$ and $Tu = 1\%$

4.7 Pressure Loss Coefficient

The total pressure loss coefficient is used to evaluate Pak-B blade performance. It is a non-dimensional quantity that takes into account total pressure deficit from inlet to exit and is normalized by dynamic pressure, which is related to the incoming kinetic energy. There are two approaches to calculating this coefficient; one is normalized by inlet dynamic pressure and the other is normalized by exit dynamic pressure. Lake measured the area-weighted average total pressure loss coefficient using the exit dynamic pressure based on exit velocity measured with a hot wire located one axial chord

downstream of the cascade along with a density calculated from room temperature and pressure, as seen below:

$$\gamma = \sqrt{\frac{(P_{t_{inlet}} - P_{t_{exit}})}{\frac{1}{2} \left(\frac{P_{amb}}{R T_{amb}} \right) (\overline{U_{exit}})^2}} \quad (28)$$

where $(P_{t_{inlet}} - P_{t_{exit}})$ is a time averaged direct total pressure differential between a fixed upstream pressure probe and a downstream traversing pressure probe, P_{amb} ambient static room pressure, T_{amb} is static temperature within the wind tunnel and $\overline{U_{exit}}$ is a time averaged exit velocity (1). Because of the very low operating Mach numbers, Lake did not apply compressibility corrections for density.

The current research measures the area-weighted average total pressure loss coefficient using the inlet dynamic pressure based on the differential of inlet total and static pressure. The equation for this measurement is seen below:

$$\omega = \left[\frac{(P_{t_{inlet}} - P_{s_{inlet}})}{(P_{t_{inlet}} - P_{s_{inlet}})} \right] \quad (29)$$

where the time-averaged total pressure differential is measured between an upstream and downstream pressure probe, traversing simultaneously such that they are both read from approximately the same streamline for each point.

The two different definitions for total pressure loss coefficient can be related to each other by applying the Pak-B designed speed-up ratio of 1.64. The speed up ratio is the ratio of exit velocity to inlet velocity and is unique to blade geometry. To correlate

the current research to Lake's results, the current calculation for loss coefficient is divided by 2.6896 (or 1.64 squared). It is important to note that the best correlation between the data is to measure the improvement of a modified blade over the baseline ($\gamma/\gamma_{baseline}$ or $\omega/\omega_{baseline}$). This method of evaluation normalizes the already non-dimensional quantities so as to account for any variations between measurement set-ups (atmospheric variations, unique tunnel characteristics, instrumentation variation, etc.), allowing an evaluation of relative improvement. As with the wake velocity profiles, the loss coefficient is evaluated pitchwise from centerline-to-centerline of the passages on either side of blade #5. A complete set of profiles is included in Appendix D.

4.7.1 Total Pressure Loss Coefficient Profiles for Baseline Pak-B

Local total pressure loss coefficient is presented to evaluate the flow structure. Whereas wake velocity profiles aid in the visualization of momentum deficit, total pressure loss coefficient profiles evaluate energy deficit, showing the deficit in total pressure (and hence energy) as normalized by velocity. Figure 61 shows the effect of Reynolds number on total pressure loss coefficient for a Pak-B blade at Tu 1%. As expected, the highest peak loss coefficient occurs at Re 25k. At this Reynolds number, the profile is widest with a peak centered at 30.5 cm. At Re 100k, the loss coefficient peaks at 25.5 cm, a 5 cm shift. The peak at Re 25k is more than two times greater than at Re 100k. Lastly, it is important to note that the curves generated at Re 25k and 45k are not symmetric, as opposed to the curve generated at Re 100k. This illustrates how dramatically losses increase on the suction side of the blade, where the boundary layer separates.

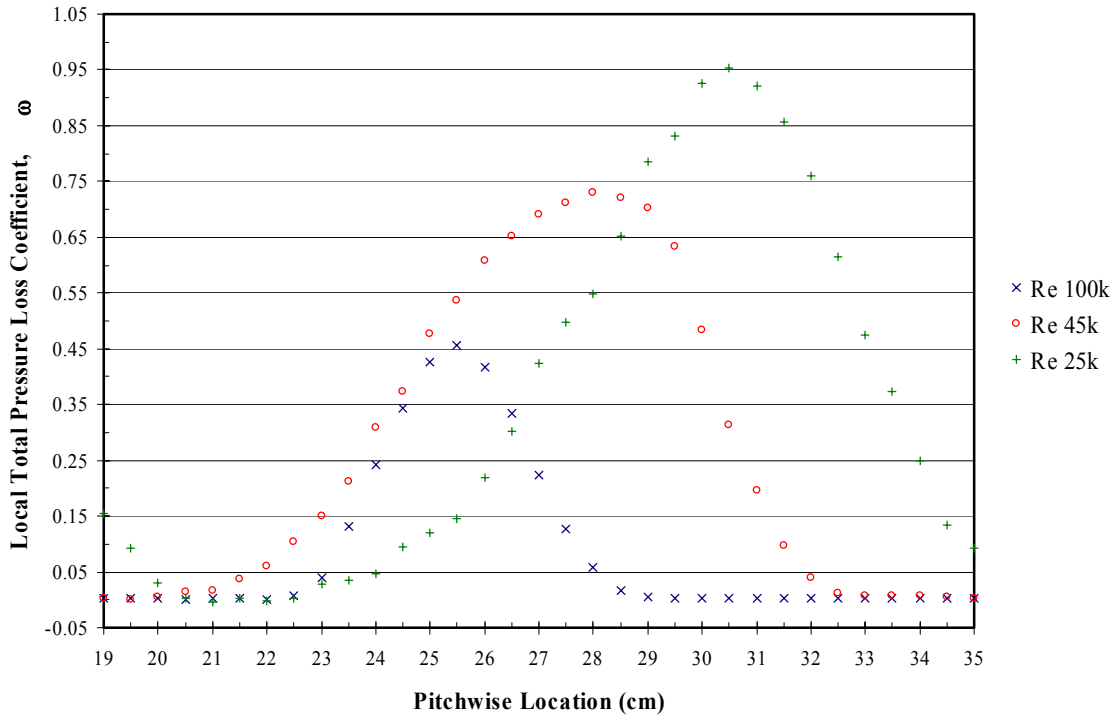


Figure 61. Reynolds effect on total pressure loss coefficient of baseline Pak-B at Tu 1%

Figure 62 shows a comparison between the experimental and computational local total loss coefficient profiles for the baseline Pak-B at Re 25k. Magnitudes of the computational numbers are not expected to match up exactly with test cell data. The computational model is an infinite cascade without wall effects or exit tailboards which influence inlet and exit flow angles. To compare trends, the loss coefficient is normalized with the maximum value in the wake traverse. Using this technique, the computational and experimental profiles match reasonably well. Some errant data appears in the inboard passage of the computational model, possibly from unsteady flow. Unsteady effects in the CFD solution would show data at different points in time, so that the steady results would artifacts from unsteady flow. Furthermore, the CFD profile is

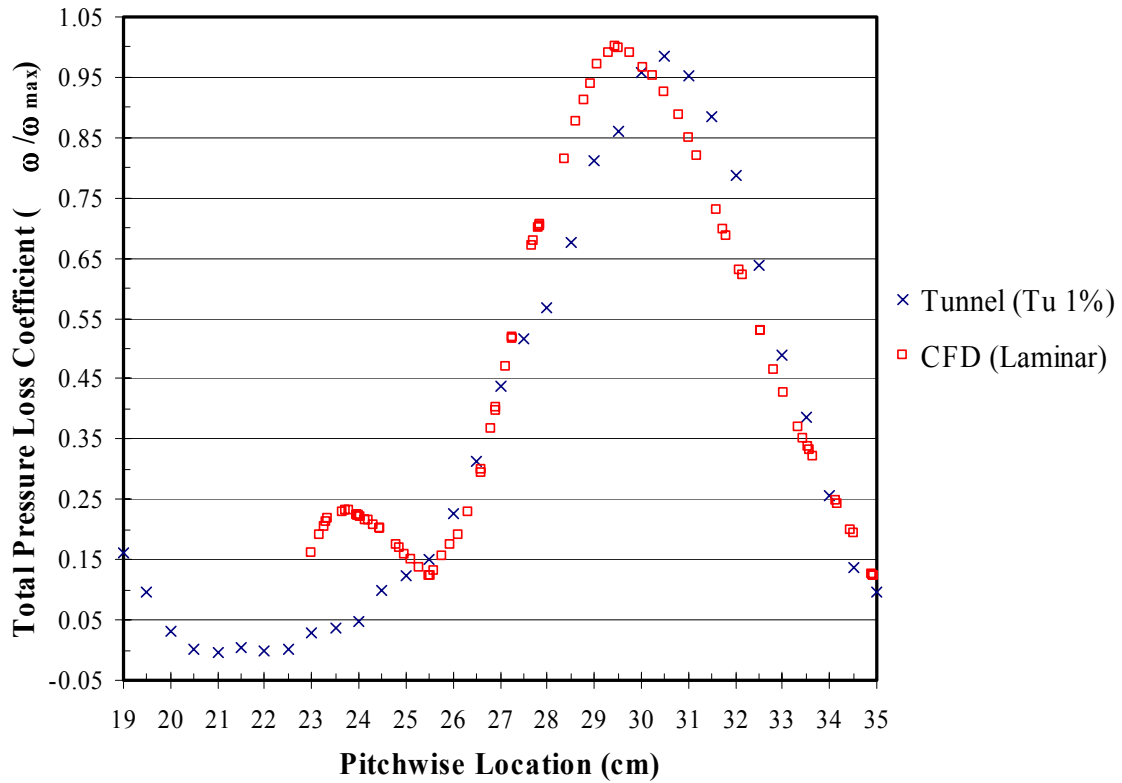


Figure 62. Comparison between experimental and computational local total pressure loss coefficient profiles for a baseline Pak-B at $Re = 25k$

more symmetric than the experimental data. The symmetry suggests that the model is not handling the separated flow very precisely, as might be expected from a laminar CFD solution. The computational model appears to be useful, however, and is a good starting point for future research.

Figure 63 shows a comparison between the experimental results for the two dimpled Pak-B configurations and the time accurate dimpled Pak-B CFD results at a Reynolds number of 25,000 in terms of local total pressure loss coefficient profiles. The data is reasonably consistent, giving credibility to the other CFD results for velocity and pressure contours, as well as streamline images.

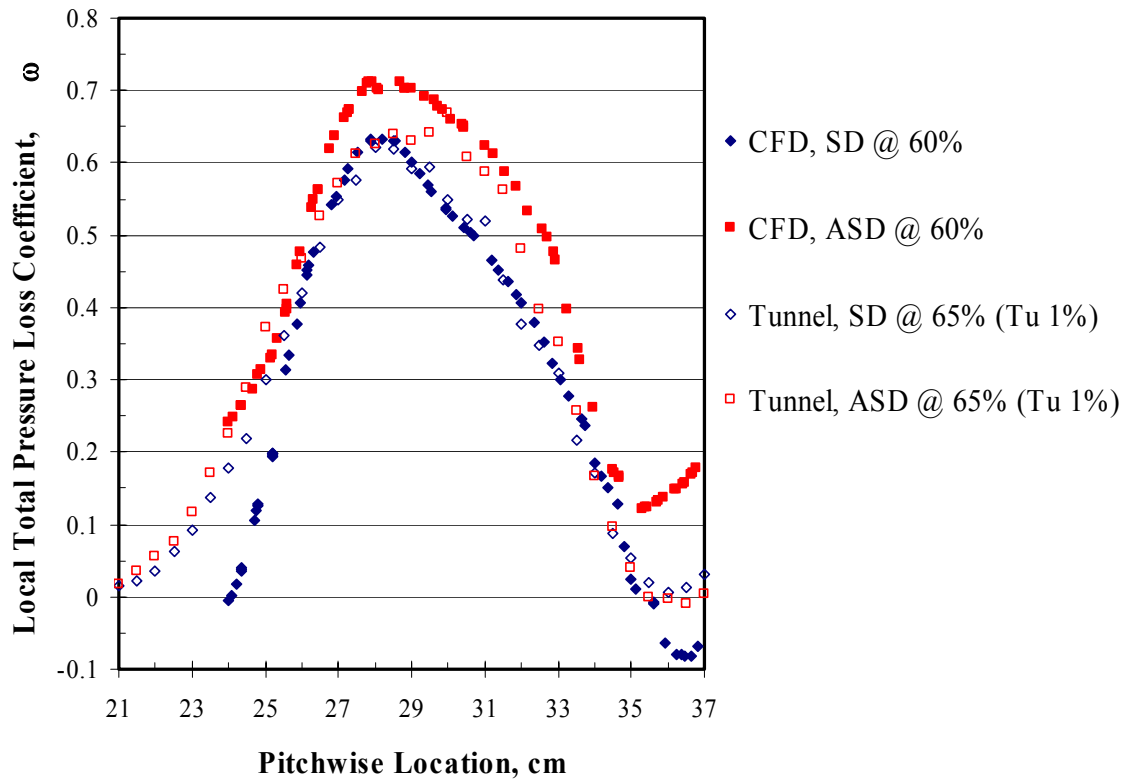


Figure 63. Comparison of dimpled Pak-B CFD and experimental local total pressure loss coefficient profiles at $Re = 25k$

4.7.2 Total Pressure Loss Coefficient Profiles for a Pak-B with Asymmetric and Spherical Dimples at 55% and 65% Axial Chord at Tu 1%

Figures 64 and 65 compare the local total pressure loss coefficient profiles of the baseline Pak-B blade and the blades modified with asymmetric and symmetric dimples at two different axial chord locations of 55% and 65%. Figure 64 compares profiles at $Re = 45k$ and $Tu = 1\%$. All of the profiles are relatively close together; however, it is clear that the spherical dimples at 55% axial chord are most effective, having the lowest peak loss coefficient and the narrowest profile. It is also the most symmetric, suggesting minimal separation loss. The asymmetric dimple at 65% axial chord is undoubtedly the worst

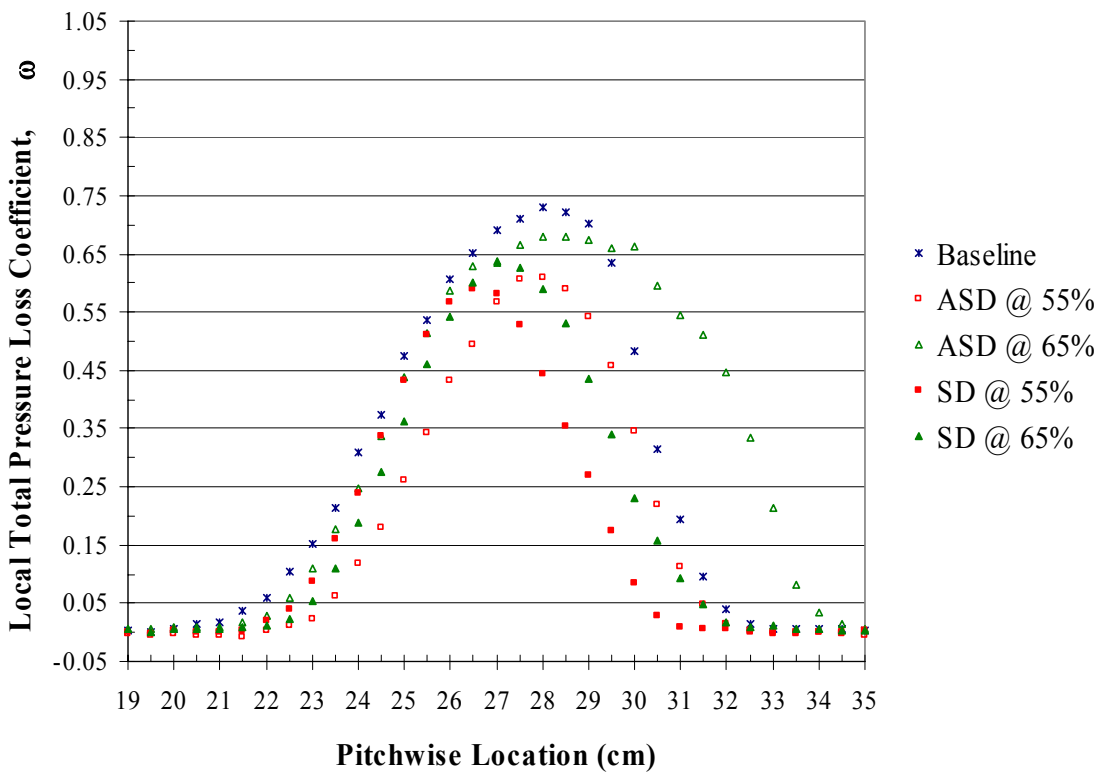


Figure 64. Local total pressure loss coefficient profile comparison of Pak-B blade with asymmetric and spherical dimples at 55% and 65% axial chord at $Re = 45k$ and $Tu = 1\%$

performer, even having a negative impact on blade performance compared to baseline.

Looking back at Figure 55, the related boundary layer profile, may indicate that the boundary layer is tripped to turbulent but does not transition to an attached turbulent boundary layer, remaining separated. The spherical dimples located at 65% axial chord and the asymmetric dimples at 55% axial chord both seem to be somewhat effective at reducing losses and should not be ruled out as candidates for further study.

Figure 65 compares local total pressure loss coefficient profiles at $Re = 25k$ and $Tu = 1\%$. There is a definite distinction between the profiles in this figure. Evidently, 55% axial chord is an ineffective location for dimples, spherical or asymmetric. Unlike the

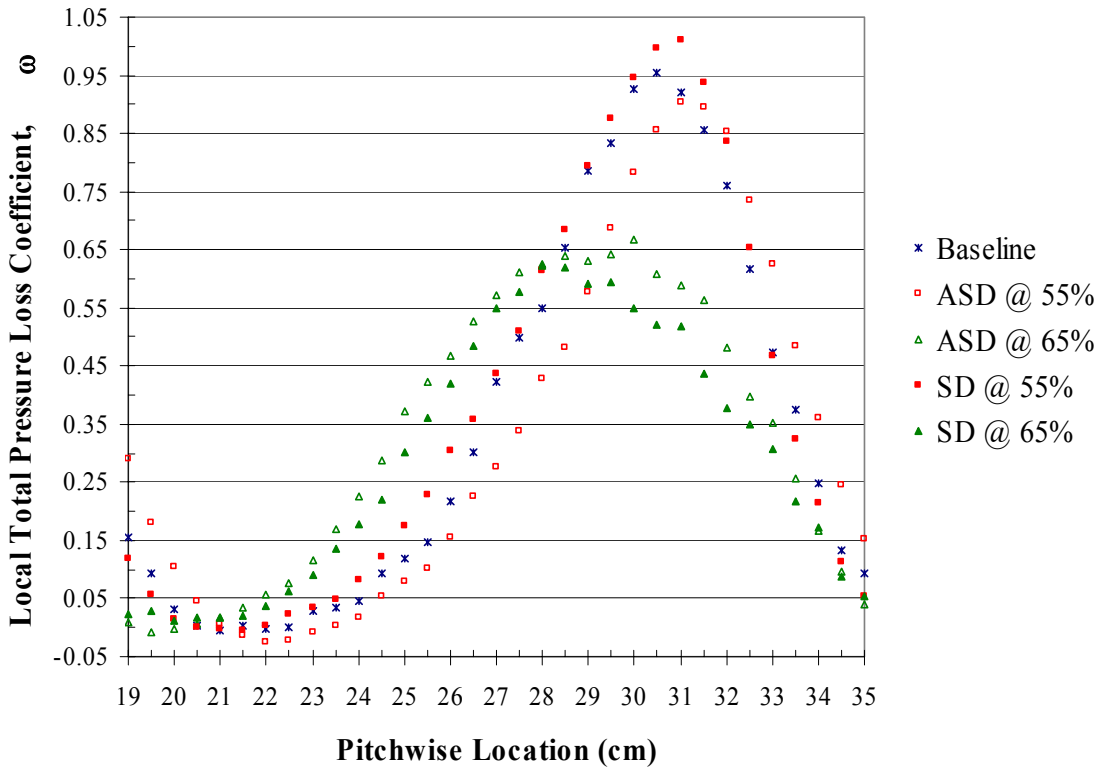


Figure 65. Local total pressure loss coefficient profile comparison of Pak-B blade with asymmetric and spherical dimples at 55% and 65% axial chord at $Re = 25k$ and $Tu = 1\%$

previous figure at $Re = 45k$, the spherical dimple is the worst performer at this operating condition and location. Ironically, the spherical dimple is also the best performer when placed at 65% axial chord. It has the lowest peak value for loss coefficient and is the narrowest profile. The asymmetric dimple is very nearly as effective when placed at the same location. This figure plainly suggests that the best location for a dimple at $Re = 25k$ is 65% chord (for those locations tested).

4.7.3 Comparison of Average Total Pressure Loss Coefficients

Averaging the pressure loss coefficients across the wake gives a bulk evaluation of performance. This is accomplished by summing the data points across a 16 cm

pitchwise distance and dividing by the number of samples. Lake did this by averaging total pressure differential, density and velocity. In this study, the mean loss coefficient is calculated by simply averaging the local total pressure loss coefficients (1). Figure 66 shows a comparison of average pressure loss coefficients from experimental data and

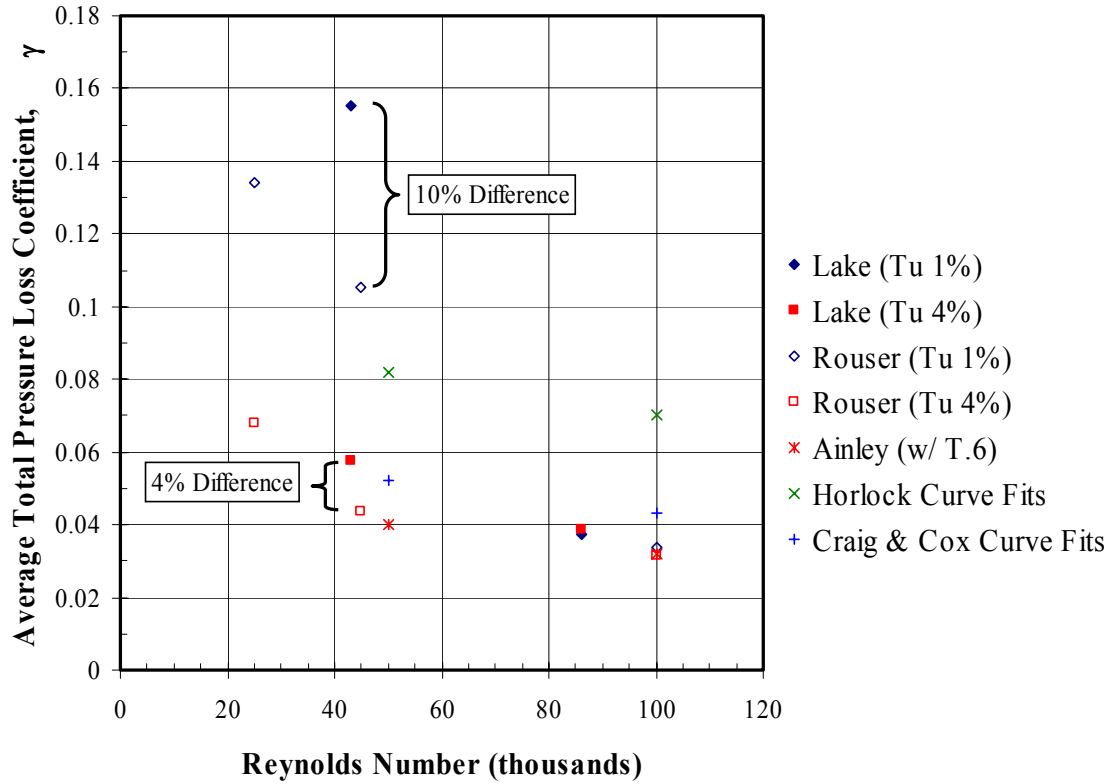


Figure 66. Comparison of previous and current average total pressure loss coefficients for baseline Pak-B related blades

curve fits (1; 49-54). Because the loss coefficients of the previous work are based on exit dynamic pressure, the speed-up ratio (1.64) is applied to the current data for correlation. The correlation is not perfect because it is based on the flow acceleration for attached flow; however, this figure demonstrates the validity of the current baseline data, placing it closely in relation to previous work. Figure 67 shows the improvement of the

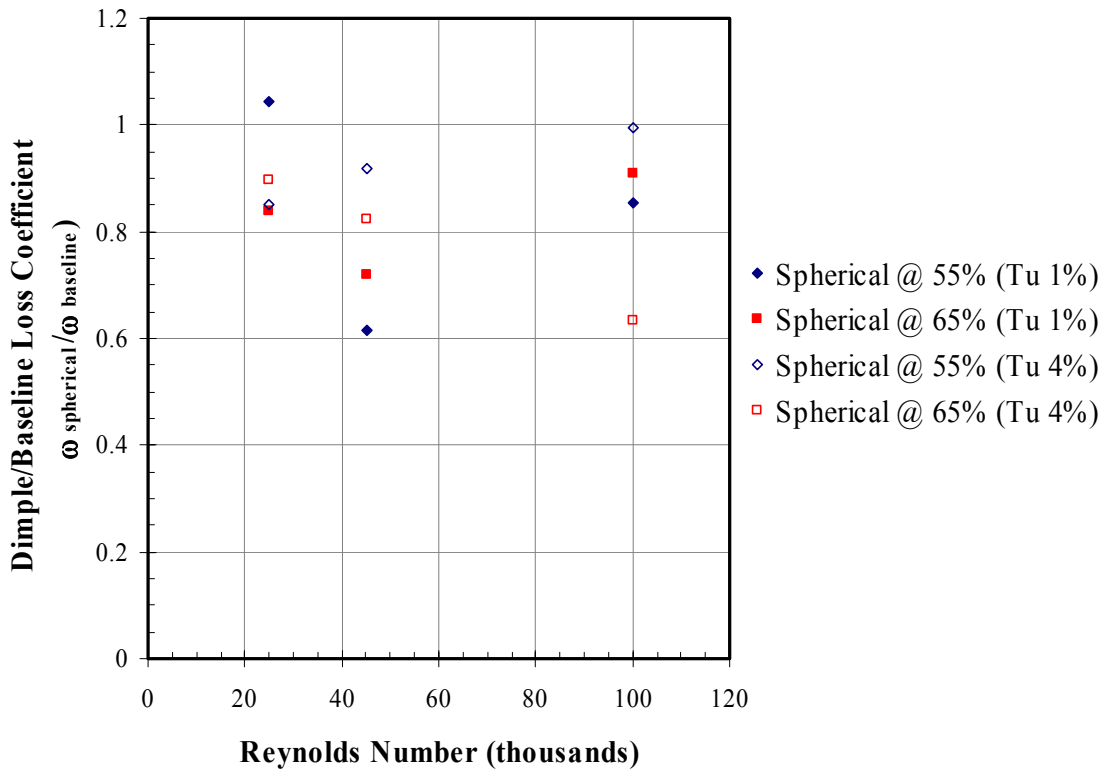


Figure 67. Comparison of current and previous experimental results for loss reduction on a Pak-B blade using spherical dimples

spherically dimpled blade over the baseline blade, the best configuration of those tested in the current research.

Figure 68 shows a comparison of the asymmetric and spherical dimples at Tu 1% and Tu 4%. Note that the figure does not indicate the optimal dimple location, but rather how one dimple performs compared to another at a specific location and operating condition. In nearly all cases, the spherical dimple out performs the asymmetric dimple. The only case in which the reverse is true is when the dimple is located at a less than optimal location. For instance, at Re 25k dimples are generally ineffective at 50% and 55% axial chord; however, the asymmetric dimple has less of a negative impact at these

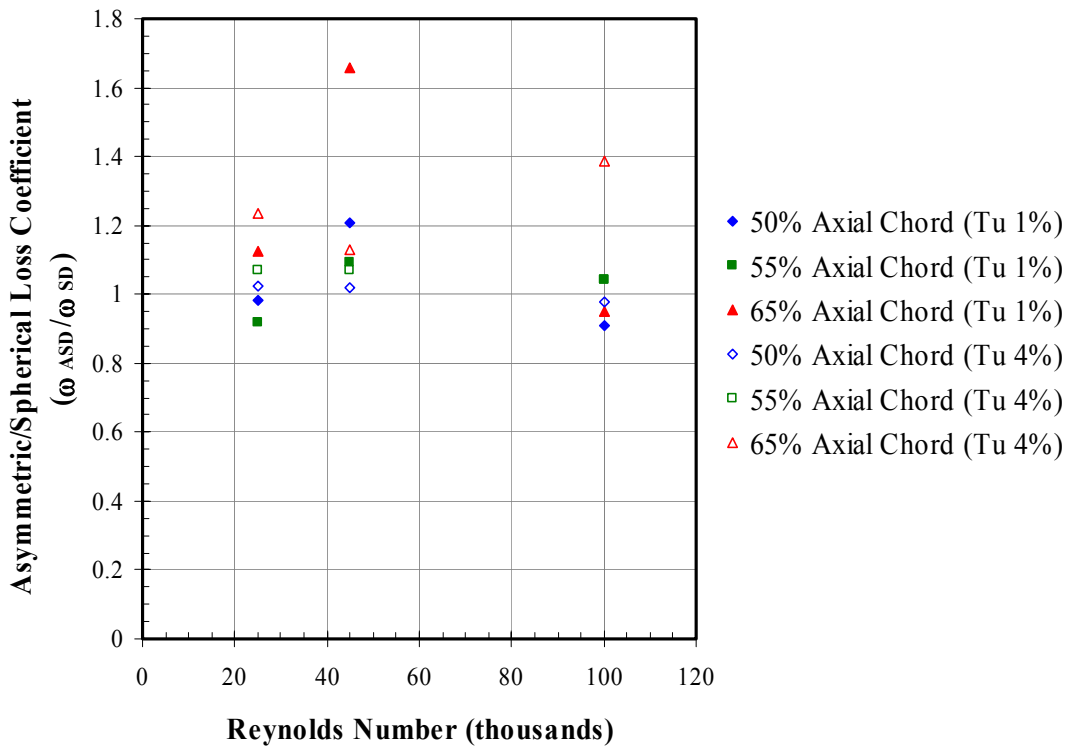


Figure 68. Comparison of asymmetric and spherical dimple loss reduction on a Pak-B blade

locations under this condition. This indicates that while the spherical dimple is more effective in controlling boundary layer separation at the optimal location under conditions where separation is known to occur, the asymmetric dimple has less of a negative impact under conditions where separation does not occur. This is important when considering the ultimate goal. Loss reduction is desirable when separation is having a very negative impact on blade efficiency; however, at other flight conditions the surface treatment can produce a negative impact, acting like surface roughness. Therefore, the overall mission of the aircraft will delineate the best use of dimples

4.8 Summary and Conclusions of Experimental Research

Empirical analysis of boundary layer profiles, wake velocity profiles, local total pressure loss coefficient profiles, and average total pressure loss coefficient are all consistent within themselves and confirm computational trends. In general, experimental results show that spherical dimples out-perform asymmetric dimples, agreeing with computational results.

Whereas the computational study showed suction to be a flow mechanism present with dimples, experimental boundary layer profiles indicate that the mechanism by which dimples suppress separation losses is through tripping the incoming laminar boundary layer to turbulent and transitioning it to a re-attached boundary layer ahead of the trailing edge. Turbulence profiles are particularly useful in observing boundary layer development, depicting a large turbulence bubble associated with the shear layer between the separation bubble and freestream and showing development of a re-attached turbulence profile. At $Re = 25k$, asymmetric dimples delay separation until about 73% axial chord and transition flow to turbulent re-attachment around 89% axial chord.

Taken together, wake velocity profiles and boundary layer profiles are very helpful in explaining flow structure. The boundary layer thickness explains the effective shape of the blade, while wake velocity profiles show the impact of the effective shape on momentum loss. The bulk performance effect, is best assessed using the total pressure loss coefficient, a good measure for energy deficit. Total pressure loss coefficient profiles indicate the origin of losses, while average total pressure loss coefficients give a good bulk determination of loss reduction.

CHAPTER 5. SUMMARY AND RECOMMENDATIONS

Aircraft operating at high altitudes and low velocities are vulnerable to laminar flow separation over suction surface of low pressure turbine (LPT) blades. Associated separation losses have a significant impact on turbine efficiency, limiting aircraft range, endurance, altitude and power extracted from the engine. Laminar boundary layer separation has been observed on a Pratt and Whitney Pak-B LPT blade at low Reynolds numbers. Passive techniques to control flow separation offer improvement in turbine efficiency without the need for additional power or hardware and are relatively easy to manufacture and maintain. Spherical dimples have been proposed as a passive control to suppress flow separation and reduce associated losses.

Mechanisms by which dimples reduce separation losses are the focus of the current research. An experimental investigation is combined with computational modeling to study two different dimple shapes on a Pak-B LPT blade at low Reynolds numbers. A cassette of eight Pak-B blades are tested in a linear cascade tunnel at Reynolds numbers of 100k, 45k and 25k with freestream turbulence levels of 4% and 1%. Configurations are tested for the baseline blade, and the blade with asymmetric and spherical dimples at 50%, 55% and 65% axial chord. The asymmetric dimple is a spherical dimple that is spanwise half-filled with a straight edge parallel to axial flow. Surface pressure coefficients, boundary layer profiles, wake velocity profiles and total pressure loss coefficient are documented. Experimental results are useful in evaluating loss reduction. A local 3-D computational model is created for each of the three configurations, placing dimples at 60% axial chord. Laminar Reynolds averaged

numerical simulations are conducted at a Reynolds number of 25k. The three turbulence models used here are ineffective in capturing flow separation. Flow is found to be very unsteady for configurations with dimples. Computational results are useful in visualizing flow structure and behavior.

Computational results indicate that dimples create a spanwise vortex. The vortex is centered within the dimple and generates suction. Suction is determined to be one of the primary mechanisms by which dimples delay separation and reduce associated losses. The spherical dimples are found to be most effective in energizing the flow and delaying separation. Asymmetric dimples offer similar benefit, indicating the presence of more than one flow mechanism by which dimples suppress separation. Additionally, flow visualization suggest little to no influence between neighboring dimples.

Experimental results indicate that dimples trip the flow from laminar to turbulent and transition the flow to a re-attached turbulent boundary layer. Both dimple shapes prove to be effective, but the spherical dimples are determined to have a more effective range and strength. Optimal dimple location is critical to loss reduction and changes with Reynolds number.

More investigation into the unsteady nature of the flow should be conducted. The computational results indicate that unsteady effects may shift separation location. Further unsteady computational modeling is warranted to assist in parametric studies. Experimental studies should also assess the unsteady nature of the flow. For example, surface taps behind dimples would be helpful in establishing shedding frequencies and could be compared to baseline wake shedding behavior. Future parameters that should be considered include dimple spacing, multiple dimple row patterns, and dimple depth.

Asymmetric dimples should not be ruled-out at this juncture. Future testing should also include asymmetric dimples with tighter spacing and at different orientations, ranging from 0° to 90° from the axial flow.

In conclusion, this research sheds new light onto flow mechanisms produced by dimples in suppressing flow separation losses. These new revelations are useful in future parametric studies but should be coupled with more analysis of unsteady flow structure. Dimples are clearly shown to be effective in reducing separation losses, and merit further attention. Aircraft mission effectiveness could be significantly improved through the application of dimples as passive separation controls on low pressure turbine blades.

REFERENCES

1. Lake, James P., "Flow Separation Prevention on a Turbine Blade in Cascade at Low Reynolds Number." PhD Dissertation, Air Force Institute of Technology, 1999. AFIT/DS/ENY/99-01.
2. Halstead, D.E., D.C. Wisler, T.H. Okiishi, G.J. Walker, H.P. Hodson and H.W. Shin, "Boundary Layer Development in Axial Compressors and Turbines Part 1 of 4: Composite Picture." International Gas Turbine Institute and Aeroengine Congress and Exposition, Houston, TX, June 1995. ASME Paper No. 95-GT-461.
3. Halstead, D.E., D.C. Wisler, T.H. Okiishi, G.J. Walker, H.P. Hodson and H.W. Shin, "Boundary Layer Development in Axial Compressors and Turbines Part 3 of 4: LP Turbines." International Gas Turbine Institute and Aeroengine Congress and Exposition, Houston, TX, June 1995. ASME Paper No. 95-GT-463.
4. Sharma. O., 1998, "Impact of Reynolds Number on LP Turbine Performance," Proceedings of the 1997 Minnowbrook II Workshop on Boundary Layer Transition in Turbomachines, NASA CP-1998-206958, 1998, pp. 65-69.
5. Murawski, C.G., T.W. Simon, R.J. Volino and K. Vafai, "Experimental Study of the Unsteady Aerodynamics in a Linear Cascade with Low Reynolds Number Low Pressure Turbine Blades." International Gas Turbine Institute and Aeroengine Congress and Exposition, Orlando, FL, June 1997. ASME Paper No. 97-GT-95.
6. Qui, S. and T.W. Simon, "An Experimental Investigation of Transition as Applied to Low Pressure Turbine Suction Surface Flows." International Gas Turbine Institute and Aeroengine Congress and Exposition, Orlando, FL, June 1997.
7. Simon, T.W. and R.J. Volino, "Separating and Separated Boundary Layers." Technical Report WL-TR-96-2092, Wright Laboratory, 1996.
8. Hourmouziadis, J. "Aerodynamic Design of Low Pressure Turbines." AGARD, pages 1-38. 1989. AGARD-LS-167.
9. Rivir, R.B. "Transition on Turbine Blades and Cascades at Low Reynolds Numbers." Technical Report WL-TR-96-2084, Wright Laboratory, 1996.
10. Werle, M.J. "Compressor and Turbine Blade Boundary Layer Separation." *AGARD Conference Proceedings*, AGARD-CP-351 (1983).
11. Mayle, R.E. "The Role of Laminar-Turbulent Transition in Gas Turbine Engines." *Journal of Turbomachinery*, 113:509-537 (October 1991). ASME Paper No. 91-GT-282.

12. Halstead, D.E. "Boundary Layer Development in Multi-Stage Low Pressure Turbines." PhD dissertation, Iowa State University, 1996.
13. Hill, P.G. and C.R. Peterson. *Mechanics and Thermodynamics of Propulsion (Second Edition)*. Addison-Wesley Publishing Company, Inc., Massachusetts. 1992.
14. Mattingly, J.D. *Elements of Gas Turbine Propulsion*. McGraw-Hill, Inc., New York, 1996.
15. Addison, J.S. and H.P. Hodson. "Modeling of Unsteady Transition Boundary Layers." International Gas Turbine and Aeroengine Congress and Exposition, Orlando, FL, June 1991. ASME Paper No. 91-GT-282.
16. Walker, G.J. "The Role of Laminar-Turbulent Transition in Gas Turbine Engines: A Discussion." *Journal of Turbomachinery*, 115:207-217 (April 1993).
17. Halstead, D.E., D.C. Wisler, T.H. Okiishi, G.J. Walker, H.P. Hodson and H.W. Shin. "Boundary Layer Development in Axial Compressors and Turbines Part 4 of 4: Computational Analysis." International Gas Turbine and Aeroengine Congress and Exposition, Houston, TX, June 1995. ASME Paper No. 95-GT-464.
18. Reed, H.L. and W.S. Saric. "Linear Stability Theory Applied to Boundary Layers." *Annual Review of Fluid Mechanics*, 28:389-428 (1996).
19. Sharma, O.P., R.A. Wells, R.H. Schlinke and D.A. Bailey. "Boundary Layer Development on Turbine Airfoil Suction Surfaces." *Journal of Engineering and Power*, 104:698-706 (July 1982).
20. Johnston, J.P. and Nishi, M. "Vortex-generator Jets-Means for Flow Separation Control." AIAA Journal, Vol. 28, No. 6, June 1990, pp. 989-994.
21. Compton, D.A. and Johnston, J.P. "Streamwise Vortex Production by Pitched and Skewed Jets in a Turbulent Boundary-Layer." AIAA Journal, Vol. 30, No. 3, March 1992, pp. 640-647.
22. Bons, Jeffrey P., Sondergaard, Rolf, and Rivir, Richard B. "Turbine Separation Control Using Pulsed Vortex Generator Jets." ASME Journal, Vol. 123, April 2001, pp. 198-206.
23. Lin, J.C., Howard, F.G., Bushnell, D.M., and Shelby, G.V. "Investigation of Several Passive and Active Methods of Turbulent Flow Separation Control." AIAA Paper #90-1598, 1990.
24. Borgeson, David. "Boundary Layer Control Using Micro-Electromechanical Systems." MS Thesis, Air Force Institute of Technology, 2002. AFIT/GSO/ENP/
25. Chang, P.K. *Separation of Flow*. Pergamon Press, 1970.

26. Austin, J.G. "Mach Number, Flow Angle, and Loss Measurements Downstream of a Transonic Fan-Blade Cascade." MS Thesis, Naval Postgraduate School, March 1994.
27. Gamerdinger, P.M. and R.P. Shreeve. "The Effects of Low-Profile Vortex Generators on Flow in a Transonic Fan-Blade Cascade." 34th Aerospace Sciences Meeting and Exhibit, Reno, NV, January 1996. AIAA Paper No. 96-0250.
28. Rao, D.M. and T.T. Kariya. "Boundary-Layer Submerged Vortex Generators for Separation Control – An Exploratory Study." 1st National Fluid Dynamic Congress, 1988. AIAA Paper No. 88-3546-CP.
29. McCormick, D.C. "Shock-Boundary Layer Interaction Control with Low-Profile Vortex Generators and Passive Cavity." 30th Aerospace Sciences Meeting and Exhibit, January 1992. AIAA Paper no. 92-0064.
30. Lin, J.C., F.G. Howard, and G.V. Shelby. "Turbulent Flow Separation Control through Passive Techniques." AIAA 2nd Shear Flow Conference, Tempe, AZ, March 1989. AIAA Paper No. 89-0976.
31. Wheeler, G. O. "Means for Maintaining Attached Flow of a Flowing Medium." June 1984. United States Patent No. 4,455,045.
32. Walsh, M.J. "Riblets as Viscous Drag Reduction Technique." AIAA Journal, 21(4):485-486 (April 1983).
33. Walsh, M.J. "Turbulent Boundary Layer Drag Reduction Using Riblets." AIAA 20th Aerospace Sciences Meeting, Orlando, FL, January 1982. AIAA Paper No. 82-0169.
34. Walsh, M.J. *Viscous Flow Drag Reduction*, volume 72 of Progress in Astronautics and Aeronautics, chapter Drag Characteristics of V-Groove and Transverse Curvature Riblets, pages 168-184. AIAA, 1980.
35. Bacher, E.V. and C.R. Smith. "Turbulent Boundary-Layer Modification by Small-Scale Riblets." *AIAA Journal*, 24(8):1382-1385. (August 1986).
36. Bacher, E.V. and C.R. Smith. "A Combined Visualization-Anemometry Study of the Turbulent Drag Reducing Mechanisms of Triangular Micro-Groove Surface Modifications." AIAA Shear Flow Control Conference, Boulder, CO, March 1985. AIAA Paper No. 85-0548.
37. Maciejewski, P.K. and R.B. Rivir. "Effects of Surface Riblets and Free-Stream Turbulence on Heat Transfer in a Linear Turbine Cascade." International Gas Turbine and Aeroengine Congress and Exposition, The Hague, Netherlands, June 1994. ASME Paper No. 94-GT-245.

38. Taylor, H.D. "Summary Report on Vortex Generators." Technical Report No. R-05280-9, United Aircraft Corporation Research Department, March 1950.

39. Bloch, D.R. and T.J. Mueller. "Effects of Distributed Grit Roughness on Separation and Transition on an Airfoil at Low Reynolds Numbers." Pages 152-161 (1986). AIAA Paper No. 86-1788.

40. Bearman, P.W. and J.K. Harvey. "Golf Ball Aerodynamics." *The Aeronautical Quarterly*, 27(2):112-122 (May 1976).

41. Bearman, P.W. and J.K. Harvey. "Control of Circular Cylinder Flow by the Use of Dimples," *AIAA Journal*, 31(10):1753-1756 (October 1993).

42. *Gridgen User Manual, Version 13.3*. Pointwise, Inc. Bedford, TX. 1999.

43. *Fluent 6: Getting Started*. Fluent, Inc. Lebanon, NH. 2001.

44. *FIELDVIEW: User Manual, Version 8*. Intelligent Light. Lyndhurst, NJ. 2001.

45. Roach, P.E. "The Generation of Nearly Isotropic Turbulence by Means of Grids." *Heat and Fluid Flow*, 8(2):82-92 (June 1987).

46. Mayle, R.E., K. Dullenkopf and A. Schulz. "The Turbulence That Matters." IGTI Conference, Orlando, FL, 1997.

47. Kline, S.J. and F.A. McClintock. "Describing Uncertainties in Single-Sample Experiments." *Mechanical Engineering*, 75 (1):3-8 (January 1953).

48. Bruun, H.H. *Hot-Wire Anemometry*. Oxford University Press, Oxford, 1995.

49. Ainley, D.G. "Performance of Axial-Flow Turbines." *Proceedings Institution of Mechanical Engineers*, 159(41):230-244 (November 1948).

50. Ainley, D.G. and G.C.R. Mathieson. "A Method of Performance Estimation for Axial-Flow Turbines." *British ARC, R and M*, 2974 (1951).

51. Horlock, J.H. "Review: Losses and Efficiencies in Axial-Flow Turbines." *International Journal of Mechanical Sciences*, 2:48-75 (1960).

52. Horlock, J.H. "Further Comments on Losses and Efficiencies in Axial-Flow Turbines." *International Journal of Mechanical Sciences*, 3:312-313 (1961).

53. Horlock, J.H. *Axial Flow Turbines*. Butterworth and Co. Ltd., London, 1966.

54. Craig, H.R.M. and H.J.A Cox. "Performance Estimation of Axial Flow Turbines." *Proceedings of the Institution of Mechanical Engineers*, 185(32):407-424 (1971).

APPENDIX A. Experimental Data Collection Procedures

A.1 Pressure Transducer Calibration

Hardware Setup

1. Carefully unpack the deadweight pressure reference device.
2. Set up pressure calibrator following instructions with deadweight reference device.
3. Connect output from positive pressure reference on calibrator to high side (+) of transducer.
4. Unhook or vent low side (-) of transducer.

Software Setup

1. Open LabVIEWTM.
2. Open the ‘Pressure Cal’ vi.
3. Set device to ‘2’ (MIO board controlling SCXI).
4. Set ‘Pxdr Ch’ to ‘sc1 ! md1 ! 0’ (SCXI device 1, module 1, channel 0).
5. Select sample rate and number (recommend 1000Hz max & 30,000 samples min).

Calibration Procedure

1. Place reference weight for max desired pressure on reference.
2. Run ‘Pressure Cal’ vi and enter data filename.
3. Enter reference pressure determined by reference weight and hit OK.
4. Wait for data acquisition.
5. Change out reference weight to reduce pressure.
6. Allow approximately 15 seconds for pressure to stabilize (watch pressure readout).
7. Press ‘TAKE DATA’ button to take next data point.
8. Repeat steps 3 to 7 until data taken at minimum reference pressure.
9. Shut off reference device and vent both sides of transducer (zero pressure point).
10. Press ‘TAKE DATA’ button.

11. Enter '0' for pressure setting and hit OK.
12. Wait for data acquisition.
13. Press 'DONE DO FIT' button.
14. Record calibration constants in notebook (Slope, Intercept, MSE). Flag with RED ink.

Hardware Takedown

1. Carefully disconnect and repack deadweight pressure reference.
2. Reconnect instruments to transducer.
3. Reset valves on transducer appropriately (all vents open if you are not using it immediately).

A.2 Hot Wire and Hot Film Calibration

IFA SET-UP PROCEDURE

Begin by ensuring that you have proper cables; Anemometer channel is set for proper length and sensor type; Anemometer is given sufficient time to stabilize temperature (30 min.). Record identifying information for the probe in the notebook.

Measuring Cable Resistance

1. Install the shorting plug(s) in the end of the probe holder to be used during testing.
2. Press RES MEAS to select the NULL DISPL mode.
3. Adjust the OPERATE RES knob to zero the display (balance the bridge)
4. Press RES MEAS to select the DISPL RES mode. The measured cable resistance will be displayed - record this value.
5. Press ENTER to store the value of the cable resistance in the IFA-100 Memory.

Measuring Probe Resistance And Calculating the Overheat Ratio

1. CAREFULLY install the probe to be calibrated in the probe holder. Tighten the probe holder into the probe holder traverse of the calibration jet so that the probe is: less than one jet

diameter (~ 0.25 in.) from the exit of the jet, centered over the jet, and perpendicular to the flow.

2. With the pressure tap disconnected, balance the base and zero-adjust the manometer. Connect the pressure tap from the calibration jet to the manometer.
3. Adjust the flow regulator on the calibration jet to = 0.05 in. H₂O.
4. Press RES MEAS to select the NULL DISPL mode and adjust the OPERATE RES to zero the display (balance the bridge).
5. Press RES MEAS to select the DISPL RES to display the measured probe resistance - record this value.
6. Calculate operating resistance:

Operating Resistance = ((Probe Resistance - Internal Probe Ω (R_{int})) * OHR) + R_{int}

where: OHR = 1.5 for a film probe (- 10/- 20)

OHR = 1.8 for a wire probe (- T1.5)

7. Press OPERATE RES and adjust the OPERATE RES knob until the display value matches your calculated value.
8. Press ENTER to store the value.

Adjust The Bridge Frequency Compensation

1. Press BRIDGE COMP and adjust the BRIDGE knob until the displayed value matches the correct value where:
BRIDGE COMP \cong 115 for a film probe (- 10/- 20)
BRIDGE COMP \cong 35 for a wire probe (- T1.5)
2. Press ENTER to store the value.
3. Increase the calibration jet flow to the maximum expected flow while testing.
4. Press RUN/STANDBY to go to “RUN” mode.
5. Turn the CABLE knob fully CCW. If the OSC light is off, then go to step 7.
6. Turn the CABLE knob CW until the OSC light goes out. Go to step 7.

7. Turn the CABLE knob CW until the OSC light turns on. Turn the CABLE knob CCW until the OSC light turns off. Frequency Compensation is roughly adjusted.
8. Connect the signal out to an oscilloscope to monitor the OUTPUT. Set the oscilloscope to 10 mV / div., $\geq 200\mu\text{Sec}$ / div. and normal trigger.
9. Press TEST SIGNAL and adjust the CABLE knob until a desirable waveform without oscillations is visible on the oscilloscope.

SINGLE ELEMENT PROCEDURES

Hardware setup

1. Verify calibration of pressure transducer if required.
2. Connect hotwire calibrator rig pressure tap to pressure transducer high side (+).
3. Vent both sides of pressure transducer, shut measure side valves.
4. Blow dust out of calibrator rig by opening valves fully.
5. Shut valves.
6. Follow instructions for IFA100 hotwire/hotfilm setup.
7. Mount hotwire/hotfilm in calibrator with sensor centered over nozzle perpendicular to flow.

Software Setup

1. Open LabVIEW™
2. Open 'Continuous AtoD' vi.
3. Set device to '2' (MIO board controlling SCXI).
4. Set 'Pxdr Ch' to 'sc1 ! md1 ! 0' (SCXI device 1, module 1, channel 0).
5. Input latest calibration constants (slope and intercept) for transducer.
6. Open 'Hot Wire cal' vi.
7. Set dewpoint and barometric pressure.
8. Set number of samples and sample rate.
9. Set correct MIO channel for wire/film (depends on IFA channel – Check IFA note or wiring).

10. Enter probe parameters from IFA100 setup procedure into hotwire block on panel.

Calibration Procedure

1. Verify that both sides of pressure transducer are vented (zero pressure)
2. Run 'Continuous AtoD' vi.
3. Verify that pressure transducer reads zero. If not, press 'set zero intercept'.
4. Stop 'Continuous AtoD' vi.
5. Enter slope and new intercept from (3) into 'Hotwire Cal' vi.
6. Run 'Hot Wire Cal' vi.
7. Enter data filename.
8. Set IFA HW channel to "RUN".
9. Open valves on calibrator until jet is at maximum desired calibration velocity.

DO NOT EXCEED TRANSDUCER MAXIMUM PRESSURE

10. When reading has stabilized, hit 'TAKE DATA' button.
11. Wait for 'Taking Data' light to go out.
12. Reduce calibrator flow to next desired calibration point.
13. When reading has stabilized, hit 'TAKE DATA' button.
14. Wait for 'Taking Data' light to go out.
15. Repeat steps 12-14 until desired calibration range has been covered.
16. Press 'DONE DO FIT' button.
17. Record calibration constants (C, D, MSE) in notebook. Flag with RED ink.

Hardware Takedown

1. Shut off isolator valve to calibrator.
2. Mount hotwire/hotfilm in tunnel.
3. Disconnect calibrator pressure tap from transducer.
4. Reconnect instrumentation lines to transducer.

5. Reset valves on transducer appropriately (all vents open if you are not using it immediately).

DUAL ELEMENT PROCEDURES

Hardware setup

1. Verify calibration of pressure transducer if required.
2. Connect hotwire calibrator pressure tap to pressure transducer high side (+).
3. Vent both sides of pressure transducer.
4. Blow dust out of calibrator by opening valves fully.
5. Shut valves.
6. Follow instructions for IFA100 hotwire/hotfilm setup for each element (two channels)
7. Mount hotwire/hotfilm in calibrator with sensor centered over nozzle and both elements perpendicular to the flow
 - a. For an x-wire, insert probe into probe holder arm such that the probe is vertical, insuring that both wires are perpendicular to the flow, and that the rotating collar is set to the R6 pin hole position
 - b. For a split film...

Software Setup

1. Open LabVIEW™
2. Open 'Continuous AtoD' vi.
3. Set device to '2' (MIO board controlling SCXI).
4. Set 'Pxder Ch' to 'sc1 ! md1 ! 0' (SCXI device 1, module 1, channel 0).
5. Input latest calibration constants (slope and intercept) for transducer.
6. Open 'X Wire Probe Cal' vi.
7. Set dewpoint (Tdew) and barometric pressure (Patm)
8. Set 'Type of Cal' switch to '90'
9. Set number of samples and sample rate

10. Set DAQ channel to correct MIO channels (depends on IFA channels)

11. Enter probe sensor parameters from IFA100 setup procedure

Calibration Procedure

1. Verify that both sides of pressure transducer are vented (zero pressure)

2. Run 'Continuous AtoD' vi.

3. Verify that pressure transducer reads zero. If not, press 'set zero intercept'.

4. Stop 'Continuous AtoD' vi.

5. Enter slope and new intercept from (3) into 'X Wire Probe Cal' vi.

6. Set IFA HW channels to "RUN".

7. Run 'X Wire Probe Cal' vi.

8. Open valves on calibrator until jet is at maximum desired calibration velocity

DO NOT EXCEED TRANSDUCER MAXIMUM PRESSURE

9. Allow approximately 15 seconds for pressures to stabilize (watch velocity chart)

10. Run 'hotwire probe calibration – bmodmatt.vi'

11. Press 'TAKE DATA' button

12. Enter data filename. First data is taken as soon as file is created.

13. Wait for 'Taking Data' light to go out

14. Reduce calibrator flow to next desired calibration point

15. Allow approximately 15 seconds for pressures to stabilize (watch velocity chart)

16. Press 'TAKE DATA' button

17. Wait for 'Taking Data' light to go out

18. Repeat steps 13-20 until full calibration range covered

19. Press 'DONE DO FIT' button

20. Record initial calibration constants in notebook (C, D, MSE). Flag with RED ink.

21. Move Probe holder arm to the horizontal position

22. Set calibrator flow to a medium speed (approximately half maximum)
23. Run ‘Xwire-checkvelocity’ vi.
24. Rotate the probe in its sheath until the indicated angle is 0 degrees and lock it down
25. Stop ‘Xwire-checkvelocity’ vi.
26. Return to ‘X Wire Probe Cal’ vi.
27. Set “Type of Cal” switch to “45” (enables yaw compensation)
28. Run ‘X Wire Probe Cal’ vi.
29. Enter data filename. First data is taken as soon as file is created.
30. Wait for ‘Taking Data’ light to go out
31. Reduce calibrator flow to next desired calibration point
32. Allow approximately 15 seconds for pressures to stabilize
33. Press ‘TAKE DATA’ button
34. Wait for ‘Taking Data’ light to go out
35. Repeat steps 31-34 until full calibration range covered
36. Press ‘DONE DO FIT’ button (At this point the angle compensation window will pop up)
37. Set jet to highest expected velocity
38. Hit “OK” button
39. Move rotating collar to the R1 pin hole
40. Hit ‘Take Data’ button
41. Wait for ‘Taking Data’ light to go out
42. Move rotating collar to next pin hole
43. Hit ‘Take Data’ button
44. Wait for ‘Taking Data’ light to go out
45. Repeat steps 42-44 until data has been taken at the last pin location (R11). At this point a new window will pop up asking you to change velocity

46. Set jet to a medium velocity
47. Hit “OK” button
48. Move rotating collar to the R1 pin hole
49. Hit ‘Take Data’ button
50. Wait for ‘Taking Data’ light to go out
51. Move rotating collar to next pin hole
52. Hit ‘Take Data’ button
53. Wait for ‘Taking Data’ light to go out
54. Repeat steps 51-53 until data has been taken at the last pin location (R11). At this point a new window will pop up asking you to change velocity
55. Set jet to a low velocity
56. Hit “OK” button
57. Move rotating collar to the R1 pin hole
58. Hit ‘Take Data’ button
59. Wait for ‘Taking Data’ light to go out
60. Move rotating collar to next pin hole
61. Hit ‘Take Data’ button
62. Wait for ‘Taking Data’ light to go out
63. Repeat steps 60-62 until data has been taken at the last pin location (R11).
64. Lucky you, that is the end!
65. Record final calibration data. Flag with RED ink.
66. Backup calibration file (this takes too long to do very often)

Hardware Takedown

1. Shut off isolator valve to calibrator

2. Before removing hotwire/hotfilm from calibrator indicate flow direction on shaft (a 90deg rotation changes the calibration constants)
3. Mount hotwire/hotfilm in tunnel making sure you attach the same sensor to the same IFA channel
4. Disconnect calibrator pressure tap from transducer
5. Reconnect instrumentation lines to transducer
6. Reset valves on transducer (vents closed, measure open)

APPENDIX B. Boundary Layer Profiles

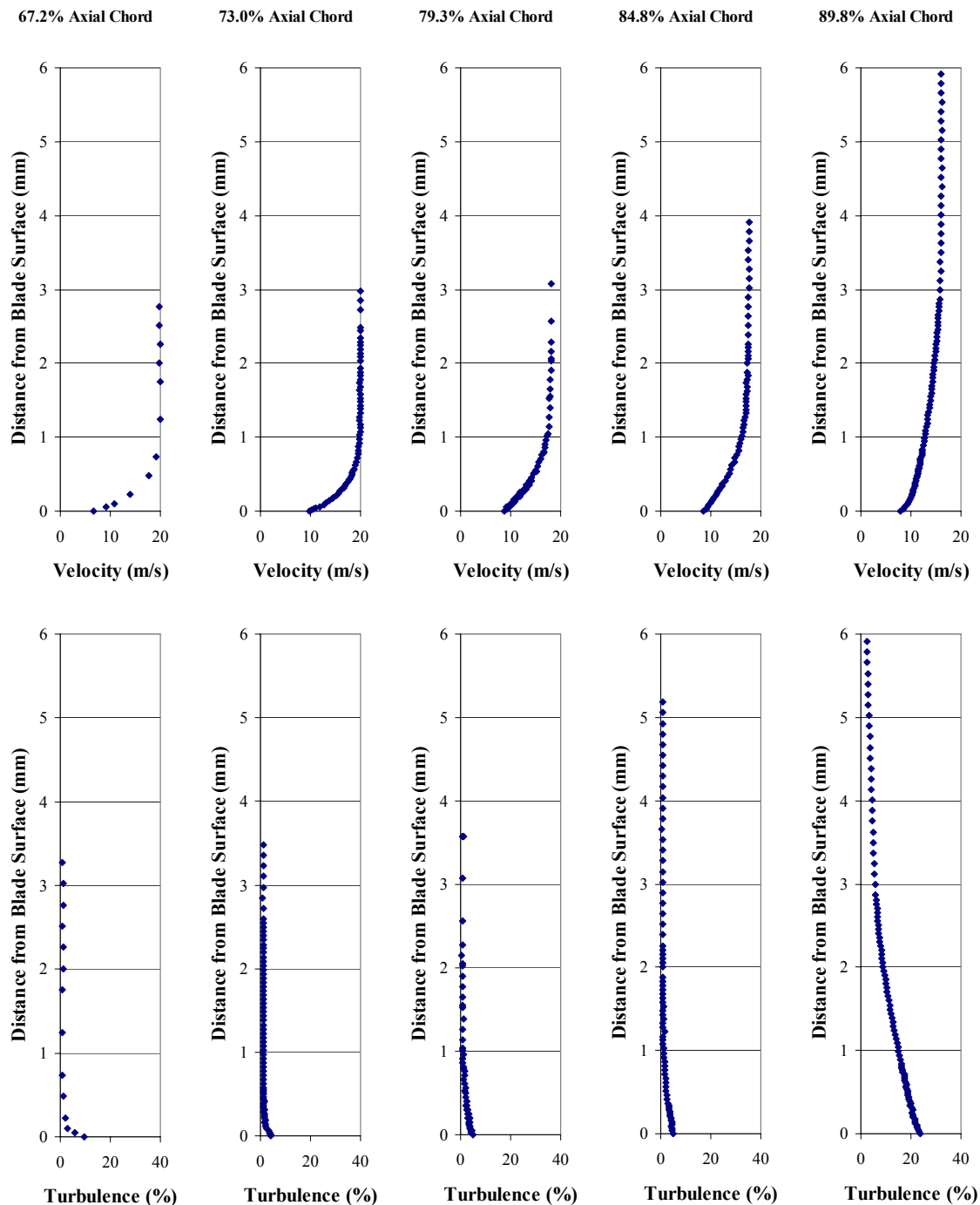


Figure 69. Boundary layer profiles for baseline Pak-B at $Re = 100k$ and $Tu = 1\%$

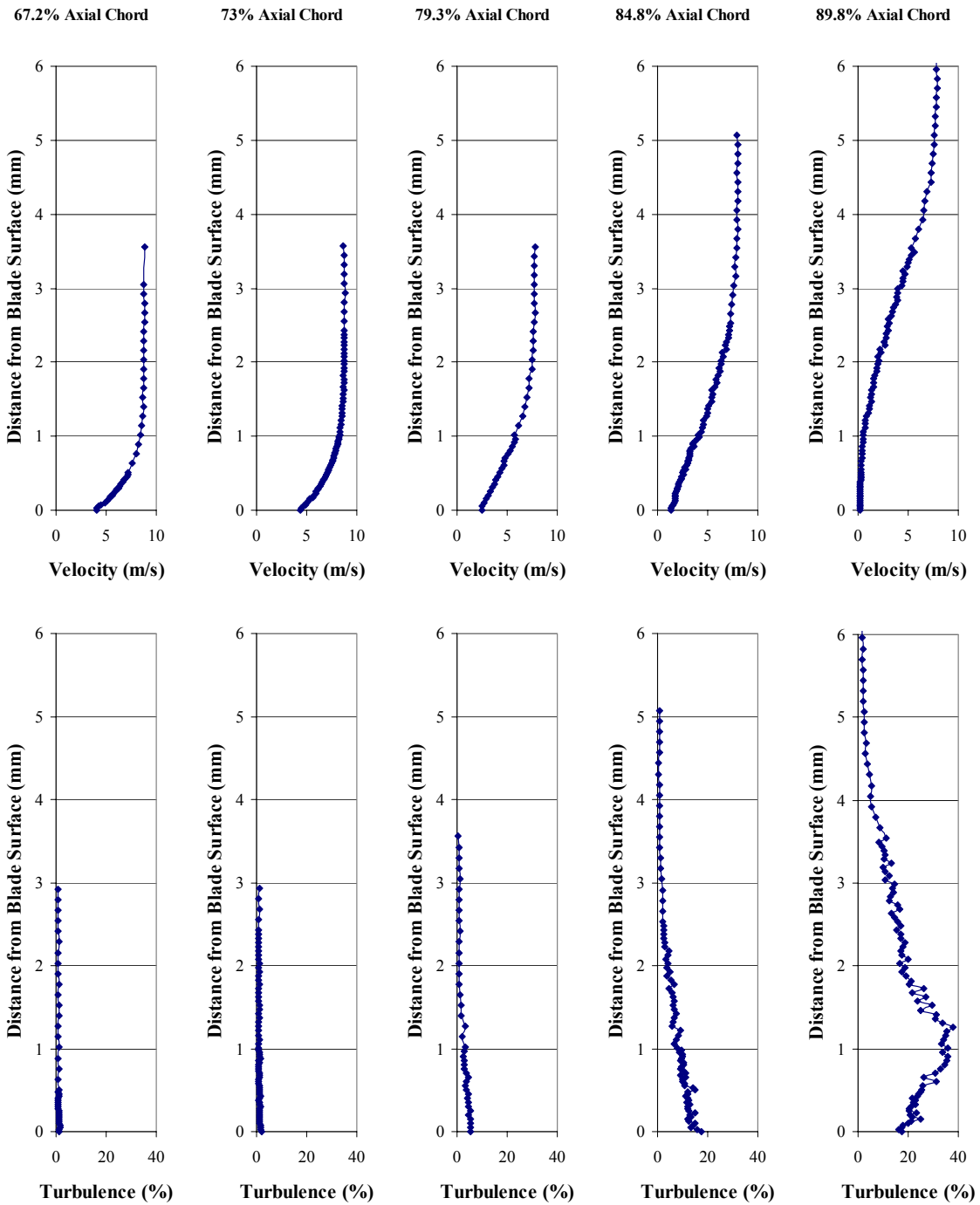


Figure 70. Boundary layer profiles for baseline Pak-B at $Re = 45k$ and $Tu = 1\%$

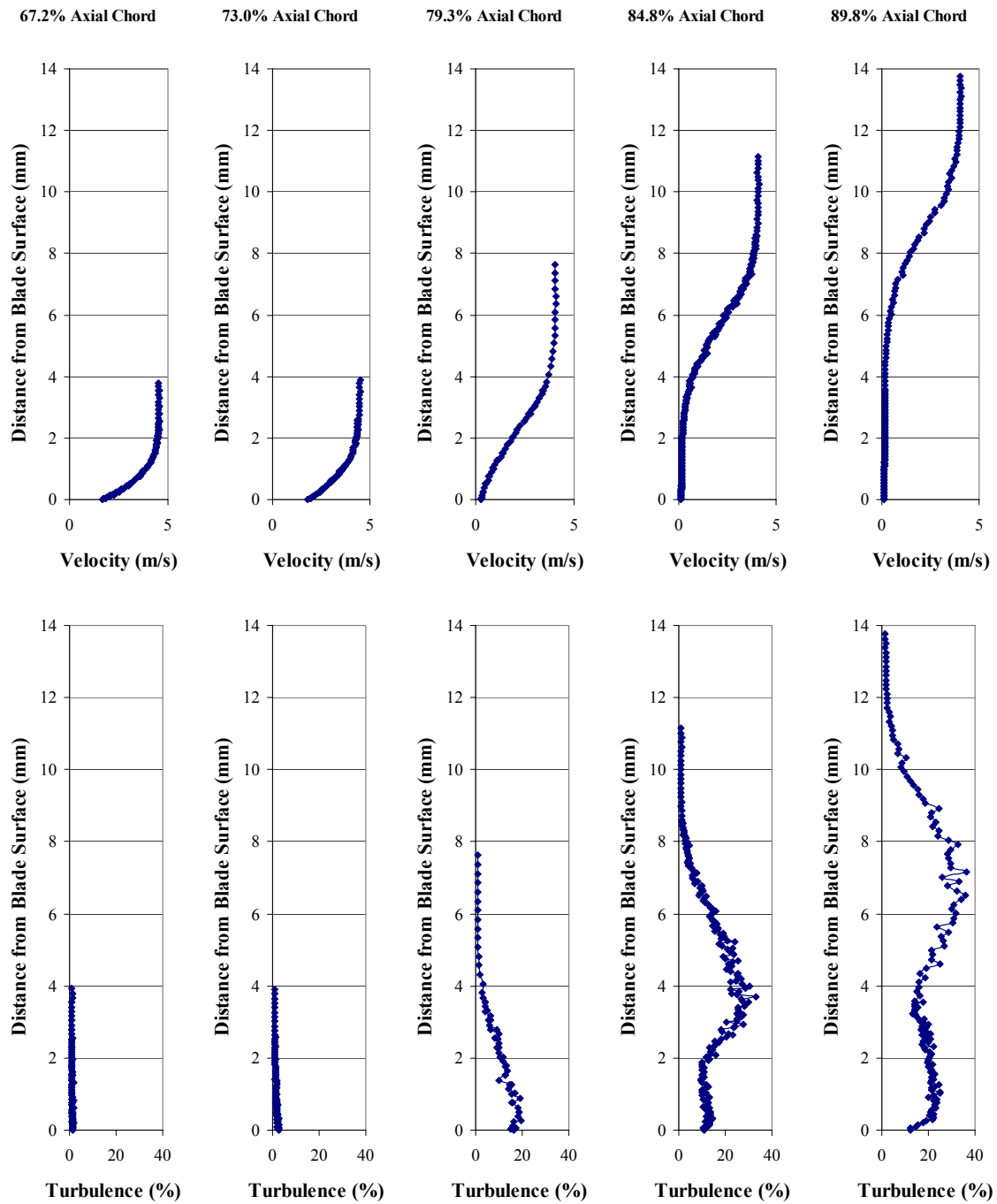


Figure 71. Boundary layer profiles for baseline Pak-B at $Re = 25k$ and $Tu = 1\%$

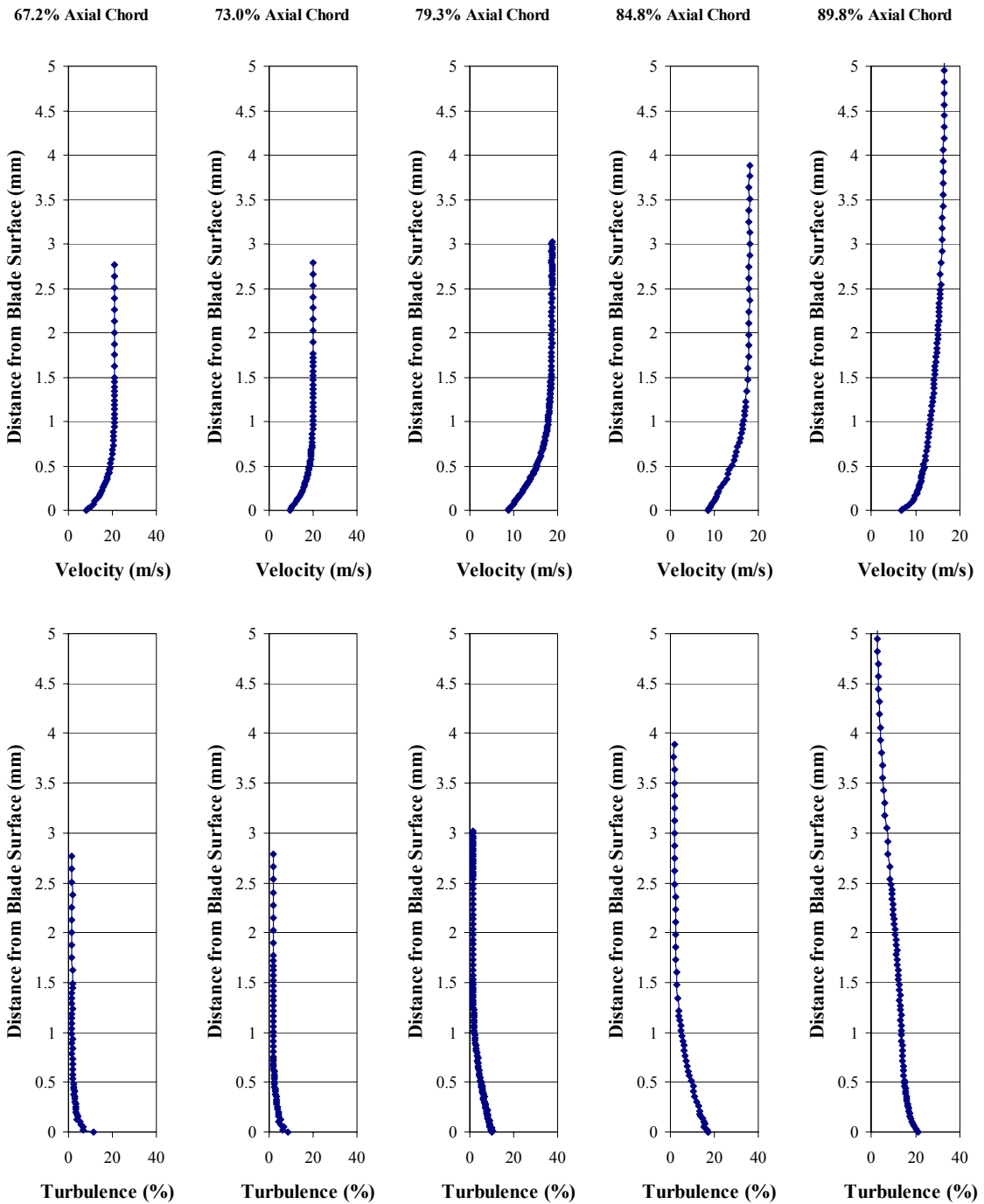


Figure 72. Boundary layer profiles for baseline Pak-B at $Re = 100k$ and $Tu = 4\%$

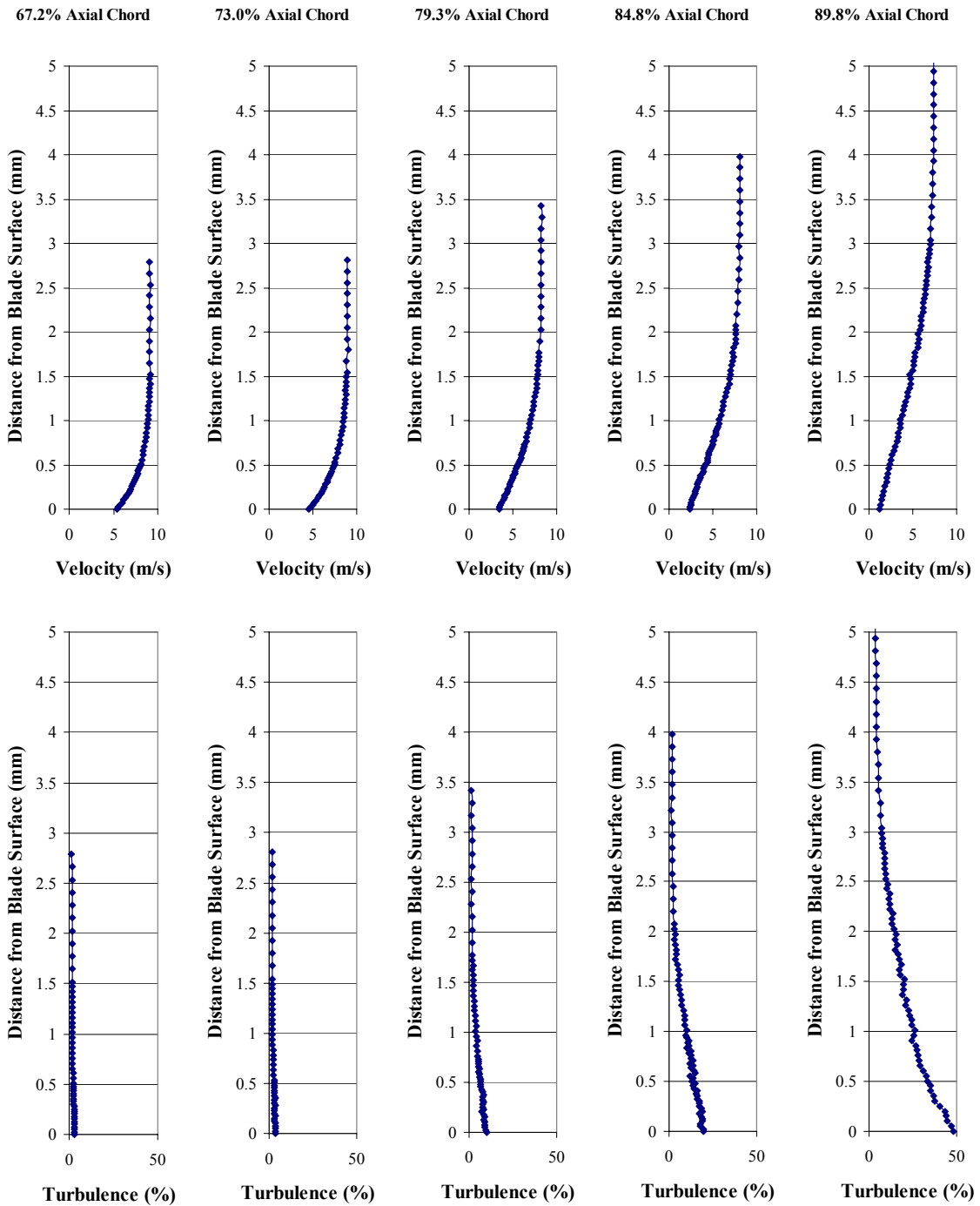


Figure 73. Boundary layer profiles for baseline Pak-B at $Re = 45k$ and $Tu = 4\%$

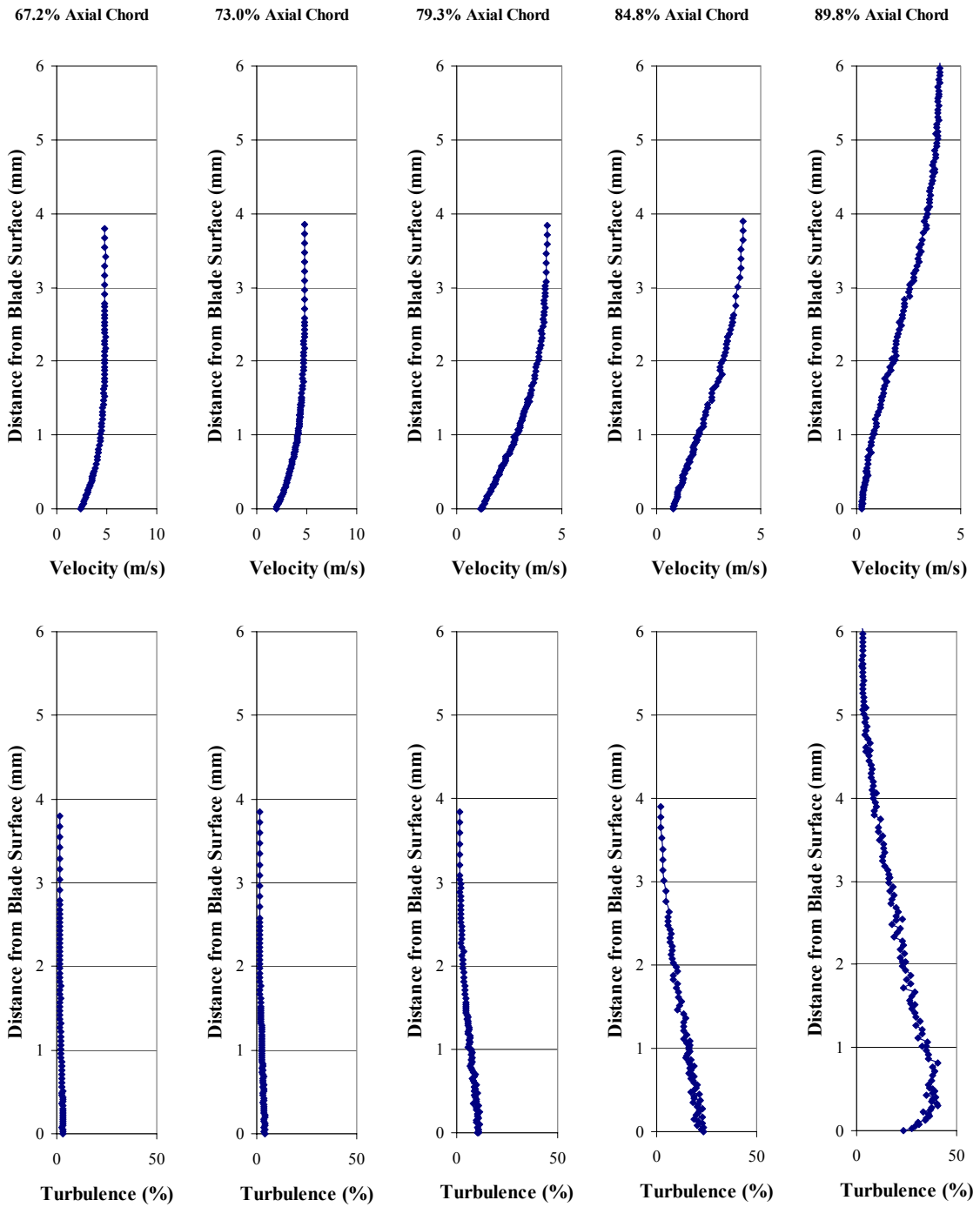


Figure 74. Boundary layer profiles for baseline Pak-B at $Re = 25k$ and $Tu = 4\%$

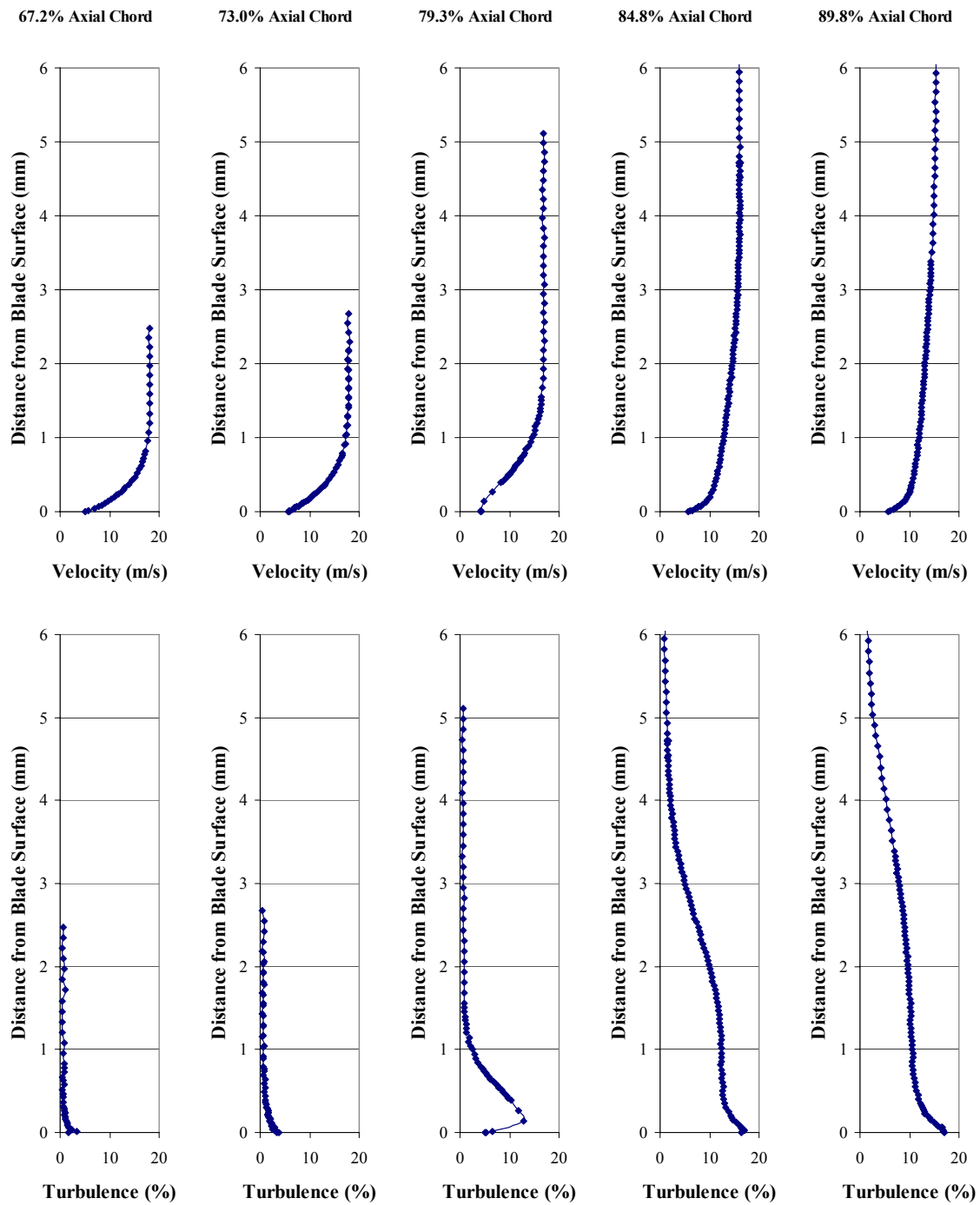


Figure 75. Boundary layer profiles for Pak-B with asymmetric dimples at 50% axial chord at $Re = 100k$ and $Tu = 1\%$

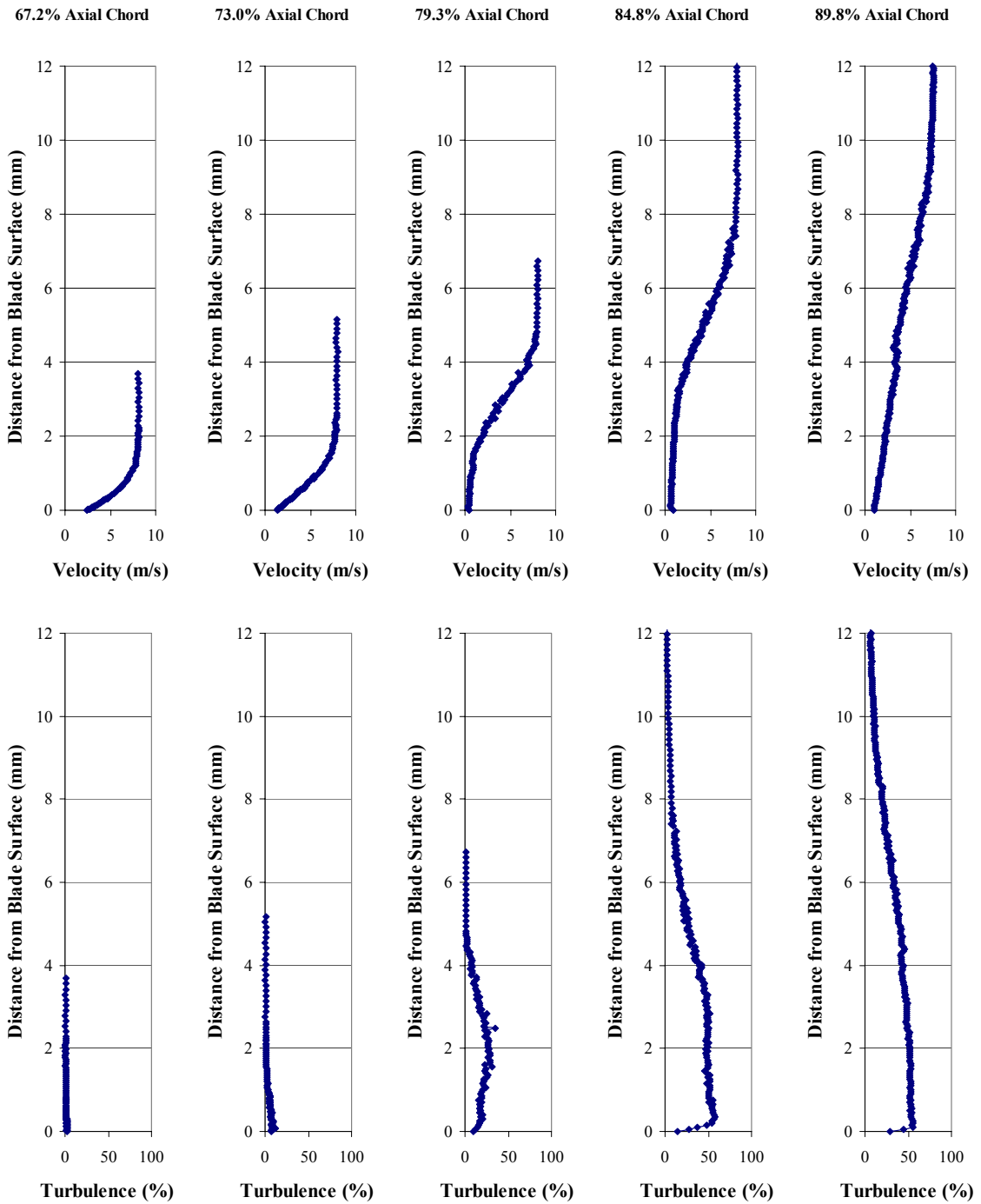


Figure 76. Boundary layer profiles for Pak-B with asymmetric dimples at 50% axial chord at $Re = 45k$ and $Tu = 1\%$

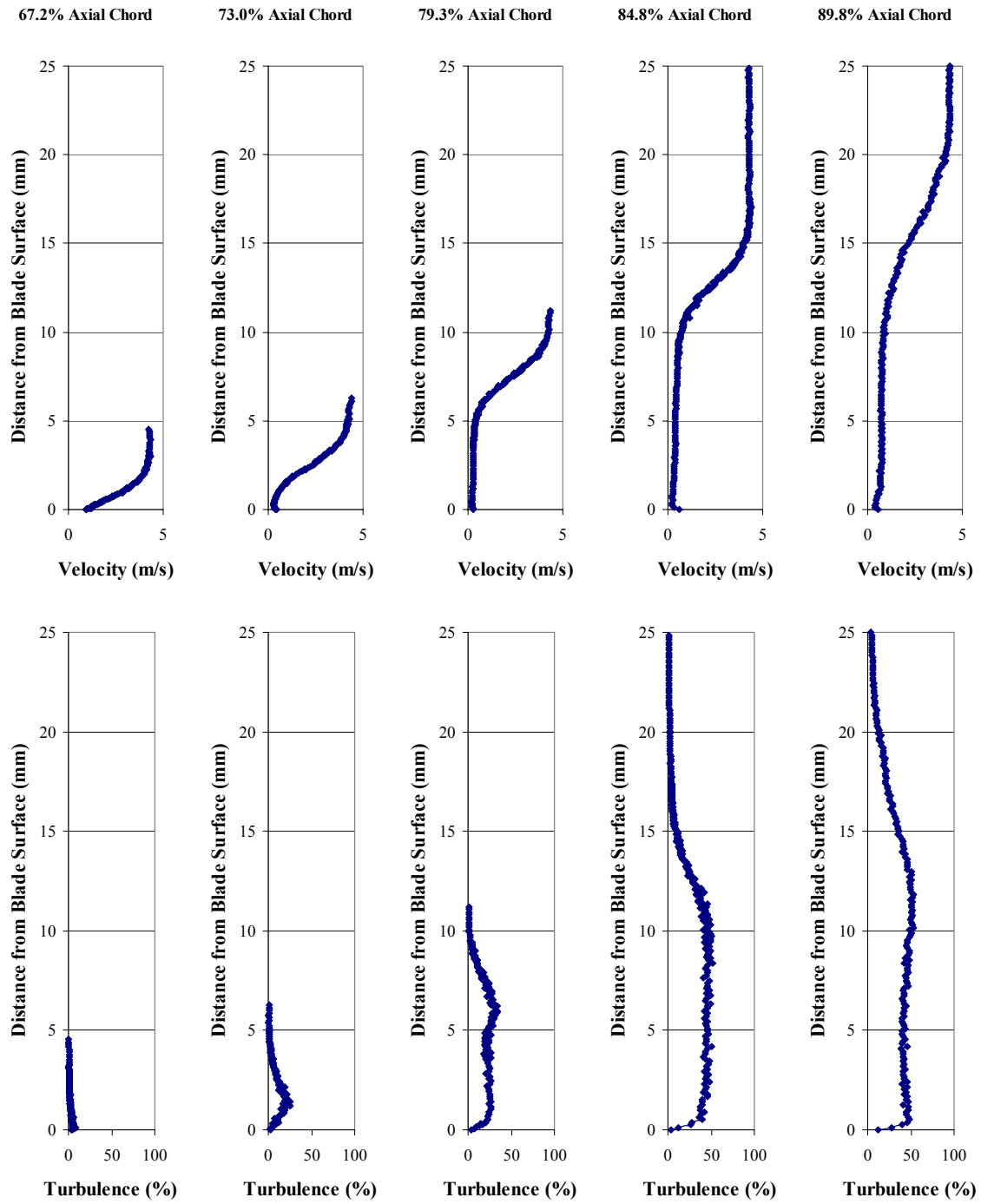


Figure 77. Boundary layer profiles for Pak-B with asymmetric dimples at 50% axial chord at $Re = 25k$ and $Tu = 1\%$

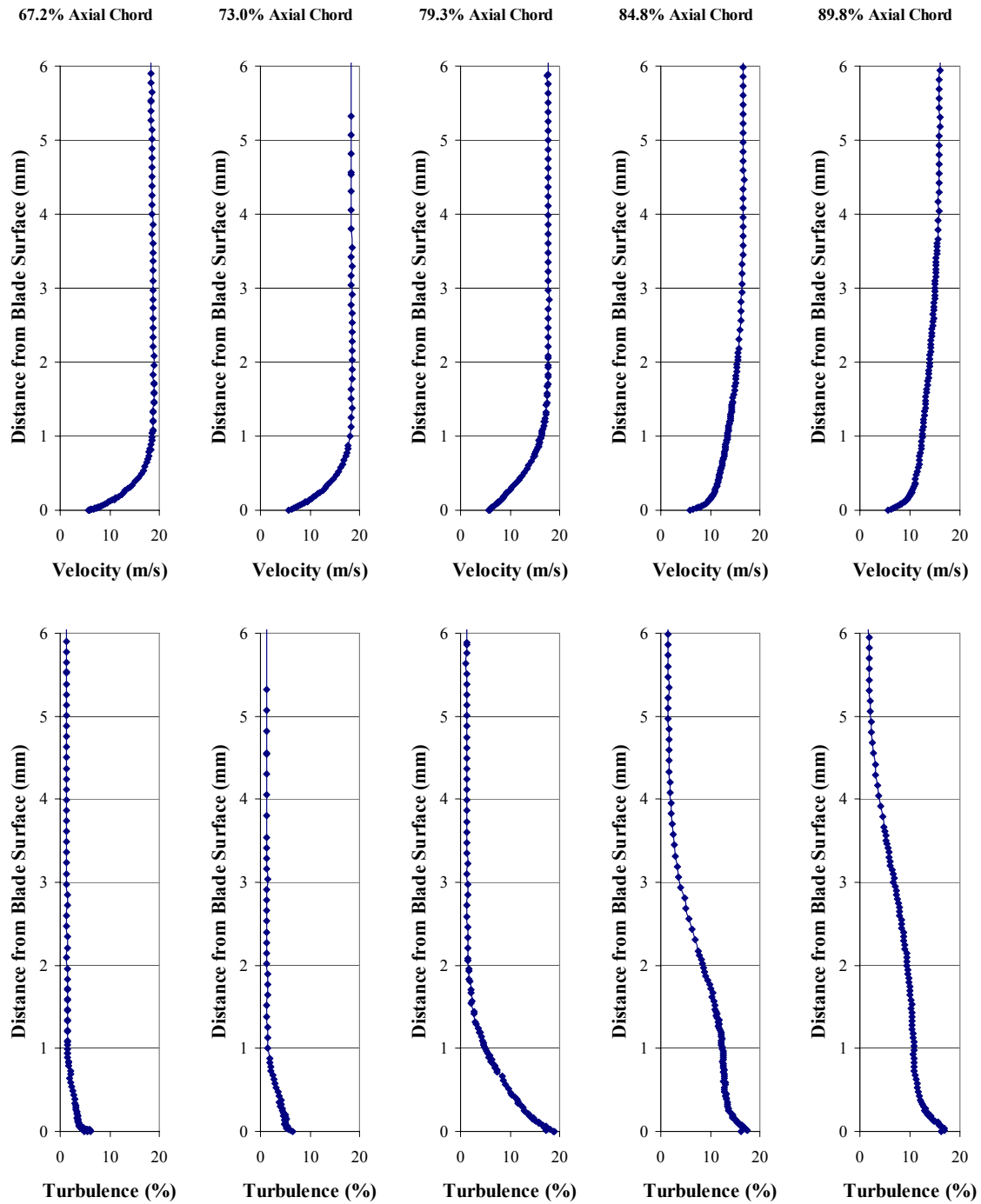


Figure 78. Boundary layer profiles for Pak-B with asymmetric dimples at 50% axial chord at $Re = 100k$ and $Tu = 4\%$

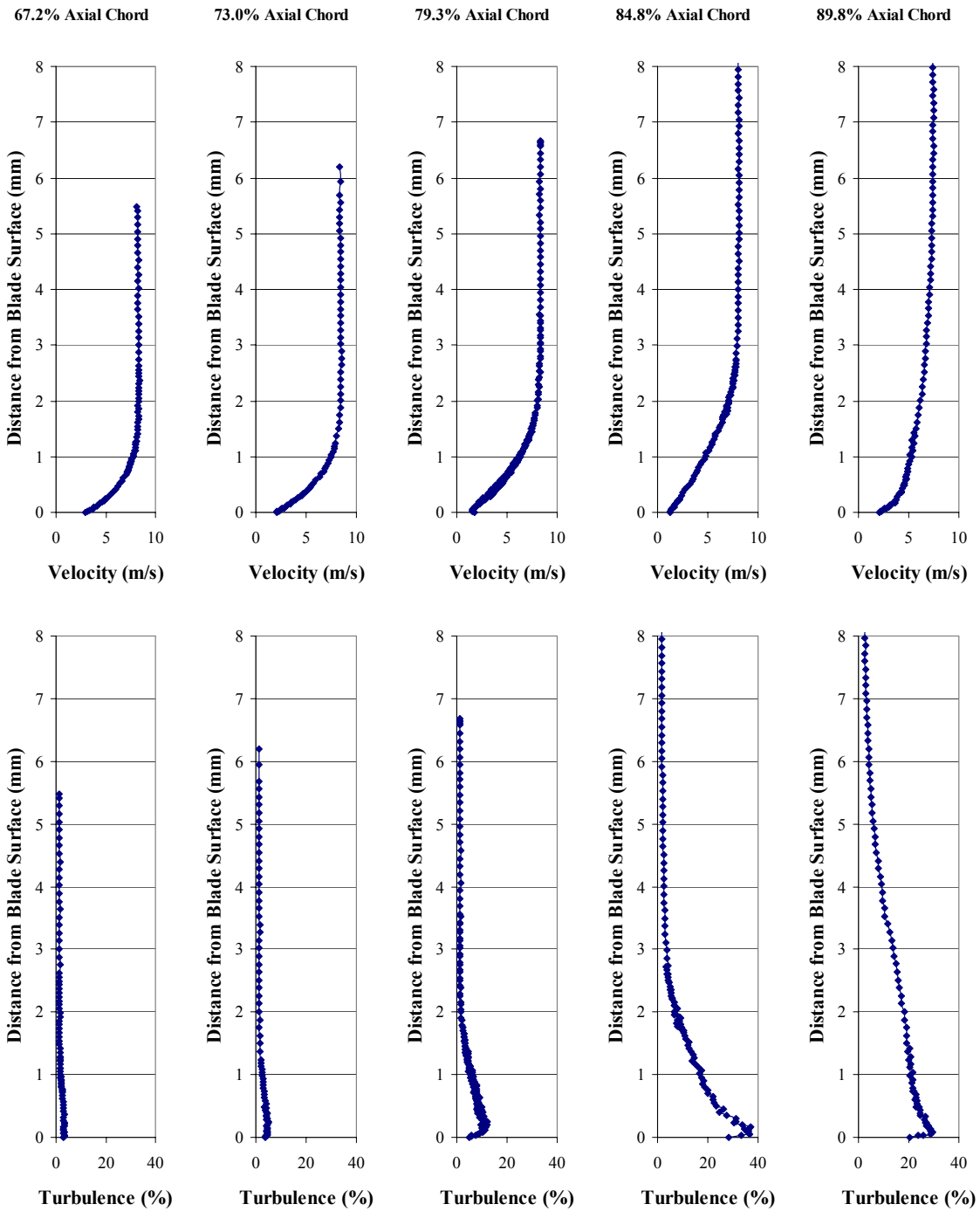


Figure 79. Boundary layer profiles for Pak-B with asymmetric dimples at 50% axial chord at $Re = 45k$ and $Tu = 4\%$

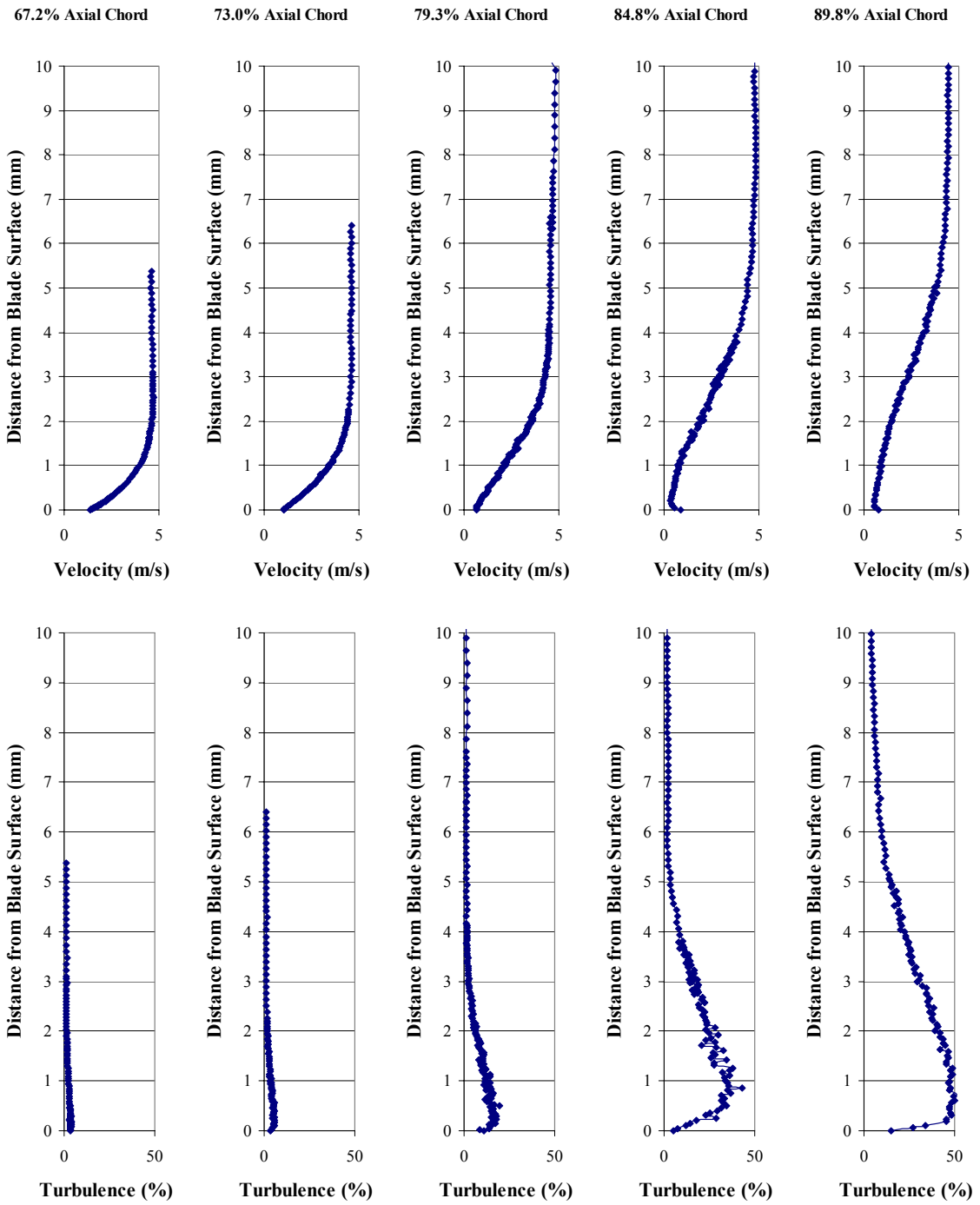


Figure 80. Boundary layer profiles for Pak-B with asymmetric dimples at 50% axial chord at $Re = 25k$ and $Tu = 4\%$

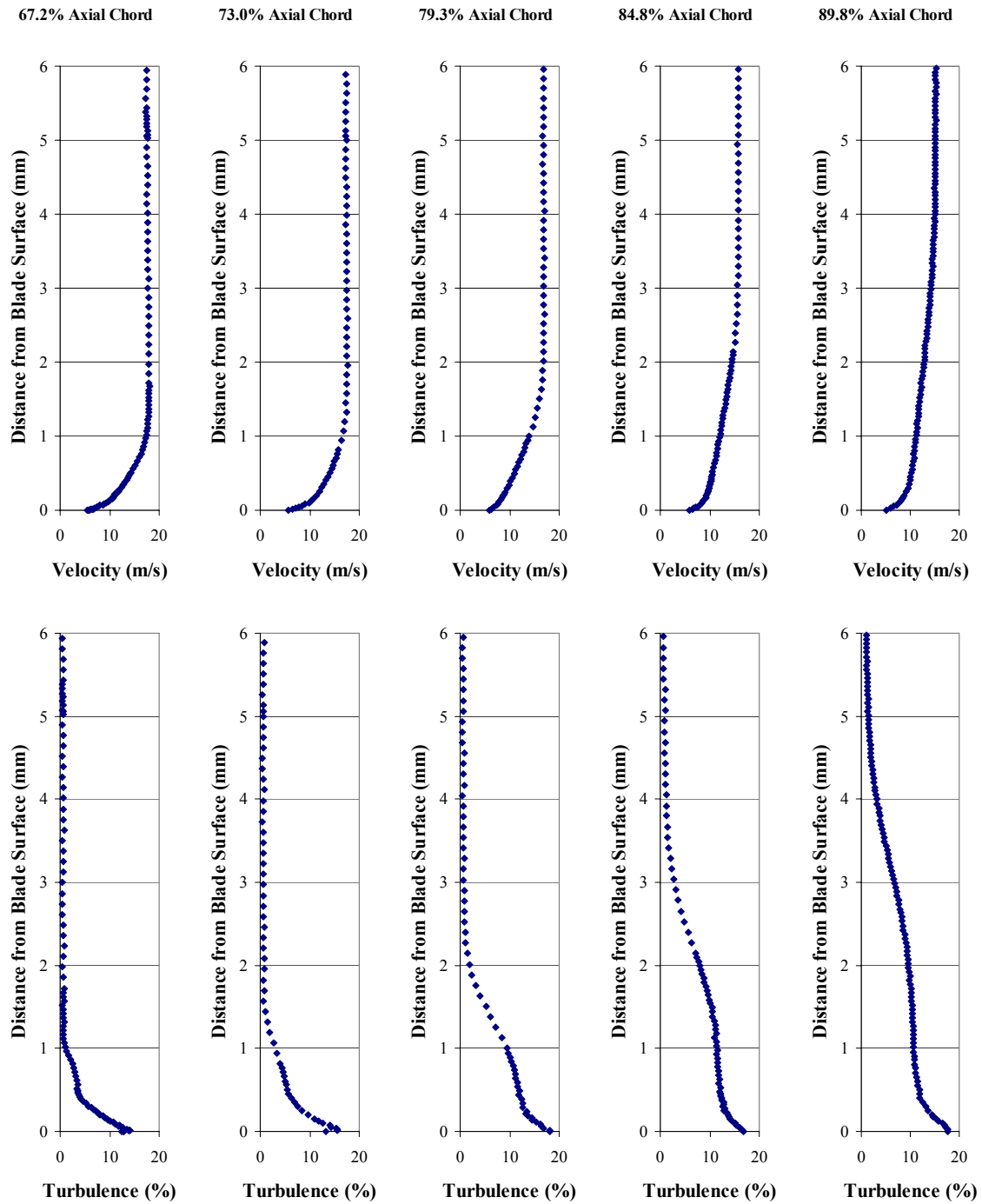


Figure 81. Boundary layer profiles for Pak-B with asymmetric dimples at 55% axial chord at $Re = 100k$ and $Tu = 1\%$

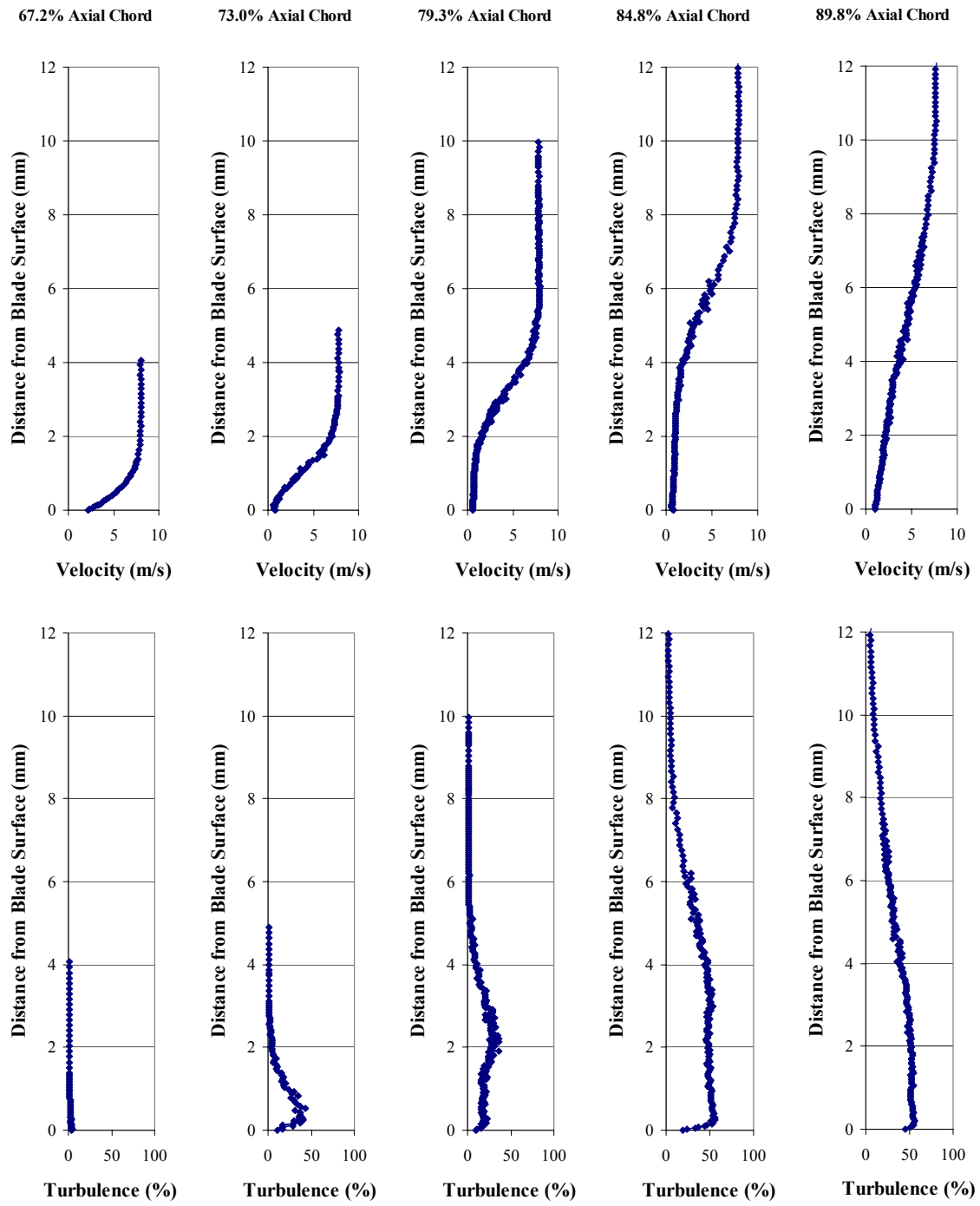


Figure 82. Boundary layer profiles for Pak-B with asymmetric dimples at 55% axial chord at $Re = 45k$ and $Tu = 1\%$

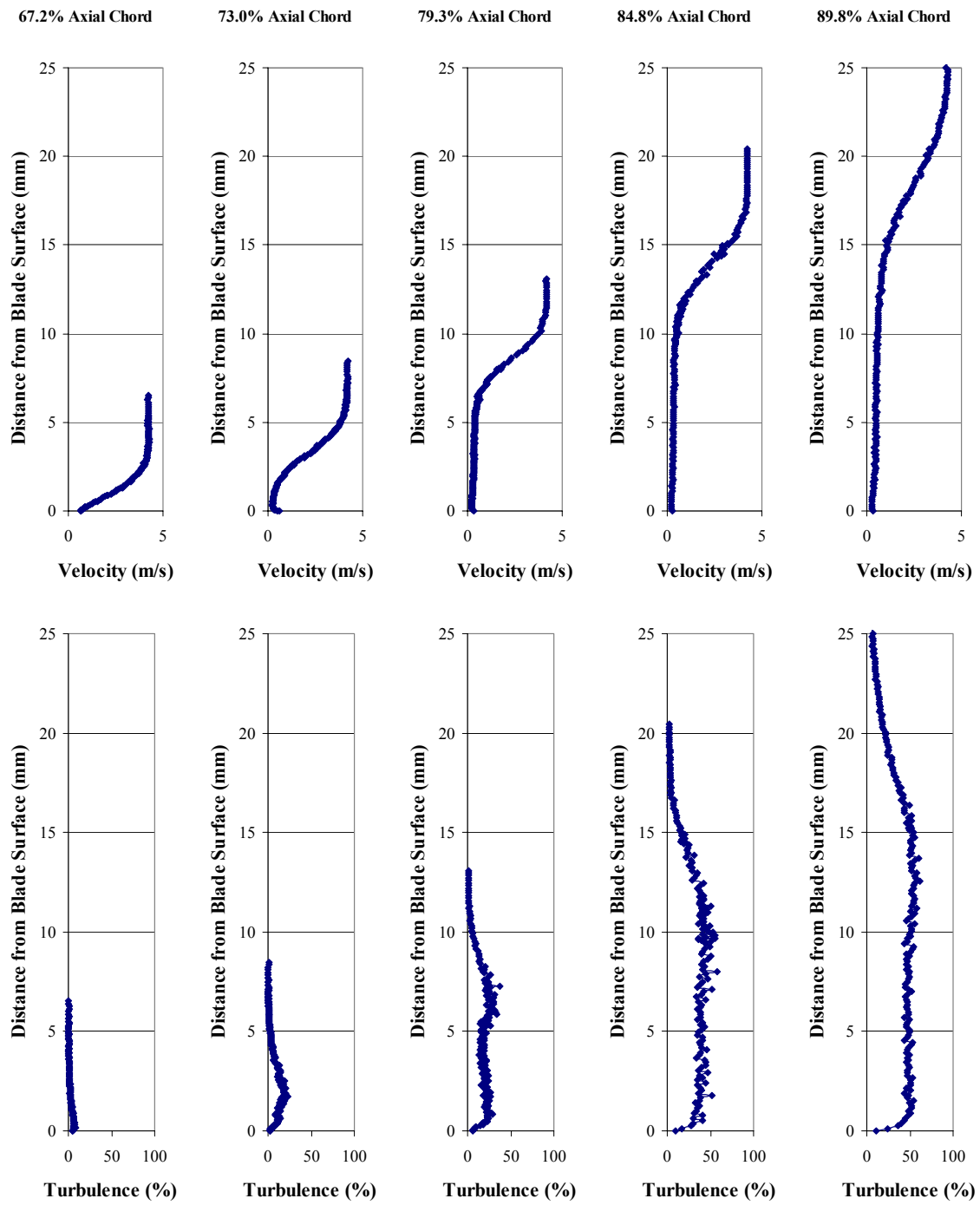


Figure 83. Boundary layer profiles for Pak-B with asymmetric dimples at 55% axial chord at $Re = 25k$ and $Tu = 1\%$

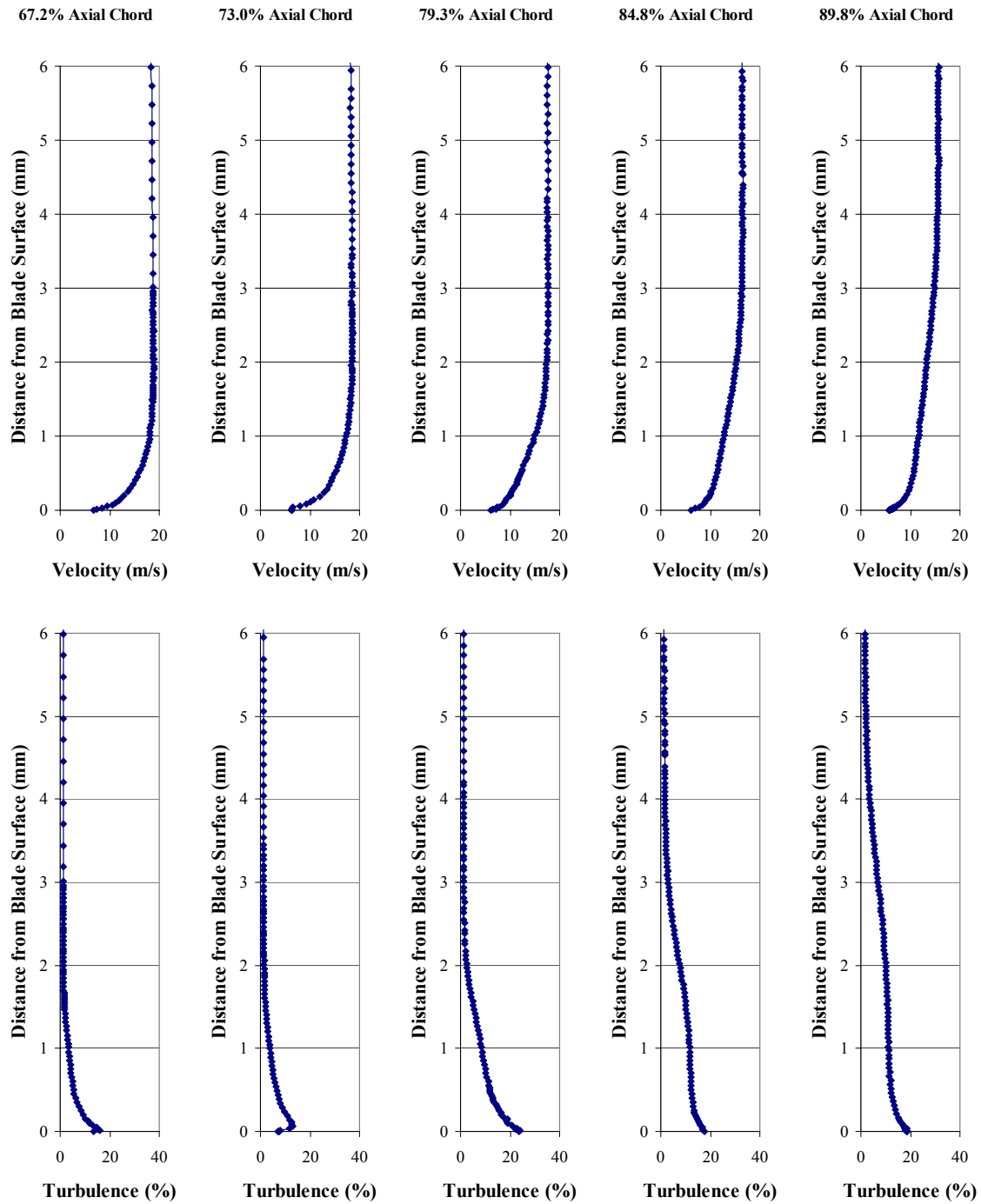


Figure 84. Boundary layer profiles for Pak-B with asymmetric dimples at 55% axial chord at $Re = 100k$ and $Tu = 4\%$

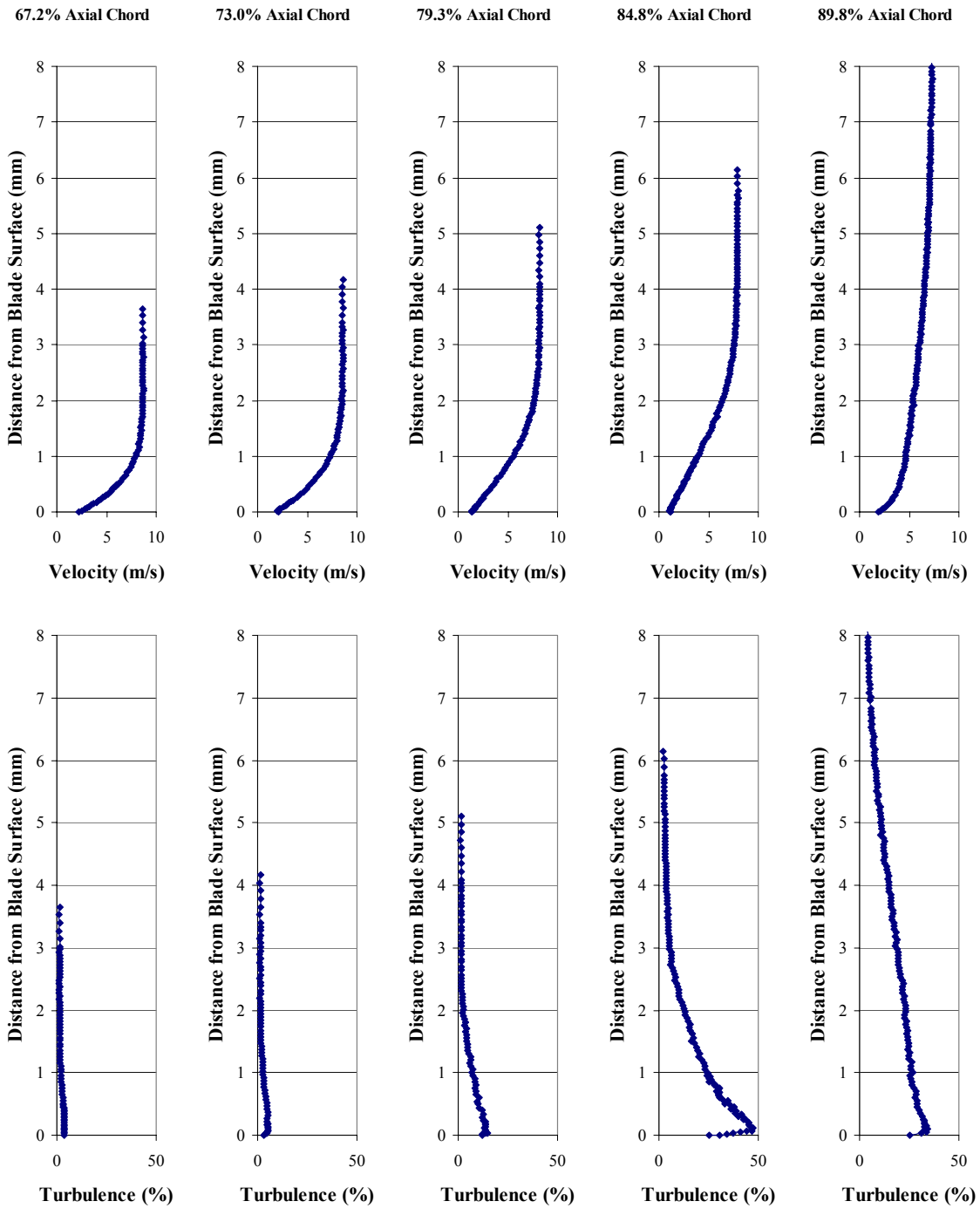


Figure 85. Boundary layer profiles for Pak-B with asymmetric dimples at 55% axial chord at $Re = 45k$ and $Tu = 4\%$

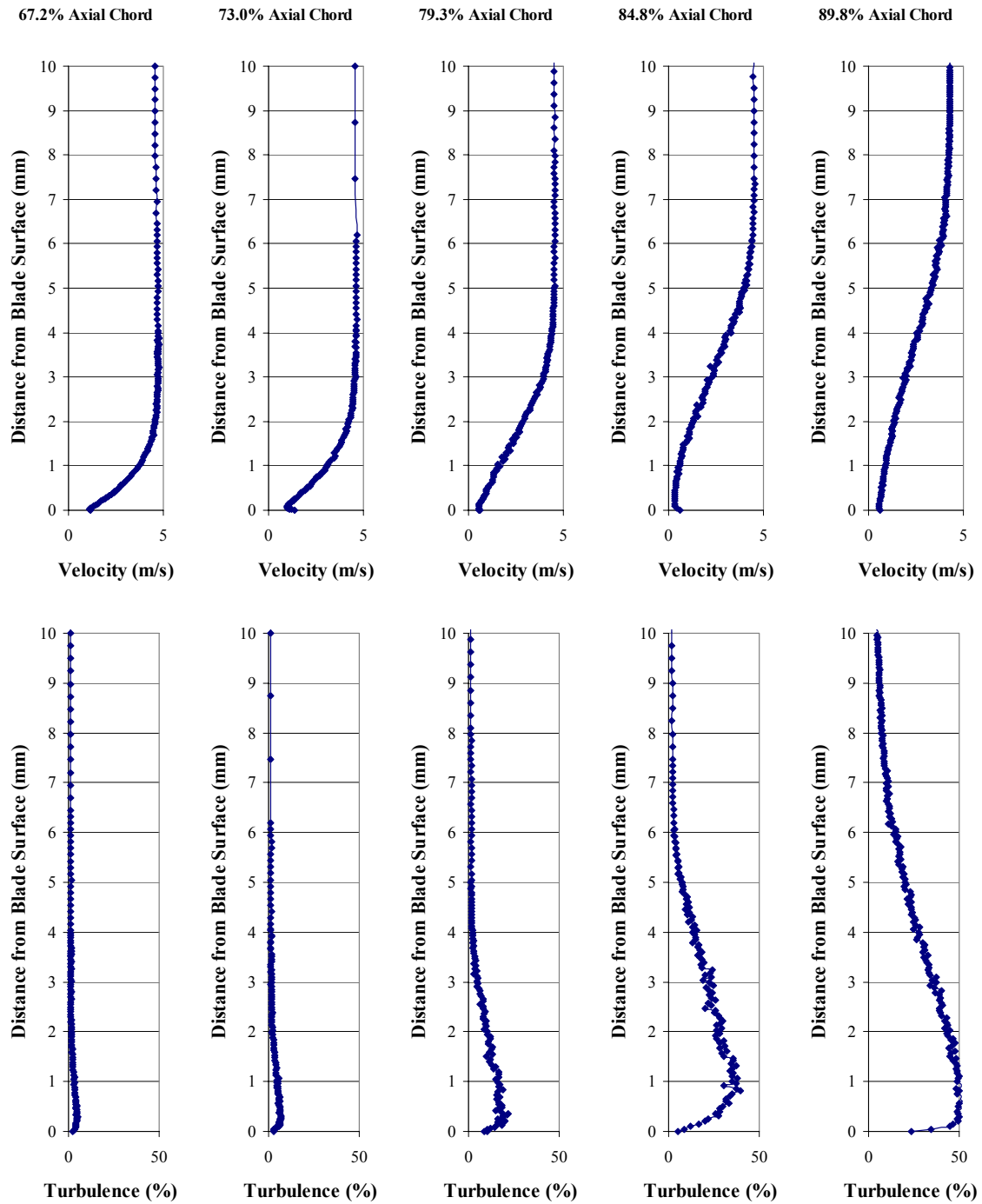


Figure 86 Boundary layer profiles for Pak-B with asymmetric dimples at 55% axial chord at $Re = 25k$ and $Tu = 4\%$

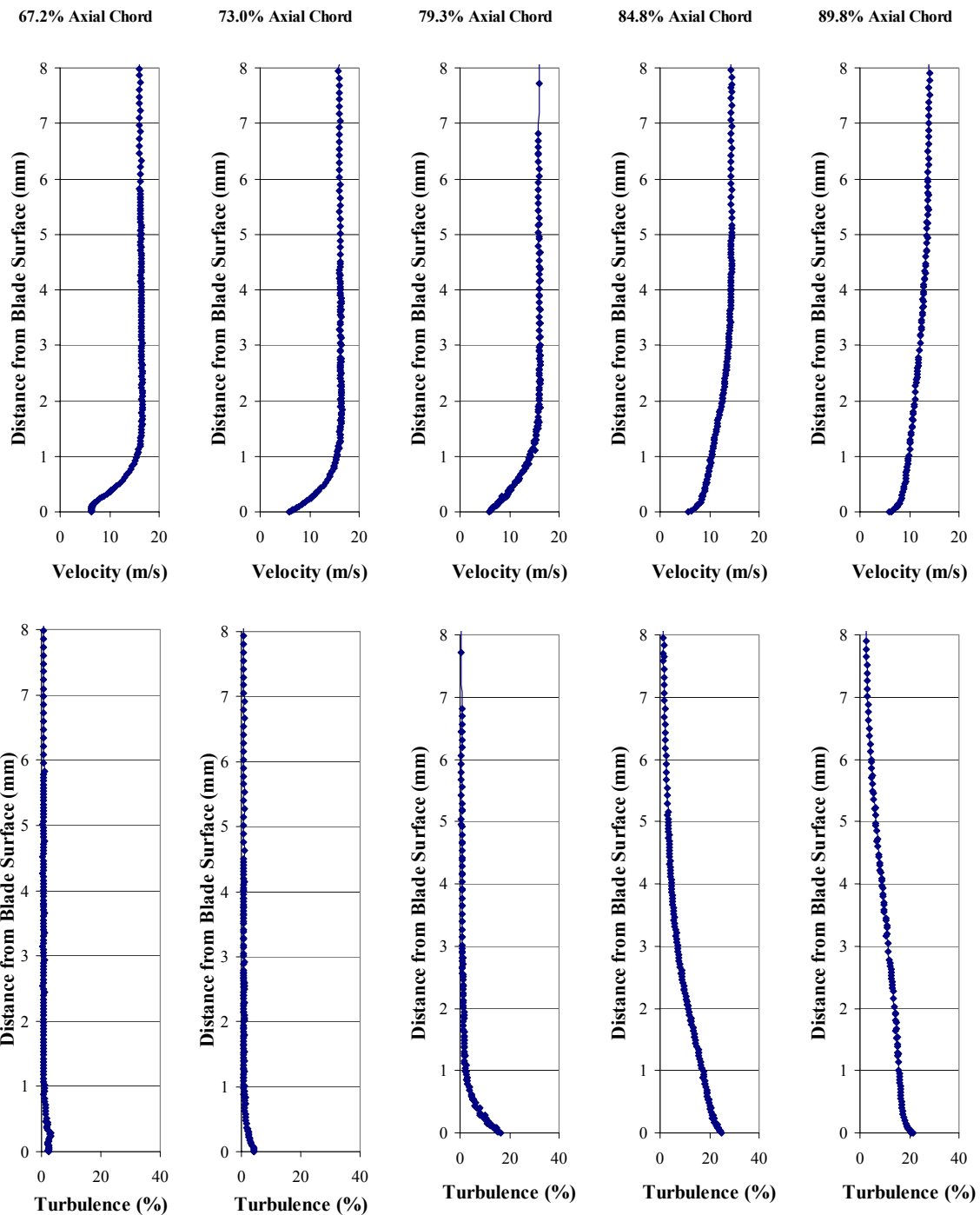


Figure 87. Boundary layer profiles for Pak-B with asymmetric dimples at 65% axial chord at $Re = 100k$ and $Tu = 1\%$

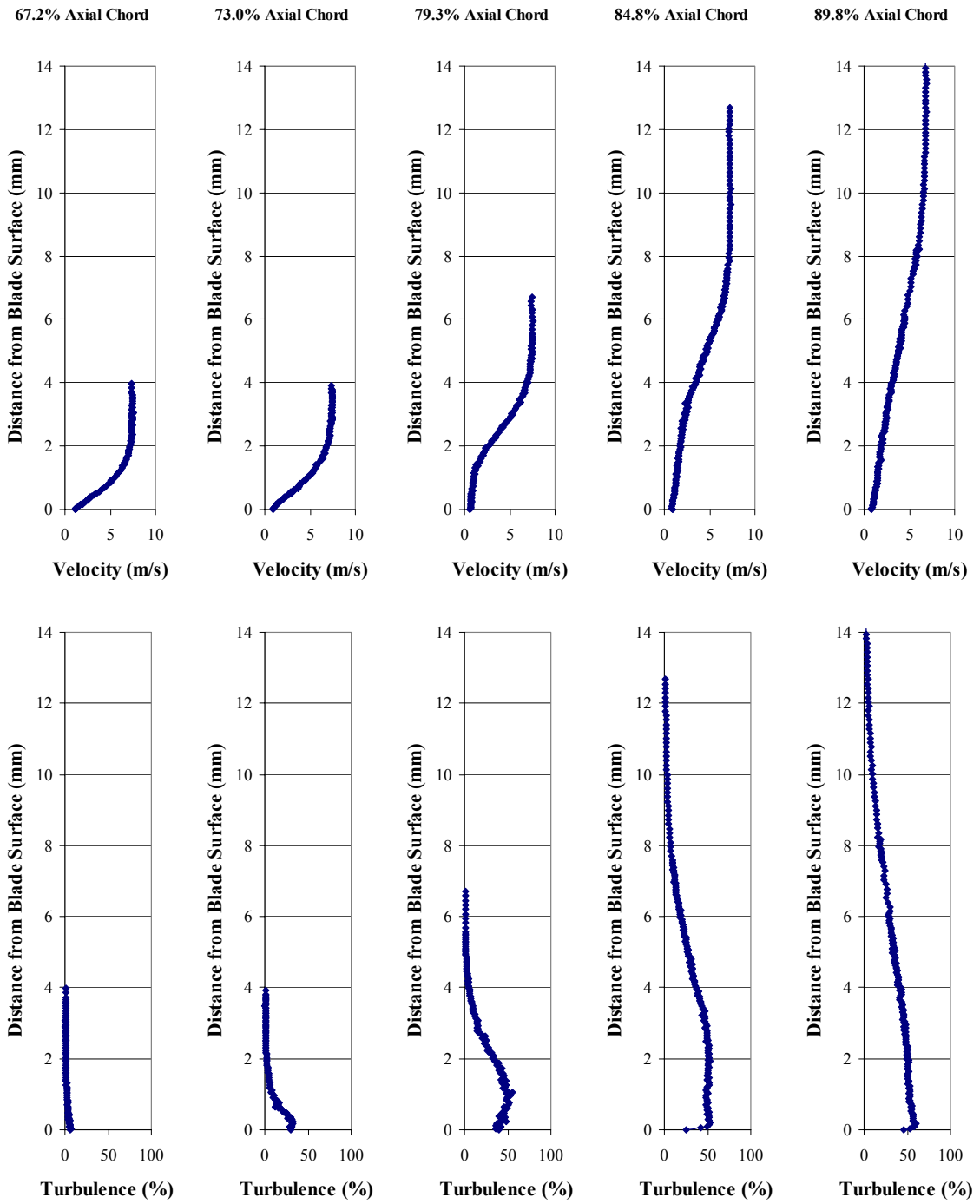


Figure 88. Boundary layer profiles for Pak-B with asymmetric dimples at 65% axial chord at $Re = 45k$ and $Tu = 1\%$

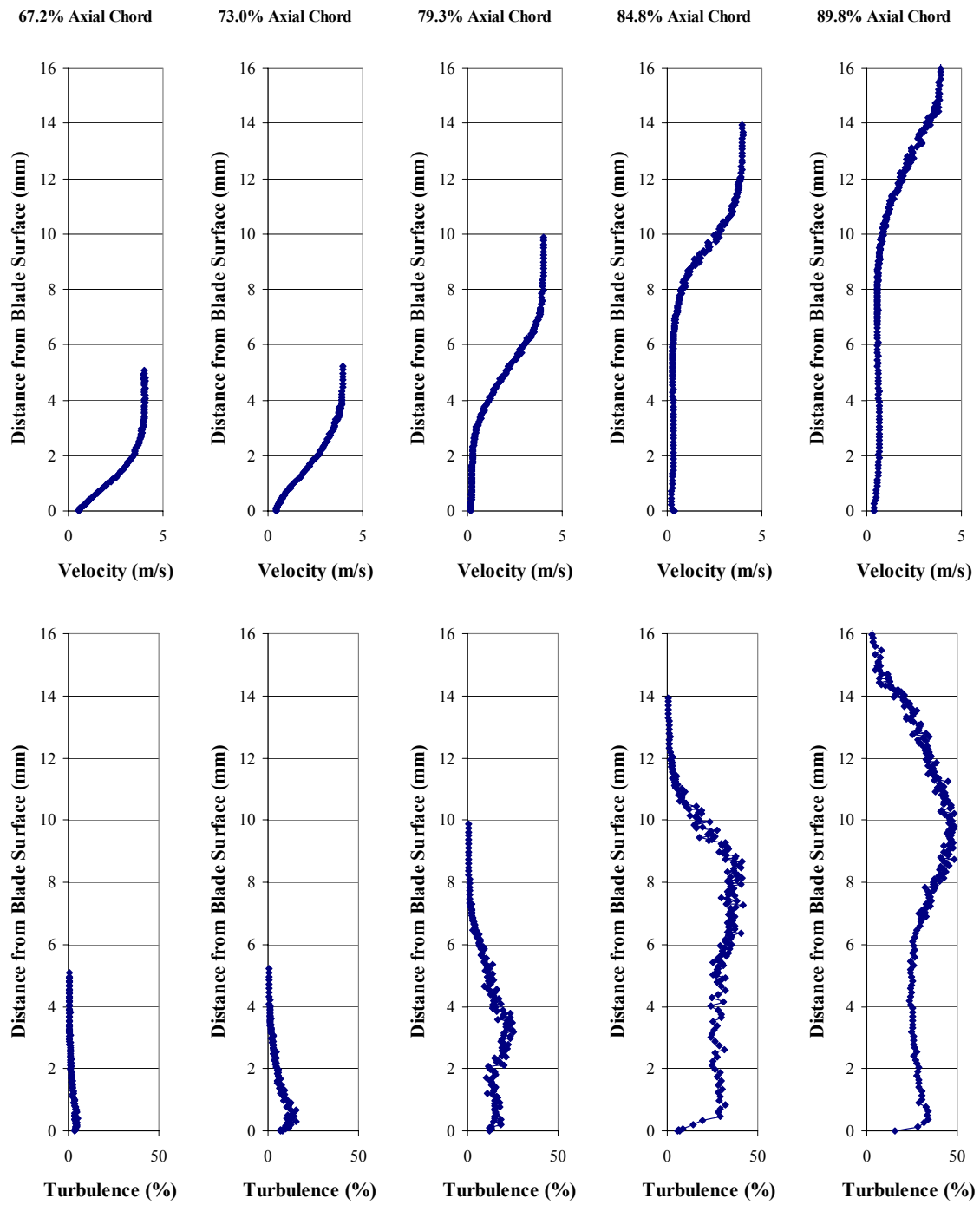


Figure 89. Boundary layer profiles for Pak-B with asymmetric dimples at 65% axial chord at $Re = 25k$ and $Tu = 1\%$

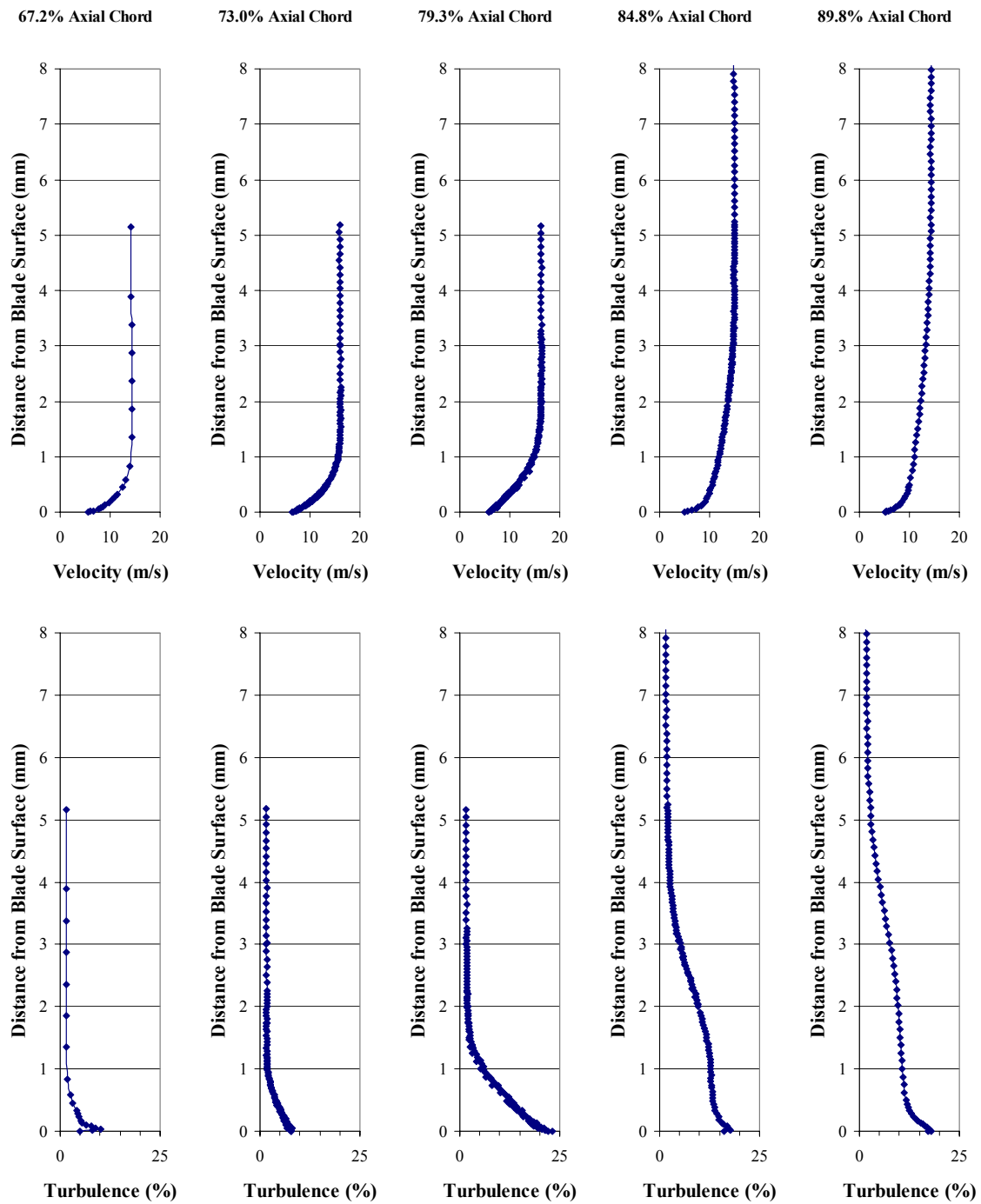


Figure 90. Boundary layer profiles for Pak-B with asymmetric dimples at 65% axial chord at $Re = 100k$ and $Tu = 4\%$

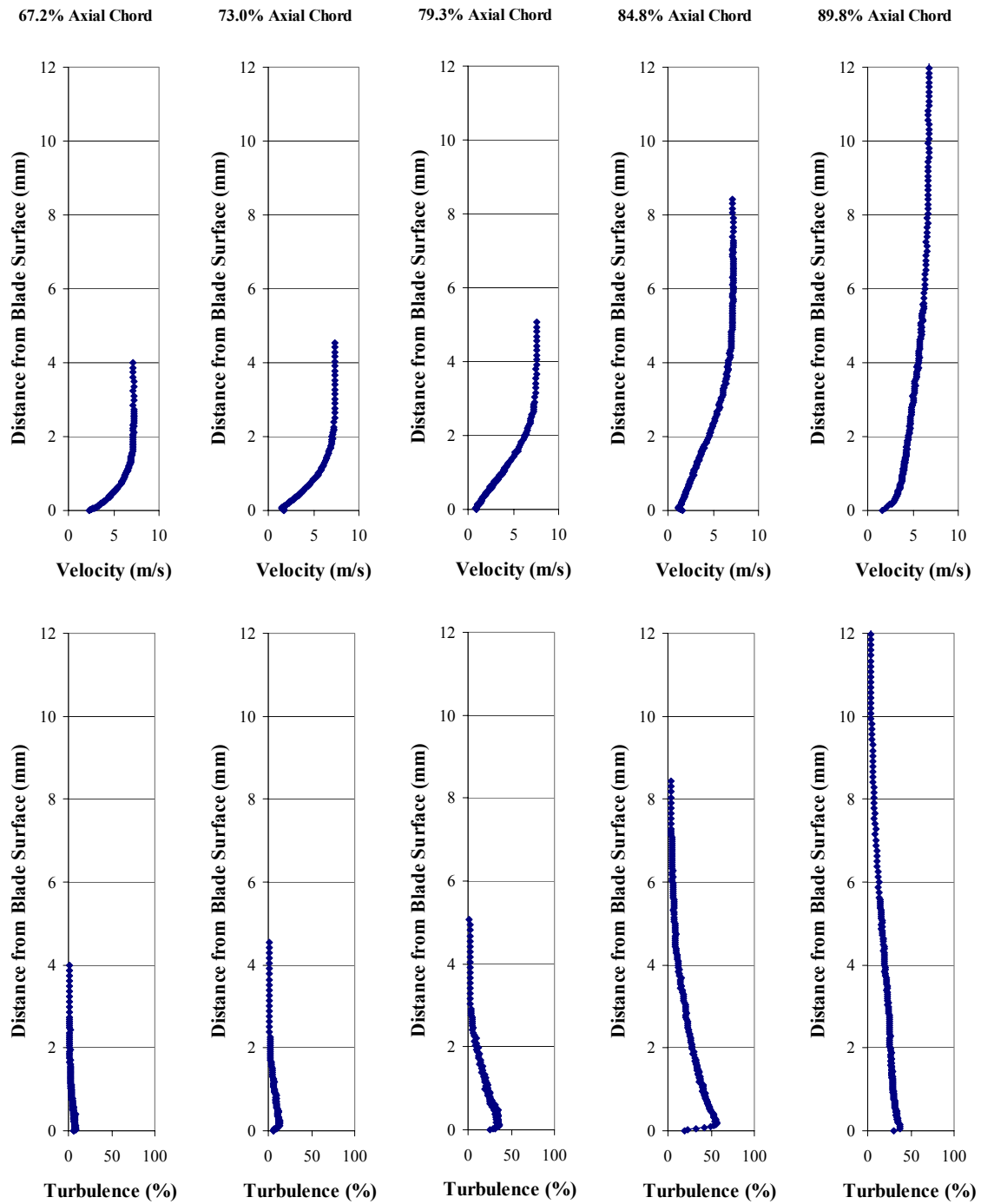


Figure 91. Boundary layer profiles for Pak-B with asymmetric dimples at 65% axial chord at $Re = 45k$ and $Tu = 4\%$

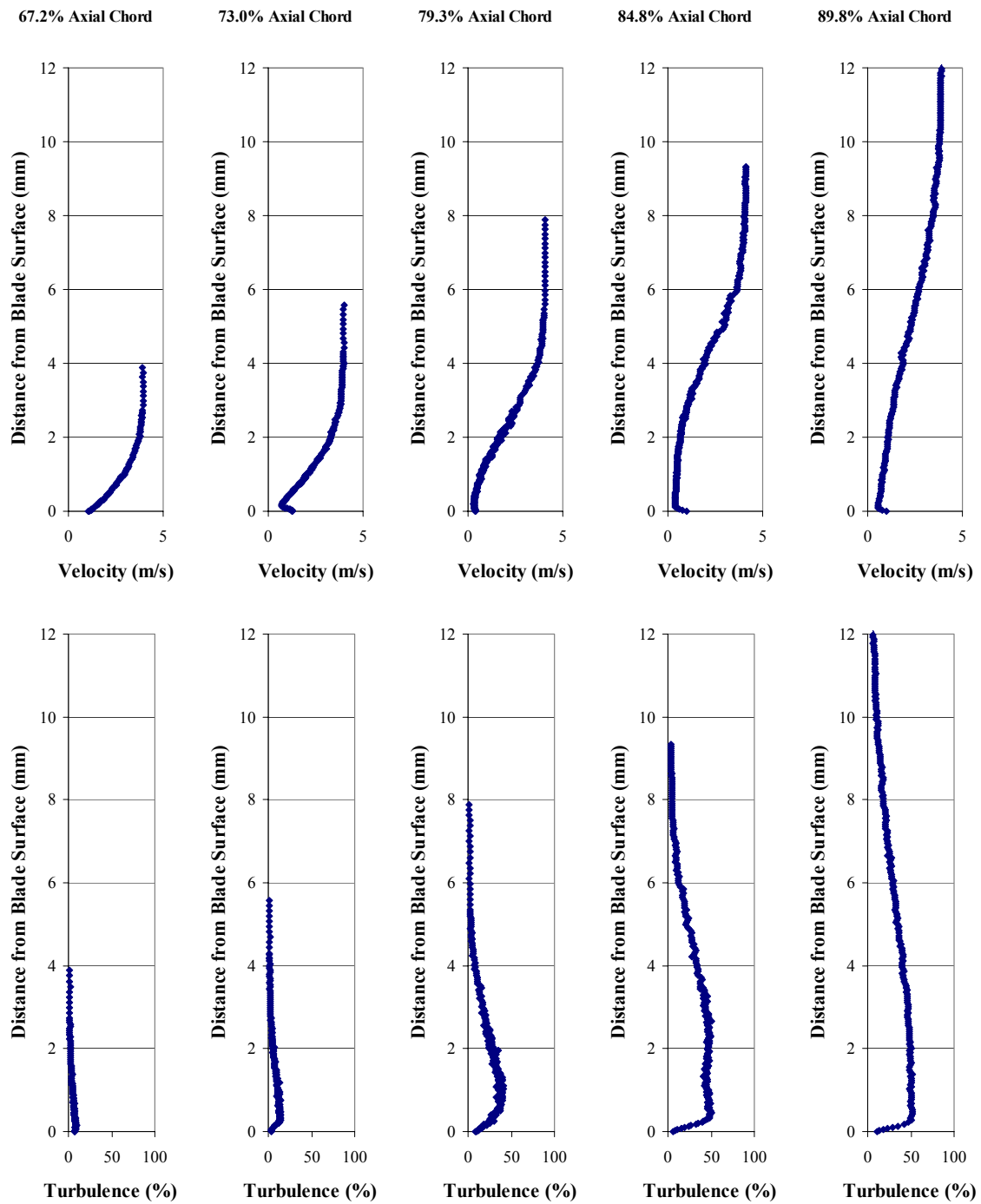


Figure 92. Boundary layer profiles for Pak-B with asymmetric dimples at 65% axial chord at $Re = 25k$ and $Tu = 4\%$

APPENDIX C. Wake Velocity Profiles

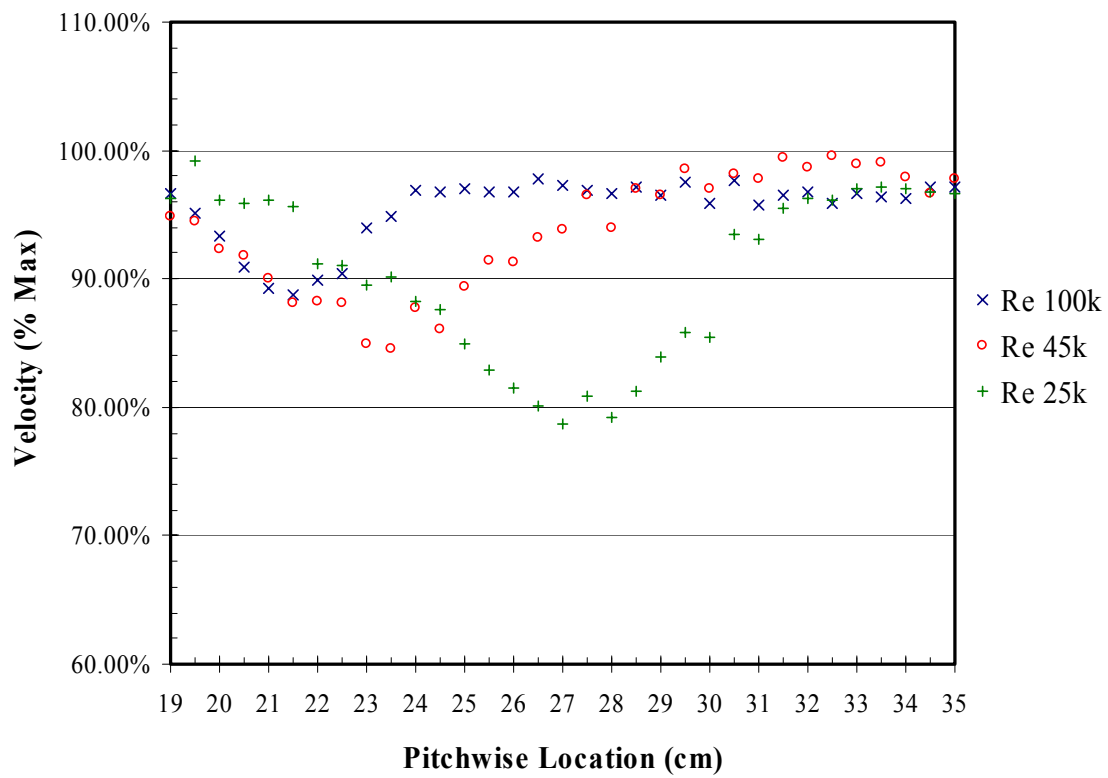


Figure 93. Wake velocity profiles for baseline Pak-B at $Tu = 1\%$

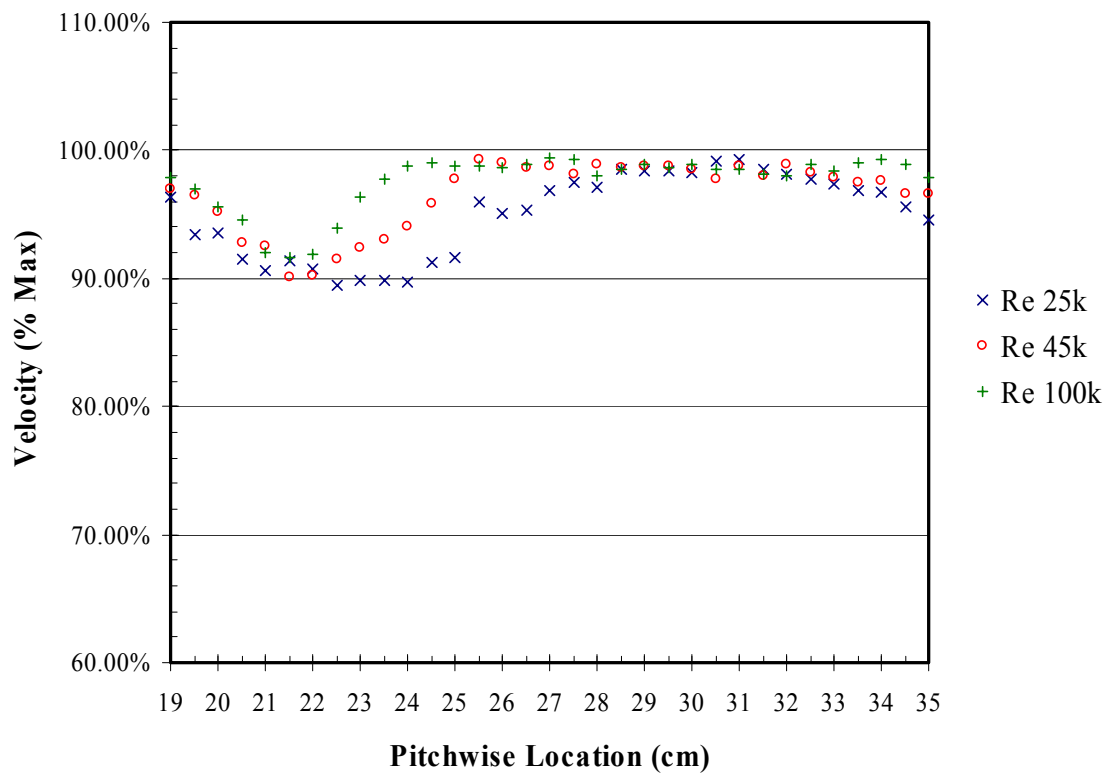


Figure 94. Wake velocity profiles for baseline Pak-B at $Tu = 4\%$

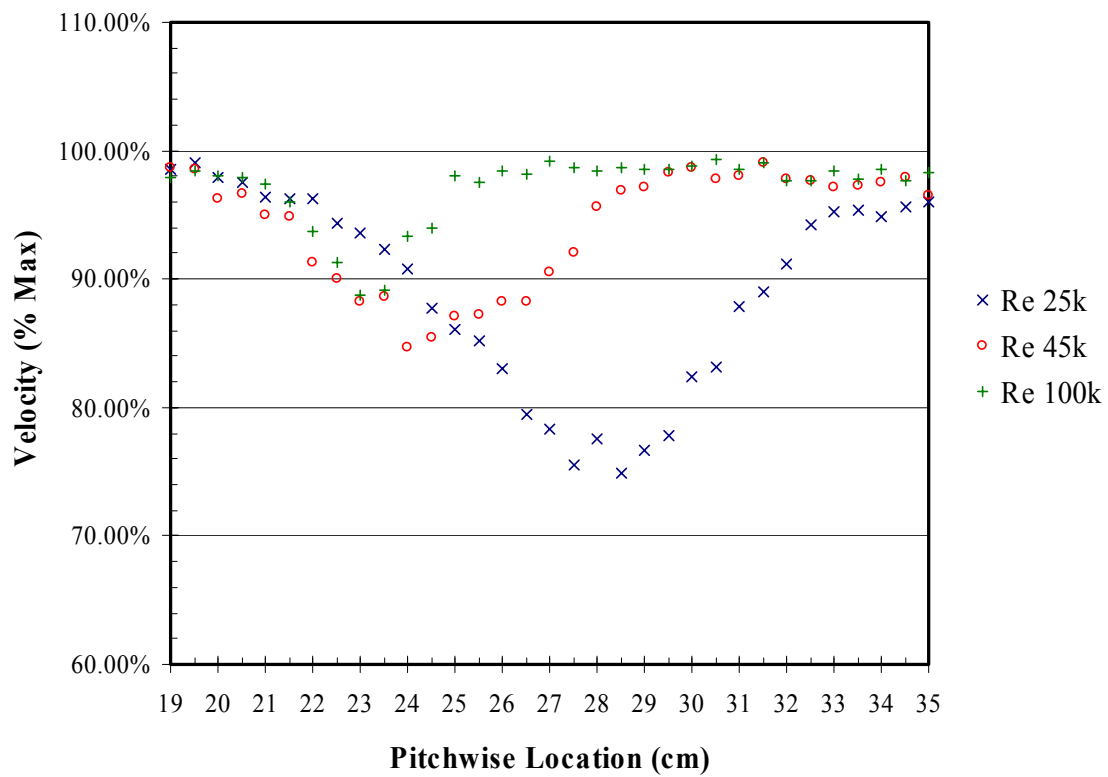


Figure 95. Wake velocity profiles for Pak-B with asymmetric dimples at 50% at $Tu = 1\%$

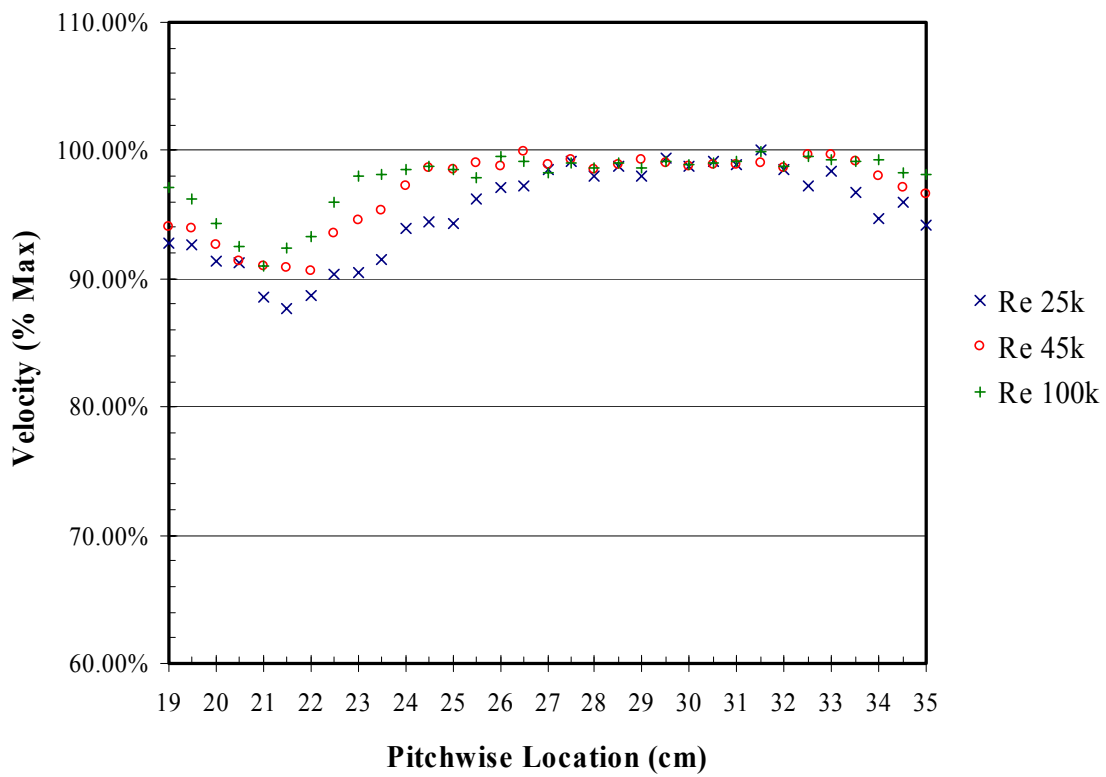


Figure 96. Wake velocity profiles for Pak-B with asymmetric dimples at 50% at $Tu = 4\%$

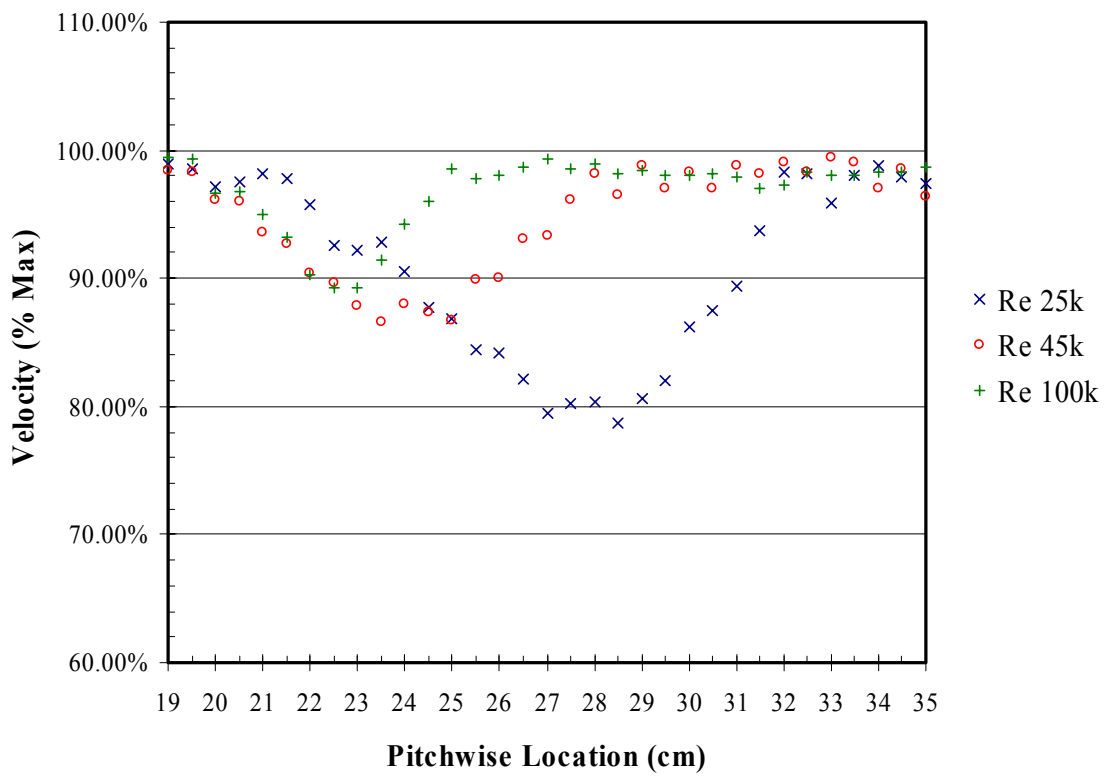


Figure 97. Wake velocity profiles for Pak-B with asymmetric dimples at 55% at Tu 1%

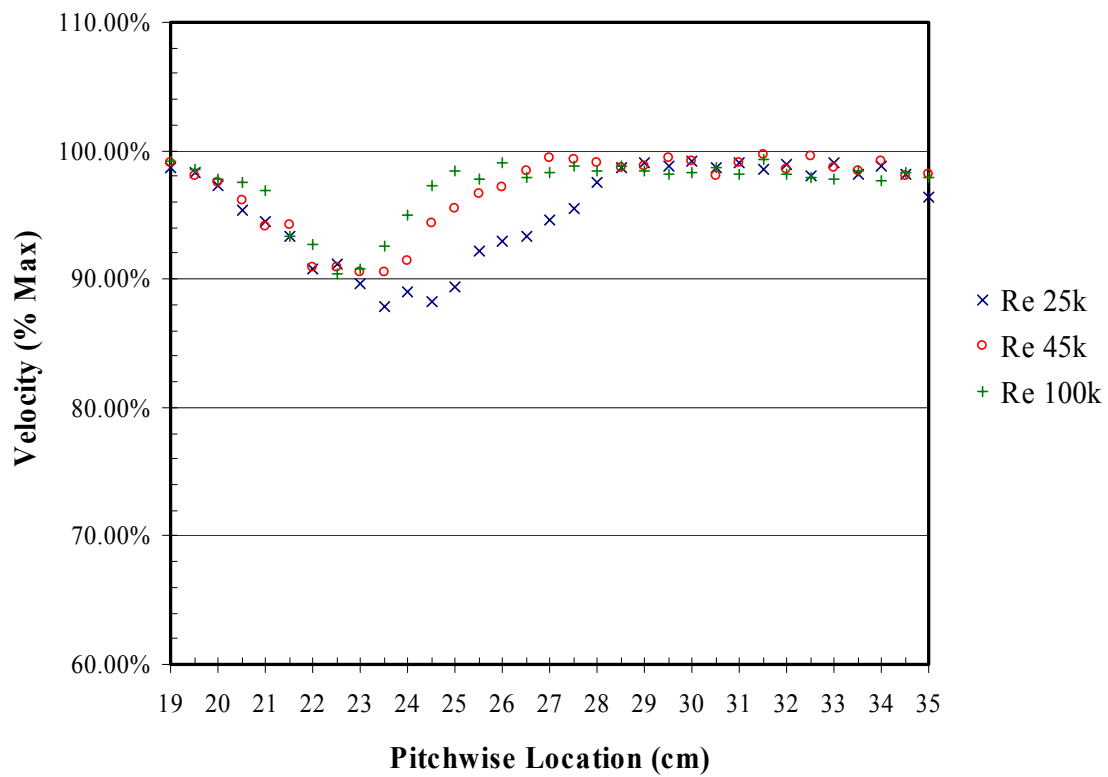


Figure 98. Wake velocity profiles for Pak-B with asymmetric dimples at 55% at $Tu = 4\%$

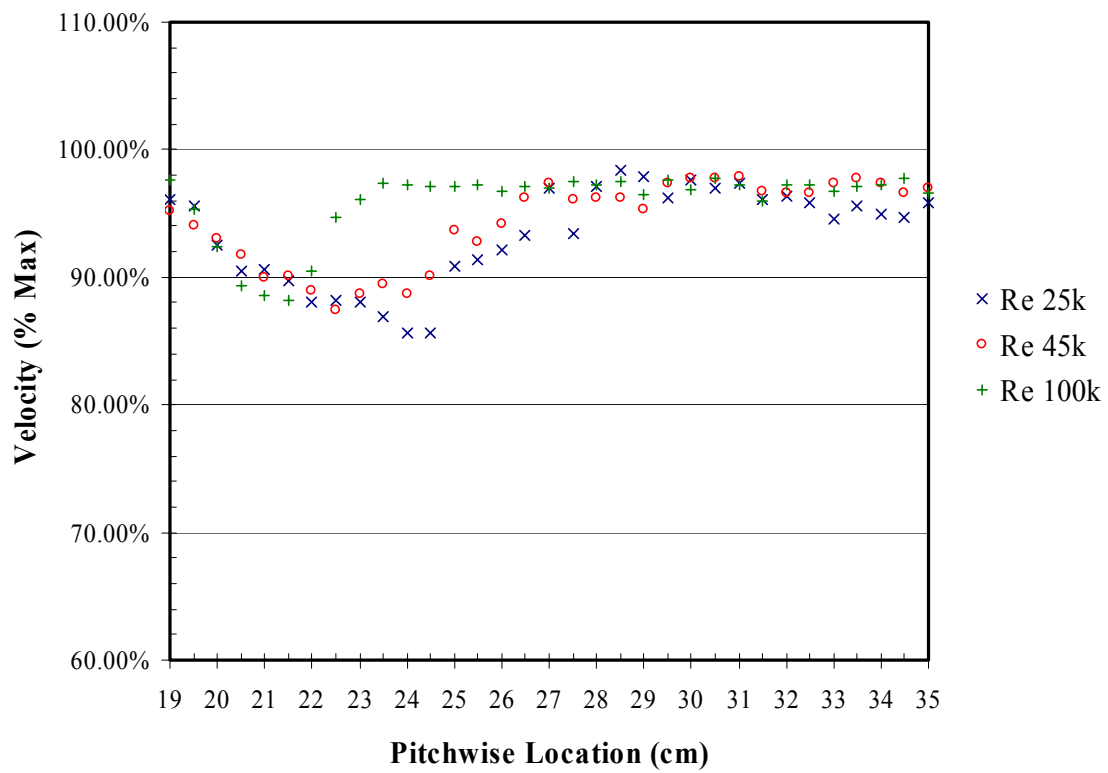


Figure 99. Wake velocity profiles for Pak-B with asymmetric dimples at 65% at Tu 1%

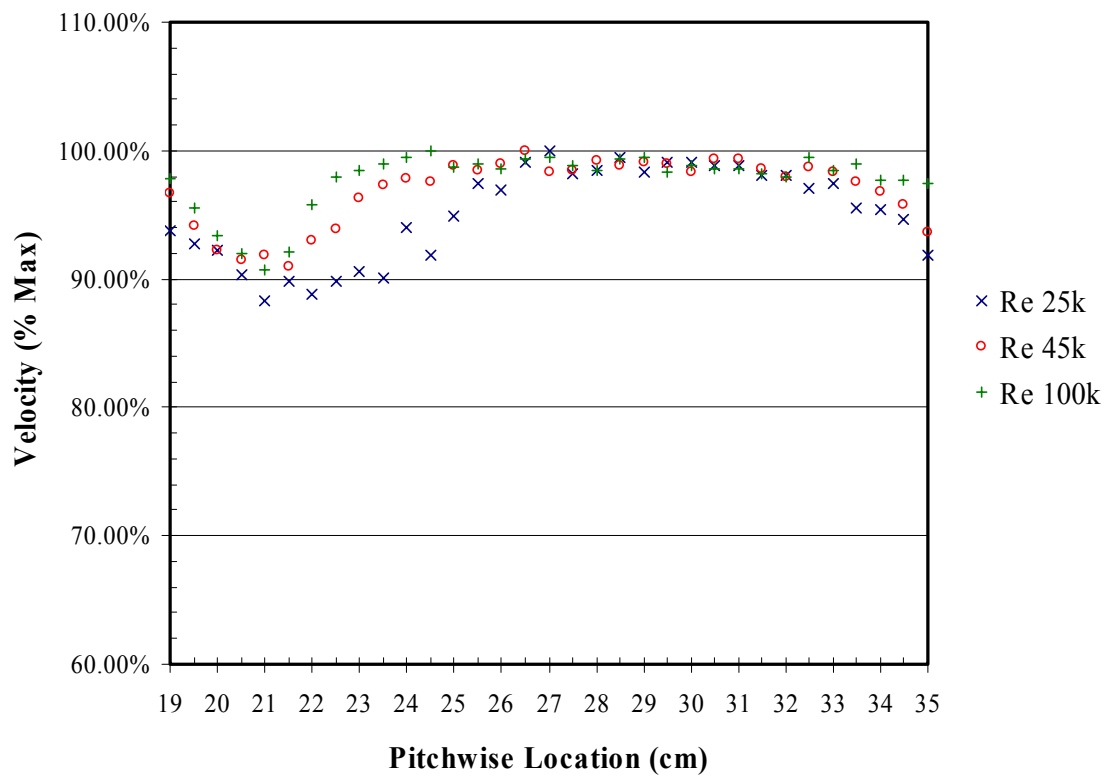


Figure 100. Wake velocity profiles for Pak-B with asymmetric dimples at 65% at $Tu = 4\%$

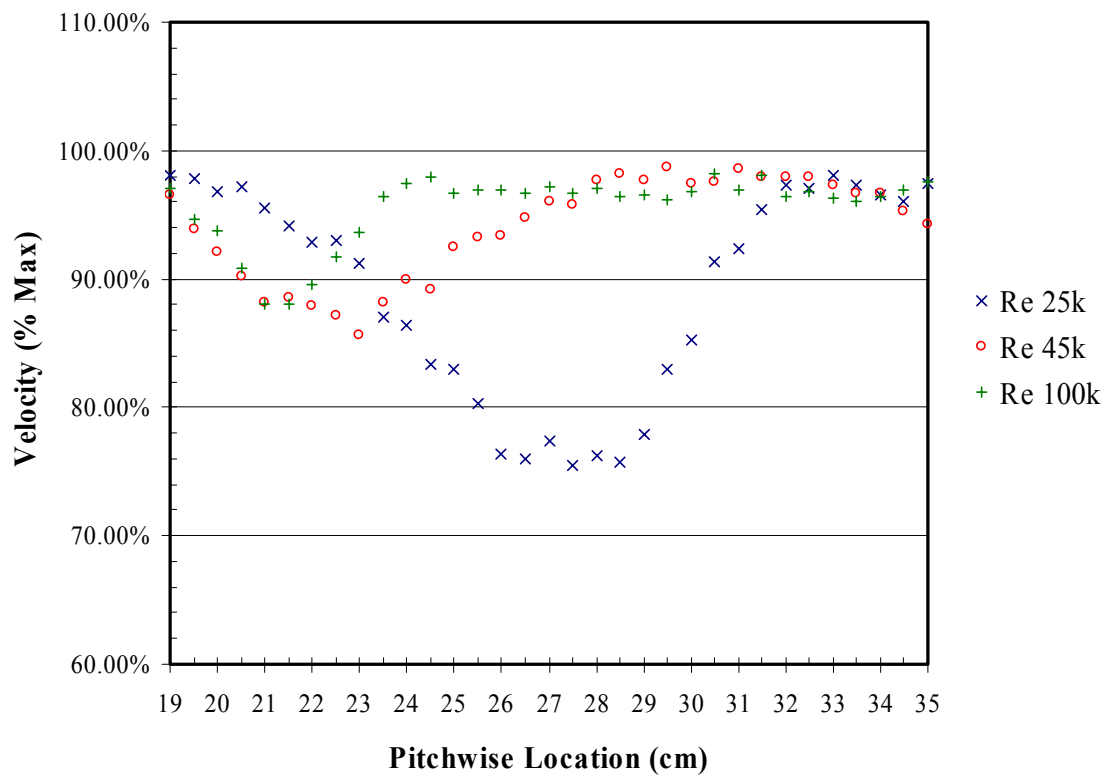


Figure 101. Wake velocity profiles for Pak-B with spherical dimples at 50% at $Tu = 1\%$

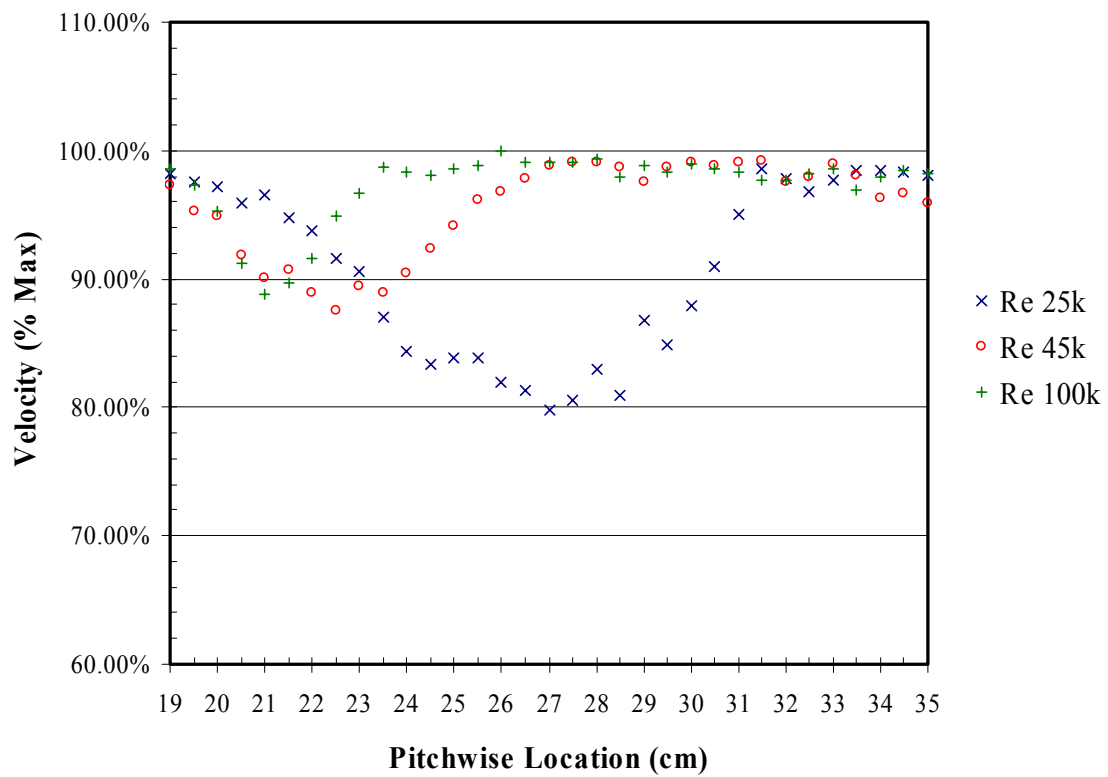


Figure 102. Wake velocity profiles for Pak-B with spherical dimples at 50% at Tu 4%

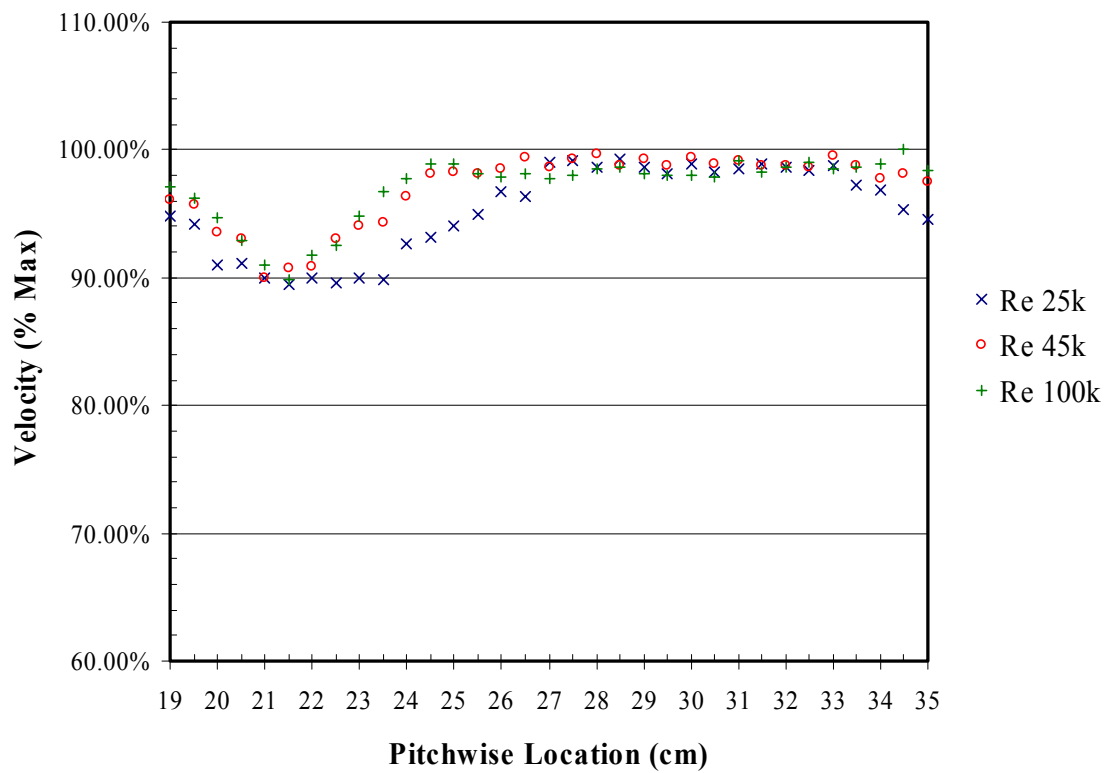


Figure 103. Wake velocity profiles for Pak-B with spherical dimples at 55% at Tu 1%

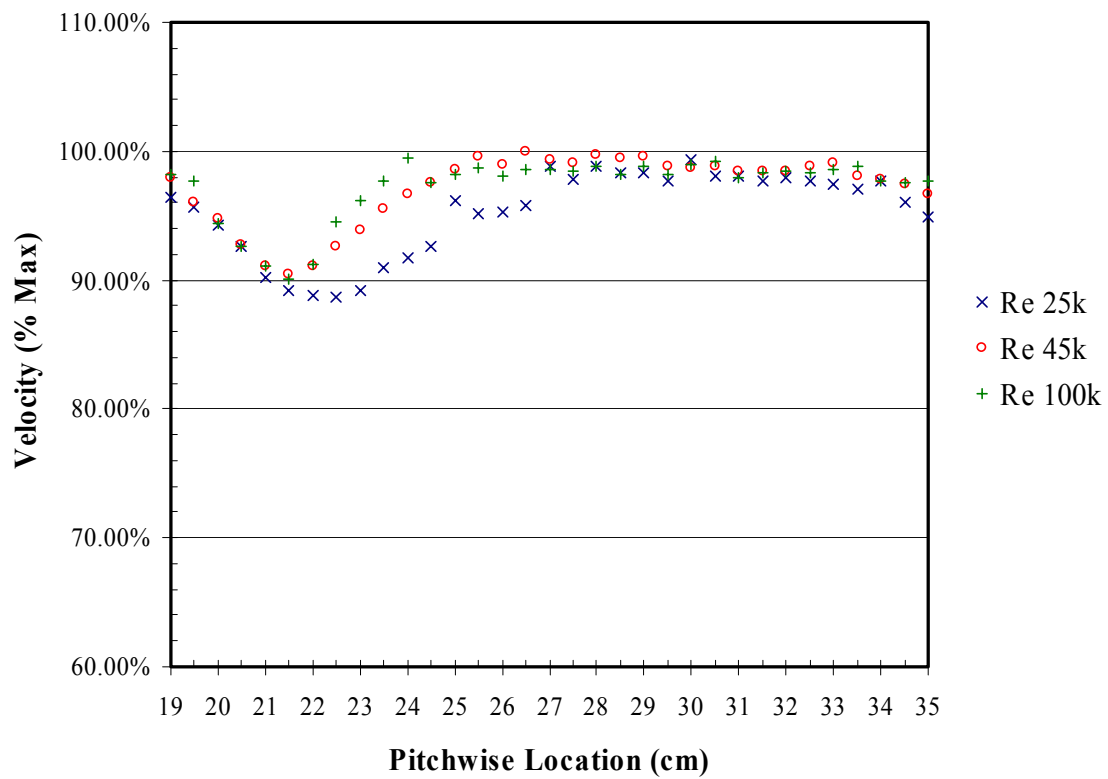


Figure 104. Wake velocity profiles for Pak-B with spherical dimples at 55% at Tu 4%

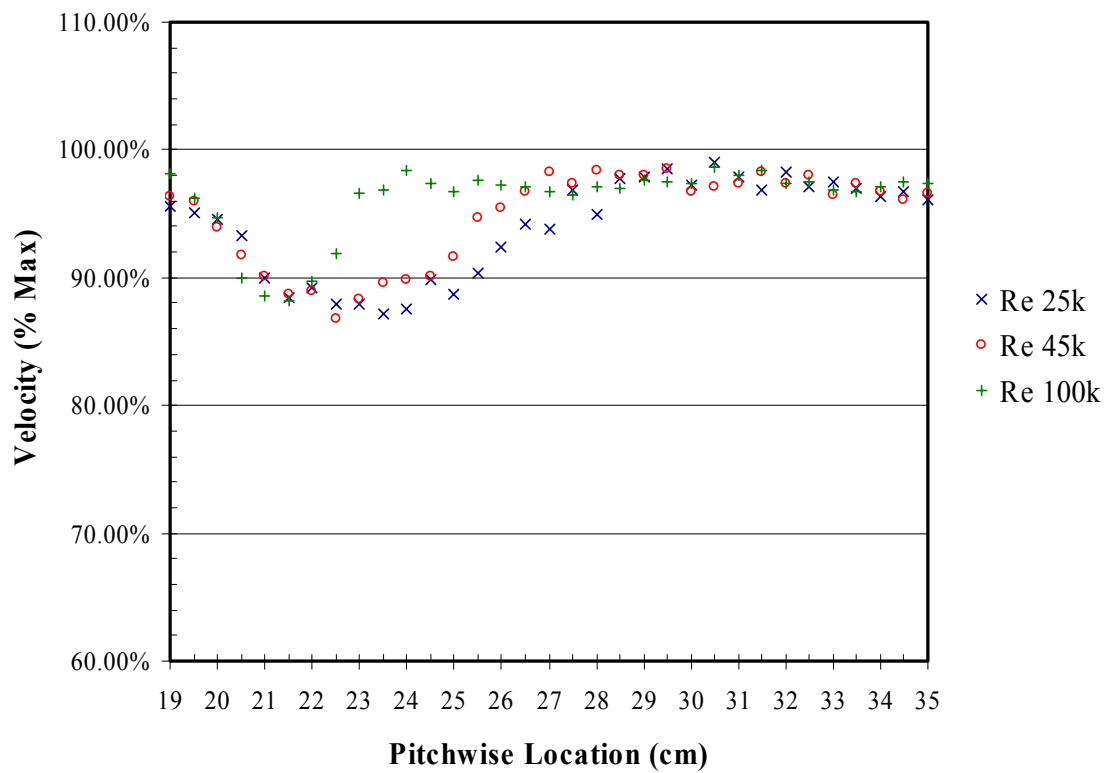


Figure 105. Wake velocity profiles for Pak-B with spherical dimples at 65% at Tu 1%

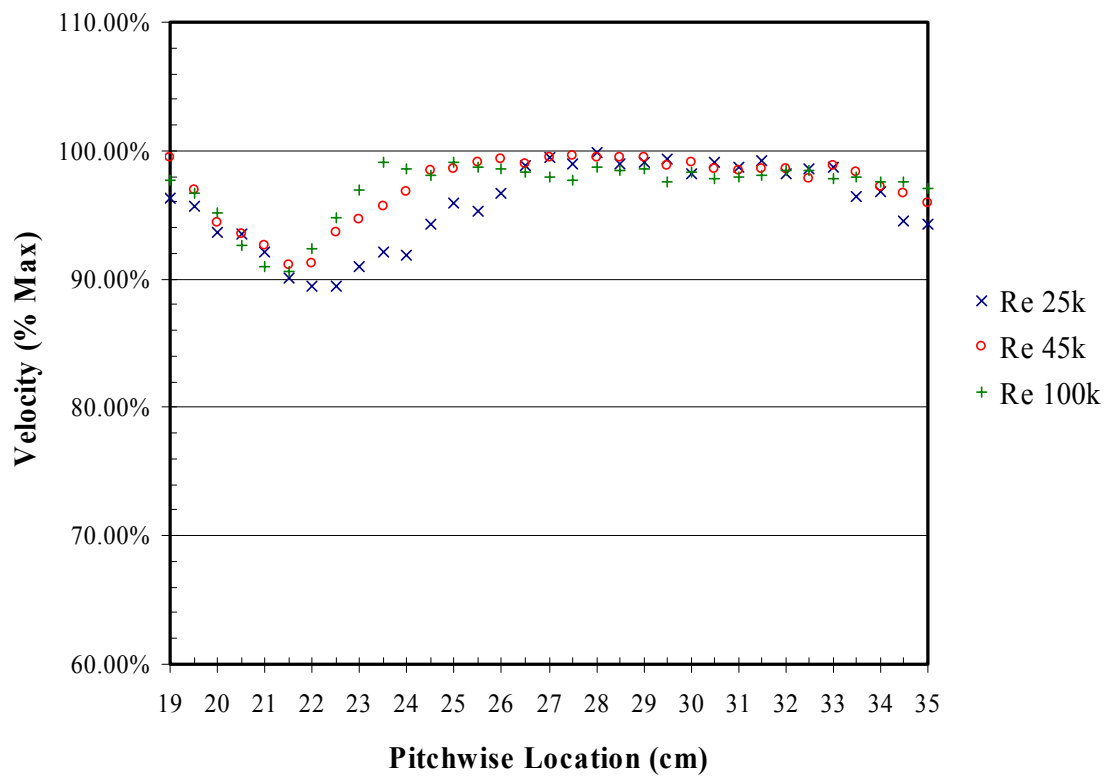


Figure 106. Wake velocity profiles for Pak-B with spherical dimples at 65% at Tu 4%

APPENDIX D. Local Total Pressure Loss Coefficient Profiles

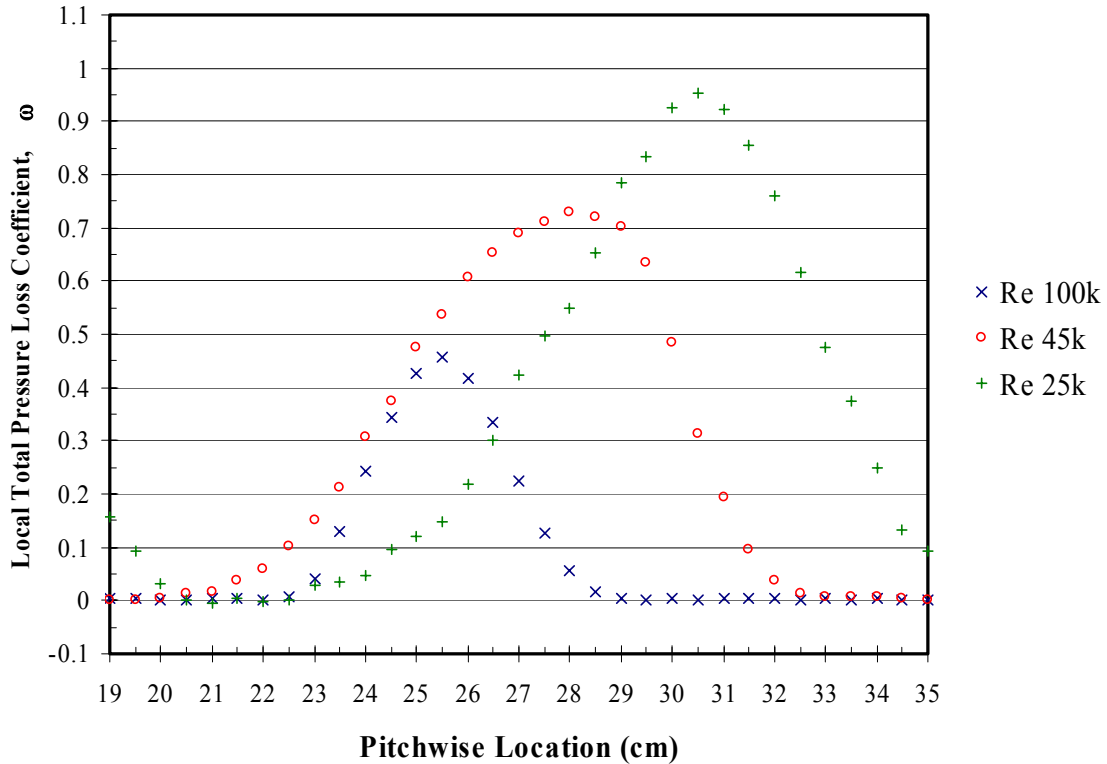


Figure 107. Total pressure loss coefficient profiles for a baseline Pak-B at $Tu = 1\%$

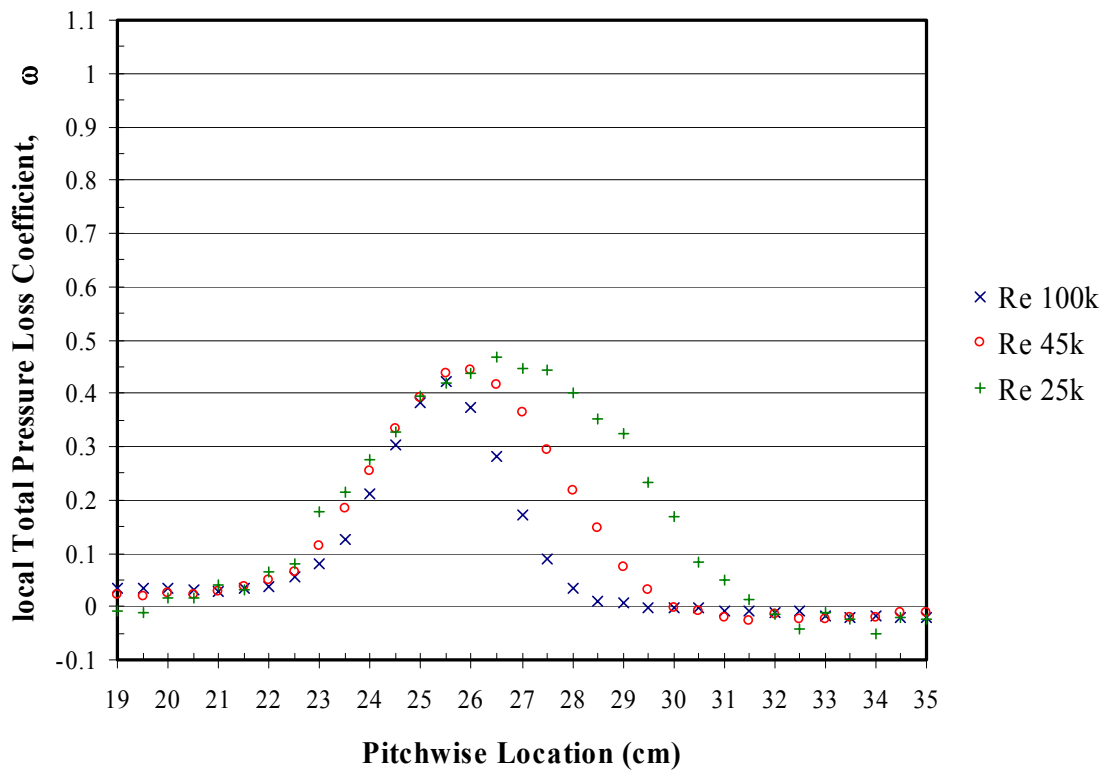


Figure 108. Total pressure loss coefficient profiles for a baseline Pak-B at Tu 4%

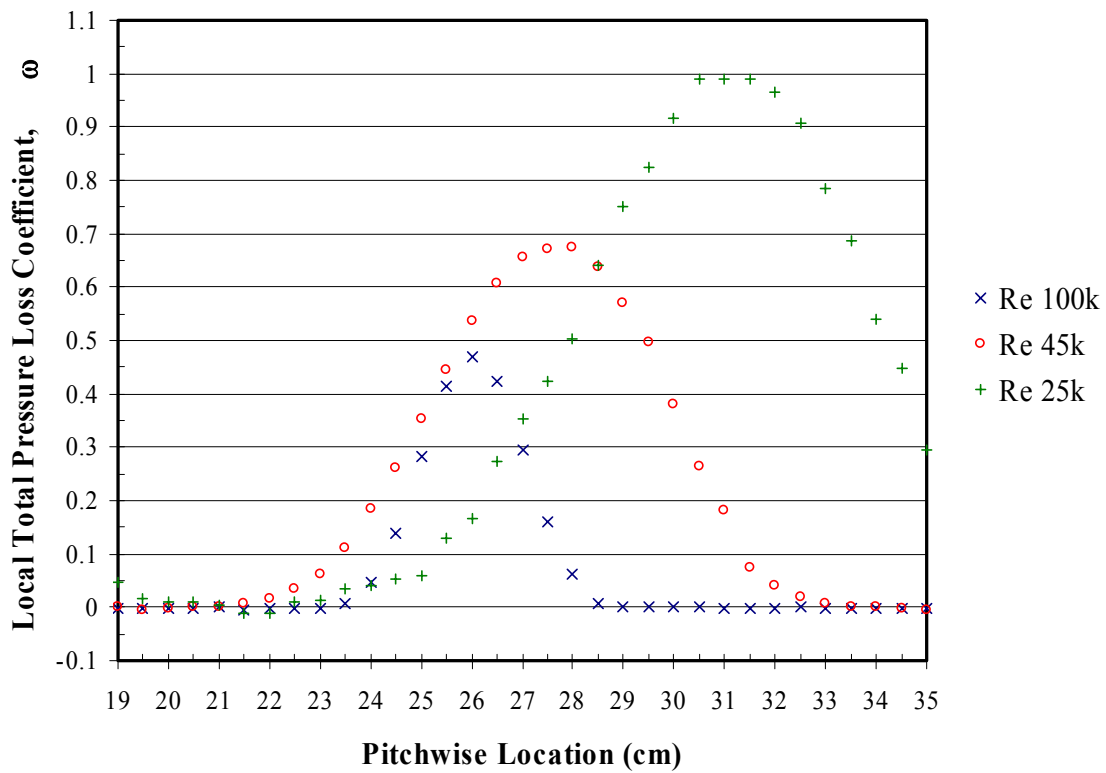


Figure 109. Total pressure loss coefficient profiles for a Pak-B with asymmetric dimples at 50% axial chord at $Tu 1\%$

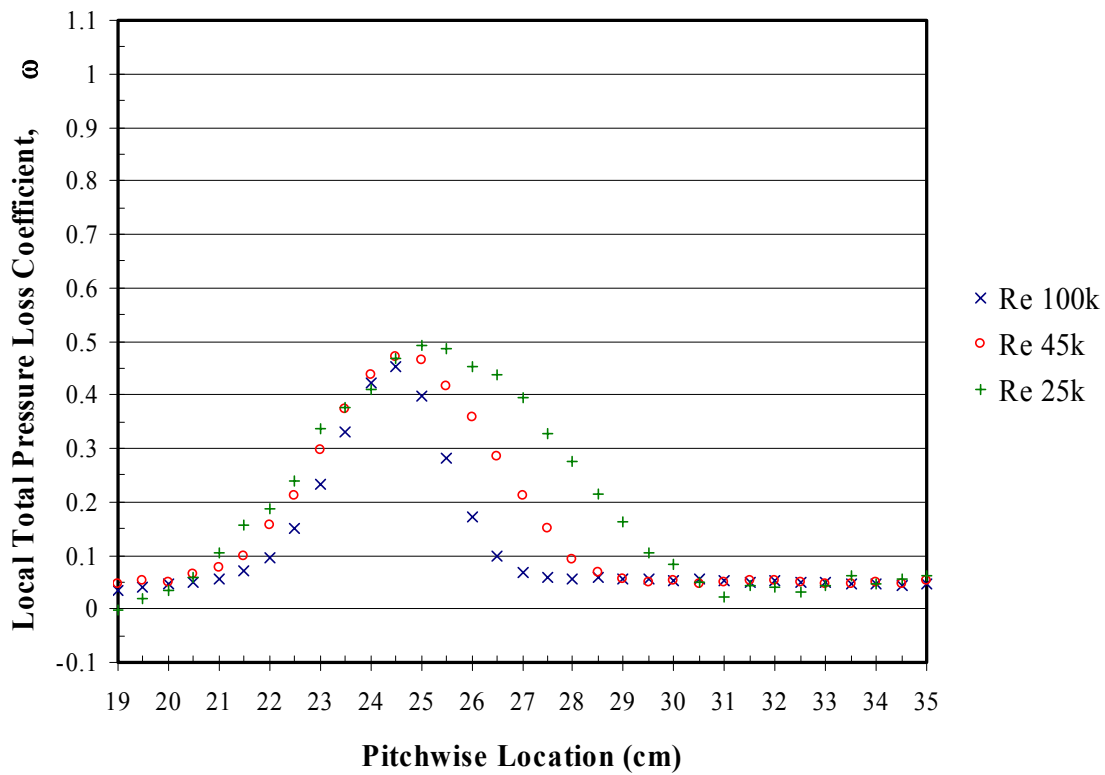


Figure 110. Total pressure loss coefficient profiles for a Pak-B with asymmetric dimples at 50% axial chord at $Tu = 4\%$

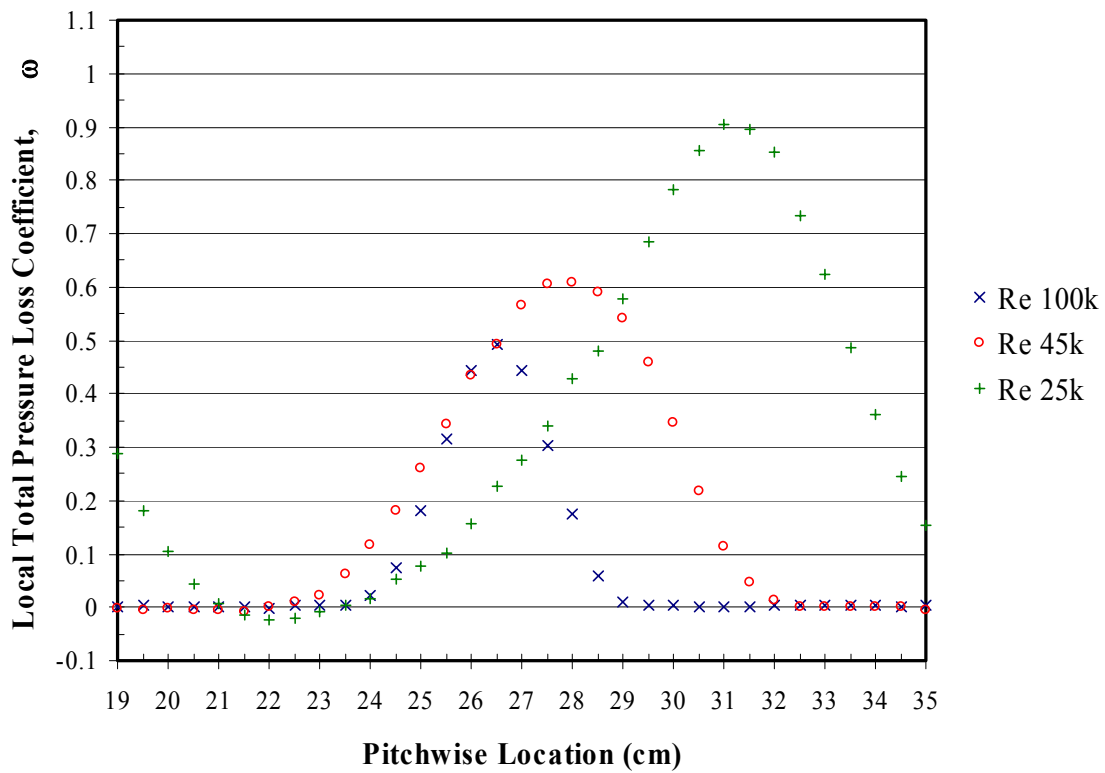


Figure 111. Total pressure loss coefficient profiles for a Pak-B with asymmetric dimples at 55% axial chord at Tu 1%

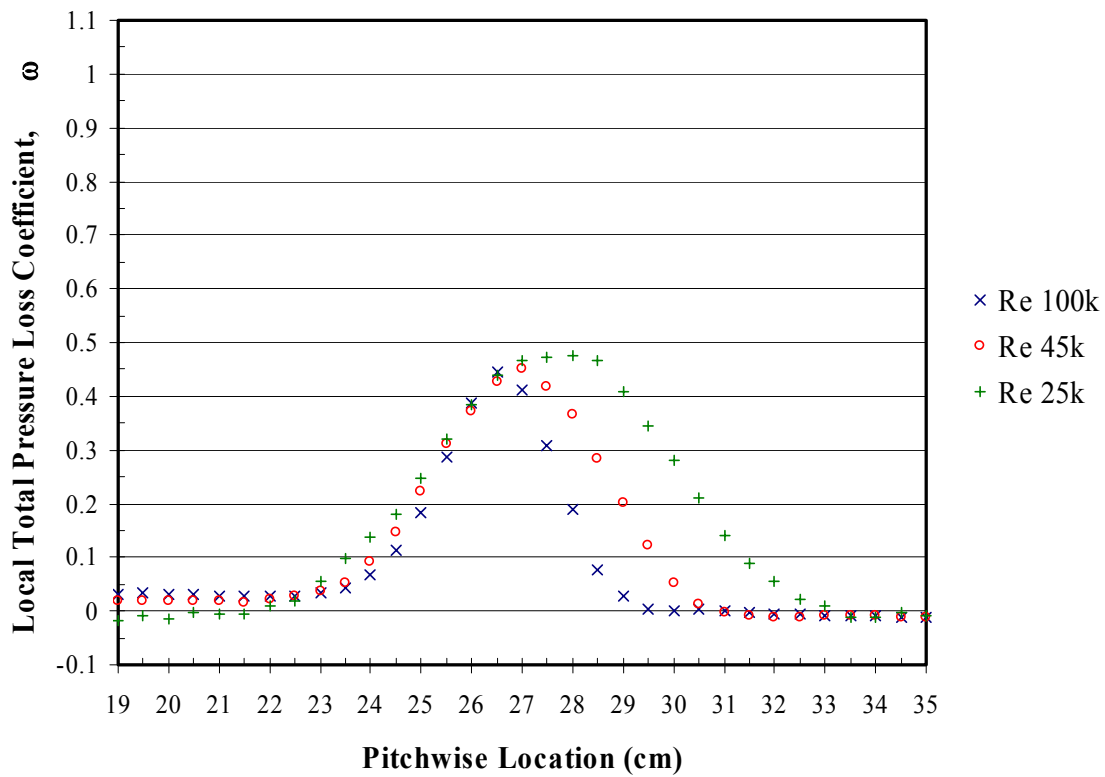


Figure 112. Total pressure loss coefficient profiles for a Pak-B with asymmetric dimples at 55% axial chord at Tu 4%

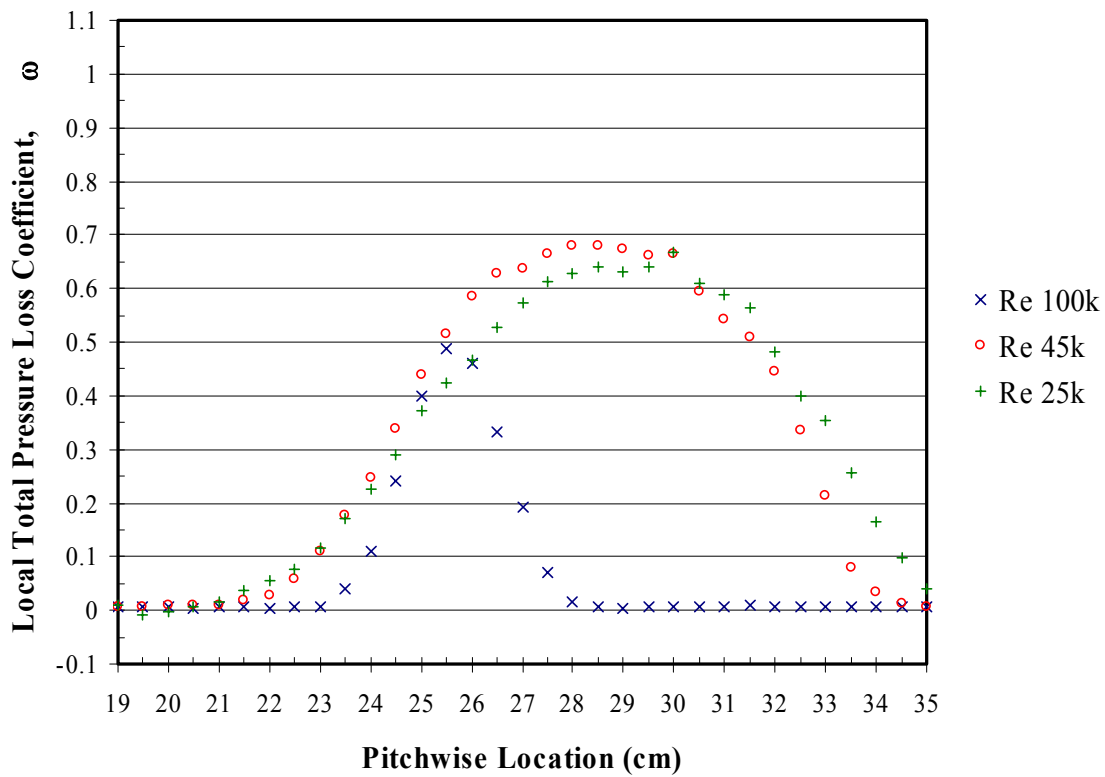


Figure 113. Total pressure loss coefficient profiles for a Pak-B with asymmetric dimples at 65% axial chord at Tu 1%

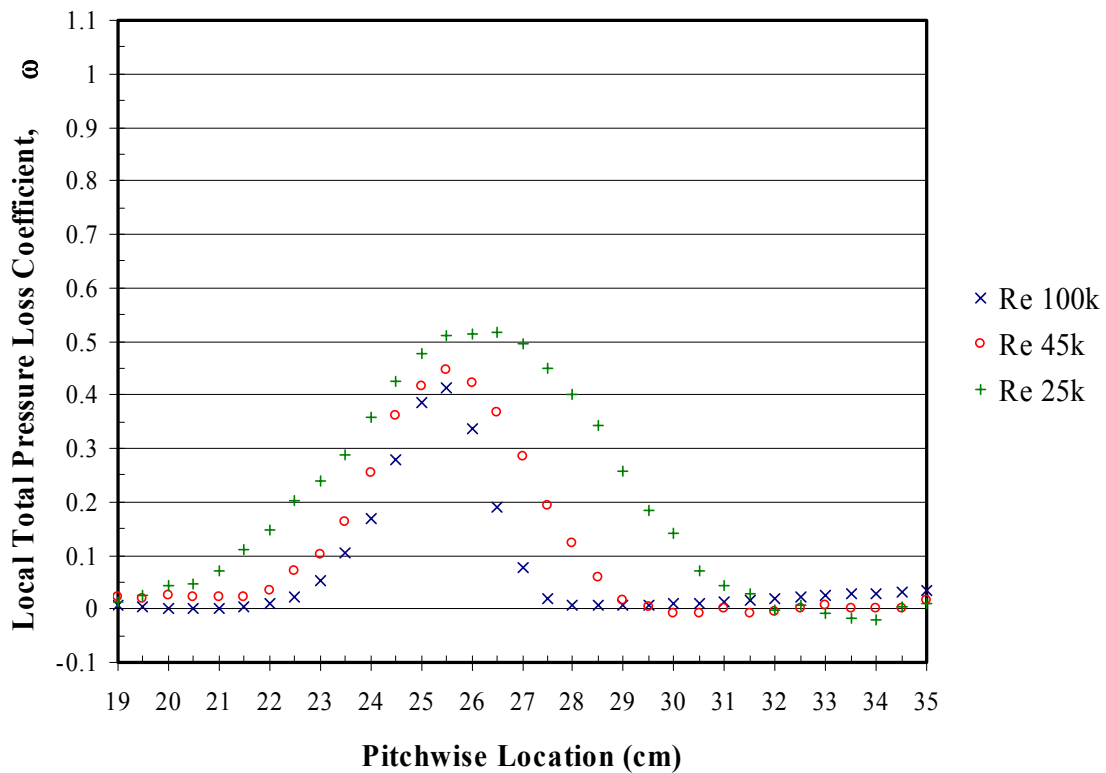


Figure 114. Total pressure loss coefficient profiles for a Pak-B with asymmetric dimples at 65% axial chord at $Tu\ 4\%$

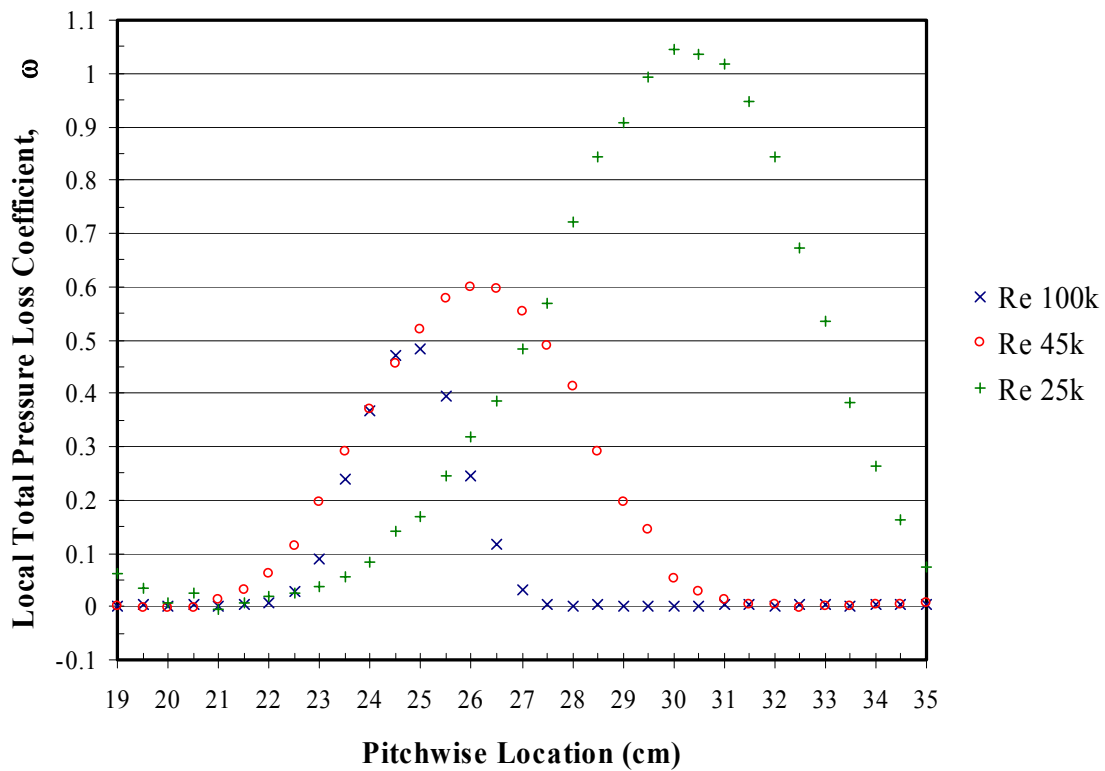


Figure 115. Total pressure loss coefficient profiles for a Pak-B with spherical dimples at 50% axial chord at Tu 1%

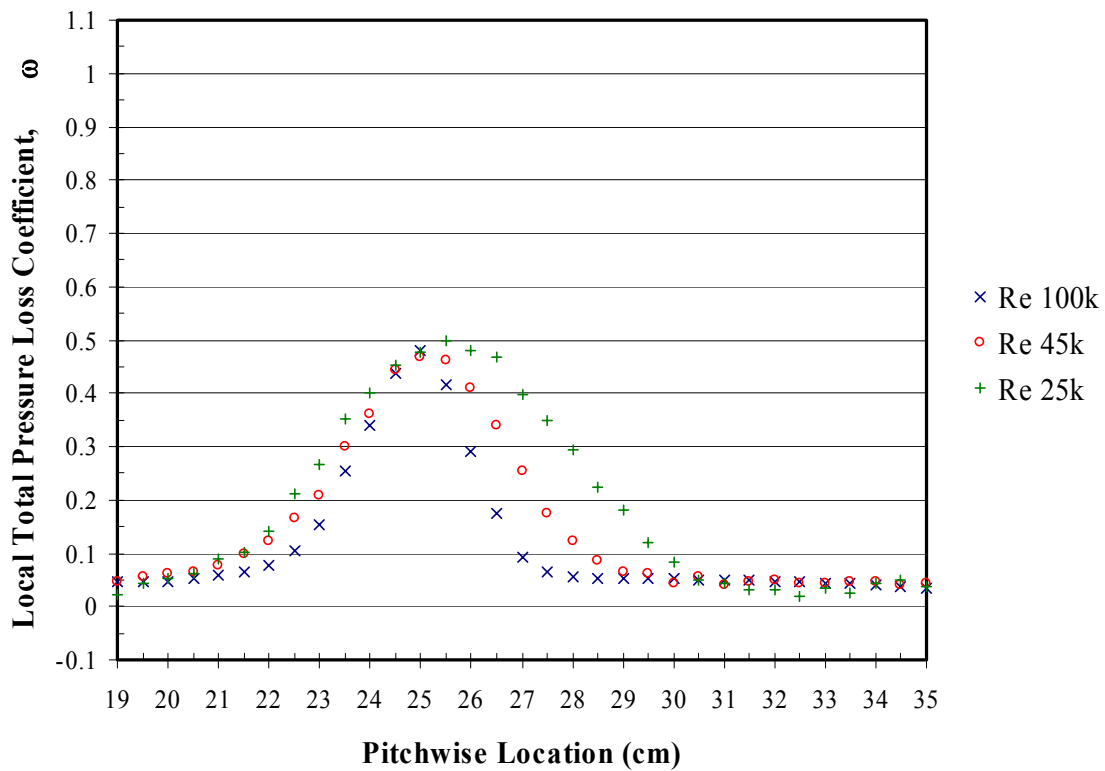


Figure 116. Total pressure loss coefficient profiles for a Pak-B with spherical dimples at 50% axial chord at Tu 4%

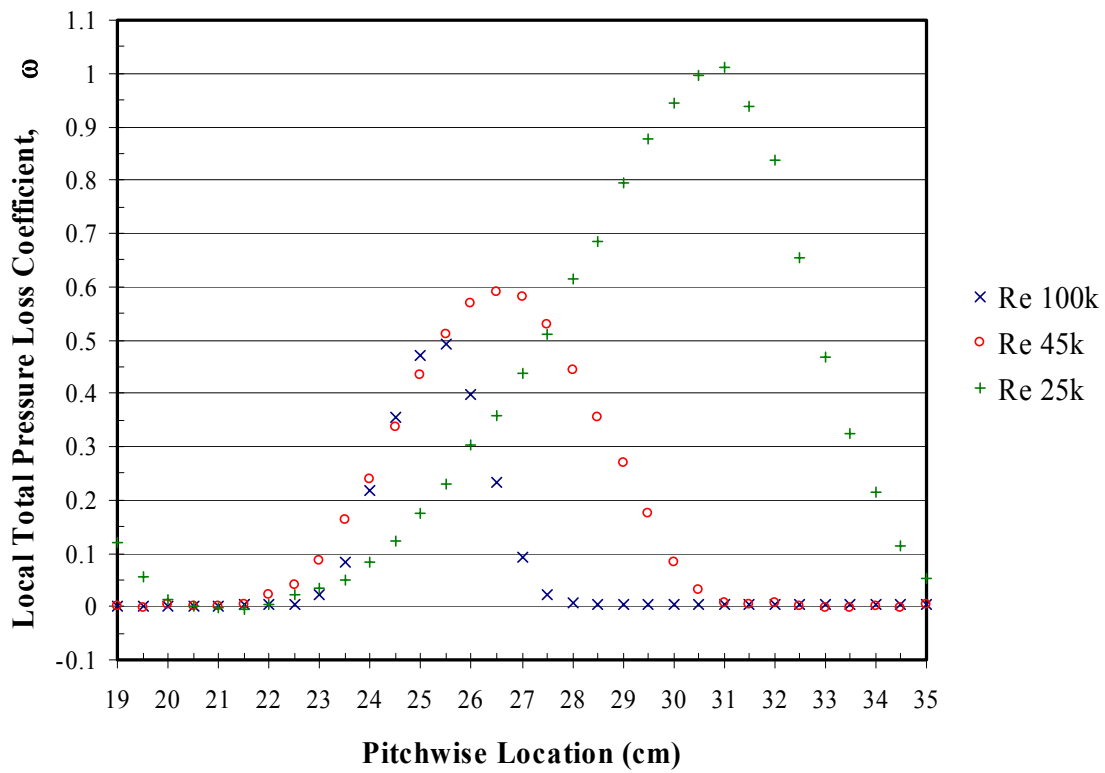


Figure 117. Total pressure loss coefficient profiles for a Pak-B with spherical dimples at 55% axial chord at Tu 1%

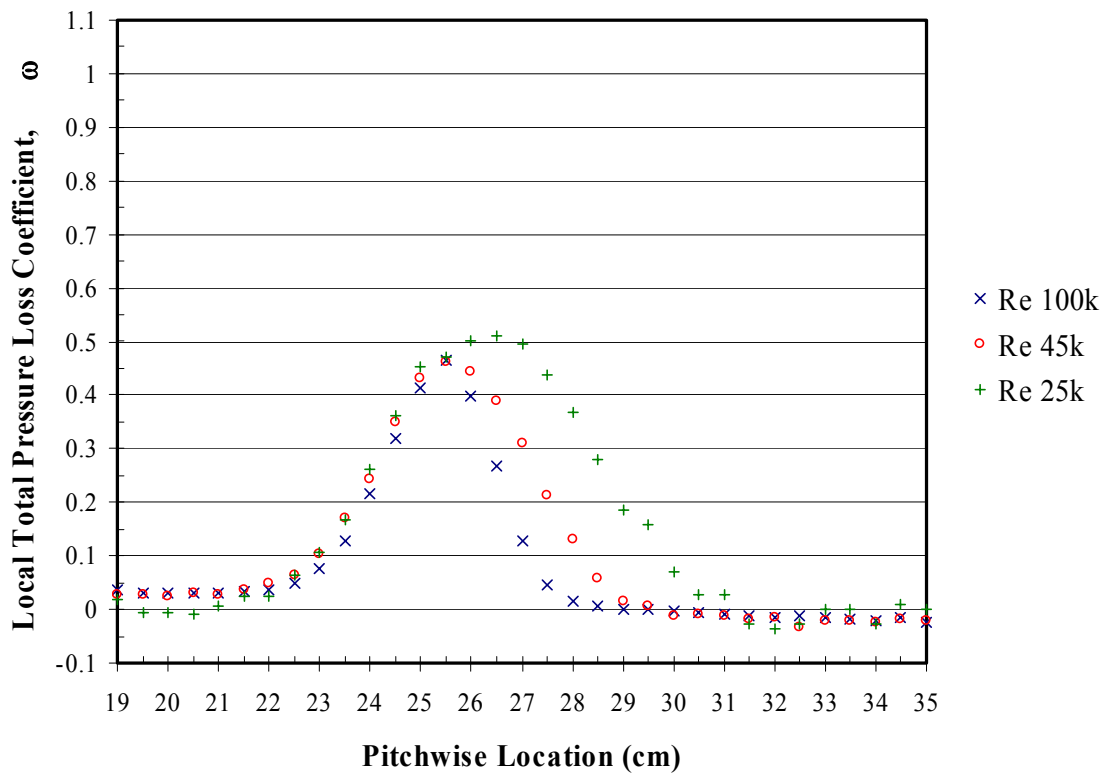


Figure 118. Total pressure loss coefficient profiles for a Pak-B with spherical dimples at 55% axial chord at Tu 4%

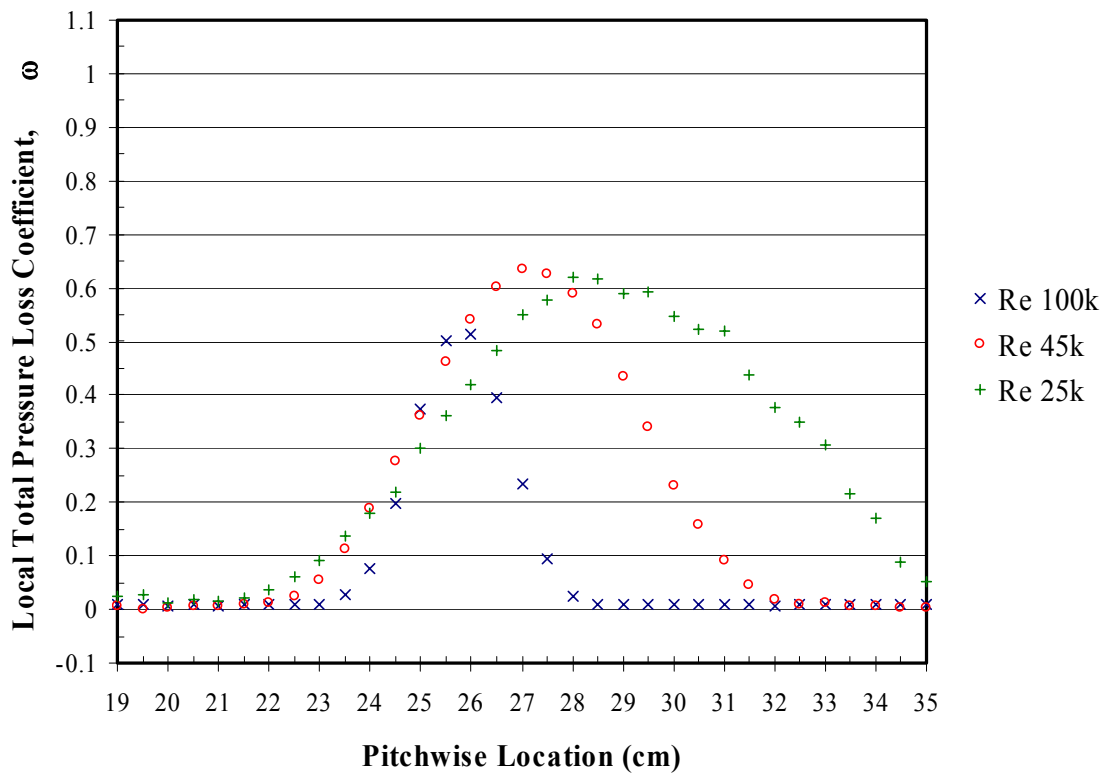


Figure 119. Total pressure loss coefficient profiles for a Pak-B with spherical dimples at 65% axial chord at Tu 1%

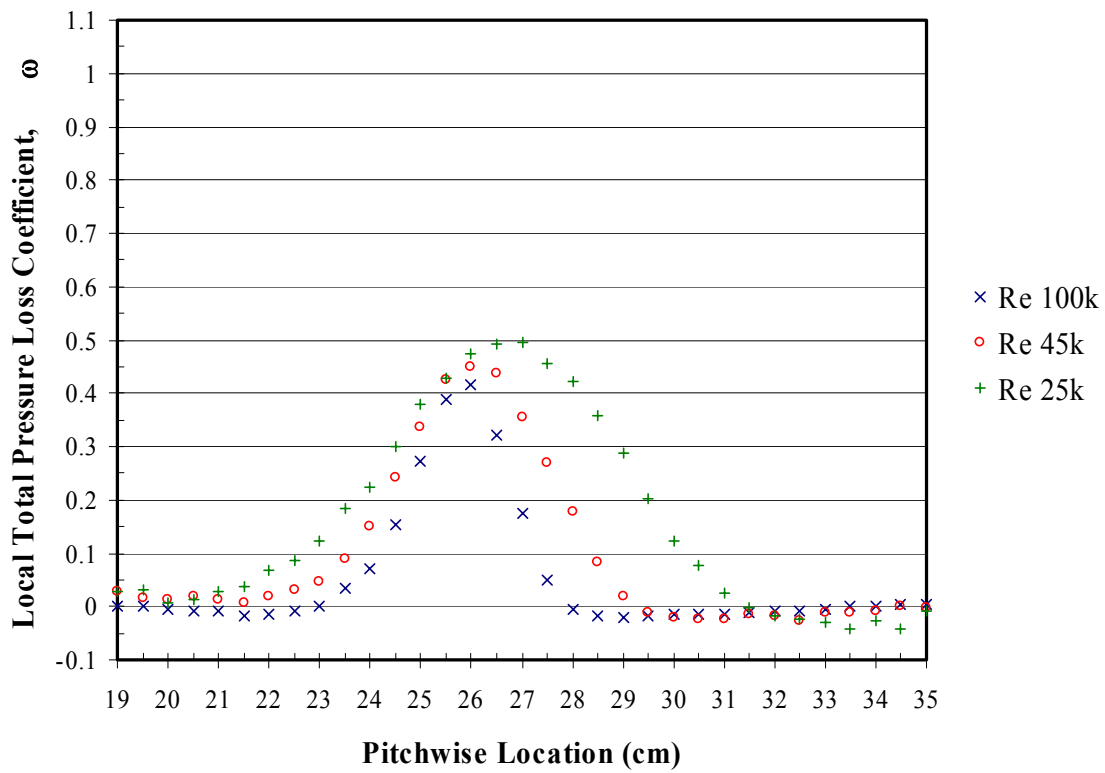


Figure 120. Total pressure loss coefficient profiles for a Pak-B with spherical dimples at 65% axial chord at $Tu = 4\%$

VITA

Captain Kurt P. Rouser graduated from San Rafael High School, California in June 1991. He entered the United States Air Force Academy (USAFA), Colorado where he graduated with a Bachelor of Science degree in Aeronautical Engineering in May 1995 and was subsequently granted a regular commission in the USAF.

His first assignment was at Wright-Patterson AFB, Ohio as a turbine engine technology analyst for the National Air Intelligence Center in August 1995. While stationed in Ohio, he was awarded a scholarship from the Dayton Area Graduate Studies Institute and began work on a Master of Science degree at the Air Force Institute of Technology (AFIT). In August 1998, he was assigned to the Propulsion Directorate, Oklahoma City Air Logistics Center at Tinker AFB, Oklahoma where he served as a TF33 maintenance engineer, a TF33 test engineer and ultimately as executive officer to the Director of Propulsion. While stationed in Oklahoma, he completed a Master of Science degree in Aviation Science from Oklahoma State University (OSU) in December 1999. Subsequently, he taught courses in jet engine operation and advanced aircraft systems as adjunct professor at OSU and Southeastern OSU. In November 2000, he was briefly assigned to the C-135 System Program Office as a mechanical systems engineer. In September 2001, he entered the AFIT Graduate School of Engineering and Management for a Master of Science in Aeronautical Engineering. Upon graduation, he will be assigned to the USAFA Department of Aeronautics.

REPORT DOCUMENTATION PAGE				<i>Form Approved OMB No. 074-0188</i>
<p>The public reporting burden for this collection of information is estimated to average 1 hour per response, including the time for reviewing instructions, searching existing data sources, gathering and maintaining the data needed, and completing and reviewing the collection of information. Send comments regarding this burden estimate or any other aspect of the collection of information, including suggestions for reducing this burden to Department of Defense, Washington Headquarters Services, Directorate for Information Operations and Reports (0704-0188), 1215 Jefferson Davis Highway, Suite 1204, Arlington, VA 22202-4302. Respondents should be aware that notwithstanding any other provision of law, no person shall be subject to a penalty for failing to comply with a collection of information if it does not display a currently valid OMB control number.</p> <p>PLEASE DO NOT RETURN YOUR FORM TO THE ABOVE ADDRESS.</p>				
1. REPORT DATE (DD-MM-YYYY) 12-12-2002		2. REPORT TYPE Master's Thesis		3. DATES COVERED (From – To) Oct 2001 – Dec 2002
4. TITLE AND SUBTITLE USE OF DIMPLES TO SUPPRESS BOUNDARY LAYER SEPARATION ON A LOW PRESSURE TURBINE BLADE			5a. CONTRACT NUMBER 5b. GRANT NUMBER 5c. PROGRAM ELEMENT NUMBER	
6. AUTHOR(S) Rouser, Kurt P., Captain, USAF			5d. PROJECT NUMBER ENR #2002-045 5e. TASK NUMBER 5f. WORK UNIT NUMBER	
7. PERFORMING ORGANIZATION NAMES(S) AND ADDRESS(S) Air Force Institute of Technology Graduate School of Engineering and Management (AFIT/EN) 2950 P Street, Building 640 WPAFB OH 45433-7765			8. PERFORMING ORGANIZATION REPORT NUMBER AFIT/GAE/ENYS/02-13	
9. SPONSORING/MONITORING AGENCY NAME(S) AND ADDRESS(ES) AFRL/PRTT Attn: Dr. Rolf Sondergaard 1950 5 th Street WPAFB OH 45433-7251			10. SPONSOR/MONITOR'S ACRONYM(S) 11. SPONSOR/MONITOR'S REPORT NUMBER(S)	
12. DISTRIBUTION/AVAILABILITY STATEMENT APPROVED FOR PUBLIC RELEASE; DISTRIBUTION UNLIMITED.				
13. SUPPLEMENTARY NOTES				
14. ABSTRACT <p>Flow separation on a low pressure turbine blade is explored at Reynolds numbers of 25k, 45k and 100k. Experimental data is collected in a low-speed, draw-down wind tunnel using a cascade of eight Pak-B blades. Flow is examined from measurements of blade surface pressures, boundary layer parameters, exit velocities, and total pressure losses across the blade. Two recessed dimple shapes are assessed for suppressing flow separation and associated losses. One dimple is spherical, and the second is asymmetric, formed from a full dimple spanwise half-filled. A single row of each dimple shape is tested at 50%, 55% and 65% axial chord. Symmetric dimples reduce separation losses by as much as 28%, while asymmetric dimples reduce losses by as much as 23%. A complementary three-dimensional computational study is conducted to visualize local flow structure. Computational analysis uses Gridgen v13.3 as a mesh generator, Fluent[®] v6.0 as a flow solver and FIELDVIEW[®] v8.0 for graphic display and analysis. Computational results for Pak-B blades at a Reynolds number of 25k indicate that both dimple shapes cause a span-wise vortex to rollup within the dimple and provide a localized pressure drop.</p>				
15. SUBJECT TERMS <p>Laminar Boundary Layer Separation, Boundary Layer Transition, Turbulent Boundary Layer, Boundary Layer Trips, Passive Boundary Layer Controls, Passive Flow Controls, Low Pressure Turbine Blade, Gas Turbine Engine Low Reynolds Number, Computational Fluid Dynamics</p>				
16. SECURITY CLASSIFICATION OF:		17. LIMITATION OF ABSTRACT	18. NUMBER OF PAGES	19a. NAME OF RESPONSIBLE PERSON Dr. Paul I. King (ENY) 19b. TELEPHONE NUMBER (Include area code) (937) 255-3636, ext 4628; e-mail: Paul.King@afit.edu
a. REPORT U	b. ABSTRACT U	c. THIS PAGE U	UU	202